DEVELOPMENT OF MALEIMIDE DERIVED FLUORESCENT ORGANIC MOLECULES TO ORGANOMETALLIC COMPLEXES

by

MARIA PERVEZ

Supervisor: Rachel K. O'Reilly

A thesis submitted to the University of Birmingham for the degree of

DOCTOR OF PHILOSOPHY

UNIVERSITY OF BIRMINGHAM

School of Chemistry

College of Engineering and Physical Sciences

University of Birmingham

June 2022

Abstract

Maleimide-based fluorophores have been effectively employed as bio-probes due to their attractive photophysical attributes, such as small size, high responsivity, and high reactivity while being non-invasive. However, their applicability in the biosystems has been limited due to the fluorescence quenching, caused by the interactions with the polar protic solvents. Therefore, this work is focused on improving the fluorescence in polar media through chemical modifications. For this purpose, the maleimide was functionalized with electron-withdrawing groups, which led to an increased fluorescence efficiency in the solution-state by reducing the interaction with protic solvents; and in the solid-state through the suppression of stacking interactions, thus providing a dual-state emission mechanism. Furthermore, the maleimide derivatives were successfully used as ligands to develop the fluorescent half-sandwich transition metal complexes, thus expanding the scope for their use as hybrid probes. Additionally, the coordination of maleimide-based chromophores to the lanthanide metal ions enhances their luminescence, by overruling the ligand-to-metal charge transfer state with ligand-centered transitions.

Thesis overview

Chapter 1 covers the general concepts of the thesis, and background literature is reviewed. This chapter provides the overview of the key concepts occurring during the process of photoluminescence and different quenching mechanisms. The remaining sections focus on maleimide-based organometallic complexes, their fluorescence and applications.

Substituted maleimides undergo fluorescence quenching in polar solvents, which limits their applicability for various biochemical applications. Chapter 2 covers the synthesis of small size substituted maleimide fluorophores through chemical modifications, and examines the changes in their fluorescence properties. This work led to the observation of fluorescence in both solution and solid-state for the synthesized derivatives, and provides mechanistic insight into dual state emission behavior.

Chapter 3 presents the synthesis of fluorescent half-sandwich transition metal maleimide complexes. The influence of complexation on the fluorescence properties of the maleimide is investigated by analyzing the optical properties of the developed fluorescent complexes. Electrochemical studies of the half-sandwich complexes describes on-to-off fluorescence switch upon oxidation.

Chapter 4 focuses on the synthesis of maleimide ligands for coordination with lanthanide metal ions. The dichloromaleimide and aminochloromaleimide derived ligands are used as chromophore ligands to enhance the luminescence of lanthanide metal ions.

Dedicated

To My Parents

For their endless love, support and encouragement.

Acknowledgements

“In the Name of Allah, the Most Merciful and the Most Kind. All praise is due to Allah, the Lord of the worlds.”

First and foremost, I would like to begin by thanking Allah Almighty, who has blessed me with good health, the opportunity and the ability to complete this PhD. Without His blessings, I would not be here today. I would also like to thank my supervisor Prof. Rachel O’Reilly for giving me this opportunity to work under her mentorship and for her continued support, guidance and understanding. I have been inspired by your strive for excellence in all your work, and your constructive criticism has allowed me to grow and improve myself in many ways.

I would also like to thank the University of Birmingham for funding my PhD research and making the transition from University of Warwick to University of Birmingham as smooth as possible.

During my 5 years at the University, I have had the opportunity to work with some great people and would like to thank everyone in the Dove and O’Reilly groups for sharing interesting ideas and knowledge. I would like to thank everyone who has helped me in proof reading my thesis - Amanda, Amrita, Jennifer, Sam, and Steve, and to Yujie and Jon for their support and guidance. And a special thanks to everyone who made my time at the lab more enjoyable, Turgay, Eirini, Irem, Marjo, and who kept me sane during the hard times with their witty humour and conversations.

I must thank my friends and family, especilly my parents to whom I would like to dedicate this thesis, for their unwavering support and encouragement throughout my studies. I am eternally grateful for my mother’s constant love and support without which

I would not have been able to complete my PhD. To my late father, who has always been so feircly proud of me and always encouraged me to work hard, pursue my studies and be the best that I can be at everything.

A special shout out to my badminton friends (especially my best friend Ramsha and her family)! I will always look back with fondness at all the fun times we spent together in Birmingham, looking for Pakistani/Indian resturants to eat at, playing boardgames and travelling together.

Declaration of Authorship

This thesis is submitted to the University of Birmingham in support for the degree of Doctor of Philosophy. It has been composed by myself and has not been submitted in any previous application for any degree.

The work presented herein, including data generated and data analysis, was carried out by the author except in the cases which are stated below and highlighted in the corresponding text.

- Chapter 2: Computational studies in support of fluorescent hypotheses were conducted by Dr. Miquel Torrent-Sucarrat (University of the Basque Country).
- Chapter 3: Electrochemical studies were carried out in collaboration with Dr. Paramaconi Rodriguez Perez (University of Birmingham).

Part of this thesis have been published by the author:

1. Pervez, M.; Pearce, A. K.; Husband, J. T.; Male, L.; Torrent-Sucarrat, M.; O'Reilly, R. K. Enhancing dual-state emission in maleimide fluorophores through fluorocarbon functionalization. Chemistry – A European Journal, **2022**, e202201877.
2. Yildirim, T.; Pervez, M.; Li, B.; O'Reilly, R. K. Size-controlled clustering of iron oxide nanoparticles within fluorescent nanogels using LCST-driven self-assembly. Journal of Materials Chemistry B, **2020**, 8, 5330–5335.

Contents

List of Figures and Schemes

List of Tables

Abbreviations

A	Absorbance
ABM	Aminobromomaleimide
ACM	Aminochloromaleimide
ACQ	Aggregation caused quenching
AFM	Atomic force microscopy
AIE	Aggregation-induced emission
APCI	Atmospheric pressure chemical ionization
ATM	Aminothiomaleimide
ATRP	Atom transfer radical polymerization
BSA	Bovine serum albumin
BuOH	Butanol
c	Concentration
CFT	Crystal field theory
CIE	Commission Internationale de l’Elcairage
CMIA	Carbonylmetalloimmunoassay
CH	Cyclohexane
Cp	Cyclopentadiene
Cp*	Pentamethylcyclopentadiene
CPET	Concerted proton-electron transfer
CT	Charge transfer
CuAAC	Copper-catalyzed alkyne and azide cycloaddition

CV	Cyclic voltammetry
DBM	Dibromomaleimide
DCM	Dichloromaleimide
DET	Dexter energy transfer
DFT	Density functional theory
DMSO	Dimethyl sulfoxide
DSE	Dual state emission
DSSCs	Dye-sensitized solar cells
DTM	Dithiomaleimide
EDPT	Electron driven proton transfer
em	Emission
Eq.	Equation
Equiv.	Equivalents
EtOH	Ethanol
ex	Excitation
FLIM	Fluorescence-lifetime imaging microscopy
FRET	Förster resonance energy transfer
FTIR	Fourier transform infrared
GC	Glassy carbon
GFP	Green fluorescent protein
GSH	Glutathione
HOMO	Highest occupied molecular orbital
HOPG	Highly oriented pyrolytic graphite
Hotf	Triflic acid

h	Hour
HRMS	High-resolution mass spectrometry
HSA	Human serum albumin
ICT	Internal charge transfer
IL	Intraligand
iPr	Isopropyl
IRF	Instrument response function
l	Path length
LC	Ligand centered
LCD	Liquid crystal display
LCST	Lower critical solution behavior
LE	Locally excited
LED	Light emitting diode
LFT	Ligand field transitions
LMCT	Ligand to metal charge transfer
LRET	Luminescence resonance energy transfer
LUMO	Lowest unoccupied molecular orbital
m/z	Mass to charge ratio
MAM	Monoaminomaleimide
MBM	Monobromomaleimide
MC	Metal centered
Me	Methyl
MeCN	Acetonitrile
MeOH	Methanol

min	Minute/s
MLCT	Metal to ligand charge transfer
MoAs	Mechanism of actions
MOs	Molecular orbitals
MS	Mass spectroscopy
Mw	Mass average molecular weight
NIR	Near Infrared
NMR	Nuclear magnetic resonance
NPs	Nanoparticles
ns	nanosecond
OCM	Alkoxychloromaleimide
OEt_2	Diethyl ether
O_h	Octahedral
OLEDs	Organic light emitting diodes
OLM	Organic luminescent materials
PCET	Proton-coupled electron transfer
PCT	Photo-induced charge transfer
PET	Photoinduced electron transfer
PLICT	Planarized intramolecular charge transfer
ppm	Parts per million
ps	picosecond
PTIM	Photothermally induced resonance
RAFT	Reversible addition-fragmentation chain-transfer polymerization
ref	Reference

RIM	Restriction of intramolecular motion
RIV	Restriction of intramolecular vibration
ROMP	Ring opening metathesis polymerization
ROP	Ring opening polymerization
ROS	Reactive oxygen species
rt	Room temperature
s	Singlet in NMR spectrum
TCEP	Tris(2-carboxyethyl)phosphine
TCSPC	Time-correlated single-photon counting
TEM	Transition electron microscopy
TGA	Thermal gravimetric analysis
THF	Tetrahydrofuran
TICT	Twisted intramolecular charge transfer
TLC	Thin layer chromatography
TMS	Tetramethyl silane
UCNPs	Upconversion nanoparticles
UV	Ultraviolet
Vis	Visible
VR	Vibrational relaxation
δ	Chemical shift in NMR spectroscopy
λ	Wavelength
ϕ_f	Quantum yield

CHAPTER 1: INTRODUCTION

1.1 Photoluminescence

1.1.1 Principles of photoluminescence

Photoluminescence is a phenomenon that happens when a molecule absorbs energy in the UV-Vis or near-infrared (NIR) region of the electromagnetic spectrum and then re-emits light at a frequency lower than that of the incident light. Comprehending the dynamics of the state-to-state electronic transitions is the key in understanding the photophysical and photochemical properties. Fig. 1.1 illustrates various photophysical events that follow the absorption process, and includes vibrational relaxation (VR) or internal conversion (IC), fluorescence, intersystem crossing (ISC), and phosphorescence. The absorbance of a photon, of a particular energy by the molecule of interest, results in the electronic transition from the ground state (S_0) to a higher-order singlet excited state (S_n, $n \neq 0$). Spin and orbital symmetry selection rules are crucial in determining the probabilities of the electronic transitions. The “Spin selection rule” forbids the transitions between electronic states of different spin multiplicities, i.e., $\Delta S = 0$. Furthermore, the “Laporte selection rule” forbids the transitions of the same parity if the molecule has a centre of symmetry. Once a molecule is excited to S_1, it can undergo further transitions, either into higher excited singlet states (S_n) or into higher excited triplet states (T_n), if another photon of matching energy is absorbed. S_n and T_n can also be reached by a direct excitation from the ground state (S_0). When a molecule is excited to the higher electronic state (S_n; $n \geq 1$), energy may be dissipated *via* a radiative or a non-radiative relaxation process. Vibrational relaxation (VR) is one of the non-radiative processes that occurs when the energy deposited by the incident photon into the molecule is given away to other vibrational modes in the form of the

kinetic energy. Moreover, the transition of an excited molecule from a vibrational energy level in one electronic state to another vibrational energy level in a lower electronic state is referred as internal conversion (IC). IC is also a non-radiative relaxation process of electrons from a higher excited state to a lower excited state or from the lowest excited state to the ground state. Fluorescence occurs from singlet→singlet ($S_1 \rightarrow S_0$) radiative relaxation, and gives a characteristic short life time on the order of nanoseconds for most organic fluorophores. Besides, if a molecule may dissipate the energy on account of the electronic transition between two isoenergic levels of different multiplicities, i.e., $S_1 \rightarrow T_1$, it is termed as intersystem crossing (ISC). Although this slow transition (ISC) is forbidden based on electronic selection rules, but by coupling vibrational factors into the selection rules, ISC may become weakly allowed. ISC followed by the radiative de-excitation from $T_1 \rightarrow S_0$, is known as phosphorescence, which exhibits a lifetime on the order of milliseconds.[1, 2] Another non-emitting transition is through quenching, which will compete with the radiative relaxation pathways, i.e., fluorescence and phosphorescence. Rapid quenching may be observed in solutions due to collision with the solvent molecules. If present, molecular oxygen may also quench the phosphorescence due to the energy transfer between the triplet excited state (T_1) of the dye and the triplet ground state of oxygen.[3]

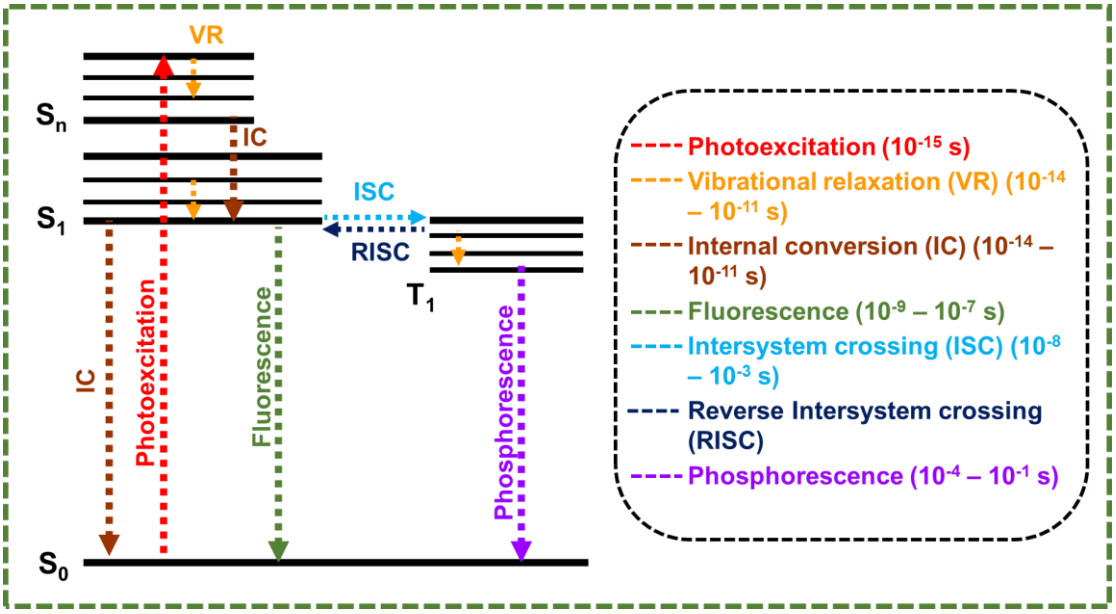

Fig. 1.1 Jablonski Diagram with the fundamental concepts that occur after irradiation.

In fluorescence spectroscopy, the emission occurs at a different wavelength compared to the absorption, and this difference between the spectral positions of maximum emission (λ_{em}) and absorption (λ_{ab}) is referred to as the Stokes shift. The photoexcitation of a molecule to a higher vibrational level (v_n; n>0) of the singlet excited state (S_1) is followed by a rapid non-radiative relaxation to the lowest vibrational state (v_0) of S_1. Subsequently, the emission from the v_0 of S_1 has a lower energy than the absorbed photon, and hence a longer wavelength. The probability of the promotion of an absorbed photon to the vibrational excited state (S_1,v>0) instead of vibrational ground state (S_1, v=0) can be explained by the Franck-Condon principle. The transition probability between each vibrational level of singlet excited state (S_1) and singlet ground state (S_0) is proportional to the overlap integral between their vibrational wavefunctions. Absorption occurs from the vibrational ground state (v=0) of S_0, which is the most populated level at room temperature, according to the Boltzmann

distribution. Fig. 1.2 shows the strong absorption transition from the v=0 of S_0 to an excited vibrational level (e.g. v=2) of S_1, that has the greatest wavefunction overlap, and defines the wavelength of maximum absorption (λ_{ab}). Similarly, the transition that has the greatest wavefunction overlap, between the v=0 of S_1 and the vibrational level of S_0, gives the strongest fluorescence, and this defines the wavelength of maximum emission (λ_{em}). The maximum wavelength of the fluorescence spectrum (λ_{em}) occurring at a longer wavelength than the maximum absorption (λ_{ab}) is the origin of the Stokes shift.[1, 4]

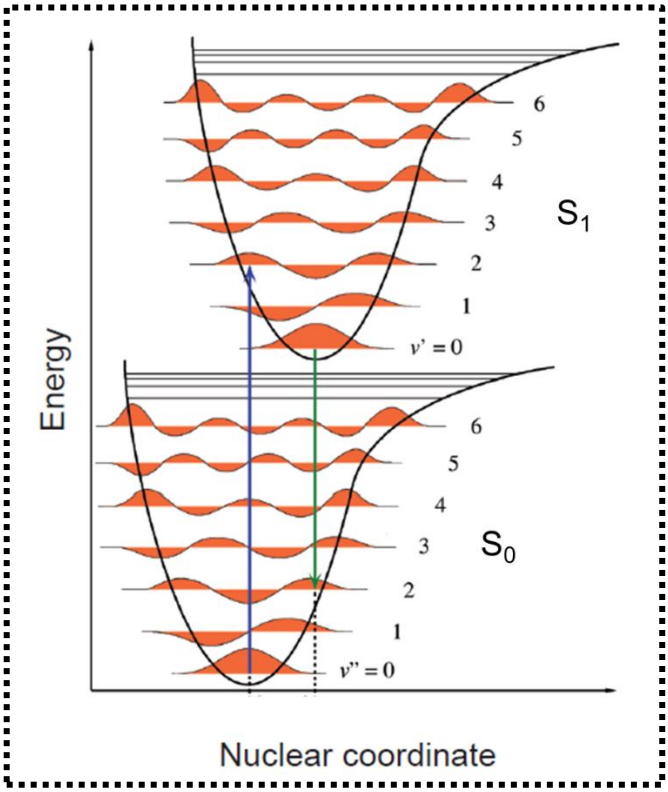

Fig. 1.2 The Franck-Condon Principle in a nuclear coordinate energy diagram showing the origin of the Stokes Shift. The potential wells are shown favoring transitions between the vibrational states v=0 and v=2. Adapted from the reference.[5]

Fluorescence spectroscopy can be classified as steady-state or time-resolved. Steady-state fluorescence spectroscopy involves the measurement of long-term average fluorescence of a molecule when irradiated with UV-Vis or NIR light, where the timescales are longer as compared to the lifetime of fluorescence. The applications such as excitation and emissions analysis, synchronous mapping, temperature mapping, kinetic measurements, anisotropy of fluorophores, etc., come under the umbrella of steady-state fluorescence. On the other hand, time-resolved fluorescence spectroscopy measures fluorescence as a function of time, for example, fluorescence lifetime imaging.[6, 7]

The emission spectrum is independent of the wavelength of excitation for most fluorophores. However, the emission intensity of a fluorophore could be influenced by various factors, such as, the fluorophore concentration, light source, temperature, solvent, etc. This could generate inaccuracy when comparing the fluorescent behavior of different dyes.[8] Therefore, the efficiency and analytical sensitivity of a fluorophore should be quantified by the fluorescence quantum yield (ϕ_f) and brightness (B). The fluorescence quantum yield (ϕ_f) is defined as the ratio of the number of emitted photons to the number of absorbed photons. It describes the efficiency of the radiative transition of the fluorophore (from $S_1 \rightarrow S_0$) as a fraction of excited states that decay through fluorescence compared to the excited states that decay non-radiatively (Eq. 1.1), where k_r and k_{nr} are the respective rate constants of radiative and non-radiative relaxation processes. The fluorophore brightness (B) can be evaluated as the product of the fluorescence quantum yield (ϕ_f) and the molar absorption coefficient (ε) (Eq. 1.2).[4] Unlike fluorescence emission intensity, ϕ_f is independent of the concentration

when using dilute solutions, while temperature may have an influence in case of thermal agitation triggered by the non-radiative processes.

$$\phi_f = \frac{k_r}{k_r + k_{nr}} \qquad \textbf{Eq. 1.1}$$

$$B = \phi_f \times \varepsilon(\lambda_{ex}) \qquad \textbf{Eq. 1.2}$$

Amongst all the optical methods for the evaluation of quantum yield, the two most common methods are: a relative method carried out by comparing to a standard dye of known fluorescence, and an absolute method that involves direct measurements using an integrating sphere.[9] The relative method evaluates the quantum yield by comparing the integrated absorption and emission spectra of the standard and the sample at a specified wavelength and is described in Eq. 1.3., where n denotes the refractive index of the solvent, f represents the absorption factor, F is the integrated fluorescence intensity at a particular wavelength, and the indices st and x indicates the standard and the sample dyes, respectively. Whereas the absolute quantum yield is computed as the ratio of the photon flux emitted from the sample (F) to the absorbed photon flux (F_{abs}) (Eq. 1.4).[9]

$$\phi_{f,x} = \phi_{f,st} \cdot \frac{F_x}{F_{st}} \cdot \frac{f_{st}}{f_x} \cdot \frac{n_x^2\,(\lambda_{em})}{n_{st}^2\,(\lambda_{em})} \qquad \textbf{Eq. 1.3}$$

$$\phi_f = \frac{F}{F_{abs}} \qquad \textbf{Eq. 1.4}$$

Fluorescent lifetime is another key concept of fluorescence spectroscopy. It is a representation of a kinetic process and measures the average amount of time a

fluorophore spends in its excited singlet state (Eq. 1.5; where k_r and k_{nr} are the respective rate constants of radiative and non-radiative relaxation). Though fluorescence lifetime is an intrinsic property of a fluorophore, it is independent of the fluorophore concentration, method of measurement, fluorescence intensity, and photobleaching. Instead, external factors such as solvent polarity, temperature, and presence of quenchers can have an effect on the stability of the excited states.[10]

$$\tau = \frac{1}{k_r + k_{nr}} \qquad \textbf{Eq. 1.5}$$

Fluorescence spectroscopy is a highly sensitive technique. The sensitivity of fluorescence detection is ~1000 times greater than UV-Vis absorption spectroscopy, and this is due to the different ways of measuring fluorescence and absorbance. In UV-Vis absorption spectroscopy, absorbance is measured as a difference in intensity between light passing through the reference and the sample. While in fluorescence measurements, fluorescence intensity is evaluated directly, without any comparison with a reference beam. The noise in absorption measurements scales with the excitation intensity, while in fluorescence measurements it scales with the concentration. The lower the concentration of the fluorophore, the lower is the noise in the data. It is also relatively easy to detect single molecules in fluorescence analysis, but single molecule detection is way more difficult with the absorption measurements.[4] An important phenomenon to take into account is known as inner-filter effect, which occurs when the concentration of a fluorophore is sufficiently high, resulting in an attenuation of the excitation beam by the fluorophore itself. Therefore, it is important to maintain the concentration of the fluorophore (i.e. µM) in a range to exhibit absorption less than 0.1, to minimize the inner filter effect.[9, 11] The presence of any

impurity in the fluorophore sample or the solvent can also absorb a fraction of the emission or excitation energy which leads to a decrease in the fluorescence intensity. Photobleaching is another phenomenon that occurs when a fluorophore loses its fluorescence permanently. This may be caused by photoinduced chemical damage or covalent modification. The T_1 state is quite long-lived compared to the S_1 state, and this permits the excited molecules to chemically interact with the components in the environment.[12]

1.1.2 Photophysics and photochemistry of fluorescence

Any process which decreases the fluorescence intensity of a fluorophore, due to the interaction of the excited states with its surroundings, is called fluorescence quenching. Fluorescence quenching can be classified into two different terms; static quenching, and dynamic quenching. Dynamic quenching occurs when a quencher molecule interacts with the excited states of a fluorophore, for example, chloride ions can act as quencher molecules for the quinine dye. Compared to that, a fluorophore (at the ground state) can interact with another molecule in the vicinity, such as oxygen or solvent molecules, leading to either no excitation or very little excitation, and this is referred to as static quenching.[13]

Several processes occur due to the changes in electronic distribution in the excited states, such as: photoinduced charge transfer (PCT), internal charge transfer (ICT), electron driven proton transfer (EDPT), Förster resonance energy transfer (FRET), etc. The manipulation of these processes occurring in the excited state could generate a

different conformation of a individual fluorophore for various applications such as, pH probes, metal sensors, dark quenchers, lifetime imaging probes, etc. FRET includes non-radiative energy transfer from the excited state of a donor (D) fluorophore to an acceptor (A) fluorophore, and relies on the relative orientation, and spectral overlap of the acceptor absorption and donor emission spectra (Fig. 1.3). Dexter energy transfer (DET) involves the orbital overlap between the donor and acceptor fluorophores at considerably shorter distances than the Förster radius, resulting in intramolecular or intermolecular bilateral electron transfer (Fig. 1.3).[10]

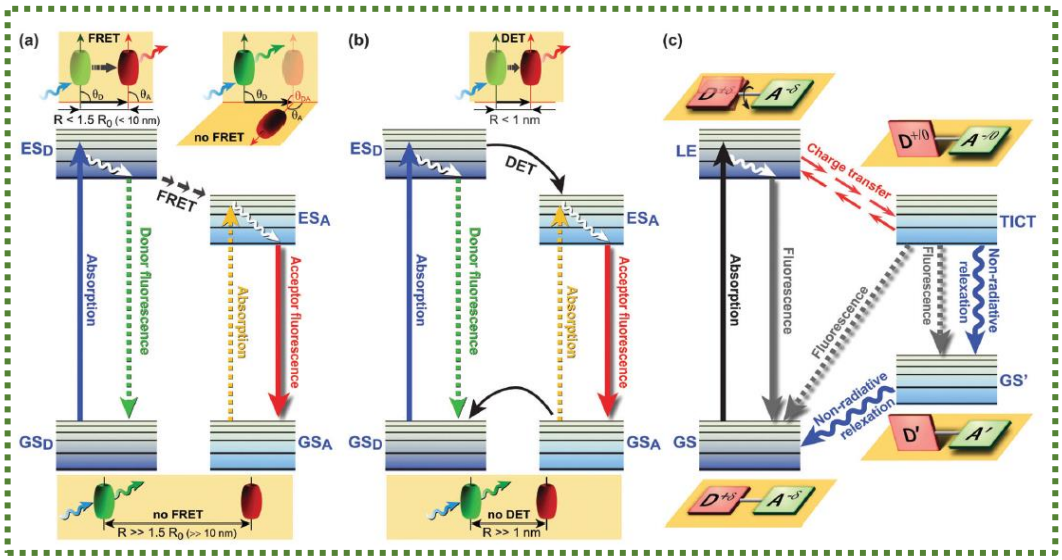

Fig. 1.3 Jablonski diagrams of various energy/electron donor–acceptor (D–A) systems. (a) Förster Resonance Energy Transfer (FRET), θ is the angle between vectors of the donor emission and the acceptor absorption; (b) Dexter Energy Transfer (DET); (c) Twisted Intramolecular Charge Transfer (TICT) dynamics. Upon excitation from the GS, the LE state equilibrates rapidly with the TICT state after fast charge transfer. GS = ground state; GS_D = ground state donor; GS_A = ground state acceptor; ES_D = excited singlet state donor; ES_A = excited singlet state acceptor; LE = locally excited state; R = effective D–A distance. Adapted from the reference.[14]

Compared to the aforementioned processes that focus on the relative arrangement of the fluorophores, intramolecular charge transfer (ICT) deals with the conformation of an individual fluorophore. In the case of a planar conformation of the fluorophore, the photon absorption causes no change in the relative orientation of the donor and acceptor moieties of the fluorophore, and their π-systems are coupled in both the ground and the excited state (Fig. 1.4).[15] In such cases, the fluorescence quantum yield is quite high due to the electronically allowed transitions, while the Stokes shift is smaller as it involves no significant change in the geometric arrangement of D-A groups.[16] In the case of twisted intramolecular charge transfer (TICT), the charge transfer from the donor to the acceptor subunit (connected by a single bond) corresponds to one-electron excitation from the highest occupied molecular orbital (HOMO) to the lowest unoccupied molecular orbital (LUMO). Internal conversion (IC) driven by rotation around the single bond minimizes the Coulombic interactions, resulting in a larger Stokes shift due to geometric relaxations. However, the electric-dipole forbidden transition causes low emission quantum yields (Fig. 1.4).[14] Compared to these two phenomena, planarized ICT gives high quantum yields as well as large Stokes shift. In this case, the acceptor (A) and the donor (D') units in the fluorophore are connected rigidly in one plane that generates high quantum yield. In addition, another donor group (D) (connected to the first donor D') has a twisted conformation showing a dihedral angle of about 90° (Fig. 1.4). This twisted conformation results in a single diradical with the positively charged D' stabilized by the interaction with free electron pair from the D, owing to the rotation around the single bond, and is defined as planarized ICT (PLICT). The excited state undergoes the geometrical relaxation in the case of PLICT, and thereby features large Stokes shift.[16]

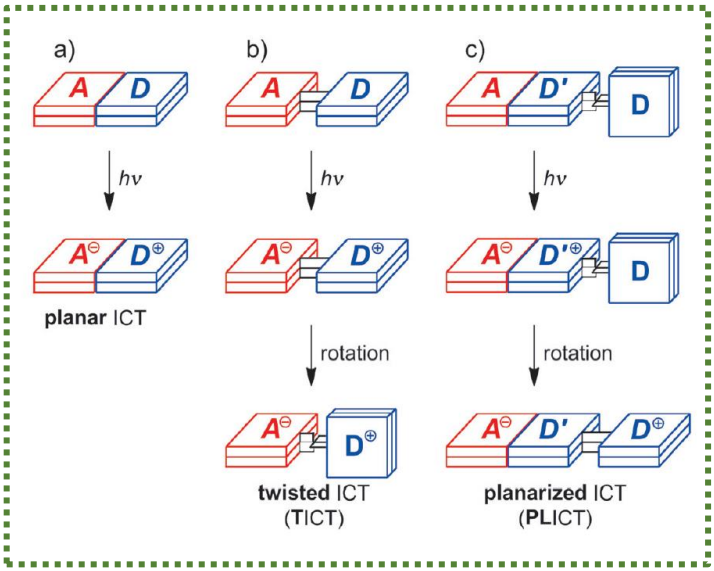

Fig. 1.4 Schematic representation of the change in the geometrical arrangement of the donor groups D and D' as well as the acceptor group A upon going from the ground state to planar ICT (a), TICT (b), and PLICT states (c). Adapted from the reference.[16] Copyright 2016 European Chemical Society.

It is also crucial to understand the labile paths of transitions, from the quencher to the fluorophore, which lead to the fluorescence quenching, especially with respect to maleimide-based dyes, which is the primary focus of the work explained in this thesis. Photoinduced electron transfer (PET) leads to the generation of a charge-separated state, comprising of the acceptor radical anion and the donor radical cation. PET, whether intramolecular or intermolecular, competes with any radiative or non-radiative relaxation process occurring in the excited state, and generates low fluorescence quantum yields and short lifetimes.[17-20] Fig. 1.5 describes the HOMO and LUMO of the fluorophore (donor, D) and the quencher (acceptor, A) molecules in the fluorescence on- or off-states. PET is thermodynamically feasible in the off-state, as the HOMO level attributes to the donor-based orbital of the quencher, while in the on-state PET is not plausible due to the HOMO level corresponding to the acceptor-based orbital.[21]

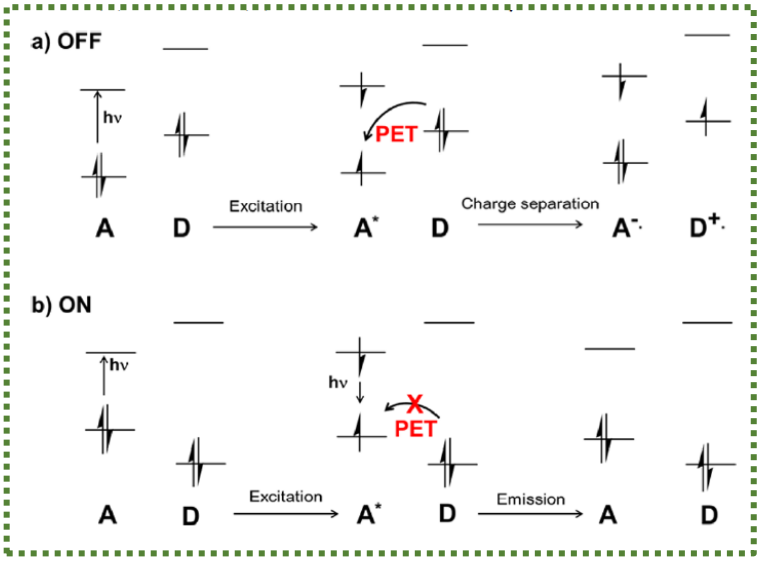

Fig. 1.5 Energy diagram of the donor-acceptor system for the photoinduced electron transfer. Adapted from the reference.[21] Copyright 2016 American Chemical Society.

Another key phenomenon involved in fluorescence quenching is electron-driven proton transfer (EDPT), also known as proton coupled electron transfer (PCET) or concerted proton electron transfer (CPET).[22, 23] Fig. 1.6 illustrates the mechanism of EDPT for the aminomaleimide dye solvated in methanol. Upon photoexcitation of the fluorophore, the photoexcited canonical state ($\pi \rightarrow \pi^*$) can be generated, and a slight delocalization of the charge density triggers electron transfer from the nearby solvent molecules (MeOH), and produces two charge separated species. This charge difference prompts the proton donation from the solvent and leads to the formation of neutral di-radical species, in which fluorescence is forbidden. The EDPT pathway is only accessible in polar protic solvents, such as methanol and water.[24]

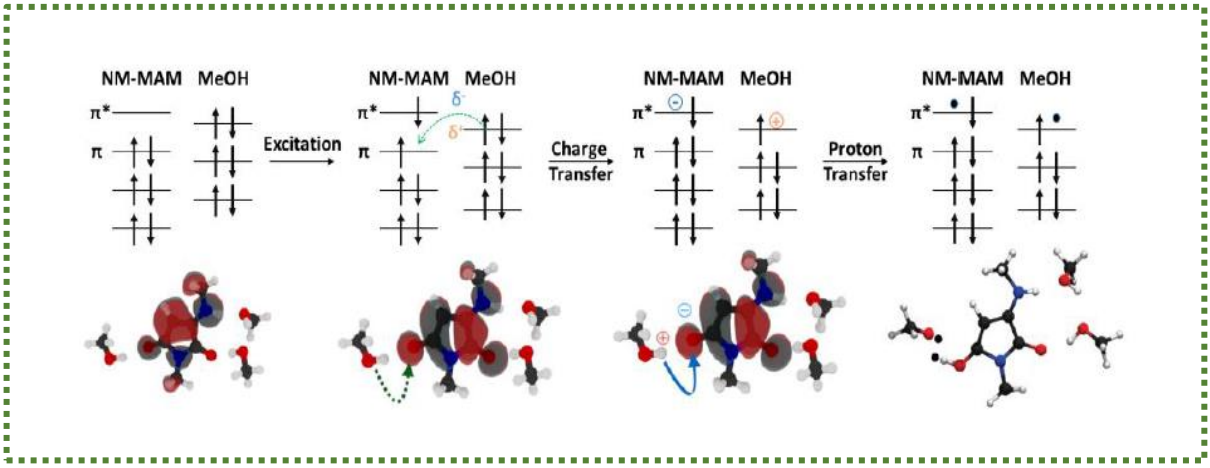

Fig. 1.6 Diagram of hypothesized EDPT mechanism for an aminomaleimide (NM-MAM) solvated in methanol (MeOH). Electronic movement is indicated by the green dashed arrow and proton movement is indicated by the blue arrow. Reproduced from the reference.[24]

1.2 Maleimide: an overview

Over the years, traditional organic fluorophores have been employed for numerous applications, such as bioimaging, sensors and other photoluminescent devices.[25-27] They exhibited good spectral window, photostability, fluorescence efficiency and lifetime, but also contained large planar and polycyclic conjugated framework, and conformational rigidity.[28] Therefore, different strategies were developed for the synthesis of small molecule fluorophores with structural tailorability and tunability of the fluorescence properties.[29, 30] The classes of dyes that have been developed towards these goals, are cyanine, fluorescein, rhodamine and xanthane (Fig. 1.7).[31-33] All these dyes comprised of aromatic π-conjugated systems and are hydrophobic in nature, hence they are limiting for certain applications in biochemical systems, such as the localization of a target.[34]

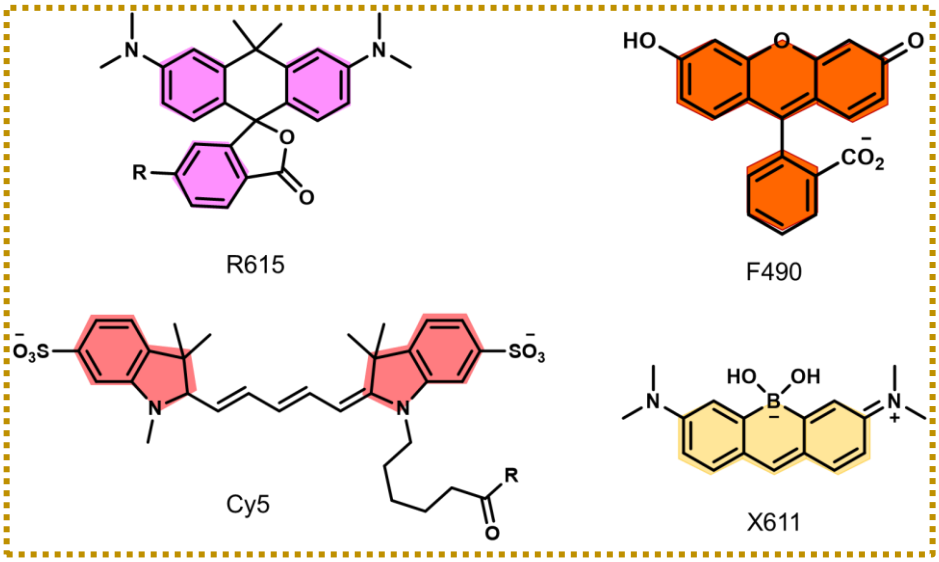

Fig. 1.7 Structures of some of the developed small-molecule fluorophores used for fluorescence imaging.

1.2.1 Unsubstituted maleimide quencher or substituted maleimide fluorophore?

Owing to the selective reactivity of maleimides, as well as their good stability and sensitivity, maleimide derivates have been steadily gaining popularity over the years. In the past, maleimides had been extensively employed as a chain-end functionalization tool for polymer synthesis,[35-37] or for protein modification.[38] Furthermore, they can readily react with chemical functionalities in the biomolecules (such as thiols, etc.) by Michael addition,[39-41] or can undergo the two-step Diels-Alder process.[42] Unsubstituted maleimides coordinated to the dyes were utilized as fluorescence quenchers in the past (by acting as an acceptor) *via* the photoinduced electron transfer (PET) mechanism owing to their underlying π^* state.[43] Thereby, various maleimide derivatives were reported to be either commercially available (CF™ 488A maleimide, AQuora® 750-Maleimide) or readily accessible *via* low cost, scalable, and high-yielding strategies. Lately, it was reported that halogen containing maleimides could undergo efficient addition-elimination reactions with thiols, thus by retaining the double bond in dithiomaleimides (DTM), they could act as a fluorophore.[44, 45] Since then, our group has been investigating the substituted maleimide-based fluorophores, and examined the correlation of their structural and optical properties. Later, a series of aminohalomaleimides (AXM) and monoaminomaleimides (MAM) exhibiting high fluorescence quantum efficiencies with large Stokes shift (~100 nm) were also reported.[46] The strategy to synthesize the amino-substitution maleimide fluorophores was of particular interest due to the availability and prevalence of amine groups in biological substrates. Furthermore, the alcohol substituted halomaleimide (alkoxyhalomaleimide; OXM) and doubly-substituted aminothiomaleimide (ATM)

exhibited blue and yellow emissions (Stokes shift = ~150 nm), respectively (Fig. 1.8). Additionally, the aminothiomaleimide structures exhibiting weak emissions (ϕ_f = 8%) in solid-state, indicates the potential of dual-state emission (DSE) behavior by preventing the quenching in the solid-state, through the introduction of a thiol group adjacent to the donor amine group.[47] Most recently, our group has investigated the influence of substituting multiple phenyl groups at the imide position of the maleimide ring on the optical properties, and has observed a high fluorescence in the solid matrix, but negligible fluorescence in solution-state.[48] The chemical diversity of maleimide-based fluorophores possessing high fluorescence emission efficiencies and large Stokes shifts in polar protic solvents and in solid-state, is explored further in Chapter 2.

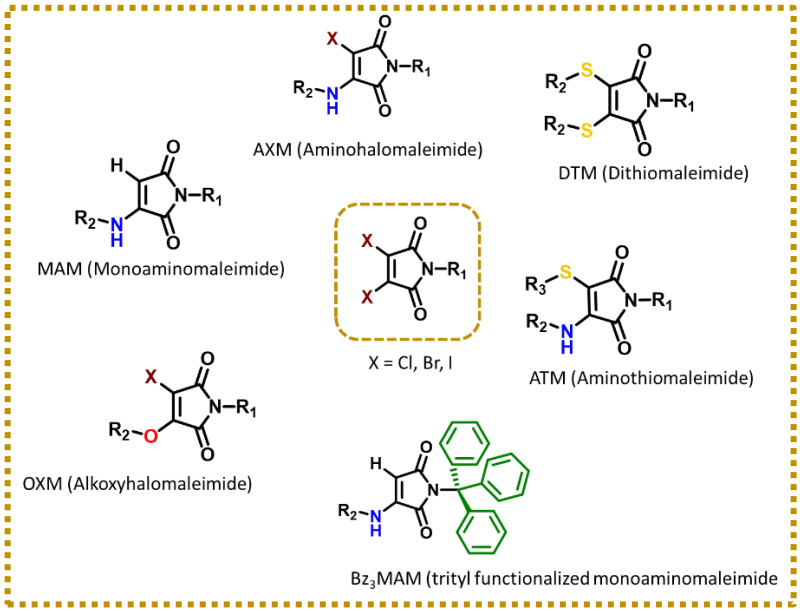

Fig. 1.8 Structures of some of the reported maleimide derived fluorophores.[46-48]

1.2.2 Factors effecting the fluorescence emission

The fluorescence emission of a fluorophore is fairly dependent on its environment, which includes factors, such as temperature, solvent, etc., and the degree of dependence varies from dye to dye. Some fluorophores display temperature-dependent quenching phenomena,[49, 50] where high temperatures trigger the non-radiative relaxation processes (thermally activated delayed fluorescence), following the photoexcitation, leading to a decrease in the fluorescence emission.[51] In addition to the temperature, fluorophores can be designed to be responsive to the pH of a solution. Some fluorophores, such as rhodamine and fluorescein, and their derivatives, are naturally dependent on pH to a certain extent.[52] Nonetheless, certain fluorophores were developed to be pH-responsive; in particular, fluorophores that can undergo protonation or deprotonation, thus exert tunable fluorescent properties.[53, 54]

Another factor that has a significant influence on the fluorescence is the solvent polarity, and highly solvent-dependent fluorophores show solvatochromic behavior. Within a solution, the dipole moment of the solvent molecules interact with the dipole moments of the fluorophore. Upon photoexcitation, the dipole moments of the fluorophore and the solvent molecules disorient and reorient themselves within the solute-solvent domain. The reordering of solvent molecules around the solvated fluorophores usually has a larger dipole moment in the excited state than in the ground state. The solvent molecules assist in stabilizing, which lowers the energy level of the excited state, thus reducing the energy separation between the ground and excited states. This effect may be more or less pronounced depending on the polarity of the solvent. An increase in solvent polarity results in a higher stabilization of a polar excited state, and therefore, such fluorophores are inclined to show high bathochromic shifts

in more polar solvents (Fig. 1.9).[55] The fluorophores that contain electron-donating and electron-withdrawing groups in conjugation, such as maleimides-based dyes, are outstanding candidates as polarity probes.[56] Thereby, the maleimide-derived fluorophores presenting large solvatochromic effects will be discussed further in Chapter 2.

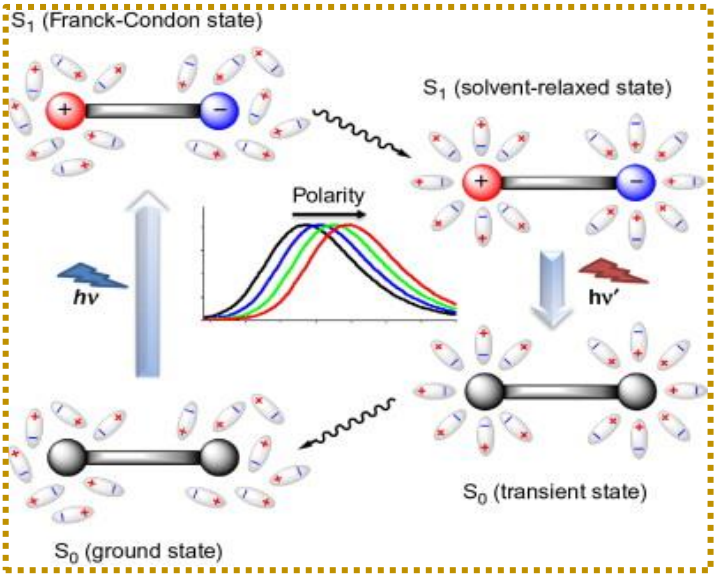

Fig. 1.9 Effect of the solvent polarity on the energy levels of the fluorophore. Adapted from the reference.[55] Copyright 2013 Elsevier.

1.2.3 Applications of maleimide fluorophores

1.2.3.1 Polymer functionalization

Owing to the small size, non-invasive nature and promising fluorescent properties substituted maleimides fluorophores have been extensively employed for polymer functionalization by our research group.[44, 57-61] The maleimide-derived structures could act as a compatible polymer functionalization handle, given its facile reactivity for a

wide range of polymerization techniques, such as RAFT polymerization,[57, 60] ROMP polymerization,[62] emulsion polymerization,[63, 64] step growth polymerization,[65] sequence controlled polymerization,[66-68] etc. The carbonyl groups in the maleimide unit provide a control of the hydrogen bonding interactions, while the electron-deficient double bond can participate in numerous applications, such as Diels-Alder reaction, Michael addition, addition-elimination reaction with thiols and amine, etc., without the need of any metal-catalyst or thermal/photochemical initiation.[66] Robin *et al*., reported embedding of the fluorescent dithiolmaleimide (DTM) monomer into the polymers *via* pre-polymerization and post-polymerization functionalization (Fig. 1.10).[57] Later, the effect of supramolecular assembly of the polymer containing DTM unit on the fluorescence intensity, wavelength, and lifetime was explored.[59] In another work, the fluorescent dithiomaleimide (DTM) unit was incorporated into either the core or the shell of the block copolymer micelles, and an increase in the fluorescence emission intensity was observed upon self-assembling, due to the shielding of DTM moiety from the solvent quenching. The core-labelled micelles also detected the uptake of the guest molecules by the Förster resonance energy transfer (FRET).[60] Maleimide-based fluorophores have also been used for monitoring the polymerization fusion process. Spyridon *et al*., investigated the fusion properties of photo-polymerization induced self-assembly (photo-PISA), by incorporating rhodamine and maleimide dyes as the fluorescent monomers, and monitored a change in the fluorescence lifetimes through confocal microscopy (Fig. 1.10).[62]

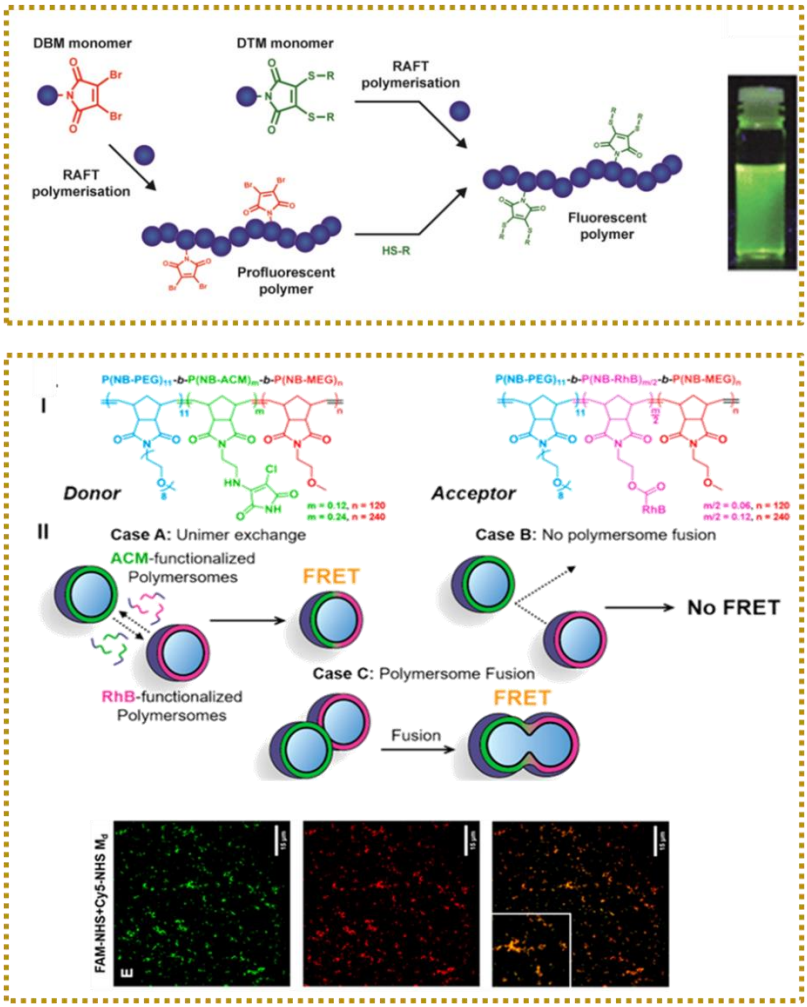

Fig. 1.10 Selected examples of reported work utilizing fluorescent maleimide derivatives for polymer functionalization (top), and monitoring the fusion process in photo-PISA reaction (bottom). Adapted from the references.[57, 62] Copyright 2014 Royal Society of Chemistry and 2019 American Chemical Society, respectively.

Another fascinating application includes the development of a photoresponsive nanogel containing the dithiomaleimide (DTM) and spiropyran (SP) components. Upon irradiation with UV-light, a fluorescence energy transfer occur from the DTM to the SP dye, that allowed the reversible alternation of the fluorescence lifetime, thus a controlled fluorescence lifetime barcoding system was achieved (Fig. 1.11).[69]

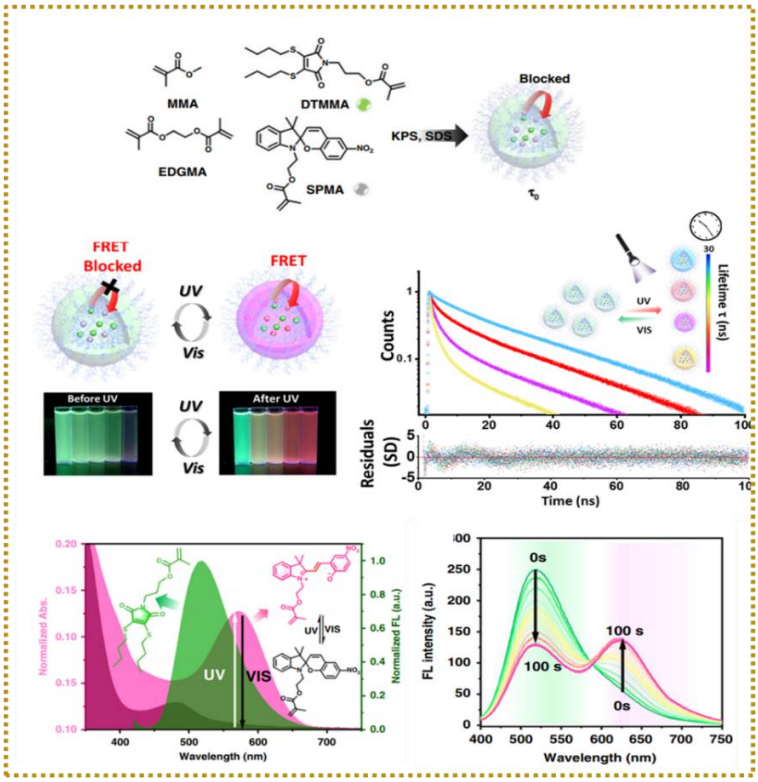

Fig. 1.11 Preparation of maleimide-based fluorescent nanogels for lifetime barcoding applications. Adapted from the reference.[69] Copyright 2020 Nature Publishing Group.

1.2.3.2 Bioconjugation and drug delivery

In order to study *in vitro* and *in vivo* biochemical mechanisms, numerous methods have been developed for efficient and specific labeling of the biomolecules.[70, 71] It is crucial that the labeling agent should be stable in bio-systems, and possess a functionality that may interact with targeted groups, that are present in biomolecules. The conjugation of maleimide derivatives with the biomolecules, such as peptides and proteins, is one of the most prevalent strategies due to their high reactivity, selectivity, and accessibility.[72] *N*-functionalized maleimide structures have been frequently reported for selective labeling of proteins and peptides.[73-75] Several reports about utilizing the dithiomaleimide derivatives, as off-on fluorescent probes, for bioimaging

applications have also been published.[40, 76, 77] Despite all this, the irreversible nature of the maleimide-based structures, while undergoing addition reactions to form stable bonds (e.g., -SH), limited its applications. Later, this problem was resolved by incorporating a leaving group (e.g. bromo) to the maleimide, which led to a shift from the addition reaction to the addition-elimination reaction (Fig.1.12).[78] Baker and coworkers reported numerous maleimide reagents for the protein conjugation, that were highly specific and could experience hydrolysis to reversibly cleave the maleimide-protein conjugates in blood serum.[38, 79] Subsequently, several strategies were reported to utilize the substituted maleimide structures for the development of the peptide-polymer conjugates in a stable and reversible manner.[80, 81] One promising work involved the *in situ* conjugation of the dithiomaleimide functionalized polymer with the oxytocin, to enhance its stability and reversibility (Fig. 1.12).[82]

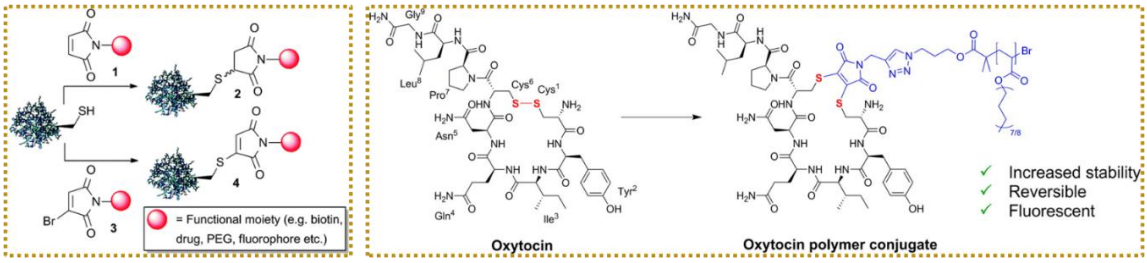

Fig. 1.12 Labeling of protein using maleimide and bromomaleimide *via* addition and addition-elimination reaction (left),[78] and peptide oxytocin and dithiomaleimide conjugate formation (right).[82] Copyright 2014 Royal Society of Chemistry and 2015 American Chemical Society, respectively.

In another interesting application, a bi-specific antibody conjugate was constructed, by reducing the disulfide bridge, using a bis-dihalogenated maleimide cross-linker. The

developed antibody-antibody conjugate maintained its binding activity, and *in vitro* binding of the targeted antigens was achieved as well (Fig. 1.13).[83]

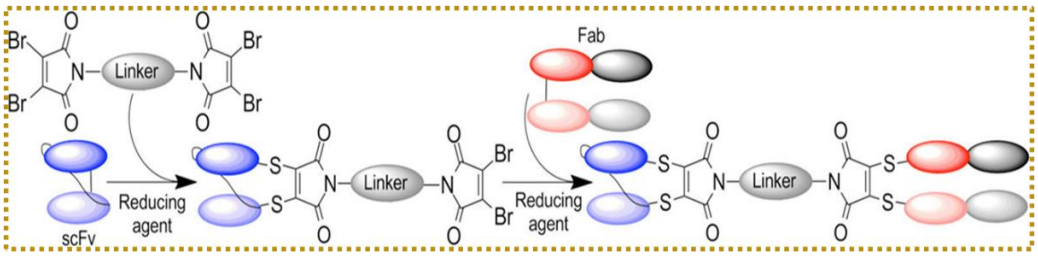

Fig. 1.13 Synthesis of homogenous bi-specific antibody conjugate using bis-dibromomaleimide cross-linker. Adapted from the reference.[83] Copyright 2014 American Chemical Society.

In another study, the thiol exchange reaction has been utilized to enable the targeted cleavage of maleimide-linked GFP-rhodamine conjugate for a drug release.[84] Stimuli responsive polymeric nanoparticles (NPs) is an emerging field for the disease (tumor) diagnosis and treatment.[85-87] In this regard, dithiomaleimide fluorophores have been utilized to synthesize the amphiphilic block copolymeric systems with pH-responsiveness. These block copolymers comprised of fluorophore (i.e., DTM) and pH-responsive segments (i.e., amine group etc.) in the polymeric backbone, which self-assembled into a drug-loaded micelles in the presence of a drug, and disassembled upon pH switch, releasing the drug.[88, 89] Furthermore, DTM containing multi-stimuli responsive polymeric nanomaterials have been developed, to obtain the controlled drug release and enhanced therapeutic efficiency. A fluorescent biocompatible amphiphilic block copolymer was synthesized by atom transfer radical polymerization (ATRP) and ring opening polymerization (ROP), followed by the introduction of a DTM unit *via* azide-alkyne click reaction. The drug camptothecin-loaded core-labeled

micelles were taken up by the tumor cells and the disulfide bonds were cleaved at high glutathione concentration, to release the CPT drug (Fig. 1.14).[90, 91] From these examples, it is evident that the substituted-maleimide containing polymeric nanoparticles, with the stimuli responsive and tunable fluorescent properties, are promising candidates for bioimaging and therapeutical applications.

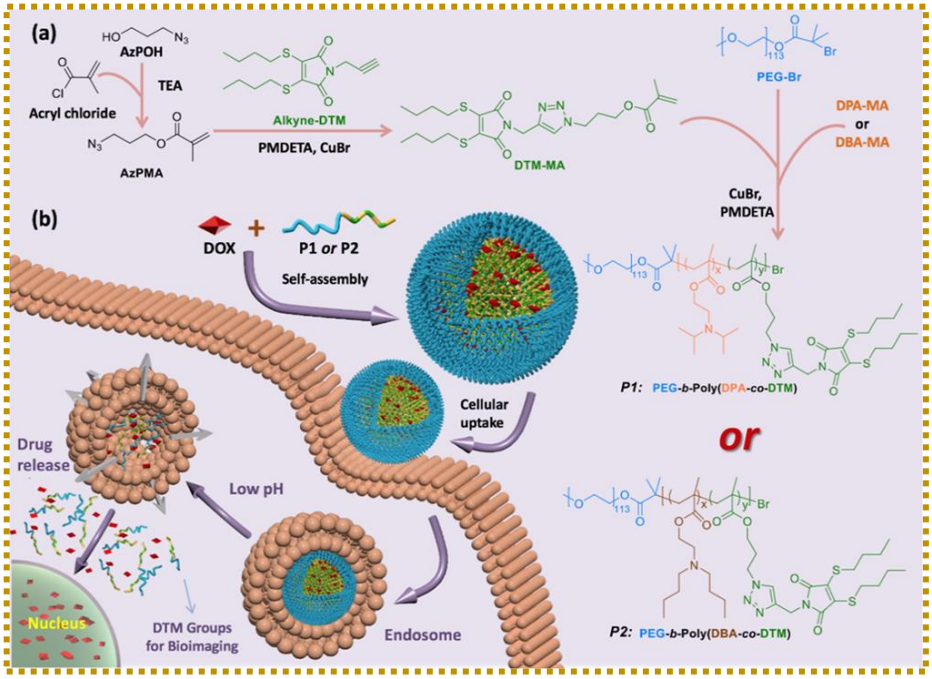

Fig. 1.14 Fluorescent dithiomaleimide-amphiphilic block copolymers for pH-responsive drug delivery into a tumor cell. Adapted from the reference.[89] Copyright 2019 Elsevier.

1.2.3.3 Surface modification and functionalization of inorganic nanoparticles

After decades of research, inorganic nanoparticles have been utilized for a variety of biomedicinal[92-94] and industrial applications.[95, 96] The major challenge experienced

over years that limited their applications in biosystems to some an extent, was the lack of biocompatibility.[97] Several attempts were made to resolve this problem by increasing the dispersity of the hydrophobic colloidal nanoparticles in the aqueous media.[98] One approach to achieve this goal is by the surface functionalization of the nanoparticles with biocompatible polymeric shells,[99] or through ligand exchange reaction.[100, 101] Maleimide-thiol chemistry has been frequently exploited to achieve the surface functionalization and covalent attachment of the inorganic nanoparticles.[102] Furthermore, inorganic nanoparticles, such as iron oxide NPs, can also be functionalized with the hydrophilic polymeric shells containing the maleimide structures *via* the active functionalities, such as hydroxyl or carboxyl groups. Thomas and co-workers reported surface functionalization of the iron-oxide based nanoparticles with dibromomaleimide-terminated methacrylate modified polyethylene glycol polymer, through multiple phosphonic groups, to achieve high colloidal stability and biocompatibility. The presence of dibromomaleimide (DBM) as end-group was used to achieve conjugation-induced fluorescence with amine-group containing biomolecules, and tracked the magnetic NPs-based conjugates through confocal microscopy.[103] In another work, dibromomaleimide containing azide functionality as an end-group was incorporated into the polymers *via* RAFT polymerization, and functionalized the sodium gadolinium fluoride ($NaGdF_4$) nanoparticles through phosphonic groups. The dibromomaleimide conjugation-induced fluorescence was achieved through a copper-free “click reaction between the azide linker and bicyclo-[6.1.0]-nonyne (BCN)-terminated antibody, and employed the conjugated polymeric system for optical imaging of thrombosis (Fig. 1.15).[104] Some other works involved the maleimide-functionalized gold-nanoparticles *via* thiol exchange reaction, for imaging the

controlled cellular interactions.[105, 106] Recently, Turgay *et al*., has utilized an amine-dichloromaleimide crosslinker to develop the hydrophilic fluorescent nanogels tethered to the iron oxide nanoparticles, and analyzed the lower critical solution behavior (LCST) behavior of the self-assembled nanoparticles.[107] Thereby, the substituted maleimides are very promising candidates for functionalizing the inorganic nanoparticles, to achieve high stability, enhanced fluorescence, excellent biocompatibility and improved targeting efficiency for various biochemical applications.

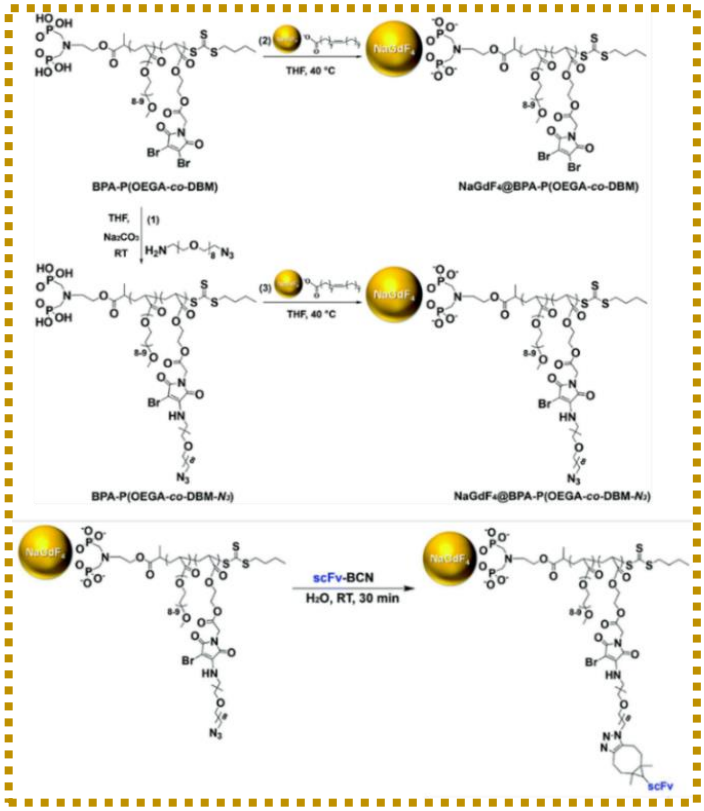

Fig. 1.15 Reaction between DBM in the BPA-P(OEGA-*co*-DBM) copolymer and azide groups (1); surface ligand exchange of the oleic acid coated $NaGdF_4$ nanoparticles (2, 3); and conjugation of $NaGdF_4$@BPA-P(OEGA-*co*-DBM-N_3) with the scFv-BCN antibody (4). Adapted from the reference.[104] Copyright 2020 Royal Society of Chemistry.

1.3 Luminescent organometallic complexes

1.3.1 Prospects of organometallic complexes

Owing to the unique physico-chemical characteristics, organometallic complexes have been widely used for applications, such as bioimaging, drug delivery, catalysis, etc. Several organometallic compounds have entered into clinical trials to be used as antimicrobial, anticancer and diagnostic agents.[108, 109] The structural privileges that organometallic complexes have over the organic compounds for the biochemical applications, includes structural diversity, solubility in aqueous phase, efficient redox and catalytic properties.[110] A chiral carbon atom in organic compounds attached to four different substituents could have two different enantiomers. Compared to that, an octahedral organometallic complex that could accommodate six substituents may occur in 30 different stereoisomers, suggesting that the structural diversity in typical organometallics exceeds that of organic compounds.[111] Additionally, the placement of the ligands around the metal center in the transition metal complexes is stereochemically stable, thus the occurrence of racemization is extremely rare. However, this criterion is not met by all the transition metals, the structural rigidity is quite pronounced with second and third row transition metal atoms. Therefore, these transition metal complexes have been occasionally used for biomedical applications.[112, 113] Another well-known physico-chemical property of organometallics is that many metal complexes could readily undergo electron transfer reactions, and this phenomenon has been widely explored. The metallocenes and half-sandwich complexes have been utilized as potential drug transport and delivery systems, by the virtue of their redox properties.[114, 115] Sadler and co-workers have reported the half-

sandwich “piano-stool” ruthenium arene complexes as potential anticancer agents, and explored their catalytical behavior. The cytotoxic effects of these complexes was explained by the redox catalytic cycle, that involved the reaction between the glutathione (GSH) and azo-pyridine ligands coordinated to the ruthenium metal.[116]

For long, it was believed that all organometallic complexes are air and moisture sensitive, and could only be handled under inert atmosphere. This stereotype was broken when technetium-based carbonyl complexes were successfully employed for the labeling of biomolecules in the aerobic aqueous environment.[117] The stability of such complexes was achieved by coordinating the metal atoms with π -back bonding ligands, such as carbonyl and phosphines, or with aromatic π-systems, such as η^6-arenes or η^5-cyclopentadiene (Cp).[118, 119] Later, several luminescent transition metal and lanthanide complexes were developed with tunable spectrochemical properties by using a wide range of ligands. Such complexes were efficiently employed as bioimaging reagent and cellular probes, due to their high photostability as well as intense and long-lived environment sensitive emissions.[120, 121] The transition metal and lanthanide metal complexes can be achieved in fewer steps with greater flexibility, and their steric and/or electronic properties can also be tuned by the modification of the auxiliary ligands.[122] Amongst the transition metal complexes, metals with d^6-configuration, such as iridium(III), rhenium(I), ruthenium(II), have been considered as potential luminophores, for bioimaging, protein labeling, and sensing applications.[123, 124] The d^6-complexes possess generally low rates of ligand exchange which is essential in mediating the toxicity of the metal ions. Owing to the spin-forbidden transitions, allowed through the spin-orbit coupling, these metal complexes have a long fluorescence lifetime (100 ns to ms), and large Stokes shifts (>100 nm). This is

advantageous for applications, such as time-gated luminiscence microscopy, which helps in the differentiation of a probe signal from the background autofluorescence.[125] Moreover, the metal atoms can coordinate to a wide range of ligands, containing the functional groups suitable for conjugation to the biomolecules, thus allows their controlled localization in the cells.[126-128] Fig. 1.16 represents the cellular uptake and localization of some of the well-known d^6-complexes. The most common luminescent ruthenium(II) complexes consists of derivatives of diimine-based ligands, such as bipyridine, phenanthroline etc., coordinated in an octahedral geometry. These luminescent complexes showed metal-to-ligand (MLCT) transitions having characteristics excitation, and emission bands around 450 nm and 610 nm, along with the fluorescence lifetime on the order of 0.6 – 6 µs. The chelating ligands provide the opportunity for functionalization as well as can modulate the luminescence efficiently.[126]

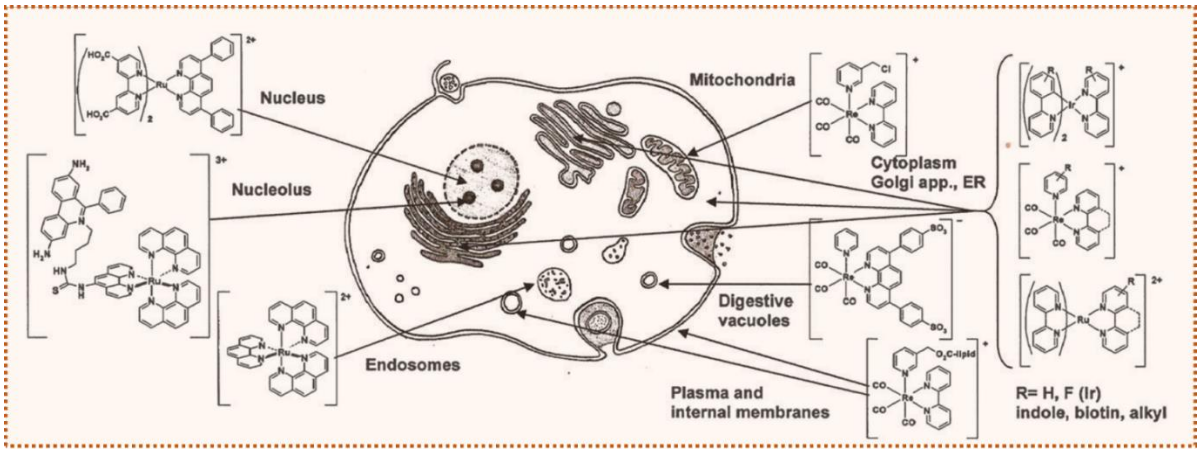

Fig. 1.16 Localization of d^6-complexes in cells. Adapted from the reference.[123] Copyright 2010 Royal Society of Chemistry.

1.3.2 Fluorescent half-sandwich transition metal complexes

Half-sandwich “piano-stool complexes” is an important class of the organometallic complexes, and have been used for a wide range of applications, such as enzyme inhibition, bioimaging, anticancer and antimicrobial agents.[129-131] For quite some time, the luminescent half-sandwich transition-metal complexes have been developed efficiently to understand the mechanism of actions (MoAs) of these complexes, as potential anticancer agents, catalytic drugs, biomarkers, etc.[132-134] Luminescent organometallic complexes could exhibit different type of electronic transitions, depending on the energy levels of the attached ligands, the metal atom and the interactions between them, which will be discussed in more detail later in Chapter 3. Notably, metal-to-ligand (MLCT) transitions are most frequently observed for the luminescent transition metal complexes, owing to their strong spin-orbit coupling induced by the metal atom, leading to intersystem crossing to the MLCT state. The ensuing emissions from the metal-to-ligand CT state are quite useful for cellular imaging applications.[135, 136]

Several half-sandwich complexes could be the ideal candidates to regulate certain redox and/or catalytical reactions in the cells, but due to their non-luminescent characteristics, it is tedious to understand their mechanism of action. For example, iridium(II) complexes can show excellent catalytic activity for detoxifying the α,β-unsaturated aldehydes which are associated with various neurodegenerative disorders, such as atherosclerosis, cancers, etc. In these cases, the common adopted strategy is to make a non-fluorescent metal complex emissive by attaching an organic

fluorophores, such as rhodamine, coumarin, etc., to the ligands, which is coordinated to the metal atom (Fig. 1.17).[137-139] Bose *et al*., developed the fluorescent half-sandwich iridium-picolinamidate complexes, using the strategy mentioned earlier. The resultant fluorescent half-sandwich complexes were used to reduce the targeted carbonyl containing compounds into the alcohols, and visualized their cellular distribution and uptake properties by using the confocal microscopy.[140]

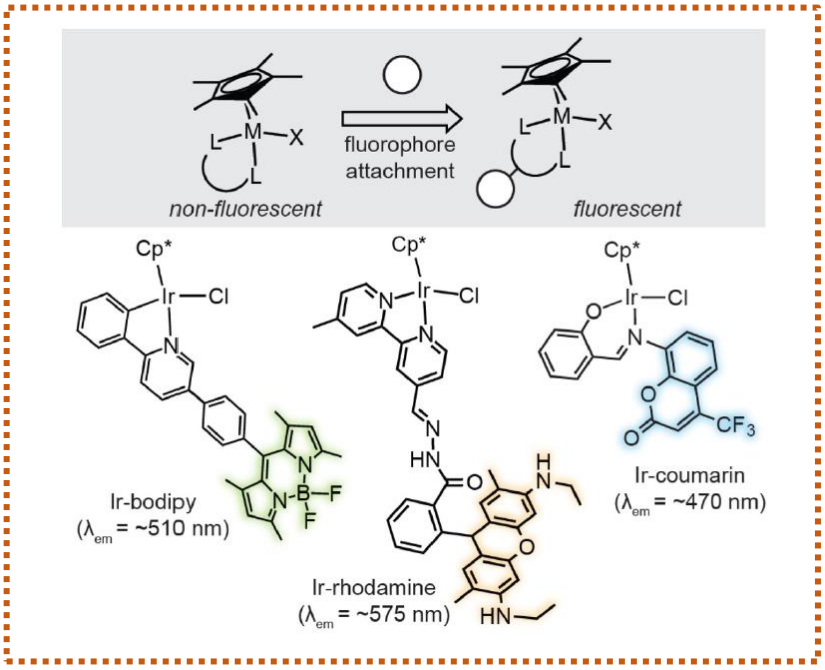

Fig. 1.17 Design of fluorescent half-sandwich iridium complexes.[137-139]

Additionally, several η^5-cyclopentadienyl containing d^6-transition metal complexes have been reported, to restrict the migration of tumor cells. Wang *et al*., reported triphenylamine/*N*-phenylcarbazole appended half-sandwich iridium(III) Schiff base complexes, and used them to catalytically generate intracellular reactive oxygen species (ROS), induced lysosomal damage, thus resulting in apoptosis. The

mechanism of action was monitored by using flow cytometry and confocal microscopy.[141] Liu and co-workers, frequently employed half-sandwich d^6-complexes of ruthenium and iridium, to trace the lysosomal-targeting imaging.[142-144] Ma *et al*., developed three-legged “piano-stool” half-sandwich naphthalimide (appended with pyrrolidine and methoxyethanol) ruthenium(II) and iridium(III) complexes and studied their intracellular behavior. The results from the flow cytometry showed that these complexes could trigger a cell arrest in the early S (DNA synthesis) and G_2 (cell growth) phases, to induce a significant increase of the intracellular ROS. The influence of using different ligands on the mechanism of action (MoA) have also been explored through confocal microscopy. The pyrrolidine-modified naphthalimide half-sandwich iridium(III) complex (**2**) was observed to target mitochondria after energy-dependent entry, while the methoxyethanol-appended naphthalimide half-sandwich iridium(III) complex (**4**) targeted lysozyme, leading to mitochondrial and lysosomal damages respectively (Fig. 1.18).[145]

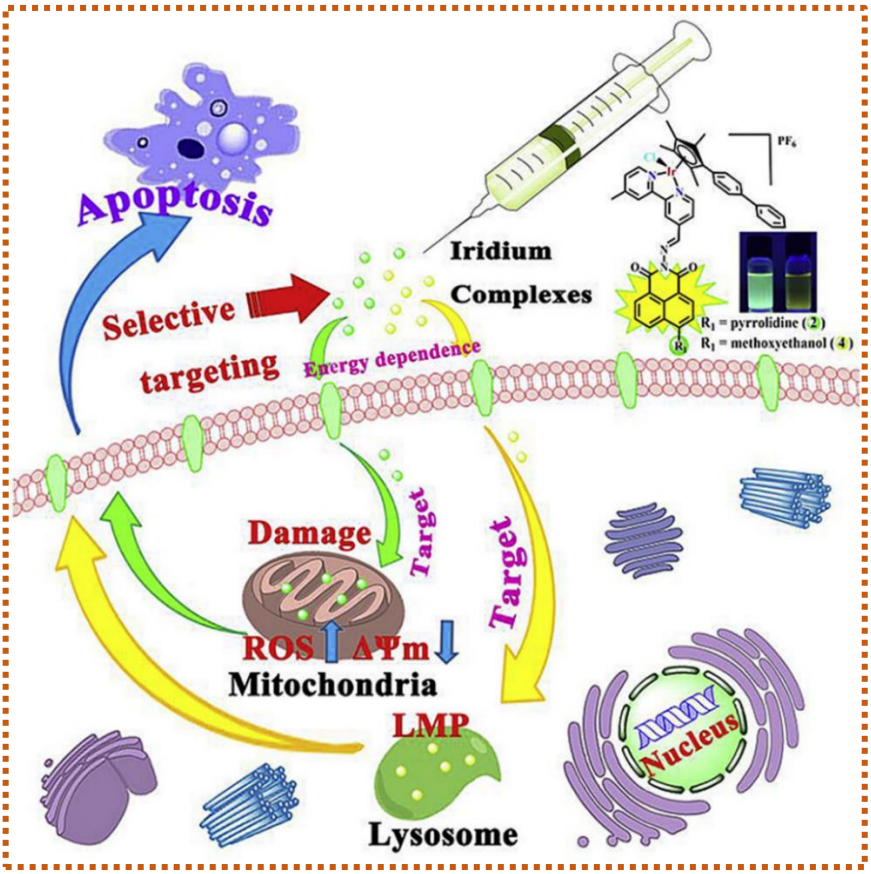

Fig. 1.18 Mechanism of action of naphthylamide-modified half-sandwich iridium(III) complexes. Adapted from the reference.[145] Copyright 2019 Elsevier.

1.3.3 Transition metal-maleimide complexes

Transition metal complexes have been successfully utilized as chemotherapeutics for many years.[146, 147] However, the most prevailing challenge encountered in the past was the low degree of selectivity, that led to serious side-effects during the medication.[148] In order to overcome this limitation, several strategies have been proposed over the years, such as tethering the bioactive functional groups to the ligands coordinated to the metal atoms.[149] Maleimide based structures are well-known to undergo addition and substitution reactions with the biomolecules, especially with macromolecules containing the sulfhydryl groups to form stable thioether bond for the

transport of bioactive moieties.[113, 135] Moreover, different organic fluorophores have also been labeled using maleimide derivatization to generate site-specific labeling reagents.[146, 147]

Organometallic complexes of various transition metal atoms (Co^{III}, Fe^{II}, Ir^{III}, Ru^{II}, Re^{I}, $Pt^{II/IV}$, etc.) containing the maleimide motif have been reported over the years.[135, 150, 151] In 2004, Warnecke *et al*., reported water soluble maleimide-appended carboplatin complexes as potential albumin binding prodrugs (Fig. 1.20).[152] Maleimide derivatives have also been frequently used to functionalize the ligands in metallocene and half-sandwich complexes (Fig. 1.20).[153, 154] Later, Hanif *et al.*, utilized the maleimide moiety to functionalize the η^6-arene half-sandwich ruthenium(II) complexes. These complexes could undergo selective reaction with the biomolecules, containing a thiol-functionality, *via* the maleimide motif (Fig. 1.20).[155] Recently, Kowol and co-workers have developed maleimide-functionalized platinum(IV) prodrugs for selective binding of thiol-containing tumor-targeting molecules, such as human serum albumin (HSA) (Fig. 1.19).[156]

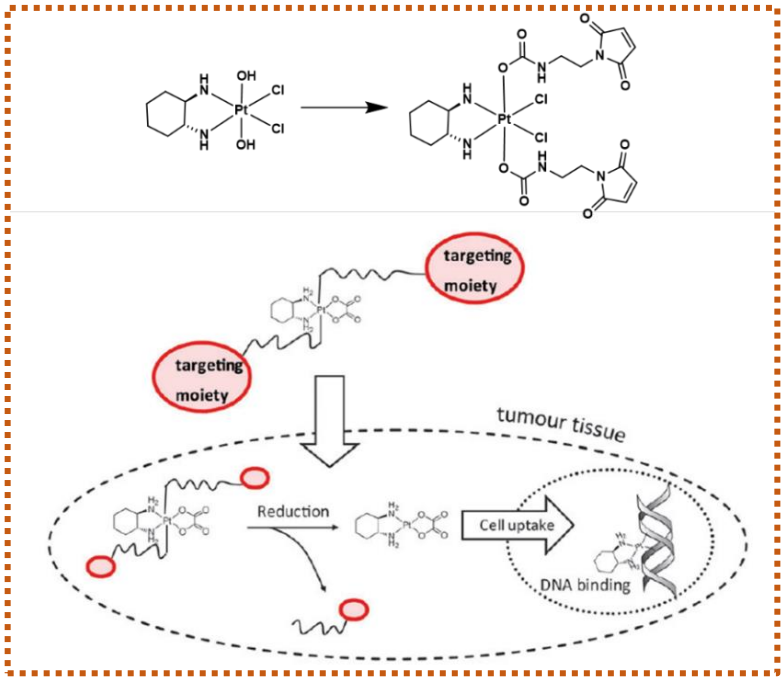

Fig. 1.19 Concept of maleimide-functionalized platinum(IV) products. Adapted from the reference.[156] Copyright 2013 Royal Society of Chemistry.

Besides, appending the ligands coordinated to the transition metal atoms, unsubstituted maleimides have also been used as a ligand in organometallic complexes. Rudolf and co-workers have repeatedly used maleimides to develop the metallocarbonyl complexes of iron, tungsten, ruthenium, etc.[157, 158] The metallocarbonyl complexes have been employed as IR-markers to monitor various biochemical processes, owing to their strong characteristic band in the infra-red region (2150–1800 cm^{-1}).[159] The developed half-sandwich metallocarbonyl complexes could undergo addition reaction with thiols, Diels alder reaction with alkenes and oxa-Michael reaction with hydroxyl containing biomolecules.[160-162] Moreover, iron and gold nanoparticles were also functionalized with these metallocarbonyl maleimide complexes, thus utilized as labeling agents, enzyme inhibitors, and carbon monoxide

releasing molecules (CORMs) (Fig. 1.20).[163-165] Despite all the fascinating work, fluorescent substituted maleimide derivatives have not been utilized as a ligand, to the best of our knowledge. Therefore, the potential half-sandwich metallocarbonyl complexes and how they were tailored to prepared the desired complexes, will be explained later in Chapter 3.

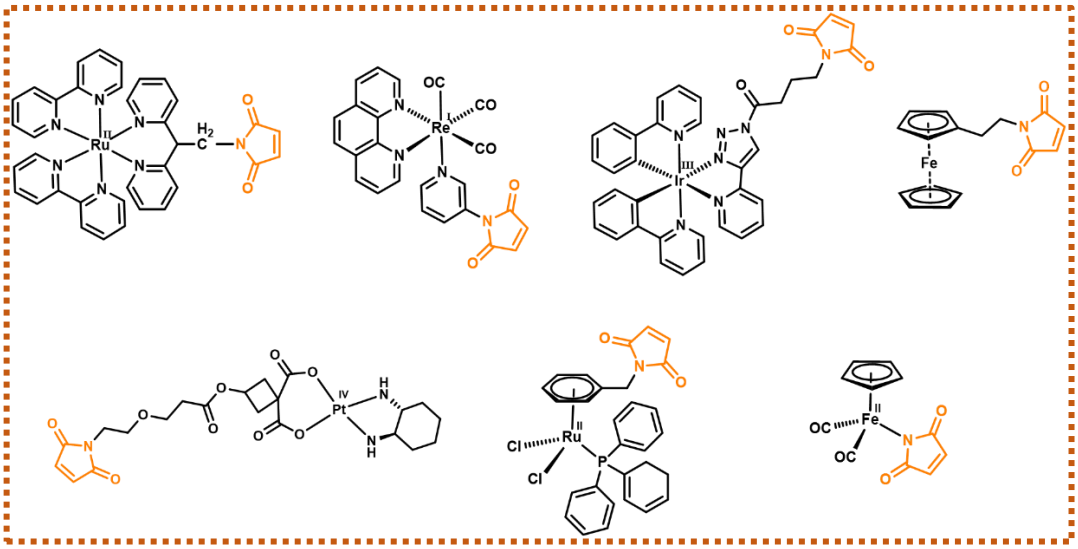

Fig. 1.20 Chemical structures of the reported transition metal–maleimide based complexes.[121, 135, 147, 152, 153, 155, 165]

1.3.4 Luminescent lanthanide complexes

For any luminescent material, the most discussed parameters are quantum yield, emission wavelength, molar absorption coefficient, and fluorescent lifetime as well as their photostability.[166] The emission spectra of lanthanide complexes tremendously depend on the lanthanide metal ions, for instance, europium(III), terbium(III) and samarium(III) ions emits red, green and orange light, respectively. Notably, the discrete line-like spectra, varying from metal to metal, originates from the overlap of the atomic

orbitals, and their fluorescent intensity is sensitive to the environment. Owing to their longer-wavelength emissions, they can penetrate various substrates, such as the human tissue, and visualize them very efficiently.[167]

Lanthanide complexes exhibit extremely long luminescence lifetimes (ms), compared to that of organic dyes (in ns range). They absorb the light in the near-UV region and show emissions in the visible or near-infrared (NIR) region of the spectrum, thus regarded as potential candidates for applications in displays and as optical imaging agents.[168] However, the long lifetimes come with the disadvantage of having weak absorptions with low extinction coefficient, owing to the Laporte forbidden $f \rightarrow f$ transitions.[169] The direct excitation of many lanthanide ions is problematic, thus utilizing the ligand as a chromophore or an antenna, to photosensitize (enhance) the absorption and emission intensity of electronic transitions is a good approach. The auxiliary ligands would absorb the energy and then transfer it to the energy levels of the lanthanide ion *via* intersystem crossing (ISC), ensuing lanthanide emissions.[170] For the effective design of a lanthanide complex with high luminescence efficiency, the ligand should contain donor energy states for efficient energy transfer, and also should eliminate other quenching pathways.[167] Furthermore, the steric shielding of the lanthanide excited state from the solvent, provided by the appropriate ligand, would enhance their luminiscence efficiency and maximize their emission lifetime.[171] The strategies for the photosensitization will be discussed in Chapter 4 in more detail. Furthermore, the coordination stability needs to be significant to use these lanthanide complexes in solution-state or doped films. The coordination sphere as well as the energy levels of lanthanide ions and attached ligands, regulate the electronic, magnetic and photophysical properties of the lanthanide complexes.[172]

For enhancing the emission efficiency, the non-radiative deactivations should be restricted in order to eliminate the quenching. This has been achieved either through a ligand modification (deuterating or fluorinating the ligands),[173, 174] or changing the environment of the lanthanide ion, by incorporating the lanthanide ions into metallacrown receptors, or doped upconversion nanoparticles (UCNPs).[175, 176] Several inorganic phosphors, such as nitrides, aluminates, silicates, oxides, etc., doped with europium metals have been tested to develop the microLEDs. These microLEDs have shown better performance than the LEDs and LCDs and are used for telecommunication devices (Fig. 1.21a).[177] The characteristic of lanthanide luminescence to absorb/excite in the UV/Vis region and display emissions in the Vis/NIR region has been exploited for security and barcoding applications, for instance, the orange-red luminescence implemented as security features in Euro bank notes is due to the Eu(III) dye. Several bar codes recognition and counterfeiting tags have been designed by combining different luminescent lanthanide ions (Eu, Tb, Sm, Dy, Tm), thus could be recognized with 99.99% confidence.[178, 179] Recently, some of lanthanide based materials, such as $SrAl_2O_4:Eu^{II}$, which showed the emissions under mechanical strain (pressure, ultrasound waves, rubbing, etc.) have been used as mechanoluminescent sensors, for health monitoring and other industrial applications (Fig. 1.21c).[180] Several advancements have been made for tailoring lanthanide-based probes for applications, such as bioimaging, drug delivery and therapeutics (Fig. 1.21b).[181-183] An interesting example of using europium–ruthenium complex as an anticancer prodrug was reported by Li *et al*. The bimetallic complex dissociated at one excitation wavelength, releasing the ruthenium-based anticancer drug, followed by the

excitation of the europium containing dissociation product at a second wavelength, thus enabled easy monitoring of a drug release behavior.[184]

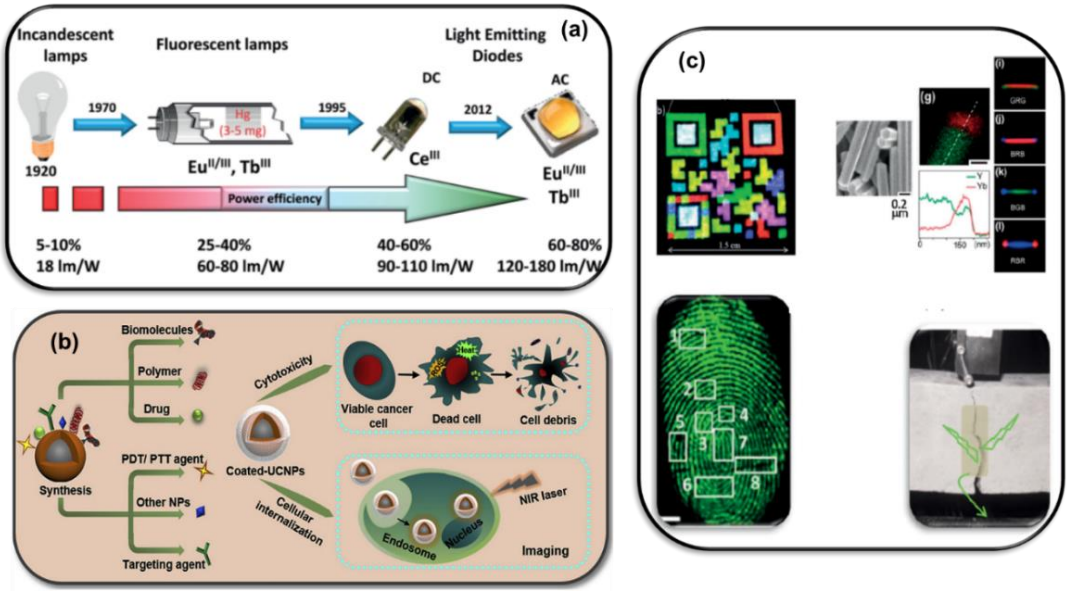

Fig. 1.21 Potential applications of lanthanides luminescence in optical devices (**a**); biochemical (**b**); and security and tagging (**c**) applications.[185, 186] Copyright 2019 Elsevier and 2017 European Chemical Society.

1.3.5 Maleimide-based complexes of lanthanide metals

Benefiting from the privilege of displaying long lifetimes, and luminiscence enhancement by the ligand moiety as well as sharp bands appearing at the same wavelengths even in different environments, lanthanide complexes (especially europium and terbium) have been used for biochemical applications. Several chromophores have been used to enhance the lanthanide-based luminescence. However, only unsubstituted maleimide have been used to couple with the ligands,

thus employed as a biorthogonal coupling tool (Fig. 1.22).[187-189] Pecoraro and coworkers functionalized the lanthanide-gallium metallacrowns with maleimido and azido derivatives, thus bio-conjugated the metallacrowns to the molecules using Michael additions, and copper-catalyzed alkyne and azide cycloaddition (CuAAC).[190] Tetradentate β-diketonate-europium chelate containing maleimide linkers were developed, for forming the stable immunoconjugates with the lysine residues and used for protein labeling and bioimaging using the confocal microscopy (Fig. 1.22).[191] Later, Faschinger *et al*., reported terpyridine-based Eu(III) complexes explored for the luminescence resonance energy transfer (LRET) applications (Fig. 1.22). The maleimide or hydrazide functionalities were incorporated with short linkers, for site specific conjugations with keto amino acids and cysteine mutants.[192] Furthermore, maleimide moiety have been introduced on the surface of the lanthanide-based upconversion nanoparticles to allow the covalent conjugation to the biomolecules, such as DNA, folic acid, peptides, proteins etc. during a phase transfer from the organic to the aqueous media.[193, 194] In all the above-mentioned examples, maleimide derivatives have only been used as conjugation tool with the biomolecules. However, maleimides as chromophore ligands have not been explored so-far.

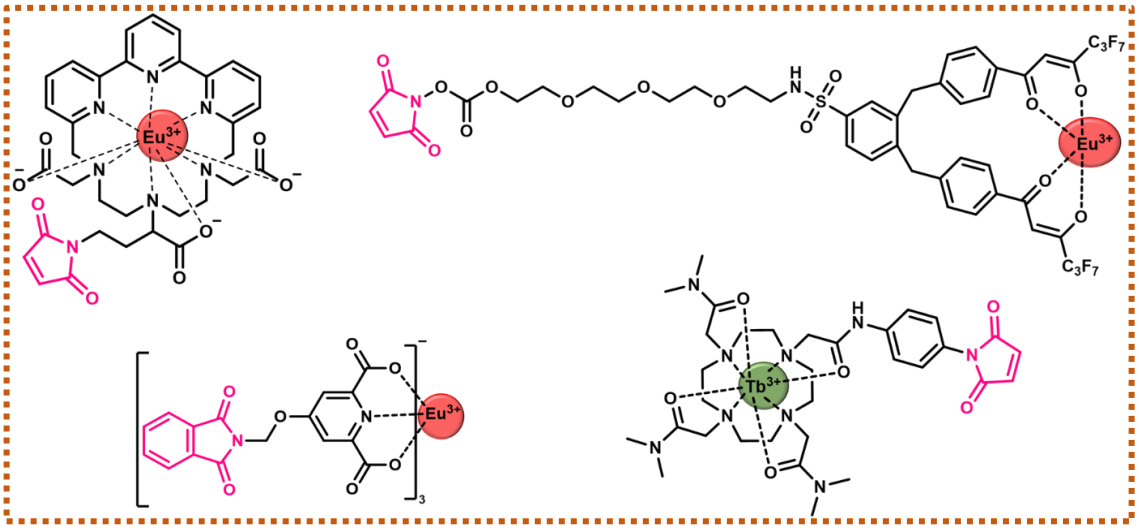

Fig. 1.22 Structures of some reported examples of lanthanide complexes containing maleimide linkers for bioconjugation applications.[187, 189, 191, 192]

1.4 Summary

In the first section of the introduction, the key concepts of fluorescence along with the different methods for quantification were introduced. This was followed by the explanation of the different photophysical processes occurring during fluorescence and the environmental factors, associated with the fluorescence quenching.

The second section of the chapter highlighted the significance and applications of maleimide derived fluorophores for a myriad of applications, such as polymer functionalization, nanoparticles tagging, bioconjugation and drug delivery. It also entails the challenges associated with the fluorescence of substituted maleimide derivatives observed in previous studies. The development of the substituted maleimide fluorophores to suppress the fluorescence quenching and the detailed fluorescent mechanism, are discussed in Chapter 2, with work focused on achieving dual-state emissions.

The final section focused on the development of metal-maleimide chemistries in the organometallic complexes. However, in these complexes the maleimide moiety has been mostly employed for ligand modification and acted as an indispensable tool for applications, such as bioconjugation. The development of the fluorescent transition metal-maleimide and lanthanide metal-maleimide complexes have been explored in Chapter 3 and 4, respectively. The fluorescent properties of maleimides have been exploited to enhance the emissions of the metal complexes, and the redox properties of the selected complexes have been investigated, to explore the potential of the newly developed hybrid probes for applications, such as catalysis, bioimaging, etc.

1.5 References

1. Bernard Valeur; Mário Nuno Berberan-Santos, *Molecular Fluorescence: Principles and Applications*. 2nd ed.; Wiley: **2012**.

2. Belmonte-Vázquez, J. L.; Amador-Sánchez, Y. A.; Rodríguez-Cortés, L. A.; Rodríguez-Molina, B., Dual-State Emission (DSE) in Organic Fluorophores: Design and Applications. *Chem. Mater.* **2021,** *33* (18), 7160-7184.

3. Borisov, S. M., Chapter 1: Fundamentals of Quenched Phosphorescence O_2 Sensing and Rational Design of Sensor Materials. In *Quenched-phosphorescence Detection of Molecular Oxygen: Applications in Life Sciences*, The Royal Society of Chemistry: **2018**; pp 1-18.

4. Lakowicz, J. R., *Principles of Fluorescence Spectroscopy*. 2nd ed.; Kluwer Academic/Plenum Press: New York, **1999**.

5. Chmyrov, A. Photo-induced dark states in fluorescence spectroscopy – investigations & applications. KTH Royal Institute of Technology, 2010.

6. Ergin, E.; Dogan, A.; Parmaksiz, M.; Elçin, A. E.; Elçin, Y. M., Time-Resolved Fluorescence Resonance Energy Transfer [TR-FRET] Assays for Biochemical Processes. *Curr. Pharm. Biotechnol.* **2016,** *17* (14), 1222-1230.

7. Kumar, K.; Tarai, M.; Mishra, A. K., Unconventional steady-state fluorescence spectroscopy as an analytical technique for analyses of complex-multifluorophoric mixtures. *TrAC Trend. Anal. Chem.* **2017,** *97*, 216-243.

8. Berlman, I. B., *Some Uses of Fluorescence Compounds*. 2nd ed.; Academic Press: **1971**.

9. Würth, C.; Grabolle, M.; Pauli, J.; Spieles, M.; Resch-Genger, U., Relative and absolute determination of fluorescence quantum yields of transparent samples. *Nat. Protoc.* **2013,** *8* (8), 1535-1550.

10. Berezin, M. Y.; Achilefu, S., Fluorescence Lifetime Measurements and Biological Imaging. *Chem. Rev.* **2010,** *110* (5), 2641-2684.

11. Sugunan, S. K.; Robotham, B.; Sloan, R. P.; Szmytkowski, J.; Ghiggino, K. P.; Paige, M. F.; Steer, R. P., Photophysics of Untethered ZnTPP–Fullerene Complexes in Solution. *J. Phy. Chem. A* **2011,** *115* (44), 12217-12227.

12. Levitus, M., Handbook of Fluorescence Spectroscopy and Imaging. From Ensemble to Single Molecules. Edited by Markus Sauer, Johan Hofkens and Jörg Enderlein. *Angew. Chem. Int. Ed.* **2011,** *50* (39), 9017-9018.

13. Fraiji, L. K.; Hayes, D. M.; Werner, T. C., Static and dynamic fluorescence quenching experiments for the physical chemistry laboratory. *J. Chem. Educ.* **1992,** *69* (5), 424.

14. Sasaki, S.; Drummen, G. P. C.; Konishi, G.-i., Recent advances in twisted intramolecular charge transfer (TICT) fluorescence and related phenomena in materials chemistry. *J. Mater. Chem. C* **2016,** *4* (14), 2731-2743.

15. Valerii F. Traven; Cheptsov, D. A., Sensory effects of fluorescent organic dyes. *Russ. Chem. Rev.* **2020,** *89*, 713.

16. Haberhauer, G.; Gleiter, R.; Burkhart, C., Planarized Intramolecular Charge Transfer: A Concept for Fluorophores with both Large Stokes Shifts and High Fluorescence Quantum Yields. *Chem. Eur. J.* **2016,** *22* (3), 971-978.

17. Guy, J.; Caron, K.; Dufresne, S.; Michnick, S. W.; Skene; Keillor, J. W., Convergent Preparation and Photophysical Characterization of Dimaleimide Dansyl

Fluorogens: Elucidation of the Maleimide Fluorescence Quenching Mechanism. *J. Am. Chem. Soc.* **2007,** *129* (39), 11969-11977.

18. Prasanna de Silva, A.; Nimal Gunaratne, H. Q.; Gunnlaugsson, T., Fluorescent PET(Photoinduced Electron Transfer) reagents for thiols. *Tetrahedron Lett.* **1998,** *39* (28), 5077-5080.

19. Daly, B.; Ling, J.; de Silva, A. P., Current developments in fluorescent PET (photoinduced electron transfer) sensors and switches. *Chem. Soc. Rev.* **2015,** *44* (13), 4203-4211.

20. Doose, S.; Neuweiler, H.; Sauer, M., Fluorescence Quenching by Photoinduced Electron Transfer: A Reporter for Conformational Dynamics of Macromolecules. *ChemPhysChem* **2009,** *10* (9-10), 1389-1398.

21. Escudero, D., Revising Intramolecular Photoinduced Electron Transfer (PET) from First-Principles. *Acc. Chem. Res.* **2016,** *49* (9), 1816-1824.

22. Wang, W.; Marshall, M.; Collins, E.; Marquez, S.; Mu, C.; Bowen, K. H.; Zhang, X., Intramolecular electron-induced proton transfer and its correlation with excited-state intramolecular proton transfer. *Nat. Commun.* **2019,** *10* (1), 1170.

23. Karas, L. J.; Wu, C.-H.; Ottosson, H.; Wu, J. I., Electron-driven proton transfer relieves excited-state antiaromaticity in photoexcited DNA base pairs. *Chem. Sci.* **2020,** *11* (37), 10071-10077.

24. Quan, W.-D. The design, construction and characterisation of self-assembled biomimetic multi-chromophoric photosystems. University of Warwick, 2017.

25. Havlík, M.; Talianová, V.; Kaplánek, R.; Bříza, T.; Dolenský, B.; Králová, J.; Martásek, P.; Král, V., Versatile fluorophores for bioimaging applications: π-expanded

naphthalimide derivatives with skeletal and appendage diversity. *Chem. Commun.* **2019,** *55* (18), 2696-2699.

26. Shimizu, M.; Hiyama, T., Organic Fluorophores Exhibiting Highly Efficient Photoluminescence in the Solid State. *Chem. Asian J.* **2010,** *5* (7), 1516-1531.

27. Massue, J.; Jacquemin, D.; Ulrich, G., Boranils: Versatile Multifunctional Organic Fluorophores for Innovative Applications. *Organics* **2021,** *2* (4), 365-375.

28. Qi, J.; Duan, X.; Cai, Y.; Jia, S.; Chen, C.; Zhao, Z.; Li, Y.; Peng, H.-Q.; Kwok, R. T. K.; Lam, J. W. Y.; Ding, D.; Tang, B. Z., Simultaneously boosting the conjugation, brightness and solubility of organic fluorophores by using AIEgens. *Chem. Sci.* **2020,** *11* (32), 8438-8447.

29. Lang, W.; Yuan, C.; Zhu, L.; Du, S.; Qian, L.; Ge, J.; Yao, S. Q., Recent advances in construction of small molecule-based fluorophore-drug conjugates. *J. Pharm. Anal.* **2020,** *10* (5), 434-443.

30. Guest, M.; Mir, R.; Foran, G.; Hickson, B.; Necakov, A.; Dudding, T., Trisaminocyclopropenium Cations as Small-Molecule Organic Fluorophores: Design Guidelines and Bioimaging Applications. *J. Org. Chem.* **2020,** *85* (21), 13997-14011.

31. Gong, W.; Das, P.; Samanta, S.; Xiong, J.; Pan, W.; Gu, Z.; Zhang, J.; Qu, J.; Yang, Z., Redefining the photo-stability of common fluorophores with triplet state quenchers: mechanistic insights and recent updates. *Chem. Commun.* **2019,** *55* (60), 8695-8704.

32. Schwechheimer, C.; Rönicke, F.; Schepers, U.; Wagenknecht, H.-A., A new structure–activity relationship for cyanine dyes to improve photostability and fluorescence properties for live cell imaging. *Chem. Sci.* **2018,** *9* (31), 6557-6563.

33. Jun, J. V.; Chenoweth, D. M.; Petersson, E. J., Rational design of small molecule fluorescent probes for biological applications. *Org. Biomol. Chem.* **2020,** *18* (30), 5747-5763.

34. Simpson, J. D.; Smith, S. A.; Thurecht, K. J.; Such, G., Engineered Polymeric Materials for Biological Applications: Overcoming Challenges of the Bio–Nano Interface. *Polymers* **2019,** *11* (9), 1441-1473.

35. Tao, L.; Kaddis, C. S.; Loo, R. R. O.; Grover, G. N.; Loo, J. A.; Maynard, H. D., Synthesis of Maleimide-End-Functionalized Star Polymers and Multimeric Protein−Polymer Conjugates. *Macromolecules* **2009,** *42* (21), 8028-8033.

36. Wright, T. A.; Rahman, M. S.; Bennett, C.; Johnson, M. R.; Fischesser, H.; Ram, N.; Tyler, A.; Page, R. C.; Konkolewicz, D., Hydrolytically Stable Maleimide-End-Functionalized Polymers for Site-Specific Protein Conjugation. *Bioconjug. Chem.* **2021,** *32* (11), 2447-2456.

37. Renault, K.; Fredy, J. W.; Renard, P.-Y.; Sabot, C., Covalent Modification of Biomolecules through Maleimide-Based Labeling Strategies. *Bioconjug. Chem.* **2018,** *29* (8), 2497-2513.

38. Smith, M. E. B.; Schumacher, F. F.; Ryan, C. P.; Tedaldi, L. M.; Papaioannou, D.; Waksman, G.; Caddick, S.; Baker, J. R., Protein Modification, Bioconjugation, and Disulfide Bridging Using Bromomaleimides. *J. Am. Chem. Soc.* **2010,** *132* (6), 1960-1965.

39. Belbekhouche, S.; Guerrouache, M.; Carbonnier, B., Thiol–Maleimide Michael Addition Click Reaction: A New Route to Surface Modification of Porous Polymeric Monolith. *Macromol. Chem. Phys.* **2016,** *217* (8), 997-1006.

40. Qu, L.; Yin, C.; Huo, F.; Li, J.; Chao, J.; Zhang, Y., A maleimide-based thiol fluorescent probe and its application for bioimaging. *Sens. Actuators B Chem.* **2014,** *195*, 246-251.

41. Liu, T.; Huo, F.; Yin, C.; Li, J.; Chao, J.; Zhang, Y., A triphenylamine as a fluorophore and maleimide as a bonding group selective turn-on fluorescent imaging probe for thiols. *Dyes Pigm.* **2016,** *128*, 209-214.

42. Li, F.; Li, X.; Zhang, X., Dynamic Diels–Alder reactions of maleimide–furan amphiphiles and their fluorescence ON/OFF behaviours. *Org. Biomol. Chem.* **2018,** *16* (42), 7871-7877.

43. Chen, Y.; Tsao, K.; Acton, S. L.; Keillor, J. W., A Green BODIPY-Based, Super-Fluorogenic, Protein-Specific Labelling Agent. *Angew. Chem. Int. Ed.* **2018,** *57* (38), 12390-12394.

44. Robin, M. P.; Jones, M. W.; Haddleton, D. M.; O'Reilly, R. K., Dibromomaleimide End Functional Polymers by RAFT Polymerization Without the Need of Protecting Groups. *ACS Macro Lett.* **2012,** *1* (1), 222-226.

45. Mabire, A. B.; Robin, M. P.; Willcock, H.; Pitto-Barry, A.; Kirby, N.; O'Reilly, R. K., Dual effect of thiol addition on fluorescent polymeric micelles: ON-to-OFF emissive switch and morphology transition. *Chem. Commun.* **2014,** *50* (78), 11492-11495.

46. Mabire, A. B.; Robin, M. P.; Quan, W.-D.; Willcock, H.; Stavros, V. G.; O'Reilly, R. K., Aminomaleimide fluorophores: a simple functional group with bright, solvent dependent emission. *Chem. Commun.* **2015,** *51* (47), 9733-9736.

47. Xie, Y.; Husband, J. T.; Torrent-Sucarrat, M.; Yang, H.; Liu, W.; O'Reilly, R. K., Rational design of substituted maleimide dyes with tunable fluorescence and solvafluorochromism. *Chem. Commun.* **2018,** *54* (27), 3339-3342.

48. Husband, J. T.; Xie, Y.; Wilks, T. R.; Male, L.; Torrent-Sucarrat, M.; Stavros, V. G.; O'Reilly, R. K., Rigidochromism by imide functionalisation of an aminomaleimide fluorophore. *Chem. Sci.* **2021,** *12* (31), 10550-10557.

49. Värkonyi, Z.; Kabók, K., Effect of temperature on light-absorption and fluorescence of the peroxidase. *Acta Biochim. Biophys. Acad. Sci. Hung.* **1975,** *10* (1-2), 129-37.

50. Deepa, H. R.; Thipperudrappa, J.; Suresh Kumar, H. M., Effect of temperature on fluorescence quenching and emission characteristics of laser dyes. *J. Phys.: Conf. Ser.* **2020,** *1473* (1), 012046.

51. Penfold, T. J.; Dias, F. B.; Monkman, A. P., The theory of thermally activated delayed fluorescence for organic light emitting diodes. *Chem. Commun.* **2018,** *54* (32), 3926-3935.

52. Martin, M. M.; Lindqvist, L., The pH dependence of fluorescein fluorescence. *J. Lumin.* **1975,** *10* (6), 381-390.

53. Qi, J.; Liu, D.; Liu, X.; Guan, S.; Shi, F.; Chang, H.; He, H.; Yang, G., Fluorescent pH Sensors for Broad-Range pH Measurement Based on a Single Fluorophore. *Anal. Chem.* **2015,** *87* (12), 5897-5904.

54. Tian, M.; Peng, X.; Fan, J.; Wang, J.; Sun, S., A fluorescent sensor for pH based on rhodamine fluorophore. *Dyes Pigm.* **2012,** *95* (1), 112-115.

55. Klymchenko, A. S.; Mely, Y., *Chapter Two: Fluorescent Environment-Sensitive Dyes as Reporters of Biomolecular Interactions*. Academic Press: **2013**; p 35-58.

56. Zhao, E.; Lam, J. W. Y.; Meng, L.; Hong, Y.; Deng, H.; Bai, G.; Huang, X.; Hao, J.; Tang, B. Z., Poly[(maleic anhydride)-*alt*-(vinyl acetate)]: A Pure Oxygenic Nonconjugated Macromolecule with Strong Light Emission and Solvatochromic Effect. *Macromolecules* **2015,** *48* (1), 64-71.

57. Robin, M. P.; O'Reilly, R. K., Fluorescent and chemico-fluorescent responsive polymers from dithiomaleimide and dibromomaleimide functional monomers. *Chem. Sci.* **2014,** *5* (7), 2717-2723.

58. Robin, M. P.; Wilson, P.; Mabire, A. B.; Kiviaho, J. K.; Raymond, J. E.; Haddleton, D. M.; O'Reilly, R. K., Conjugation-Induced Fluorescent Labeling of Proteins and Polymers Using Dithiomaleimides. *J. Am. Chem. Soc.* **2013,** *135* (8), 2875-2878.

59. Robin, M. P.; Mabire, A. B.; Damborsky, J. C.; Thom, E. S.; Winzer-Serhan, U. H.; Raymond, J. E.; O'Reilly, R. K., New Functional Handle for Use as a Self-Reporting Contrast and Delivery Agent in Nanomedicine. *J. Am. Chem. Soc.* **2013,** *135* (25), 9518-9524.

60. Robin, M. P.; Osborne, S. A. M.; Pikramenou, Z.; Raymond, J. E.; O'Reilly, R. K., Fluorescent Block Copolymer Micelles That Can Self-Report on Their Assembly and Small Molecule Encapsulation. *Macromolecules* **2016,** *49* (2), 653-662.

61. Tang, Z.; Wilson, P.; Kempe, K.; Chen, H.; Haddleton, D. M., Reversible Regulation of Thermoresponsive Property of Dithiomaleimide-Containing Copolymers via Sequential Thiol Exchange Reactions. *ACS Macro Lett.* **2016,** *5* (6), 709-713.

62. Varlas, S.; Keogh, R.; Xie, Y.; Horswell, S. L.; Foster, J. C.; O'Reilly, R. K., Polymerization-Induced Polymersome Fusion. *J. Am. Chem. Soc.* **2019,** *141* (51), 20234-20248.

63. Mabire, A. B.; Brouard, Q.; Pitto-Barry, A.; Williams, R. J.; Willcock, H.; Kirby, N.; Chapman, E.; O'Reilly, R. K., CO_2/pH-responsive particles with built-in fluorescence read-out. *Polym. Chem.* **2016,** *7* (38), 5943-5948.

64. Robin, M. P.; Raymond, J. E.; O'Reilly, R. K., One-pot synthesis of super-bright fluorescent nanogel contrast agents containing a dithiomaleimide fluorophore. *Mater. Horiz.* **2015,** *2* (1), 54-59.

65. He, B.; Zhang, J.; Zhang, H.; Liu, Z.; Zou, H.; Hu, R.; Qin, A.; Kwok, R. T. K.; Lam, J. W. Y.; Tang, B. Z., Catalyst-Free Multicomponent Tandem Polymerizations of Alkyne and Amines toward Nontraditional Intrinsic Luminescent Poly(aminomaleimide)s. *Macromolecules* **2020,** *53* (10), 3756-3764.

66. Shi, Q.; Zhang, Y.; Huang, Z.; Zhou, N.; Zhang, Z.; Zhu, X., Precise sequence regulation through maleimide chemistry. *Polym. J.* **2020,** *52* (1), 21-31.

67. Mejia, G.; Wang, Y.; Huang, Z.; Shi, Q.; Zhang, Z., Maleimide Chemistry: Enabling the Precision Polymer Synthesis. *Chin. J. Chem.* **2021,** *39* (12), 3177-3187.

68. Yan, J.; Wang, R.; Pan, D.; Yang, R.; Xu, Y.; Wang, L.; Yang, M., Thiolactone-maleimide: a functional monomer to synthesize fluorescent aliphatic poly(amide-imide) with excellent solubility via in situ PEGylation. *Polym. Chem.* **2016,** *7* (40), 6241-6249.

69. Xie, Y.; Arno, M. C.; Husband, J. T.; Torrent-Sucarrat, M.; O'Reilly, R. K., Manipulating the fluorescence lifetime at the sub-cellular scale via photo-switchable barcoding. *Nat. Commun.* **2020,** *11* (1), 2460.

70. Holmes, K. L.; Lantz, L. M., Chapter 9 Protein labeling with fluorescent probes. In *Methods Cell Biol.*, Academic Press: 2001; Vol. 63, pp 185-204.

71. Jäger, M.; Nir, E.; Weiss, S., Site-specific labeling of proteins for single-molecule FRET by combining chemical and enzymatic modification. *Protein Sci.* **2006,** *15* (3), 640-6.

72. Ravasco, J. M. J. M.; Faustino, H.; Trindade, A.; Gois, P. M. P., Bioconjugation with Maleimides: A Useful Tool for Chemical Biology. *Chem. Eur. J.* **2019,** *25* (1), 43-59.

73. Zhang, Y.; Zang, C.; An, G.; Shang, M.; Cui, Z.; Chen, G.; Xi, Z.; Zhou, C., Cysteine-specific protein multi-functionalization and disulfide bridging using 3-bromo-5-methylene pyrrolones. *Nat. Commun.* **2020,** *11* (1), 1015.

74. Akkapeddi, P.; Azizi, S.-A.; Freedy, A. M.; Cal, P. M. S. D.; Gois, P. M. P.; Bernardes, G. J. L., Construction of homogeneous antibody–drug conjugates using site-selective protein chemistry. *Chem. Sci.* **2016,** *7* (5), 2954-2963.

75. Kim, Y.; Ho, S. O.; Gassman, N. R.; Korlann, Y.; Landorf, E. V.; Collart, F. R.; Weiss, S., Efficient site-specific labeling of proteins via cysteines. *Bioconjug. Chem.* **2008,** *19* (3), 786-91.

76. Zhang, Y.; Huo, F.; Yin, C.; Yue, Y.; Hao, J.; Chao, J.; Liu, D., An off–on fluorescent probe based on maleimide for detecting thiols and its application for bioimaging. *Sens. Actuators B Chem.* **2015,** *207*, 59-65.

77. Yang, Y.; Huo, F.; Yin, C.; Chao, J.; Zhang, Y., An 'OFF–ON' fluorescent probe for specially recognize on Cys and its application in bioimaging. *Dyes Pigm.* **2015,** *114*, 105-109.

78. Marculescu, C.; Kossen, H.; Morgan, R. E.; Mayer, P.; Fletcher, S. A.; Tolner, B.; Chester, K. A.; Jones, L. H.; Baker, J. R., Aryloxymaleimides for cysteine

modification, disulfide bridging and the dual functionalization of disulfide bonds. *Chem. Commun.* **2014,** *50* (54), 7139-7142.

79. Castañeda, L.; Wright, Z. V. F.; Marculescu, C.; Tran, T. M.; Chudasama, V.; Maruani, A.; Hull, E. A.; Nunes, J. P. M.; Fitzmaurice, R. J.; Smith, M. E. B.; Jones, L. H.; Caddick, S.; Baker, J. R., A mild synthesis of *N*-functionalised bromomaleimides, thiomaleimides and bromopyridazinediones. *Tetrahedron Lett.* **2013,** *54* (27), 3493-3495.

80. Husband, J. T.; Hill, A. C.; O'Reilly, R. K., Utilizing functionalized bromomaleimides for fluorogenic conjugation and PEGylation of enzymes. *Polym. Int.* **2019,** *68* (7), 1247-1254.

81. Grison, C. M.; Burslem, G. M.; Miles, J. A.; Pilsl, L. K. A.; Yeo, D. J.; Imani, Z.; Warriner, S. L.; Webb, M. E.; Wilson, A. J., Double quick, double click reversible peptide “stapling”. *Chem. Sci.* **2017,** *8* (7), 5166-5171.

82. Collins, J.; Tanaka, J.; Wilson, P.; Kempe, K.; Davis, T. P.; McIntosh, M. P.; Whittaker, M. R.; Haddleton, D. M., In Situ Conjugation of Dithiophenol Maleimide Polymers and Oxytocin for Stable and Reversible Polymer–Peptide Conjugates. *Bioconjug. Chem.* **2015,** *26* (4), 633-638.

83. Hull, E. A.; Livanos, M.; Miranda, E.; Smith, M. E. B.; Chester, K. A.; Baker, J. R., Homogeneous Bispecifics by Disulfide Bridging. *Bioconjug. Chem.* **2014,** *25* (8), 1395-1401.

84. Moody, P.; Smith, M. E. B.; Ryan, C. P.; Chudasama, V.; Baker, J. R.; Molloy, J.; Caddick, S., Bromomaleimide-Linked Bioconjugates Are Cleavable in Mammalian Cells. *ChemBioChem* **2012,** *13* (1), 39-41.

85. Zhang, J.; Lin, Y.; Lin, Z.; Wei, Q.; Qian, J.; Ruan, R.; Jiang, X.; Hou, L.; Song, J.; Ding, J.; Yang, H., Stimuli-Responsive Nanoparticles for Controlled Drug Delivery in Synergistic Cancer Immunotherapy. *Adv. Sci.* **2022,** *9* (5), 2103444.

86. Mura, S.; Nicolas, J.; Couvreur, P., Stimuli-responsive nanocarriers for drug delivery. *Nat. Mater.* **2013,** *12* (11), 991-1003.

87. Hershberger, K. K.; Gauger, A. J.; Bronstein, L. M., Utilizing Stimuli Responsive Linkages to Engineer and Enhance Polymer Nanoparticle-Based Drug Delivery Platforms. *ACS Appl. Bio. Mater.* **2021,** *4* (6), 4720-4736.

88. Li, T.; Takeoka, S., A novel application of maleimide for advanced drug delivery: *in vitro* and *in vivo* evaluation of maleimide-modified pH-sensitive liposomes. *Int. J. Nanomedicine* **2013,** *8*, 3855-3866.

89. Bai, T.; Shao, D.; Chen, J.; Li, Y.; Xu, B. B.; Kong, J., pH-responsive dithiomaleimide-amphiphilic block copolymer for drug delivery and cellular imaging. *J. Colloid Interface Sci.* **2019,** *552*, 439-447.

90. Bai, T.; Du, J.; Chen, J.; Duan, X.; Zhuang, Q.; Chen, H.; Kong, J., Reduction-responsive dithiomaleimide-based polymeric micelles for controlled anti-cancer drug delivery and bioimaging. *Polym. Chem.* **2017,** *8* (46), 7160-7168.

91. Wang, H.; Xu, M.; Xiong, M.; Cheng, J., Reduction-responsive dithiomaleimide-based nanomedicine with high drug loading and FRET-indicated drug release. *Chem. Commun.* **2015,** *51* (23), 4807-4810.

92. Quan, Q.; Xie, J.; Gao, H.; Yang, M.; Zhang, F.; Liu, G.; Lin, X.; Wang, A.; Eden, H. S.; Lee, S.; Zhang, G.; Chen, X., HSA Coated Iron Oxide Nanoparticles as Drug Delivery Vehicles for Cancer Therapy. *Mol. Pharmaceutics* **2011,** *8* (5), 1669-1676.

93. Wierzbinski, K. R.; Szymanski, T.; Rozwadowska, N.; Rybka, J. D.; Zimna, A.; Zalewski, T.; Nowicka-Bauer, K.; Malcher, A.; Nowaczyk, M.; Krupinski, M.; Fiedorowicz, M.; Bogorodzki, P.; Grieb, P.; Giersig, M.; Kurpisz, M. K., Potential use of superparamagnetic iron oxide nanoparticles for *in vitro* and *in vivo* bioimaging of human myoblasts. *Sci. Rep.* **2018,** *8* (1), 3682.

94. Murakami, T.; Tsuchida, K., Recent advances in inorganic nanoparticle-based drug delivery systems. *Mini Rev. Med. Chem.* **2008,** *8* (2), 175-183.

95. Jiang, C.-c.; Cao, Y.-k.; Xiao, G.-y.; Zhu, R.-f.; Lu, Y.-p., A review on the application of inorganic nanoparticles in chemical surface coatings on metallic substrates. *RSC Adv.* **2017,** *7* (13), 7531-7539.

96. Wiechers, J. W.; Musee, N., Engineered Inorganic Nanoparticles and Cosmetics: Facts, Issues, Knowledge Gaps and Challenges. *J. Biomed. Nanotechnol.* **2010,** *6* (5), 408-431.

97. Zhang, T.; Ge, J.; Hu, Y.; Yin, Y., A General Approach for Transferring Hydrophobic Nanocrystals into Water. *Nano Lett.* **2007,** *7* (10), 3203-3207.

98. Kango, S.; Kalia, S.; Celli, A.; Njuguna, J.; Habibi, Y.; Kumar, R., Surface modification of inorganic nanoparticles for development of organic–inorganic nanocomposites — A review. *Prog. Polym. Sci.* **2013,** *38* (8), 1232-1261.

99. Palui, G.; Aldeek, F.; Wang, W.; Mattoussi, H., Strategies for interfacing inorganic nanocrystals with biological systems based on polymer-coating. *Chem. Soc. Rev.* **2015,** *44* (1), 193-227.

100. Bloemen, M.; Brullot, W.; Luong, T. T.; Geukens, N.; Gils, A.; Verbiest, T., Improved functionalization of oleic acid-coated iron oxide nanoparticles for biomedical applications. *J. Nanopat. Res.* **2012,** *14* (9), 1100-1100.

101. Wang, Y.; Wong, J. F.; Teng, X.; Lin, X. Z.; Yang, H., “Pulling” Nanoparticles into Water: Phase Transfer of Oleic Acid Stabilized Monodisperse Nanoparticles into Aqueous Solutions of α-Cyclodextrin. *Nano Lett.* **2003,** *3* (11), 1555-1559.

102. Erathodiyil, N.; Ying, J. Y., Functionalization of Inorganic Nanoparticles for Bioimaging Applications. *Acc. Chem. Res.* **2011,** *44* (10), 925-935.

103. Qiao, R.; Esser, L.; Fu, C.; Zhang, C.; Hu, J.; Ramírez-arcía, P.; Li, Y.; Quinn, J. F.; Whittaker, M. R.; Whittaker, A. K.; Davis, T. P., Bioconjugation and Fluorescence Labeling of Iron Oxide Nanoparticles Grafted with Bromomaleimide-Terminal Polymers. *Biomacromolecules* **2018,** *19* (11), 4423-4429.

104. Li, Y.; Xin, F.; Hu, J.; Jagdale, S.; Davis, T. P.; Hagemeyer, C. E.; Qiao, R., Functionalization of $NaGdF_4$ nanoparticles with a dibromomaleimide-terminated polymer for MR/optical imaging of thrombosis. *Polym. Chem.* **2020,** *11* (5), 1010-1017.

105. Lee, J. C.; Donahue, N. D.; Mao, A. S.; Karim, A.; Komarneni, M.; Thomas, E. E.; Francek, E. R.; Yang, W.; Wilhelm, S., Exploring Maleimide-Based Nanoparticle Surface Engineering to Control Cellular Interactions. *ACS Appl. Nano Mater.* **2020,** *3* (3), 2421-2429.

106. R. A. Sperling; Parak, W. J., Surface modification, functionalization and bioconjugation of colloidal inorganic nanoparticles. *Phil. Trans. R. Soc. A.* **2010,** *368*, 1333–1383.

107. Yildirim, T.; Pervez, M.; Li, B.; O’Reilly, R. K., Size-controlled clustering of iron oxide nanoparticles within fluorescent nanogels using LCST-driven self-assembly. *J. Mater. Chem. B* **2020,** *8* (24), 5330-5335.

108. Gianferrara, T.; Bratsos, I.; Alessio, E., A categorization of metal anticancer compounds based on their mode of action. *Dalton Trans.* **2009,** (37), 7588-7598.

109. Ronconi, L.; Sadler, P. J., Using coordination chemistry to design new medicines. *Coord. Chem. Rev.* **2007,** *251* (13), 1633-1648.

110. Abd-El-Aziz, A. S.; Shipman, P. O.; Boden, B. N.; McNeil, W. S., Synthetic methodologies and properties of organometallic and coordination macromolecules. *Prog. Polym. Sci.* **2010,** *35* (6), 714-836.

111. Meggers, E., Asymmetric Synthesis of Octahedral Coordination Complexes. *Eur. J. Inorg. Chem.* **2011,** *2011* (19), 2911-2926.

112. Gasser, G.; Metzler-Nolte, N., The potential of organometallic complexes in medicinal chemistry. *Curr. Opin. Chem. Biol.* **2012,** *16* (1), 84-91.

113. Che, C. M.; Siu, F. M., Metal complexes in medicine with a focus on enzyme inhibition. *Curr. Opin. Chem. Biol.* **2010,** *14* (2), 255-61.

114. Singh, M., Transferrin as a targeting ligand for liposomes and anticancer drugs. *Curr. Pharm. Des.* **1999,** *5* (6), 443-452.

115. Geiger, W. E.; Barrière, F., Organometallic Electrochemistry Based on Electrolytes Containing Weakly-Coordinating Fluoroarylborate Anions. *Acc. Chem. Res.* **2010,** *43* (7), 1030-1039.

116. Dougan, S. J.; Habtemariam, A.; McHale, S. E.; Parsons, S.; Sadler, P. J., Catalytic organometallic anticancer complexes. *Proc. Natl. Acad. Sci. USA* **2008,** *105* (33), 11628-11633.

117. Alberto, R.; Schibli, R.; Egli, A.; Schubiger, A. P.; Abram, U.; Kaden, T. A., A Novel Organometallic Aqua Complex of Technetium for the Labeling of Biomolecules: Synthesis of $[^{99m}Tc(OH_2)_3(CO)_3]^+$ from $[^{99m}TcO_4]^-$ in Aqueous Solution and Its Reaction with a Bifunctional Ligand. *J. Am. Chem. Soc.* **1998,** *120* (31), 7987-7988.

118. Metzler-Nolte, N., Labeling of Biomolecules for Medicinal Applications—Bioorganometallic Chemistry at Its Best. *Angew. Chem. Int. Ed.* **2001,** *40* (6), 1040-1043.

119. Peacock, A. F. A.; Sadler, P. J., Medicinal Organometallic Chemistry: Designing Metal Arene Complexes as Anticancer Agents. *Chem. Asian J.* **2008,** *3* (11), 1890-1899.

120. Thorp-Greenwood, F. L.; Balasingham, R. G.; Coogan, M. P., Organometallic complexes of transition metals in luminescent cell imaging applications. *J. Organomet. Chem.* **2012,** *714*, 12-21.

121. Lo, K. K.-W.; Choi, A. W.-T.; Law, W. H.-T., Applications of luminescent inorganic and organometallic transition metal complexes as biomolecular and cellular probes. *Dalton Trans.* **2012,** *41* (20), 6021-6047.

122. Ma, D.-L.; He, H.-Z.; Leung, K.-H.; Chan, D. S.-H.; Leung, C.-H., Bioactive Luminescent Transition-Metal Complexes for Biomedical Applications. *Angew. Chem. Int. Ed.* **2013,** *52* (30), 7666-7682.

123. Fernández-Moreira, V.; Thorp-Greenwood, F. L.; Coogan, M. P., Application of d^6 transition metal complexes in fluorescence cell imaging. *Chem. Commun.* **2010,** *46* (2), 186-202.

124. Salmain, M., Labeling of Proteins with Organometallic Complexes: Strategies and Applications. In *Bioorganometallics*, **2005**; pp 181-213.

125. Thorp-Greenwood, F. L., An Introduction to Organometallic Complexes in Fluorescence Cell Imaging: Current Applications and Future Prospects. *Organometallics* **2012,** *31* (16), 5686-5692.

126. Juris A.; Balzani V.; Barigelletti F.; Campagna S.; Belser P.; Zelewsky A.v., Ru(II) polypyridine complexes: photophysics, photochemistry, eletrochemistry, and chemiluminescence. *Coord. Chem. Rev.* **1988,** *84*, 85-277.

127. Lowry, M. S.; Hudson, W. R.; Pascal, R. A.; Bernhard, S., Accelerated Luminophore Discovery through Combinatorial Synthesis. *J. Am. Chem. Soc.* **2004,** *126* (43), 14129-14135.

128. Stufkens, D. J.; Vlček, A., Ligand-dependent excited state behaviour of Re(I) and Ru(II) carbonyl–diimine complexes. *Coord. Chem. Rev.* **1998,** *177* (1), 127-179.

129. Patra, M.; Gasser, G., Organometallic Compounds: An Opportunity for Chemical Biology? *ChemBioChem* **2012,** *13* (9), 1232-1252.

130. Kilpin, K. J.; Dyson, P. J., Enzyme inhibition by metal complexes: concepts, strategies and applications. *Chem. Sci.* **2013,** *4* (4), 1410-1419.

131. Allardyce, C. S.; Dorcier, A.; Scolaro, C.; Dyson, P. J., Development of organometallic (organo-transition metal) pharmaceuticals. *Appl. Organometal. Chem.* **2005,** *19* (1), 1-10.

132. Płotek, M.; Starosta, R.; Komarnicka, U. K.; Skórska-Stania, A.; Kołoczek, P.; Kyzioł, A., Ruthenium(II) piano stool coordination compounds with aminomethylphosphanes: Synthesis, characterisation and preliminary biological study in vitro. *J. Inorg. Biochem.* **2017,** *170*, 178-187.

133. Wang, W.; Li, J.; Yin, L.; Zhao, Y.; Ouyang, Z.; Wang, X.; Wang, Z.; Song, Y.; Power, P. P., Half-Sandwich Metal Carbonyl Complexes as Precursors to Functional Materials: From a Near-Infrared-Absorbing Dye to a Single-Molecule Magnet. *J. Am. Chem. Soc.* **2017,** *139* (34), 12069-12075.

134. Khan, T. A.; Bhar, K.; Thirumoorthi, R.; Roy, T. K.; Sharma, A. K., Design, synthesis, characterization and evaluation of the anticancer activity of water-soluble half-sandwich ruthenium(ii) arene halido complexes. *New. J. Chem.* **2020,** *44* (1), 239-257.

135. Connell, T. U.; James, J. L.; White, A. R.; Donnelly, P. S., Protein Labelling with Versatile Phosphorescent Metal Complexes for Live Cell Luminescence Imaging. *Chem. Eur. J.* **2015,** *21* (40), 14146-14155.

136. Marloye, M.; Inam, H.; Moore, C. J.; Debaille, V.; Pritchard, J. R.; Gelbcke, M.; Meyer, F.; Dufrasne, F.; Berger, G., Synthesis, structure and anticancer properties of new biotin- and morpholine-functionalized ruthenium and osmium half-sandwich complexes. *J. Biol. Inorg. Chem.* **2021,** *26* (5), 535-549.

137. Chu, G. M.; Fernández, I.; Guerrero-Martínez, A.; Ramírez de Arellano, C.; Sierra, M. A., Fluorescence Quenching in BODIPYs Having Ir- and Rh-Tethered Complexes. *Eur. J. Inorg. Chem.* **2016,** *2016* (6), 844-852.

138. Liu, C.; Liu, X.; Ge, X.; Wang, Q.; Zhang, L.; Shang, W.; Zhang, Y.; Yuan, X. A.; Tian, L.; Liu, Z.; You, J., Fluorescent iridium(iii) coumarin-salicylaldehyde Schiff base compounds as lysosome-targeted antitumor agents. *Dalton Trans.* **2020,** *49* (18), 5988-5998.

139. Ma, W.; Guo, L.; Tian, Z.; Zhang, S.; He, X.; Li, J.; Yang, Y.; Liu, Z., Rhodamine-modified fluorescent half-sandwich iridium and ruthenium complexes: potential application as bioimaging and anticancer agents. *Dalton Trans.* **2019,** *48* (15), 4788-4793.

140. Bose, S.; Nguyen, H. D.; Ngo, A. H.; Do, L. H., Fluorescent half-sandwich iridium picolinamidate complexes for in-cell visualization. *J. Inorg. Biochem.* **2022,** *234*, 111877.

141. Wang, L.; Huang, C.; Hu, F.; Cui, W.; Li, Y.; Li, J.; Zong, J.; Liu, X.; Yuan, X.-A.; Liu, Z., Preparation and antitumor application of *N*-phenylcarbazole/triphenylamine-modified fluorescent half-sandwich iridium(iii) Schiff base complexes. *Dalton Trans.* **2021,** *50* (43), 15888-15899.

142. Li, J.; Tian, Z.; Xu, Z.; Zhang, S.; Feng, Y.; Zhang, L.; Liu, Z., Highly potent half-sandwich iridium and ruthenium complexes as lysosome-targeted imaging and anticancer agents. *Dalton Trans.* **2018,** *47* (44), 15772-15782.

143. Du, Q.; Yang, Y.; Guo, L.; Tian, M.; Ge, X.; Tian, Z.; Zhao, L.; Xu, Z.; Li, J.; Liu, Z., Fluorescent half-sandwich phosphine-sulfonate iridium(III) and ruthenium(II) complexes as potential lysosome-targeted anticancer agents. *Dyes Pigm.* **2019,** *162*, 821-830.

144. Li, J.; Guo, L.; Tian, Z.; Zhang, S.; Xu, Z.; Han, Y.; Li, R.; Li, Y.; Liu, Z., Half-Sandwich Iridium and Ruthenium Complexes: Effective Tracking in Cells and Anticancer Studies. *Inorg. Chem.* **2018,** *57* (21), 13552-13563.

145. Ma, W.; Zhang, S.; Tian, Z.; Xu, Z.; Zhang, Y.; Xia, X.; Chen, X.; Liu, Z., Potential anticancer agent for selective damage to mitochondria or lysosomes: Naphthalimide-modified fluorescent biomarker half-sandwich iridium (III) and ruthenium (II) complexes. *Eur. J. Med. Chem.* **2019,** *181*, 111599.

146. Nanda, J.; Lorsch, J., Chapter Seven: Labeling of a Protein with Fluorophores Using Maleimide Derivitization. *Methods Enzymol.* **2014,** *536*, 79-86.

147. Lo, K. K.-W.; Hui, W.-K.; Ng, D. C.-M.; Cheung, K.-K., Synthesis, Characterization, Photophysical Properties, and Biological Labeling Studies of a Series of Luminescent Rhenium(I) Polypyridine Maleimide Complexes. *Inorg. Chem.* **2002,** *41* (1), 40-46.

148. Jakupec, M. A.; Galanski, M.; Arion, V. B.; Hartinger, C. G.; Keppler, B. K., Antitumour metal compounds: more than theme and variations. *Dalton Trans.* **2008,** (2), 183-194.

149. Zutphen, S. v.; Reedijk, J., Targeting platinum anti-tumour drugs: Overview of strategies employed to reduce systemic toxicity. *Coord. Chem. Rev.* **2005,** *249* (24), 2845-2853.

150. Hulubei, C.; Cazacu, M.; Morariu, S., Metal Complexes of Maleimide Compounds. *High Perform. Polym.* **2006,** *18* (1), 101-111.

151. Gabano, E.; Perin, E.; Bonzani, D.; Ravera, M., Conjugation between maleimide-containing Pt(IV) prodrugs and furan or furan-containing drug delivery vectors *via* Diels-Alder cycloaddition. *Inorganica Chim. Acta* **2019,** *488*, 195-200.

152. Warnecke, A.; Fichtner, I.; Garmann, D.; Jaehde, U.; Kratz, F., Synthesis and Biological Activity of Water-Soluble Maleimide Derivatives of the Anticancer Drug Carboplatin Designed as Albumin-Binding Prodrugs. *Bioconjug. Chem.* **2004,** *15* (6), 1349-1359.

153. Seiwert, B.; Karst, U., Analysis of cysteine-containing proteins using precolumn derivatization with *N*-(2-ferroceneethyl)maleimide and liquid chromatography/electrochemistry/mass spectrometry. *Anal. Bioanal. Chem.* **2007,** *388* (8), 1633-1642.

154. Zhang, W.; Xu, W.; Ma, C.; Li, Y., Synthesis of ferrocene-based polysubstituted pyrrolidines. *Chem. Heterocycl. Comp.* **2019,** *55* (10), 939-942.

155. Hanif, M.; Nazarov, A. A.; Legin, A.; Groessl, M.; Arion, V. B.; Jakupec, M. A.; Tsybin, Y. O.; Dyson, P. J.; Keppler, B. K.; Hartinger, C. G., Maleimide-functionalised organoruthenium anticancer agents and their binding to thiol-containing biomolecules. *Chem. Commun.* **2012,** *48* (10), 1475-1477.

156. Pichler, V.; Mayr, J.; Heffeter, P.; Dömötör, O.; Enyedy, É. A.; Hermann, G.; Groza, D.; Köllensperger, G.; Galanksi, M.; Berger, W.; Keppler, B. K.; Kowol, C. R., Maleimide-functionalised platinum(iv) complexes as a synthetic platform for targeted drug delivery. *Chem. Commun.* **2013,** *49* (22), 2249-2251.

157. Rudolf, B.; Kubicka, A.; Salmain, M.; Palusiak, M.; Rybarczyk-Pirek, A. J.; Wojtulewski, S., Synthesis and characterization of new M(II) carbonyl complexes (M = Fe or Ru) including an η^1-*N*-maleimidato ligand. Reactivity studies with biological thiols. *J. Organomet. Chem.* **2016,** *801*, 101-110.

158. Rudolf, B.; Salmain, M.; Martel, A.; Palusiak, M.; Zakrzewski, J., η^1-*N*-succinimidato complexes of iron, molybdenum and tungsten as reversible inhibitors of papain. *J. Inorg. Biochem.* **2009,** *103* (8), 1162-1168.

159. Butler, I. S.; Vessières, A.; Jaouen, G., Application of Organotransition Metal Carbonyl Complexes as Infrared Markers for Hormonal Steroids in Biological Processes. *Comments Inrog. Chem.* **1989,** *8* (6), 269-286.

160. Rudolf, B.; Palusiak, M.; Zakrzewski, J., Diels-Alder reaction with cyclopentadiene and electronic structures of (η^5-cyclopentadienyl)M$(CO)_x$(η^1-*N*-maleimidato) (M=Fe, Mo, W, x=2 or 3). *J. Organomet. Chem.* **2009,** *694* (9), 1354-1358.

161. Kubicka, A.; Fornal, E.; Olejniczak, A. B.; Rybarczyk-Pirek, A. J.; Wojtulewski, S.; Rudolf, B., Oxa-Michael reaction of metallocarbonyl complexes bearing the maleimidato ligand. Reactivity studies with selected hydroxy compounds. *Polyhedron* **2016,** *107*, 38-47.

162. Rudolf, B.; Salmain, M.; Fornal, E.; Rybarczyk-Pirek, A., Metallocarbonyl complexes of bromo- and dibromomaleimide: synthesis and biochemical application. *Appl. Organometal. Chem.* **2012,** *26* (2), 80-85.

163. Rudolf, B.; Palusiak, M.; Zakrzewski, J.; Salmain, M.; Jaouen, G., Sulfhydryl-Selective, Covalent Labeling of Biomolecules with Transition Metallocarbonyl Complexes. Synthesis of (η^5-C_5H_5)M$(CO)_3$(η^1-*N*-Maleimidato) (M = Mo, W), X-ray Structure, and Reactivity Studies. *Bioconjug. Chem.* **2005,** *16* (5), 1218-1224.

164. Salmain, M.; Jaouen, G.; Rudolf, B.; Zakrzewski, J., Inhibition and photo-deinhibition of glutathione (*S*)-transferase activity by an organometallic complex: (*S*)-[3-CpFe$(CO)_2$(η^1-*N*-succinimidato)]glutathione. *J. Organomet. Chem.* **1999,** *589* (1), 98-102.

165. Kubicka, A.; Parfieniuk, E.; Fornal, E.; Palusiak, M.; Lizińska, D.; Gumieniczek, A.; Rudolf, B., Metallocarbonyl complexes: (η^5-C_5H_5)M$(CO)_n$(η^1-*N*-imidato) (M = Fe, Ru, Mo, W; n = 2, 3) as new photoactive CO-releasing molecules (CORMs). *J. Photochem. Photobiol. A: Chem.* **2018,** *351*, 115-123.

166. Bünzli, J.-C. G.; Piguet, C., Taking advantage of luminescent lanthanide ions. *Chem. Soc. Rev.* **2005,** *34* (12), 1048-1077.

167. Wei, C.; Ma, L.; Wei, H.; Liu, Z.; Bian, Z.; Huang, C., Advances in luminescent lanthanide complexes and applications. *Sci. China Technol. Sci.* **2018,** *61* (9), 1265-1285.

168. Montgomery, C. P.; Murray, B. S.; New, E. J.; Pal, R.; Parker, D., Cell-Penetrating Metal Complex Optical Probes: Targeted and Responsive Systems Based on Lanthanide Luminescence. *Acc. Chem. Res.* **2009,** *42* (7), 925-937.

169. Song, B.; Vandevyver, C. D. B.; Chauvin, A.-S.; Bünzli, J.-C. G., Time-resolved luminescence microscopy of bimetallic lanthanide helicates in living cells. *Org. Biomol. Chem.* **2008,** *6* (22), 4125-4133.

170. Faulkner, S.; Pope, S. J. A.; Burton-Pye, B. P., Lanthanide Complexes for Luminescence Imaging Applications. *Appl. Spectrosc. Rev.* **2005,** *40* (1), 1-31.

171. Parker, D.; Fradgley, J. D.; Wong, K.-L., The design of responsive luminescent lanthanide probes and sensors. *Chem. Soc. Rev.* **2021,** *50* (14), 8193-8213.

172. Armelao, L.; Quici, S.; Barigelletti, F.; Accorsi, G.; Bottaro, G.; Cavazzini, M.; Tondello, E., Design of luminescent lanthanide complexes: From molecules to highly efficient photo-emitting materials. *Coord. Chem. Rev.* **2010,** *254* (5), 487-505.

173. Hernández, I.; Gillin, W. P., Chapter 269: Organic Chromophores-Based Sensitization of NIR-Emitting Lanthanides: Toward Highly Efficient Halogenated Environments. In *Handbook Phys. Chem. Rare Earths*, Bünzli, J.-C.; Pecharsky, V. K., Eds. Elsevier: **2015**; pp 1-100.

174. Hasegawa, Y.; Kimura, Y.; Murakoshi, K.; Wada, Y.; Kim, J.-H.; Nakashima, N.; Yamanaka, T.; Yanagida, S., Enhanced Emission of Deuterated Tris(hexafluoroacetylacetonato)neodymium(III) Complex in Solution by Suppression of Radiationless Transition via Vibrational Excitation. *J. Phys. Chem.* **1996,** *100* (24), 10201-10205.

175. Chow, C. Y.; Eliseeva, S. V.; Trivedi, E. R.; Nguyen, T. N.; Kampf, J. W.; Petoud, S.; Pecoraro, V. L., Ga^{3+}/Ln^{3+} Metallacrowns: A Promising Family of Highly

Luminescent Lanthanide Complexes That Covers Visible and Near-Infrared Domains. *J. Am. Chem. Soc.* **2016,** *138* (15), 5100-5109.

176. Li, Y.; Chen, C.; Liu, F.; Liu, J., Engineered lanthanide-doped upconversion nanoparticles for biosensing and bioimaging application. *Microchim. Acta* **2022,** *189* (3), 109.

177. McCall, J. G.; Kim, T.-i.; Shin, G.; Huang, X.; Jung, Y. H.; Al-Hasani, R.; Omenetto, F. G.; Bruchas, M. R.; Rogers, J. A., Fabrication and application of flexible, multimodal light-emitting devices for wireless optogenetics. *Nat. Protoc.* **2013,** *8* (12), 2413-2428.

178. Nguyen, H. Q.; Baxter, B. C.; Brower, K.; Diaz-Botia, C. A.; DeRisi, J. L.; Fordyce, P. M.; Thorn, K. S., Programmable Microfluidic Synthesis of Over One Thousand Uniquely Identifiable Spectral Codes. *Adv. Opt. Mater.* **2017,** *5* (3).

179. Guillou, O.; Daiguebonne, C.; Calvez, G.; Bernot, K., A Long Journey in Lanthanide Chemistry: From Fundamental Crystallogenesis Studies to Commercial Anticounterfeiting Taggants. *Acc. Chem. Res.* **2016,** *49* (5), 844-856.

180. Bünzli, J.-C. G.; Wong, K.-L., Lanthanide mechanoluminescence. *J. Rare Earths* **2018,** *36* (1), 1-41.

181. Bao, G.; Wen, S.; Lin, G.; Yuan, J.; Lin, J.; Wong, K.-L.; Bünzli, J.-C. G.; Jin, D., Learning from lanthanide complexes: The development of dye-lanthanide nanoparticles and their biomedical applications. *Coord. Chem. Rev.* **2021,** *429*, 213642.

182. Wang, Z.; Xing, B., Near-Infrared Multipurpose Lanthanide-Imaging Nanoprobes. *Chem. Asian J.* **2020,** *15* (14), 2076-2091.

183. Sy, M.; Nonat, A.; Hildebrandt, N.; Charbonnière, L. J., Lanthanide-based luminescence biolabelling. *Chem. Commun.* **2016,** *52* (29), 5080-5095.

184. Li, H.; Xie, C.; Lan, R.; Zha, S.; Chan, C.-F.; Wong, W.-Y.; Ho, K.-L.; Chan, B. D.; Luo, Y.; Zhang, J.-X.; Law, G.-L.; Tai, W. C. S.; Bünzli, J.-C. G.; Wong, K.-L., A Smart Europium–Ruthenium Complex as Anticancer Prodrug: Controllable Drug Release and Real-Time Monitoring under Different Light Excitations. *J. Med. Chem.* **2017,** *60* (21), 8923-8932.

185. Rafique, R.; Kailasa, S. K.; Park, T. J., Recent advances of upconversion nanoparticles in theranostics and bioimaging applications. *TrAC Trend. Anal. Chem.* **2019,** *120*, 115646.

186. Bünzli, J.-C. G., Rising Stars in Science and Technology: Luminescent Lanthanide Materials. *Eur. J. Inorg. Chem.* **2017,** *2017* (44), 5058-5063.

187. An, B.-L.; Huang, X.-D.; Zhang, J.-M.; Zhu, X.-Y.; Xu, J.-Q., Synthesis and strong luminescence of water soluble lanthanide complexes sensitized by a new tridentate organic ligand. *J. Lumin.* **2017,** *187*, 340-346.

188. Deslandes, S.; Galaup, C.; Poole, R.; Mestre-Voegtlé, B.; Soldevila, S.; Leygue, N.; Bazin, H.; Lamarque, L.; Picard, C., Synthesis and optical properties of macrocyclic lanthanide(iii) chelates as new reagents for luminescent biolabeling. *Org. Biomol. Chem* **2012,** *10* (42), 8509-8523.

189. McMahon, B. K.; Gunnlaugsson, T., Selective Detection of the Reduced Form of Glutathione (GSH) over the Oxidized (GSSG) Form Using a Combination of Glutathione Reductase and a Tb(III)-Cyclen Maleimide Based Lanthanide Luminescent 'Switch On' Assay. *J. Am. Chem. Soc.* **2012,** *134* (26), 10725-10728.

190. Lutter, J. C.; Lopez Bermudez, B. A.; Nguyen, T. N.; Kampf, J. W.; Pecoraro, V. L., Functionalization of luminescent lanthanide-gallium metallacrowns using copper-catalyzed alkyne-azide cycloaddition and thiol-maleimide Michael addition. *J. Inorg. Biochem.* **2019,** *192*, 119-125.

191. Sayyadi, N.; Justiniano, I.; Connally, R. E.; Zhang, R.; Shi, B.; Kautto, L.; Everest-Dass, A. V.; Yuan, J.; Walsh, B. J.; Jin, D.; Willows, R. D.; Piper, J. A.; Packer, N. H., Sensitive Time-Gated Immunoluminescence Detection of Prostate Cancer Cells Using a TEGylated Europium Ligand. *Anal. Chem.* **2016,** *88* (19), 9564-9571.

192. Faschinger, F.; Ertl, M.; Zimmermann, M.; Horner, A.; Himmelsbach, M.; Schöfberger, W.; Knör, G.; Gruber, H. J., Stable Europium(III) Complexes with Short Linkers for Site-Specific Labeling of Biomolecules. *ChemistryOpen* **2017,** *6* (6), 721-732.

193. Chen, G.; Qiu, H.; Prasad, P. N.; Chen, X., Upconversion Nanoparticles: Design, Nanochemistry, and Applications in Theranostics. *Chem. Rev.* **2014,** *114* (10), 5161-5214.

194. Bagheri, A.; Arandiyan, H.; Boyer, C.; Lim, M., Lanthanide-Doped Upconversion Nanoparticles: Emerging Intelligent Light-Activated Drug Delivery Systems. *Adv. Sci.* **2016,** *3* (7), 1500437.

CHAPTER 2: RATIONAL DESIGN OF SMALL SIZE ORGANIC PROBES BASED ON THE FLUORO-SUBSTITUTION OF THE MALEIMIDES TO ENHANCE THE FLUORESCENCE EMISSION

2.1 Abstract

In the past decade, there has been an increasing interest in the development of luminophores that can exhibit emissions in both the solution and solid-states, thus named as dual-state emission (DSE) dyes. These compounds are expected to underpin a variety of applications in the future. Based on this nascent topic, this chapter covers the investigation into fluoroalkyl substituents on maleimide fluorophores, with the aim of enhancing the emissions in both solution and solid-states. This was achieved by substituting the trifluoroethyl groups at the imide and/or amine positions of the aminomaleimide derivatives. Photophysical analysis of these derivatives showed high fluorescence quantum yields, large Stokes shift and solvatochromic properties in solution-state, attributed to the prevention of electron-driven proton transfer (EDPT). Additionally, due to the suppression of π-π stacking interactions in the solid-state, fluorescence quenching was reduced leading to impressive solid-state quantum yield. The unexpected dual-state fluorescence behavior in these fluoroalkyl derivatives was further explained through crystal structure analysis and computational simulation of electron distributions.

2.2 Introduction

2.2.1 Different substitution patterns for designing the maleimide derivatives

Maleimide based fluorophores have good structure-to-property tunability, non-invasive nature, high sensitivity and responsivity to the physical environment, in comparison to the traditional fluorophores.[1-4] Unsubstituted maleimides have been effectively used as fluorescence quenchers, either due to low lying n-π* transitions providing non-radiative relaxation,[5, 6] or due to photo-induced electron transfer (PET) when the maleimide is linked to the fluorophore by a spacer.[7, 8] On the other hand, if maleimides are functionalized with amino or thiol groups, a fluorophore center is generated instead of quenching emission.[9] In 1970, Heindel *et al.*, reported the synthesis of anilinomaleimides as a by-product of the reaction between aryl amines and acetylene dicarboxylate.[10] Since then, many advancements have been made to develop the substituted maleimide compounds, either from alkyne/maleic anhydride derivatives,[11-13] or by modifying bromo/chloro maleimides (Fig. 2.1).[14-16] However, limited attention has been given to their optical properties.

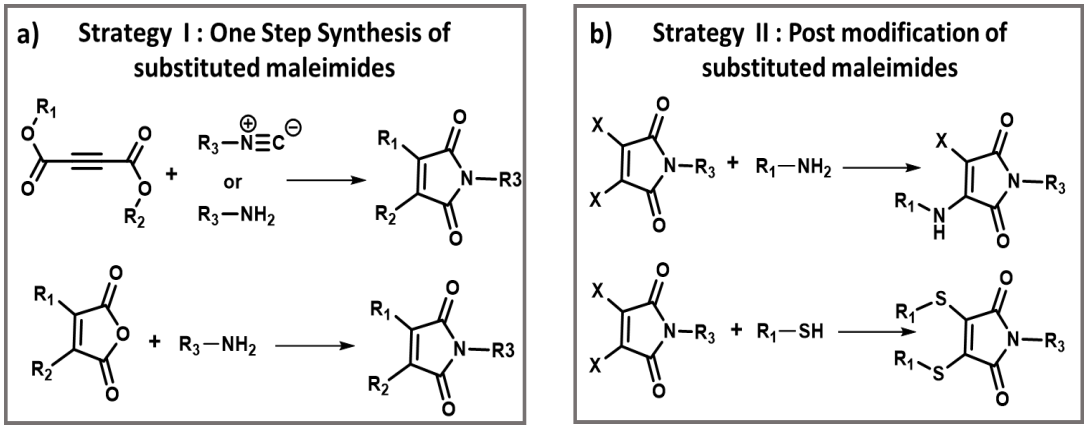

Fig. 2.1 Synthesis of substituted maleimides: a) one-step synthesis of substituted maleimides, b) maleimides derivation *via* addition–elimination reactions.

Later, in 2002, Chen's group reported a series of 3,4-diaryl substituted maleimides synthesized from acetonitrile derivatives in a single step. These products displayed the fluorescence emissions spanning the entire visible region. This was achieved by modifying the electron-withdrawing or electron-donating aryl substituents, that determine the molecular energy levels and consequently influence the emission wavelength.[17] However, the inefficient quantum yields observed, limited the future advancement of these multi-colored maleimide derivatives. Lately, Tang *et al.*, synthesized monoaminomaleimides employing two methods, and investigated the optical properties both in monomer and in aggregated states (Fig. 2.2). The monoaminomaleimides exhibited red-shifted emissions, when aggregated in comparison to the monomeric forms.[11]

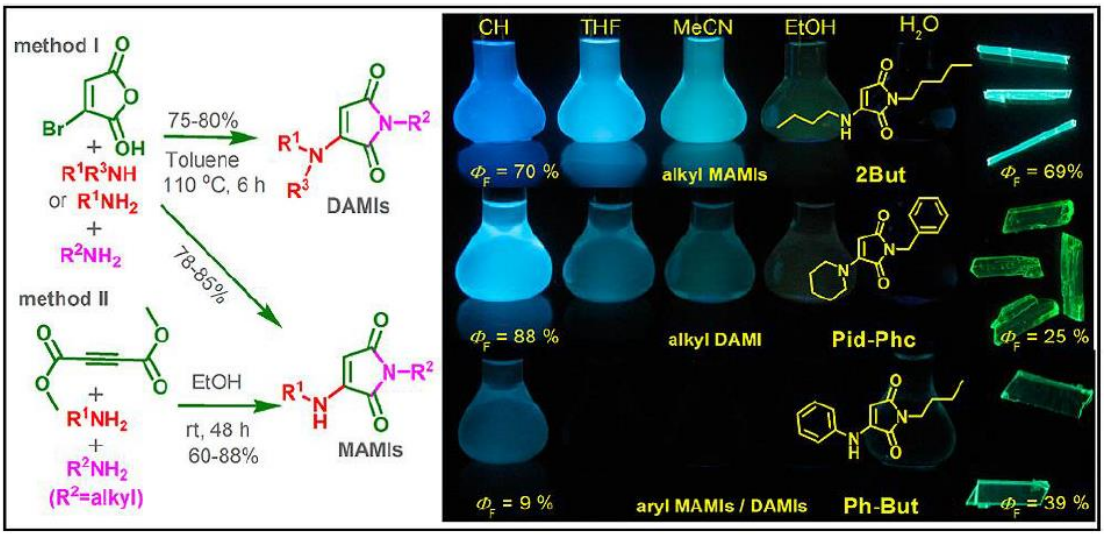

Fig. 2.2 Two strategies for the synthesis of amino-substituted maleimides and the compared fluorescent properties in solution and solid-states. CH; Cyclohexane, THF; Tetrahydrofuran, MeCN; Acetonitrile, EtOH; Ethanol, and H_2O; Water. Adapted from the reference.[11] Copyright 2016 American Chemical Society.

In order to expand the emissions of the maleimide-derivatives towards the red region with higher sensitivity and less background influence, our group reported the synthesis of fluorescent thiol-substituted[15] and amino-substituted maleimides[18] with intense blue-green fluorescence emissions. Owing to their facile and versatile modifications, maleimides can undergo different substitution patterns by various reactions, including single and double substitutions. Single substituted maleimides, typically containing one or two different functional groups, could be achieved *via* strategies like a one-pot synthesis from anhydrides or alkynes,[19] addition-elimination reactions with groups like amine or alcohol,[16] and Suzuki coupling reactions.[20] Double substitution patterns potentially provides a higher degree of functionalization than single substitutions. This method either generates symmetrical structures, such as dithiol substitute maleimides,

or unsymmetrical structures, e.g., aminohalomaleimide or aminothiol maleimide derivatives (Fig. 2.3).[21]

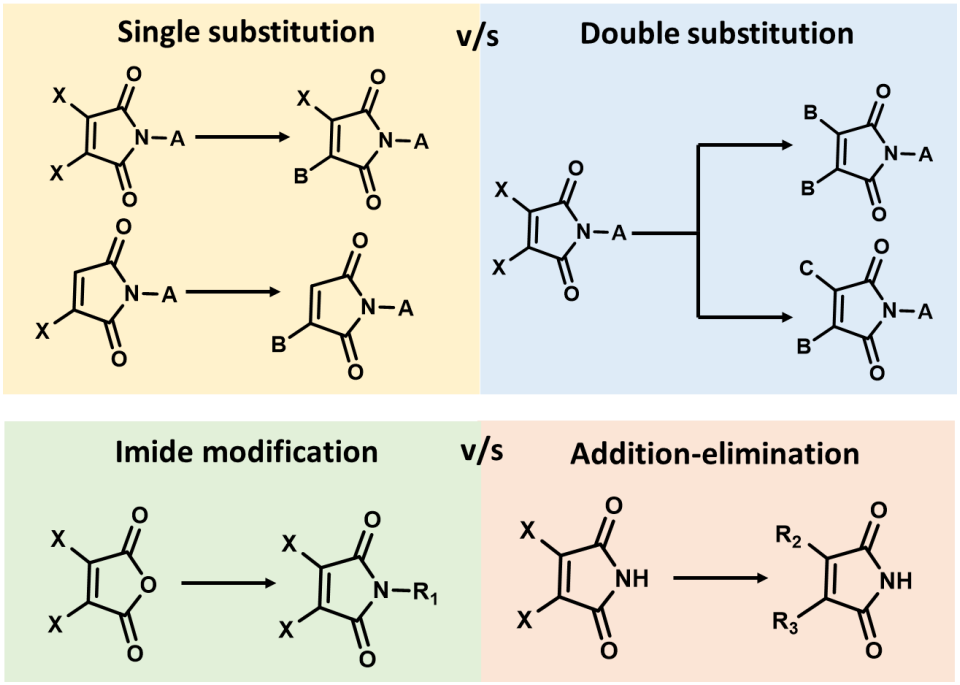

Fig. 2.3 Various strategies to synthesize multi-functional maleimide structures.

These substitution possibilities enable maleimides to bear multiple functionalities, by imide functionalization and/or addition-elimination reactions, within a single molecule and made them an excellent candidate to be employed as linkers for numerous purposes, for example material modifications,[22, 23] material functionalizations[24] and drug design applications.[25]

2.2.2 Photophysical processes affecting fluorescence emission of maleimides

A range of dyes along with maleimides, incorporated into the extended π-systems, giving good fluorescence efficiency and large Stokes shifts (> 100 nm), have also been reported.[26-30] In addition, there are some reports of heteroatom substitution of maleimides, but their optical properties have not been thoroughly investigated.[31, 32] However, the knowledge of the quenching mechanisms of maleimides is important, as these can influence the design of future fluorophores employed for various applications, e.g., imaging of biomolecules,[33] and nanoparticle tagging.[34]

To date, some studies have explored the mechanisms of fluorescence quenching by maleimides, involving phenomena such as photoinduced electron transfer (PET)[35] to the rearrangement of molecular orbitals.[36, 37] The optical properties of the aminomaleimide derivatives are greatly influenced by their physical environment due to photoinduced charge transfer (PCT), as discussed in Chapter 1. Additionally, in cases of intramolecular charge transfer (ICT) fluorophores, excitation leads to a charge separation, and generates a diradical in the HOMO and LUMO orbitals. Thus, in order to reduce the columbic interactions, the molecule may rotate around a single bond, leading to the formation of a twisted intramolecular charge transfer (TICT) state, which consequently prohibits the fluorescence emission.[38, 39] In the solution-state, solvent molecules tend to stabilize the electronic distribution. This process of charge stabilization is more prevalent in polar solvents, for instance, methanol and water.

For maleimides, bright fluorescence emissions are observed in non-polar solvents, such as hexane, in which the photoexcited state (S_1) relaxes, *via* fluorescence, back to the ground state (S_0) in $\gg$2 ns (Fig. 2.4). In the case of polar aprotic solvents (e.g.,

acetonitrile), quenching takes place in ~5 ps, due to charge transfer (CT) photorelaxation. The electronic population from both the CT and locally excited (LE) states, returning to the ground state with competition between internal conversion and fluorescence, result in fluorescence quenching (Fig. 2.4). However, this effect is more pronounced in polar protic solvents, such as methanol. In addition to the charge transfer, an electron driven proton transfer (EDPT) occurs, which quenches the fluorescence to even a greater extent (ϕ_f = 1% in methanol and <0.1% in water).[21]

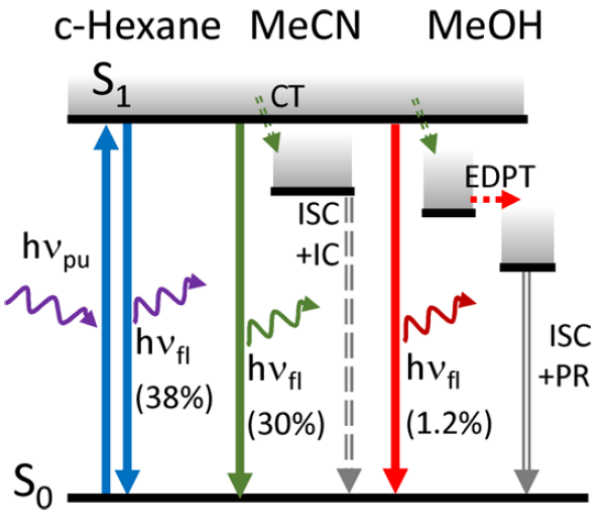

Fig. 2.4 Illustration of absorption and relaxation events in a generalized maleimide skeleton in different solvents. $h\nu_{pu}$= photoexcitation; $h\nu_{fl}$, fluorescence from the S_1. CT= charge transfer; EDPT= electron driven proton transfer; ISC= intersystem crossing; PR= proton recombination (ϕ_f given in parentheses). Adapted from the reference.[40] Copyright 2017 American Chemical Society.

2.2.3 Dual state emission (DSE)

In this chapter, an unexpected phenomenon, namely dual state emission (DSE) is discussed in maleimides, in contrast to the typical aggregation caused quenching (ACQ) and aggregation induced emission (AIE) mechanisms. Conventional luminophores usually emit efficiently in solution-state, whereas in the aggregated state they undergo strong π-π stacking interactions, thus leading to the undesirable ACQ effect.[41] In comparison to ACQ dyes, AIE dyes are non-emissive when dissolved but become emissive when aggregated, owing to the restriction to the intramolecular rotations (RIR) and intramolecular vibrations (RIV).[42, 43] The structural properties of the AIE dyes, that can exhibit intramolecular charge-transfer (ICT), can be manipulated to be emissive in the solution-state (to achieve the dual-state emissions),[44, 45] and thereby initiate the exploration of a new class of luminophores, named as dual-state emission (DSE) dyes. Dual state emitters (DSE) are the compounds that exhibit fluorescence in both the solution and solid-state, and thus can overcome the limitation of single-state luminescence. This duality was considered rare for a long time, but has recently gained attention by several research groups. It is anticipated that DSE luminophores ought to concurrently fulfil the requirements of substantial twisting conformations in the solid-state, and considerable rigidity with limited intramolecular motions (RIR+RIV) in solution-state, to avoid detrimental quenching mechanisms.[46] It is worth noting that despite this academic interest, to date there are not many studies reporting the synthesis of DSE molecules, and therefore is an area rich for investigation.

In order to enable DSE behavior, some design strategies have been reported. For example, one strategy to design DSE molecules by using twisted molecular conformations to reduce the π-π aromatic stacking. For such structures, the torsion

angle between the conjugated aromatic rings plays a vital role in the DSE features (Fig. 2.5a). Wu and collaborators investigated the influence of torsion angle on the intermolecular interactions. They reported fluorine derivatives with weak quantum yields in THF solvent (ϕ_f = 11%),[47] and moderate-strong quantum yields in solids (ϕ_f = 36–98%)[48], caused by the dihedral torsion angle 36.6°, which eliminated the π-π interactions. Subsequently, studies have reported a series of large heterocyclic aryl-maleimide systems, and demonstrated how the π-π interactions can be prevented due to the twisted dihedral angle between the aryl/heterocycle group (ϕ_f in the range of 2–80%).[49-51] In addition, polyarylpyrroles[52] and ketocoumarin[53] based DSE dyes have been reported, that exhibited good quantum yields in both solution (ϕ_f = 20 to 55%) and solid-states (ϕ_f = 25 to 76%) due to the molecular distortion. Another strategy to achieve DSE is by incorporating long flexible alkyl chains or bulky groups into the molecular structures to prohibit π-π stacking in the solid-state (Fig. 2.5b).[54-57] Dual-state emission can also be attained by employing Donor-Acceptor (D-A) architectures (Fig. 2.5c).[58-61] This strategy is more versatile as it allows the judicious selection of the conjugated D-A components.

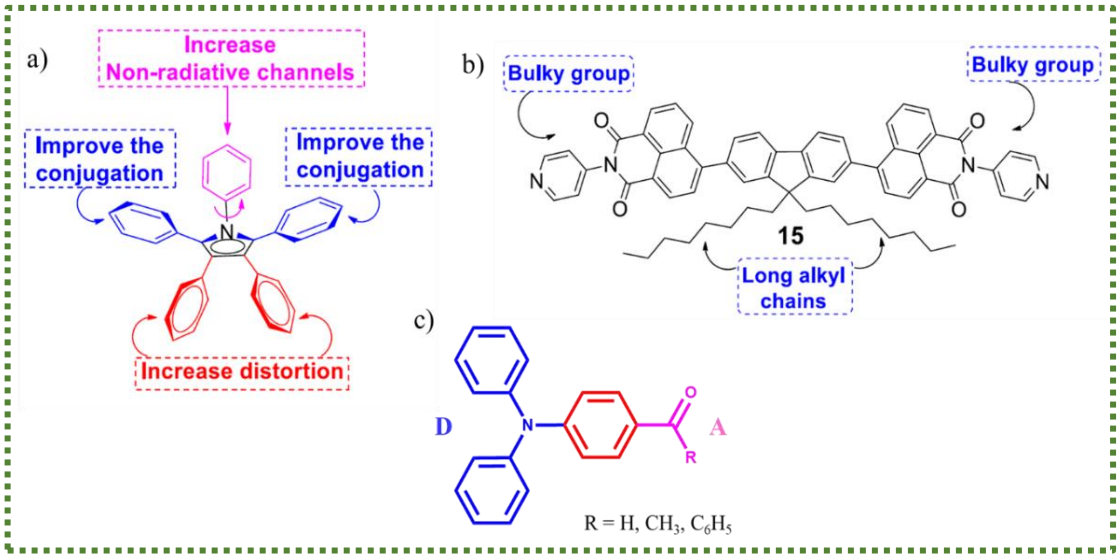

Fig. 2.5 Representation of three strategies for the synthesis of DSE molecules using (a) twisted molecular conformations; (b) long alkyl chains or bulky groups; and (c) donor-acceptor architectures.

Some of the above mentioned DSE dyes displayed good fluorescence emissions and photophysical properties. DSE based dyes have potential applications as sensors,[62] anti-counterfeiting agents,[58] and for labelling of molecules.[57] However, either multi-step or complex synthetic methodologies have been required to prepare these systems. In addition, to the best of our knowledge, the ability to design DSE based fluorophores with solvatochromism has not been demonstrated. This chapter entails the scope of small non-invasive maleimide fluorophores with no aromatic framework, by employing straightforward single or double substitution patterns, to obtain higher quantum yields in both solution and solid-states. Moreover, the relationship between the structural and optical properties of these dyes is explored.

2.3 Results and Discussion

2.3.1 Design and synthesis of fluoroalkyl substituted aminohalomaleimides

Various aminohalomaleimide derivatives have been investigated previously by our group as small molecule fluorophores. The attached functionalities to the ring and the dye environment are the two factors that significantly affect the fluorescent properties of the maleimide-based dyes. The fluorescence quantum efficiency varies largely, depending on the type of group substituted on the maleimide ring, e.g., amino, alcohol, halogen, or thiol. It has also been reported that the fluorescence of the maleimide derivatives relies on small charge differences between the carbon atoms (adjacent to the electron donating (C=C) and withdrawing (C=O) groups), implementing the push-pull mechanism (Fig. 2.6).[16, 21] In a recent study, the fluorescence properties were explored by tailoring the halogen substituents (from chloro to iodo groups), to selectively change the electron density of the maleimide ring (Fig. 2.6).[21] However, no successful attempt was made involving the direct substitution of fluoro groups on the ring, due to its expected high reactivity.

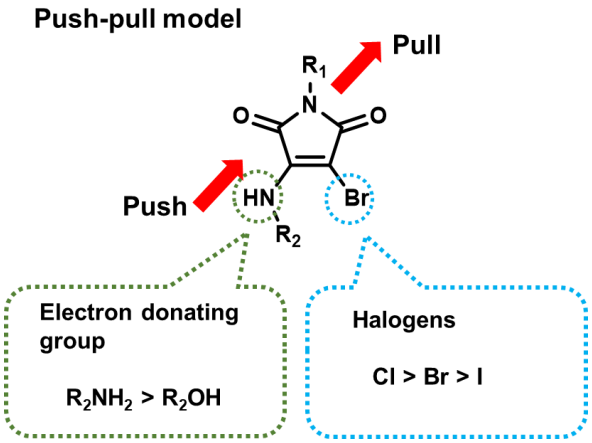

Fig. 2.6 Design strategy of the substituted maleimides structures *via* varying the substitution groups.

In this chapter, we aimed to expand the variety of structures of aminohalomaleimides using alkyfluoro substituents, and explore their effect on the fluorescent behavior. The initial strategy was to find an appropriate fluoroalkyl group that would result in increased quantum yields (ϕ_f), by reducing the photoinduced intramolecular charge transfer. The target fluoroalkyl group can be substituted at different positions on the maleimide ring, allowing us to rationalize the relationship between the structural and optical properties of the maleimide-derived structures. Firstly, a compound in which fluorine would be directly linked with the nitrogen atom in the maleimide ring was targeted (Scheme 2.1), for which no stable compound was obtained successfully even by employing several protocols.[63, 64] It was hypothesized, that no stable carbocation was formed during the reaction, which proceeds through an S_N1 reaction route. Therefore, a linker was required between the imide nitrogen and the fluoro groups in order to successfully attach electron withdrawing groups to the maleimide ring.

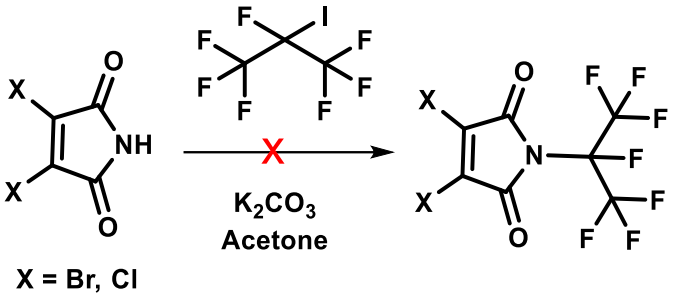

Scheme 2.1 Synthesis of *N*-fluoroalkyl substituted dihalomaleimide derivatives.

Based on this, we designed a strategy to synthesize alkyl fluoro-substituted aminochloromaleimides (ACMs) *via* two routes, producing dyes with different functionalities attached to the maleimide ring and the amino groups. Route I comprises of two stages; the first stage involves the *N*-functionalization of dichloromaleic anhydride. 2,3-dichloromaleic anhydride was allowed to react with trifluoroethylamine and/or ethylamine in 1:1 equiv. to obtain the intermediates 3,4-dichloro-1-(2,2,2-trifluoroethyl)-maleimide (**2.1**) and 3,4-dichloro-1-ethyl-maleimide (**2.3**), respectively. The 2,3-dihalomomaleimides are able to undergo an addition-elimination reaction with amines and resulted in the formation of mono-substituted products (Fig. 2.7), as reported previously.[18] Based on this method, the intermediates were allowed to react with the selected amines, to undergo the substitution reactions, which resulted in the formation of the targeted aminochloromaleimide; i.e. 3-chloro-4-(ethylamino)-1-(2,2,2-trifluoroethyl)-maleimide (**2.2**) and 3-chloro-1-ethyl-4-((2,2,2-trifluoroethyl)amino)-maleimide (**2.4**) (Scheme 2.2).

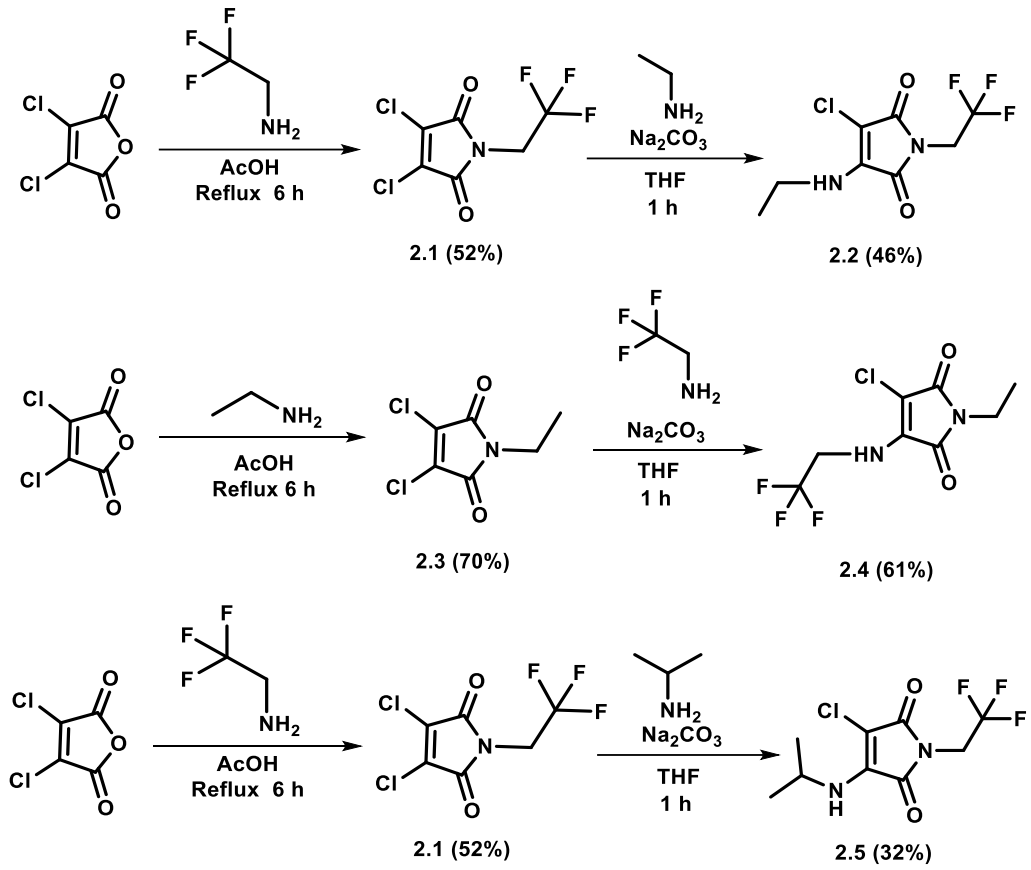

Scheme 2.2 Synthesis of trifluoroethyl substituted aminochloromaleimides **2.2, 2.4** and **2.5** *via* intermediates **2.1** and **2.3**.

To further establish the effect of using different amino groups on the fluorescent properties of fluoroalkyl substituted maleimide, another compound 3-chloro-4-(isopropylamino)-1-(2,2,2-trifluoroethyl)-maleimide (**2.5**) was targeted. This was obtained by subjecting the intermediate **2.1** to an addition-elimination reaction with isopropyl amine *via* route I (Scheme 2.2).

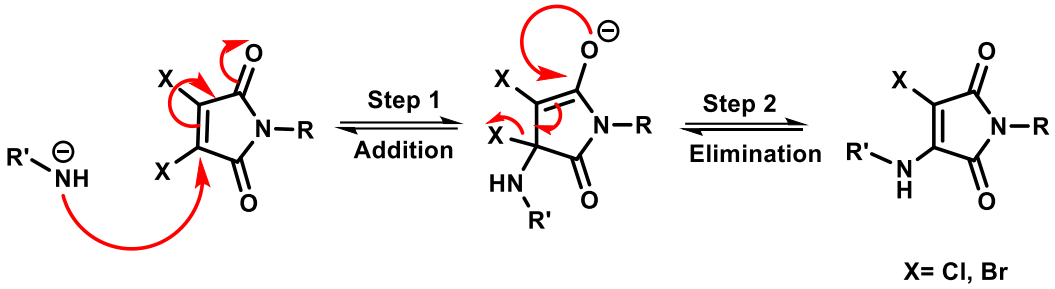

Fig. 2.7 Proposed mechanism for the two-step formation of amino-substituted maleimides.

Alternatively, route II comprised of double substitution with an amine at two different sites of the five-membered maleimide ring in a single step, thus giving the products with the same functional group at both attachment positions. Based upon this, 3-chloro-1-(2,2,2-trifluoroethyl)-4-((2,2,2-trifluoroethyl)amino)-maleimide (**2.6**) was prepared by reacting 2,3-dichloromaleic anhydride with trifluoroethylamine in 1:2 equivalents, and refluxing at 80°C under basic conditions. Further, to illustrate the effect of the fluoro groups attached to the maleimide on the fluorescence properties, a non-fluorine analogue of **2.6**, 3-chloro-1-ethyl-4-(ethylamino)-maleimide (**2.7**), was also synthesized using ethylamine under similar reaction conditions (Scheme 2.3).

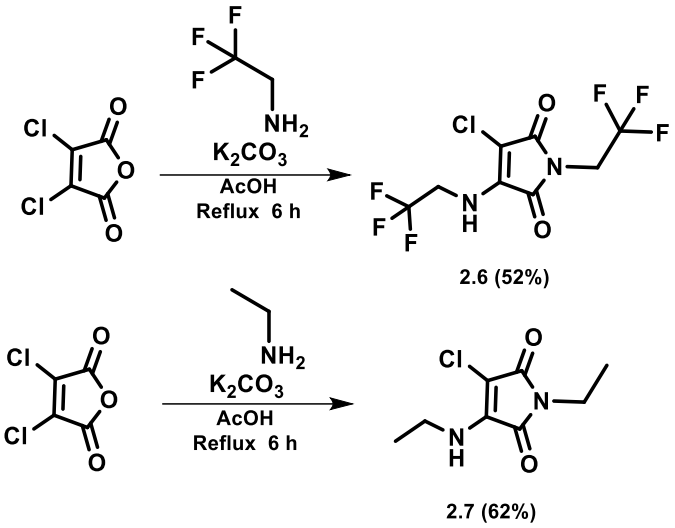

Scheme 2.3 Synthesis of di-substituted trifluoroethyl aminochloromaleimides **2.6**, and a non-fluoro aminochloromaleimide benchmark molecule **2.7** in a single step.

In the ^{13}C NMR spectra (Fig. 2.8) of the fluorinated maleimide derivative **2.6**, -CF_3 peaks can be observed, rather than the -CH_3 peaks present in **2.7** (non-fluoro control molecule). Furthermore, a clear shift in the CH_2 peaks from roughly 38.1 and 33.3 ppm to 53.0 and 41.8 ppm respectively, can be observed for compound **2.6**, attributed to the electron withdrawing effect of the attached fluoro groups (see experimental section). For the compound **2.6**, both one-bond and two-bond coupling of ^{13}C to ^{19}F were observed**,** which was absent in case of **2.7.** The large quartet for the trifluoromethyl carbon (-CF_3) was caused by the one-bond coupling to the three attached fluorine atoms (n + 1 = 4). Additionally, a quartet was observed for the methylene carbon (–CH_2) adjacent to CF_3, which was shifted downfield in the ^{13}C NMR spectrum, compared to the standard methylene carbon (Fig. 2.8).

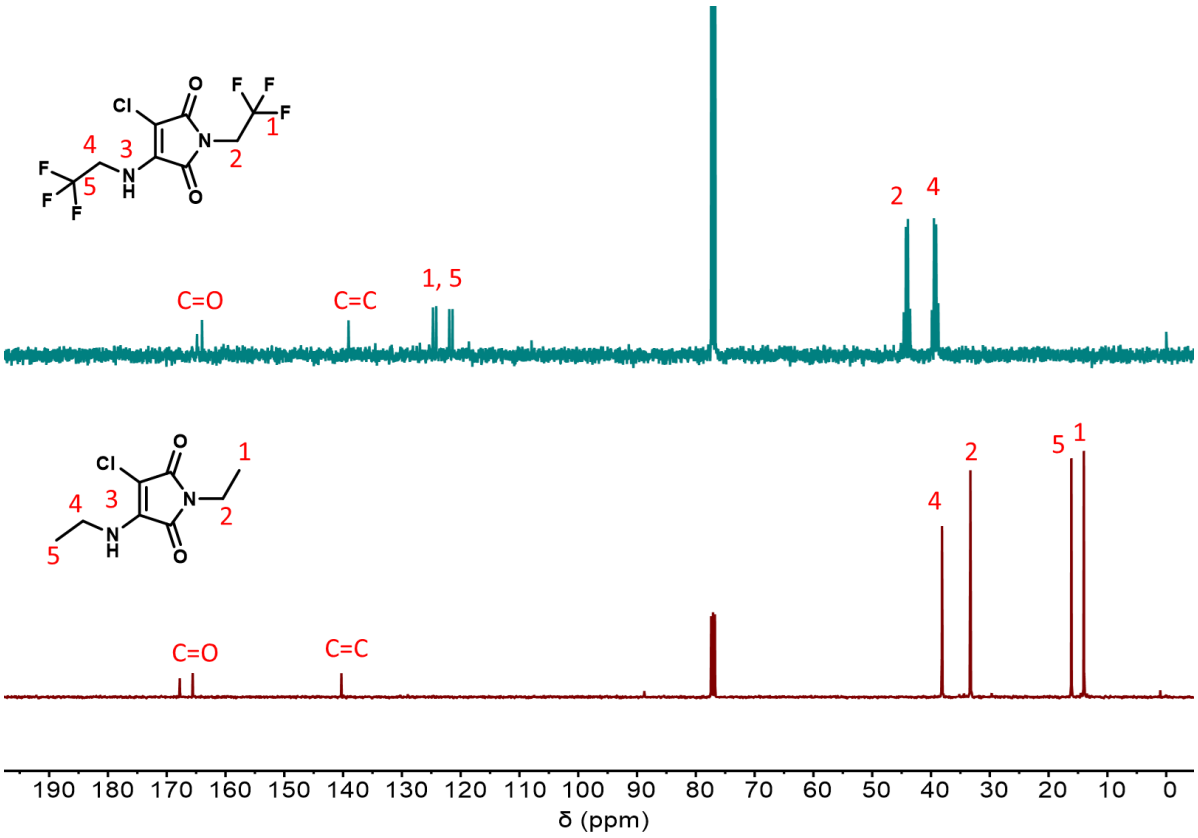

Fig. 2.8 ^{13}C ($CDCl_3$, 101 MHz) NMR spectra of **2.6** (top) and its non-fluorocarbon analogue **2.7** (bottom).

2.3.2 Design and synthesis of fluoroalkyl substituted monoaminomaleimides

A library of mono and di-CH_2CF_3 substituted monoaminomaleimides (MAMs) were synthesized, by reacting with targeted amines in 1:1 equiv. and 1:2 equiv. respectively, similarly to the fluoroalkyl substituted aminochloromaleimides (ACMs). The monosubstituted products, 3-(ethylamino)-1-(2,2,2-trifluoroethyl)-maleimide (**2.9**), and 3-(isopropylamino)-1-(2,2,2-trifluoroethyl)-maleimide (**2.12**), were synthesized utilizing monobromomaleic anhydride *via* intermediate 3-bromo-1-(2,2,2-trifluoroethyl)-maleimide (**2.8**). In addition, to investigate the effect of position of fluoro groups in the

monoaminomaleimides, 1-ethyl-3-((2,2,2-trifluoroethyl)amino)-maleimide (**2.11**) was synthesized in two stages by *N*-functionalization followed by the amine substitution (Scheme 2.4). Due to the decrease of the reactivity of the bromo group, compared to the chloro groups, a higher temperature (110°C) and longer reaction time (12 h) was required for the synthesis of monoaminomaleimides.

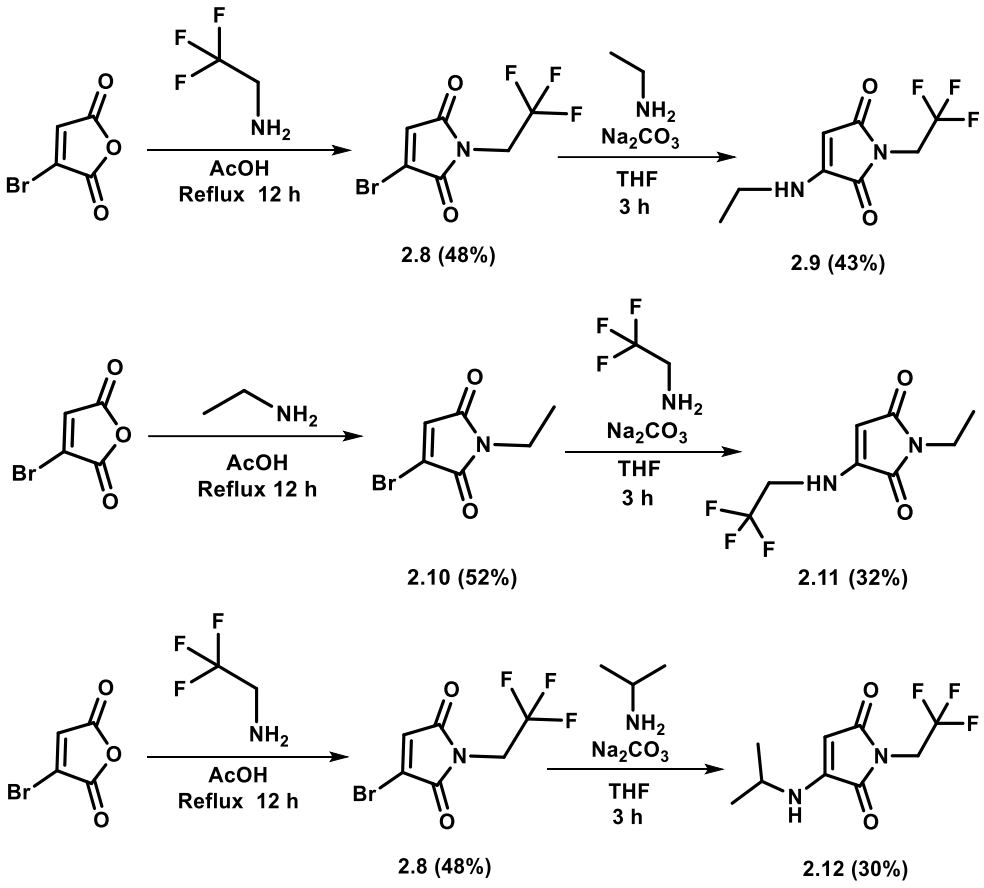

Scheme 2.4 Synthesis of trifluoroethyl substituted monoaminomaleimides **2.9, 2.11** and **2.12** *via* intermediates **2.8** and **2.10**.

Similarly, to the di-substituted aminochloromaleimides (section 2.3.1), 1-(2,2,2-trifluoroethyl)-3-((2,2,2-trifluoroethyl)amino)-maleimide (**2.13**) and 1-ethyl-3-

(ethylamino)-maleimide (**2.14**) were generated through analogous reactions (Scheme 2.5), and the major products confirmed by NMR spectroscopy and HR-MS (experimental section 2.5.5). All compounds exhibited good solubility in common organic solvents. Once the purity and structure of these compounds were confirmed, the optical properties regarding the different substitution structures were explored.

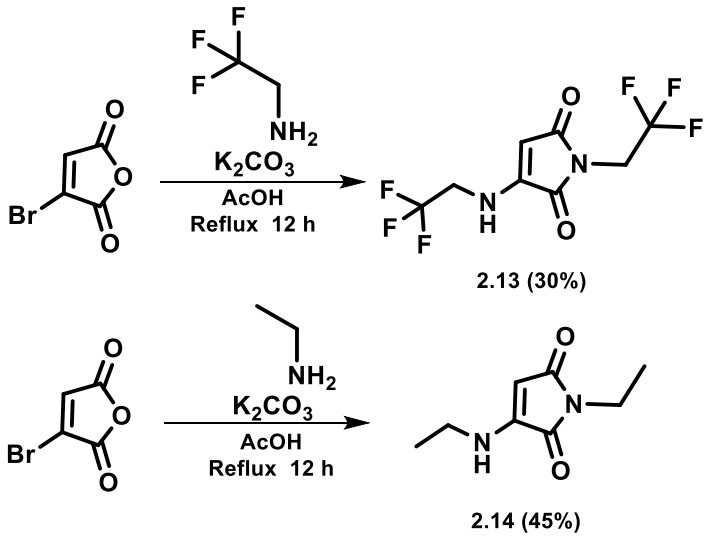

Scheme 2.5 Synthesis of di-substituted trifluoroethyl monoaminomaleimides **2.13**, and a non-fluoro monoaminomaleimide benchmark molecule **2.14** in a single step.

2.3.3 Photophysical properties of fluoroalkyl substituted maleimide

2.3.3.1 Solution-state fluorescence analysis

To establish the effect of fluoro groups attached to the maleimide ring, the optical properties of the fluoroalkyl substituted aminochloromaleimide dyes **2.2**, **2.4**, **2.5**, and **2.6**, were measured and compared to the standard **2.7**. The absorption and emission spectra of the fluoroalkyl substituted aminochloromaleimide (ACM) series were compared at the same concentration (10 μM) in a range of solvents with different polarities (Table 2.2). It is noteworthy, that the Stokes shifts in the series varied only slightly between the different dyes, indicating similar HOMO-LUMO separation. For **2.6** a noticeable red shift in absorption (λ_{ab} = 352 to 367 nm) and emission peaks (λ_{em} = 461 to 503 nm) was observed, when moving from a nonpolar solvent (diethyl ether) to a polar solvent (methanol) (Table 2.2), exhibiting solvatochromism. Moreover, lower quantum yield (ϕ_f ≈6–10%) observed in protic solvents was attributed to the hydrogen bonding between the protic solvents and the C=O group in the maleimide, causing quenching effects through the electron driven proton transfer (EDPT) from solvent to the fluorophore. This correlates with the trends observed for the non-fluorine systems, as reported previously.[16]

To gain further insight, the fluorescent properties of the series were investigated in different solvents (diethyl ether, toluene, tetrahydrofuran, dioxane, dimethyl sulfoxide, and methanol). Upon dissolving these dyes in a solvent, the ground and excited states are stabilized due to the solute-solvent interactions, implying solvatochromic properties. To quantify this, solution-state fluorescence quantum yield (ϕ_f) analysis, as

a ratio between the emitted photons to the absorbed photons, was undertaken for the series using a relative method (ϕ_{st} = 59% quinine sulfate as the reference, in 0.105 M $HClO_4$).[65] It was observed that among the synthesized aminochloromaleimides (ACMs), compound **2.6** gave relatively higher quantum yield (ϕ_f), both in non-polar and polar environments, specifically in comparison to its non-fluorinated analogue **2.7** (Fig. 2.9). However, an increment of quantum yield, from <1 to 8% was observed in methanol for **2.6**, along with a longer fluorescence lifetime of 2.32 ns in methanol for **2.6** versus 0.48 ns for **2.7** (Fig. 2.9; Table 2.1). It is noteworthy, that the lifetimes observed for the di-CH_2CF_3 substituted aminochloromaleimide **2.6** and monoaminomaleimide **2.13**, were higher compared to their non-fluorinated analogues **2.7** and **2.14**, respectively. This difference was more noticeable in dioxane relative to methanol. Additionally, in dioxane the di-CF_3 substituted aminochloromaleimide **2.6**, exhibited a slightly longer lifetime than its analogous fluorinated monoaminomaleimide **2.13** (Table 2.1). High reduced chi-squared values (i.e. χ^2 >1.5) were observed for all the fluorophores (Table 3.6), indicating high deviations from the degree of exponentially fitted data,[66] and the fitting of additional decay components did not yield any improvement.

Furthermore, quantum yields for **2.2** (an imide substituted CH_2CF_3) and **2.4** (an amine substituted CH_2CF_3) were compared, to illustrate the effect of the position of the fluoroalkyl group attached to the maleimide ring. **2.2** exhibited higher ϕ_f, particularly in the non-polar solvents, suggesting that a fluoroalkyl group (CH_2CF_3) when directly linked to the imide nitrogen has a greater electron withdrawing effect compared to the amino position (Fig. 2.9). This was numerically assessed through the integration of electron density in the ring, and calculated as Q using equations **2.1** and **2.2**. High Q

values depicts lower electron density on the maleimide ring and *vice versa* (see experimental section 2.5.6).

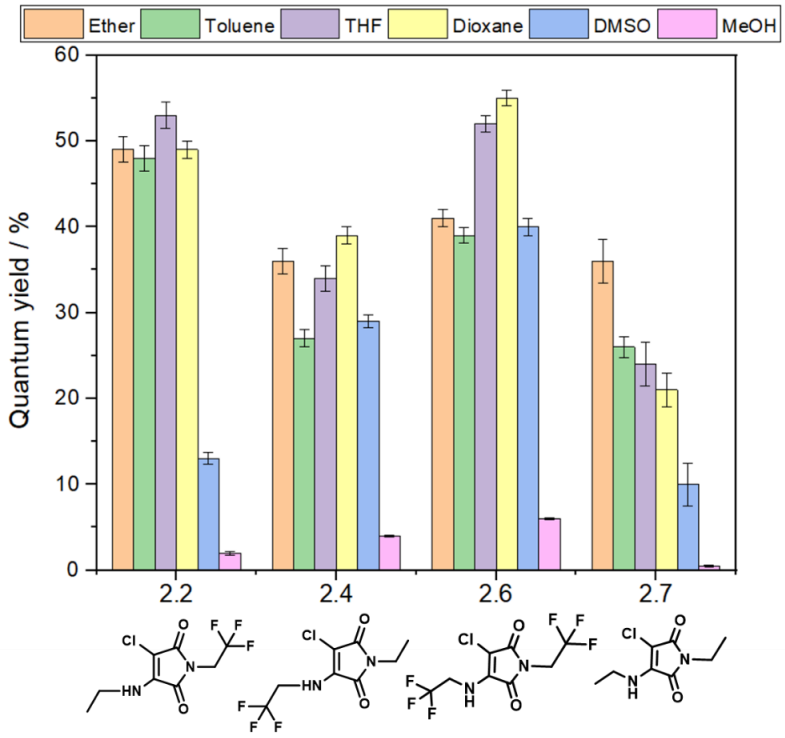

Fig. 2.9 Fluorescence quantum yield of the fluorinated aminochloromaleimide derivatives **2.2**, **2.4**, **2.6**, and the non-fluorinated aminochloromaleimide **2.7** in six different solvents (diethyl ether, toluene, tetrahydrofuran, dioxane, dimethyl sulfoxide and methanol) using quinine sulfate (ϕ_{st} = 59% in 0.105 M $HClO_4$) as the reference. Error bars represent standard deviation over three repeats.

$$Q_{NBO1} = q_{NBO,C1} + q_{NBO,C2} + q_{NBO,C3} + q_{NBO,C4} + q_{NBO,O1} + q_{NBO,O2} \quad \textbf{(Eq. 2.1)}$$

$$Q_{NBO2} = Q_{NBO1} + q_{NBO,N1} + q_{NBO,N2} \quad \textbf{(Eq. 2.2)}$$

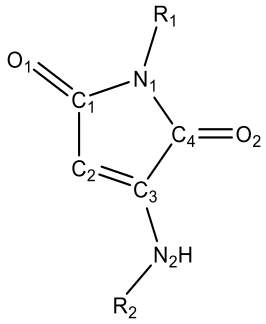

Scheme 2.6 Schematic representation of the atom enumeration used in the simulation of NBO1 and HOMO1 orbitals.

Table 2.1 Fluorescence life time decay measurements by Time-Correlated Single-Photon Counting (TCSPC) of the selected di-substituted fluoroalkyl aminomaleimide derivatives, for comparison with the non-fluoro analogues in solvents (dioxane and methanol). Data was simulated using "Reconvolution Fit" model; and Instrument response function (IRF) was determined using 10% w/w Ludox in water, as detailed in section 2.5.1 (10 μM; λ_{ex} = 375 nm; 25°C).

Solvent	Compound	τ_1 (ns)	Rel. %	τ_2 (ns)	Rel. %	χ^2
Dioxane	**2.6**	6.57	61.56	12.95	34.44	2.016
	2.7	2.49	1.57	7.9	98.43	1.863
	2.13	2.14	0.68	12.44	99.32	2.096
	2.14	2.06	2.44	5.6	97.56	1.938
MeOH	**2.6**	2.32	60.6	3.27	39.4	1.267
	2.7	0.48	99.11	7.26	0.89	1.683
	2.13	2.62	2.28	5.51	97.72	1.796
	2.14	2.54	1.77	4.34	98.23	1.562

To gain further insight into the influence of fluoroalkyl groups on the imide position, when using different substituents on the amine side, the optical properties of **2.5** (containing isopropyl amine) were evaluated, and compared with **2.2** (containing ethyl amine). The slight increase in quantum efficiency displayed by **2.5** compared to the **2.2**, could be attributed to the inductive effect of the isopropyl group (Table 2.2).

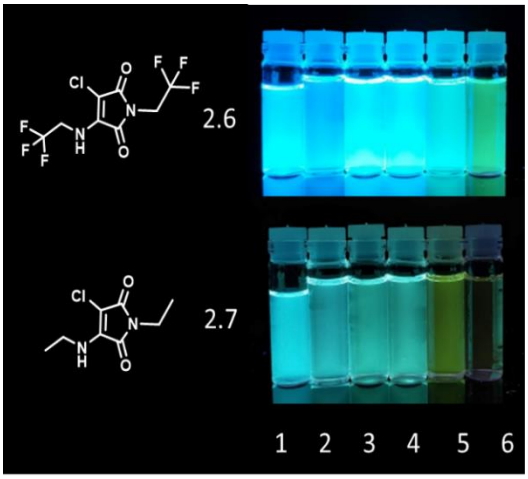

Fig. 2.10 Photographs illustrating fluorescence of aminochloromaleimides (**2.6** and **2.7**) and in six solvents (1–6: diethyl ether, toluene, tetrahydrofuran, dioxane, dimethyl sulfoxide, and methanol) under UV light (365 nm).

The molar absorption coefficient for the synthesized ACMs and MAMs in different solvents was calculated by dilution method and tabulated in Table 2.2 and Table 2.3, respectively. The solutions of six different concentrations were made (5 μM, 7.5 μM, 10 μM, 12.5 μM, 15 μM and 20 μM); each in six different solvents and run their absorptions spectra. The plot of concentration *vs* absorption followed a linear equation, and molar absorption coefficient was identified as a slope. Molar absorptivities observed in the range of 10^3 – 10^4 $M^{-1}cm^{-1}$, attributed to the intraligand (IL) excited states.

Table 2.2 Fluorescent properties of the fluoroalkyl substituted aminochloromaleimides (ACMs) series in solution-state (10 μM) and in solid-state (ϕ_f = relative quantum yield in different solvents using quinine sulfate as reference, and absolute quantum yield in solid-state using integrating sphere; λ_{max} = maximum absorption wavelength; ε_{max} = molar absorption coefficient; λ_{ex} = excitation wavelength; λ_{em} = maximum emission wavelength; $\Delta\lambda$ = Stokes shift; slit width ex 2.0 nm, em 2.0 nm; 25°C).

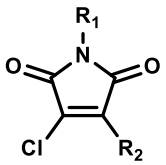

#	R_1	R_2	Solvent	ϕ_f (%)	λ_{max} (nm)	ε_{max} ($M^{-1}cm^{-1}$)	λ_{ex} (nm)	λ_{em} (nm)	$\Delta\lambda$ (nm)
2.2	CH_2CF_3	$NHCH_2CH_3$	Ether	49	–,368	6647	363	468	100
			Toluene	48	–,369	7252	363	471	102
			THF	53	233,341	5983	363	476	135
			Dioxane	49	234,371	6040	364	475	104
			DMSO	13	275,381	6752	379	494	113
			Methanol	2	232,377	4132	376	514	137
			Solid	36	-	-	452	496	-
2.4	CH_2CH_3	$NHCH_2CF_3$	Ether	36	236,359	4634	355	469	110
			Toluene	27	290,360	5358	356	471	111
			THF	34	279,364	4495	364	475	111
			Dioxane	39	276,363	3070	363	475	112
			DMSO	29	265,376	3482	369	494	118
			Methanol	4	239,369	4030	365	513	144
			Solid	30	-	-	420	486	-
2.5	CH_2CF_3	$NHCH(CH_3)_2$	Ether	51	– ,368	6971	364	467	99
			Toluene	48	–, 367	6657	364	470	103
			THF	56	230,369	6514	363	476	107
			Dioxane	51	235,371	6172	363	475	104
			DMSO	16	–, 378	5905	379	499	121
			Methanol	2	232,375	4013	374	508	133

			Solid	22	-	-	439	480	-
2.6	CH_2CF_3	$NHCH_2CF_3$	Ether	41	-, 352	7798	352	461	103
			Toluene	39	-, 358	7569	353	460	108
			THF	52	231,357	6700	355	467	110
			Dioxane	55	237,356	6649	353	467	111
			DMSO	40	276,361	6019	363	490	123
			Methanol	6	231,367	5783	359	503	142
			Solid	53	-	-	409	475	-
2.7	CH_2CH_3	$NHCH_2CH_3$	Ether	36	241,373	130377	373	460	87
			Toluene	26	-,371	86308	372	462	91
			THF	24	274,374	89378	375	476	102
			Dioxane	21	244,375	92341	375	475	100
			DMSO	10	264,383	34830	384	482	99
			Methanol	<1	241,383	1054	379	532	116
			Solid	8	-	-	432	505	-

The fluorescence properties of the synthesized monoaminomaleimides **2.9**, **2.11**, **2.12**, and **2.13**, and the standard **2.14** were further measured in solution-state, using a relative method. The ϕ_f of all the fluorinated monoaminomaleimides (MAMs) across the solvent series exhibited a trend similar to the aminochloromaleimide (ACMs) series, though the MAMs overall demonstrated slightly lower ϕ_f relative to their respective ACMs (Fig. 2.9 and 2.11). For example, the di-CF_3 dye falls from around 55% in dioxane for the ACM (**2.6**) to around 35% for the MAM (**2.13**) (Table 2.3). This was due to the electron withdrawing nature of the chlorine atom, reducing the electron density on the maleimide ring, which is consistent with our group's previously reported work.[21]

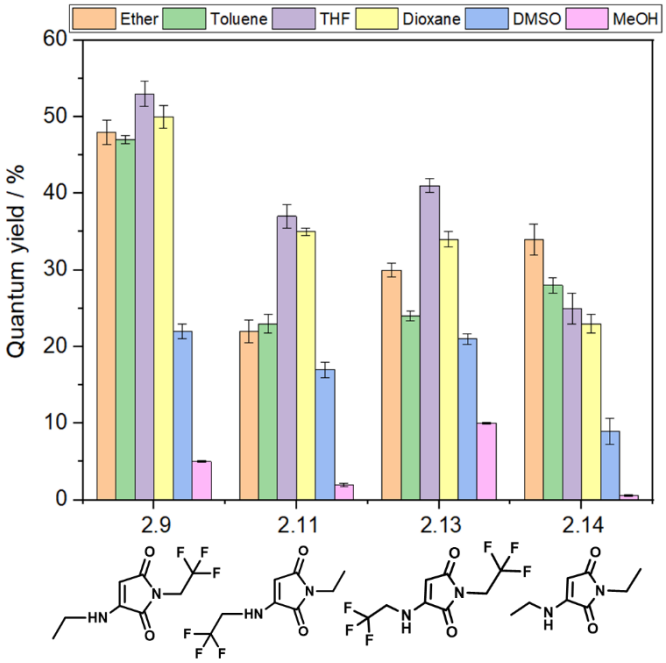

Fig. 2.11 Fluorescence quantum yield of the fluorinated monoaminomaleimide derivatives **2.9**, **2.11**, **2.13**, and the non-fluorinated monoaminomaleimide **2.14** in six different solvents (diethyl ether, toluene, tetrahydrofuran, dioxane, dimethyl sulfoxide and methanol) using quinine sulfate (ϕ_{st} = 59% in 0.105 M $HClO_4$) as the reference. Error bars represent standard deviation over three repeats.

Fig. 2.12 Photographs illustrating fluorescence of monoaminomaleimides (**2.13** and **2.14**) in six solvents (1–6: diethyl ether, toluene, tetrahydrofuran, dioxane, dimethyl sulfoxide, and methanol) under UV light (365 nm).

Table 2.3 Fluorescent properties of the fluoroalkyl substituted monoaminomaleimides (MAMs) series in solution-state (10 μM) and in solid-state (ϕ_f = relative quantum yield in different solvents using quinine sulfate as reference, and absolute quantum yield in solid-state using integrating sphere; λ_{max} = maximum absorption wavelength; ε_{max} = molar absorption coefficient; λ_{ex} = excitation wavelength; λ_{em} = maximum emission wavelength; $\Delta\lambda$ = Stokes shift; slit width ex 2.0 nm, em 2.0 nm; 25°C).

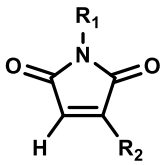

#	R_1	R_2	Solvent	ϕ_f (%)	λ_{max} (nm)	ε_{max} ($M^{-1}cm^{-1}$)	λ_{ex} (nm)	λ_{em} (nm)	$\Delta\lambda$ (nm)
2.9	CH_2CF_3	$NHCH_2CH_3$	Ether	48	235,351	7964	345	451	100
			Toluene	47	285,351	7619	347	457	106
			THF	53	–, 372	6637	349	457	85
			Dioxane	50	235,352	7438	348	461	109
			DMSO	22	–, 363	6576	363	474	111
			Methanol	5	234,357	5100	358	489	124
			Solid	17	-	-	433	489	-
2.11	CH_2CH_3	$NHCH_2CF_3$	Ether	22	-,340	6552	342	452	112
			Toluene	23	-,340	5958	344	455	115
			THF	37	232,341	5921	346	456	115
			Dioxane	35	229,345	4906	348	460	115
			DMSO	17	-,359	3937	359	472	113
			Methanol	2	240,354	3393	353	498	144
			Solid	12	-	-	415	495	-
2.12	CH_2CF_3	$NHCH(CH_3)_2$	Ether	48	230,349	7718	348	457	108
			Toluene	43	291,350	7532	349	459	109
			THF	44	268,352	6610	351	461	109
			Dioxane	26	235,351	7102	349	460	109
			DMSO	15	–,363	6365	364	477	114
			Methanol	4	237,365	5103	362	490	125

	Solid	15	-	-	420	475	-
2.13 CH_2CF_3 $NHCH_2CF_3$	Ether	30	233,335	7798	338	434	99
	Toluene	24	-,335	7569	340	440	105
	THF	41	263,340	6700	341	443	103
	Dioxane	34	230,339	6649	342	445	106
	DMSO	21	-,353	6019	349	467	114
	Methanol	10	234,344	5783	346	477	133
	Solid	50	-	-	409	478	-
2.14 CH_2CH_3 $NHCH_2CH_3$	Ether	34	236,359	3547	366	477	118
	Toluene	28	290,360	3620	369	478	118
	THF	25	279,364	4632	372	484	120
	Dioxane	23	276,363	2917	373	488	125
	DMSO	9	265,376	2571	384	505	129
	Methanol	<1	239,369	2877	381	531	162
	Solid	10	-	-	419	561	-

Most notably, higher emissions in methanol were observed for the fluoroalkyl substituted maleimides, compared to the non-fluorinated analogues, and therefore the fluorescence properties of the fluoroalkyl substituted aminomaleimide series in alcoholic solvents, was further investigated using four different alcohols (methanol, ethanol, propanol and butanol). It was observed that the quantum efficiency (ϕ_f) increased with a decrease in the polarity of the alcoholic solvents – from methanol to butanol for the MAM series (**2.9**, **2.11**, **2.13** and **2.14**). This is in agreement with previous results, where a decrease in fluorescence emission efficiency was observed with an increase in solvent polarity. **2.13** gave higher fluorescence efficiencies in all of the investigated alcoholic solvents (10–25%) in comparison to the single CF_3-substituted maleimide derivatives (**2.9** and **2.11**) (Table 2.4), emphasizing the significance of the CH_2CF_3 groups attached to the maleimide ring. In contrast to MAMs,

the aminochloromaleimide series (**2.2**, **2.4**, **2.6** and **2.7**) displayed a reverse trend, for instance, **2.6** exhibited highest ϕ_f in methanol (6%) instead of butanol (3%), for which further insight can be obtained by computational modelling.

Table 2.4 Fluorescence quantum yield evaluated in alcoholic solvents for the fluorinated aminochloromaleimides, **2.2**, **2.4**, **2.6**, and monoaminomaleimides, **2.9**, **2.11**, **2.13**, and the non-fluoro analogues, **2.7** and **2.14**, respectively (10 μM; ϕ_f = relative quantum yield using quinine sulfate as a reference; slit width ex 2.0 nm, em 2.0 nm; 25°C).

Compound	ϕ_f (%)			
	MeOH	**Ethanol**	**Propanol**	**Butanol**
Aminochloromaleimides				
2.2	2	2	1	1
2.4	4	2	1	<1
2.6	6	5	4	3
2.7	<1	<1	<1	<1
Monoaminomaleimides				
2.9	5	8	10	14
2.11	~3	3	4	5
2.13	10	20	21	25
2.14	<1	<1	1	1

In order to assess the role of electron distribution within the aminomaleimide ring, the HOMO and LUMO Kohn-Sham orbital isosurfaces, representing π-bonding and π*-antibonding respectively, were examined (Fig. 2.13). It has been reported in previous

work of our group, that decreased electron density in the aminomaleimide ring was correlated with improved fluorescence efficiency ϕ_f.[21, 67]

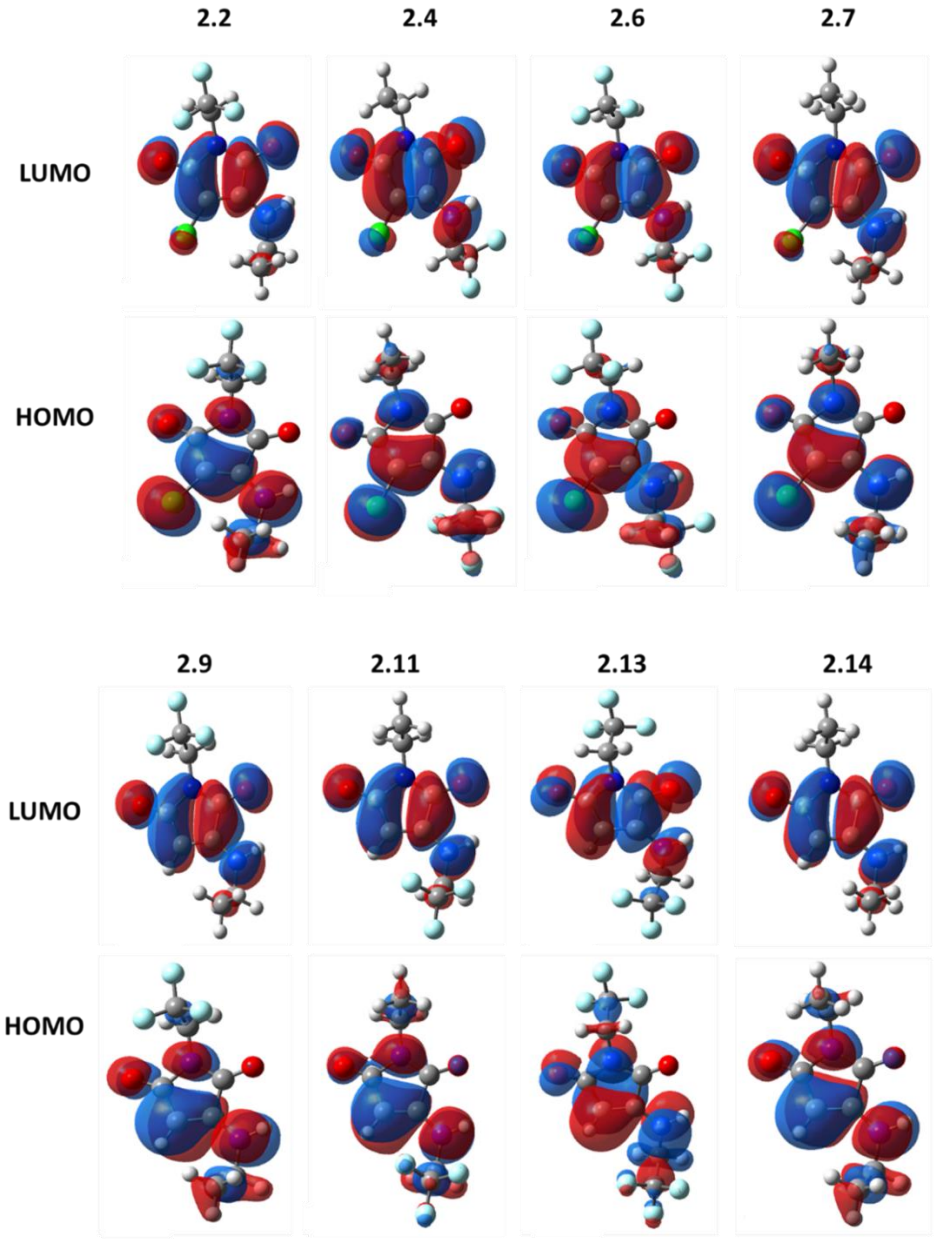

Fig. 2.13 HOMO and LUMO Kohn-Sham orbital isosurfaces of aminochloromaleimides (**2.2**, **2.4, 2.6**, and **2.7**) and monoaminomaleimides (**2.9**, **2.11, 2.13**, and **2.14**) evaluated at CAM-B3LYP-D3BJ/6-311G(d,p) level of theory in solution, using the PCM with ε = 4.24.

The descriptors, Q_{NBO1} and Q_{NBO2} can be used to understand the fluorescence quantum yield (ϕ_f) behavior. The chlorine substituent attached to the aminomaleimide ring contributes a significant electron-withdrawing effect in the π-conjugated structure of the ring. Consequently, Q_{NBO1} and Q_{NBO2} values were required to be analyzed separately for aminochloromaleimide (ACMs) and monoaminomaleimide (MAMs). Q_{NBO1} values indicate that the chlorine substituent redistributes electron density away from the π-conjugated structure of the ring, which aligns with the positive, and null or negative values for ACMs and MAMs respectively. Lower Q values indicate greater electron density on the maleimide ring, and consequently lower quantum yields.[39] Thus, in accordance with Q_{NBO1}, lower fluorescence efficiency (ϕ_f) was exhibited by the MAMs in comparison to their respective ACMs.

Further to rationalize the effect of positioning and number of the fluoroalkyl groups attached to the aminomaleimide ring, Q_{NBO1} and Q_{NBO2} values were analyzed. The trifluoromethyl group (CH_2CF_3), being one of the most powerful electron-withdrawing substituents, withdraws the electron density across the quaternary carbon occurring in the CH_2CF_3 group. The evaluated Q_{NBO1} and Q_{NBO2} values indicate that imide CH_2CF_3-substituted aminomaleimides (**2.2** and **2.9**) provide a more electron withdrawing effect than their respective amine CH_2CF_3-substituted compounds (**2.4** and **2.11**, respectively). For example, in diethyl ether using the PCM model, Q_{NBO2} values of **2.2** and **2.4** (**2.9** and **2.11**) are 0.168 a.u. and 0.170 a.u. (-0.028 a.u. and -0.023 a.u., respectively) (see experimental section 2.5.6). This was in accordance with the higher quantum yields for **2.2** (49%) and **2.9** (48%) in comparison to the **2.4** (36%) and **2.11** (22%), respectively (Table 2.2, 2.3). Furthermore, **2.6** and **2.13**, with di-substituted trifluoroethyl groups, display the largest Q_{NBO1} and Q_{NBO2} values, signifying a greater

reduction in the electron density on the aminomaleimide ring, w.r.t., the single substituted derivatives (**2.2**, **2.4**, **2.9**, and **2.11**), and the non-fluorinated aminomaleimides (**2.7** and **2.14**) (Fig. 2.14). These results suggest that the Q value trends were in accordance with the ϕ_f (%) evaluated for the studied aminomaleimides. However, it is worth noting that the general trends showed herein were not followed exactly by all the solvents.

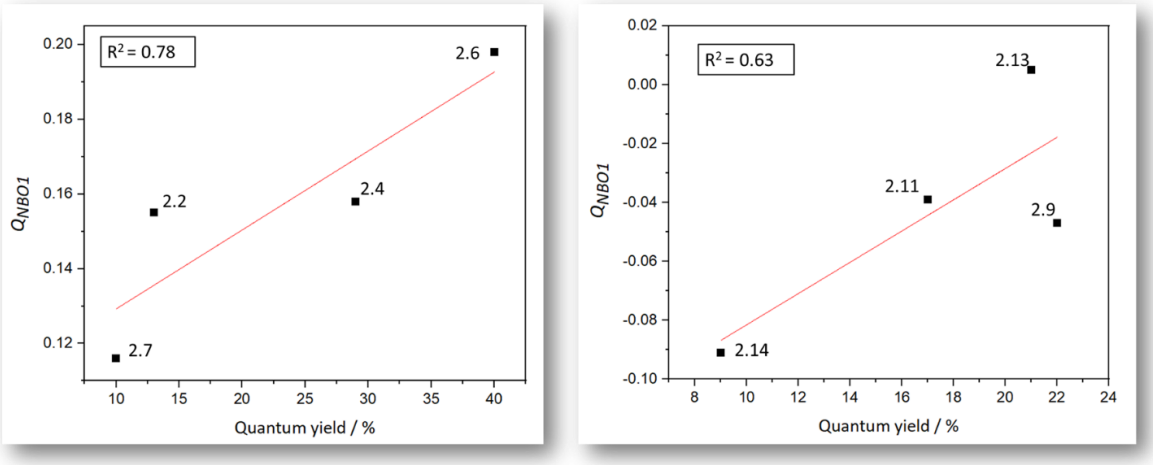

Fig. 2.14 Correlation between quantum yield (in dimethyl sulfoxide) and the atomic integration of NBO1 along the π-conjugated structure of the aminomaleimide ring (Q_{NBO1}) for ACMs (left) and MAMs (right).

This phenomenon demonstrates that the fluorescence intensity of these fluorophores can be tuned, as a result of tuning the electron density to or from the maleimide ring. Particularly, the conjugation of electron density of the aminomaleimide ring was correlated with the quantum yield in the solution-state (e.g. dimethyl sulfoxide) by linear fit, R^2 = 0.78 for ACMs and R^2 =0.63 for MAMs series (Fig. 2.14). It could also be

illustrated by two quadrants in which a low ϕ_f (< 10%) correlates to a lower Q_{NBO1} (< 0.12) and a higher ϕ_f (> 40%) correlates to a high Q_{NBO1} (> 0.2).

The solvent also plays a significant role in the optical properties of these fluoroalkyl substituted aminomaleimide derivatives. With an increase in the solvent polarity, theoretical and experimental bathochromic shifts of λ_{ex} (less than 40 nm) and λ_{em} (less than 20 nm) were observed (Table 2.7–2.14; experimental section 2.5.6). Additionally, fluorescence quenching was observed in dimethyl sulfoxide and methanol, owing to the electron driven proton transfer (EDPT) from the hydrogen bonds formed between the aminomaleimide fluorophores and the solvent molecules.[68] To explore this further, the interaction of the aminomaleimide with two explicit solvent molecules, particularly focusing on polar solvents, were studied (Fig. 2.15 and 2.16). The sum of all natural population charges in the aminomaleimide molecule, denoted as Q_{NBO3}, was specified for polar solvents (DMSO and methanol) (Table 2.15; experimental section 2.5.6).

When two explicit dimethyl sulfoxide solvent molecules were employed, the Q_{NBO3} values were calculated to be negative, implying the electron-withdrawing nature of these aminomaleimide derivatives. On the other hand, for methanol as solvent, the ACM and MAM showed positive and negative Q_{NBO3} values, respectively. The acidic (hydrogen) and basic (oxygen) centers in the alcohol group regulate the electron density to and from the aminomaleimide ring. For ACMs, due to the electron-withdrawing chlorine group, the methanol molecules withdraw less electron density from the aminomaleimide ring. Consequently, the fluorescence quenching of fluoroalkyl substituted ACMs (**2.6**; ϕ_f = 6%), in methanol, was more significant than fluoroalkyl substituted MAMs (**2.13**; ϕ_f = 10%), in comparison to the other solvents.

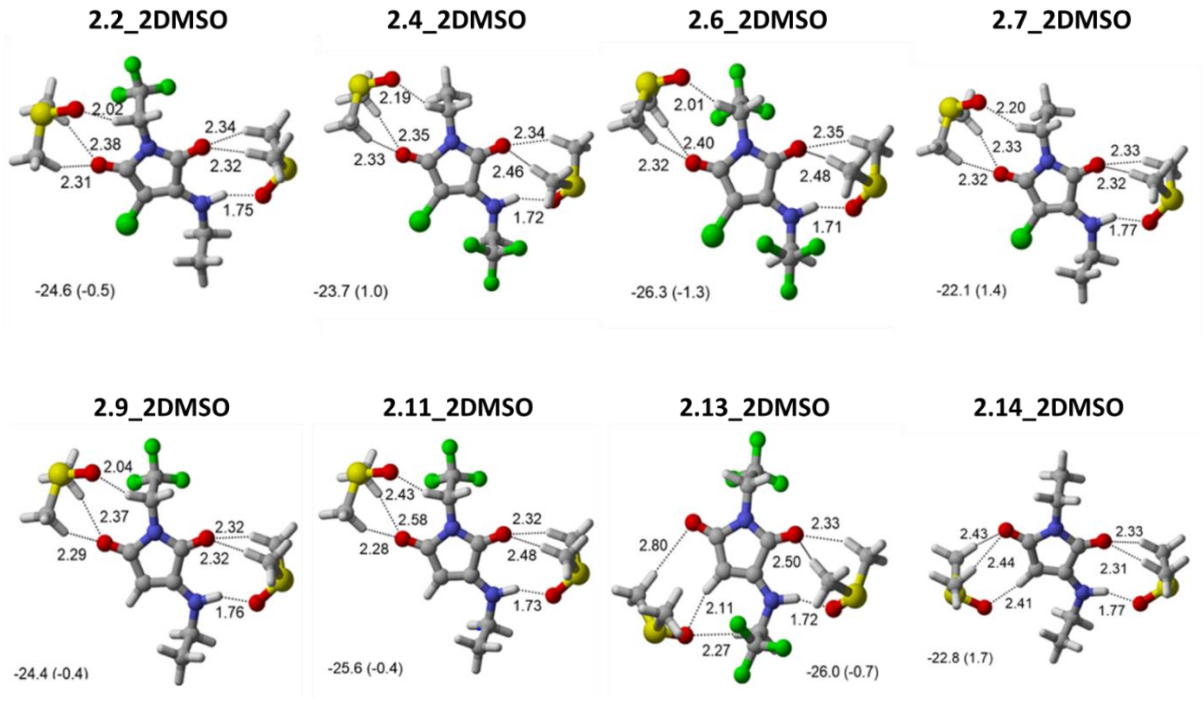

Fig. 2.15 CAM-B3LYP-D3BJ/6-311G(d,p) optimized geometries for complexes formed between aminochloromaleimides (**2.2**, **2.4, 2.6**, and **2.7**), and monoaminomaleimides (**2.9**, **2.11, 2.13**, and **2.14**), and two solvent molecules of dimethyl sulfoxide. Bond distances are given in Å. The adjacent values to the name of the complexes correspond to their relative stability with respect to their isolated solvent molecules (the parentheses values are the relative Gibbs energies at 298 K), and they are given in kcal/mol.

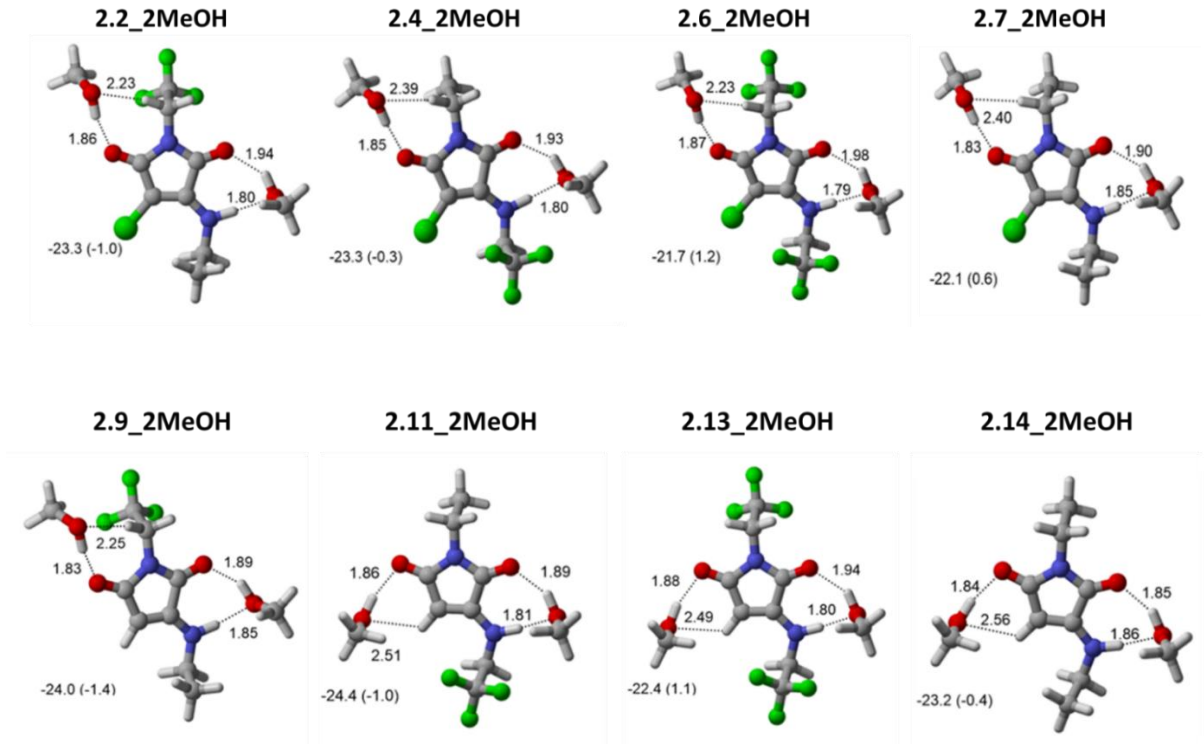

Fig. 2.16 CAM-B3LYP-D3BJ/6-311G(d,p) optimized geometries for complexes formed between aminochloromaleimides (**2.2**, **2.4, 2.6**, and **2.7**), and monoaminomaleimides (**2.9**, **2.11, 2.13**, and **2.14**), and two solvent molecules of methanol. Bond distances are given in Å. The adjacent values to the name of the complexes correspond to their relative stability with respect to their isolated solvent molecules (the parentheses values are the relative Gibbs energies at 298 K). and they are given in kcal/mol.

2.3.3.2 Solid-state fluorescence analysis

Following on from the solution-state study, the solid-state quantum yield (ϕ_f) was investigated to gain deeper insight into the influence of fluoroalkyl groups, for the fluorinated aminomaleimide series; **2.2**, **2.4**, **2.6**, **2.9**, **2.11**, **2.13**, and compared against the benchmark molecules **2.7** and **2.14**. The absolute quantum yields in the solid-state were quantified by an absolute method, using the integrating sphere set-up. Among them, the mono fluoroalkyl-substituted maleimides, **2.2**, **2.4**, **2.9** and **2.11**, exhibited solid-state ϕ_f in the range of 12–36%, compared to the standard non-fluorinated dyes, **2.7** (8%) and **2.14** (10%). It is noteworthy, that the di-substituted maleimides **2.6** and **2.13** displayed the highest solid-state ϕ_f (%) of 53% and 49%, respectively (Fig. 2.17). It is hypothesized, that the notable increase of solid-state quantum yield for these dyes was due to the attached CF_3 groups providing the steric hindrance and restrict the π–π^* stacking interactions, with these results suggesting the existence of dual state emission (DSE) behavior.

The solid-state emission wavelengths (λ_{em}) of fluoroalkyl substituted aminochloromaleimides (**2.2**, **2.4**, and **2.6**), and monoaminomaleimides (**2.9**, **2.11**, and **2.13**), were also compared with the benchmark compounds (**2.7** and **2.14**). The non-fluoro maleimides (**2.7** and **2.14**) displayed red shifted emissions (Fig. 2.18). The formation of dimers in the crystal lattice/packing generally show red shifted emissions, which was observed in case for **2.7** and **2.14**. Therefore, the hypsochromic shift emissions observed for fluoroalkyl maleimide derivatives, implies their crystal structure consists of monomers rather than dimers in the unit cell.

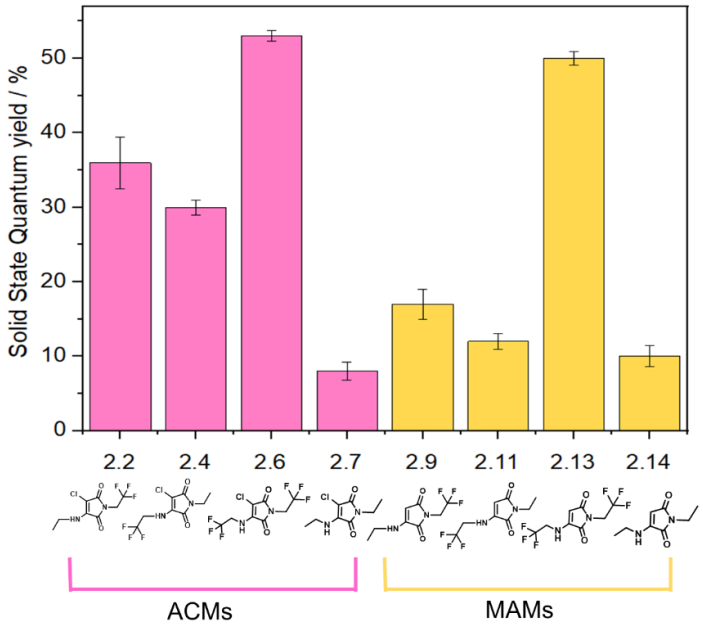

Fig. 2.17 Solid-state quantum yields of studied aminomaleimide fluorophores; measured by absolute method, using an integrating sphere. Error bars represent standard deviation over three repeats.

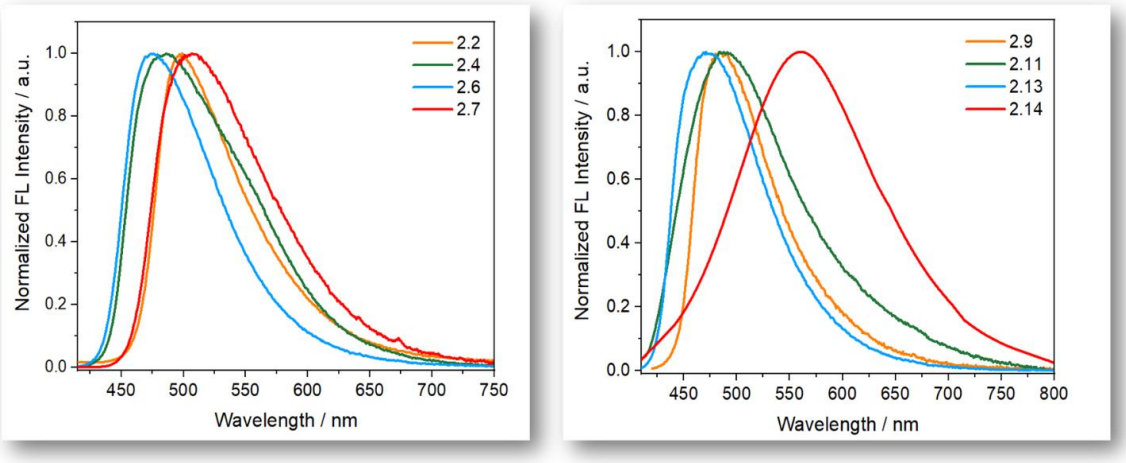

Fig. 2.18 Comparison of the normalized emission spectra in solid-state for fluorinated aminochloromaleimides (**2.2**, **2.4**, and **2.6**), fluorinated monoaminomaleimides (**2.9**, **2.11**, and **2.13**), and their non-fluorinated analogues (**2.7** and **2.14**).

In an attempt to further investigate the origin of the fluorescence efficiency of the fluoroalkyl substituted maleimides, X-ray crystal structures were successfully obtained for the aminochloromaleimides, **2.2**, **2.4**, and **2.6**; monoaminomaleimides, **2.9**, and **2.13;** and control molecule **2.7**. Unfortunately, owing to their amorphous nature, the compounds **2.11** and **2.14** didn't crystallize, and hence were unable to be compared with the other members of the series. It was observed from the molecular packing for the aminochloromaleimide (ACMs) series that **2.4** and **2.7** form a chain of maleimide motifs with N−H···O bond lengths of 2.12 Å and 2.10 Å, respectively. In comparison, **2.2** and **2.6** dimerized connected by N−H···O bonds with bond lengths of 2.13 Å and 2.14 Å, respectively, possibly due to steric hindrance caused by the fluoro groups (Table 2.5). It was also notable that **2.6** possess an interlayer H···F hydrogen bond, with a bond length of 2.52 Å. For the monoaminomaleimides (MAMs) series, the crystal structures were analyzed for **2.9** and **2.13** only**.** The molecules were shown to be alternately arranged up and down and formed parallel layers through N–H···O interactions 2.10 to 2.15 Å long (Table 2.5). Moreover, for fluoroalkyl MAMs, dimers were connected by weak C–H···O interactions of bond lengths 2.42–2.44 Å, which were not present in the aminochloromaleimide dyes. Additionally, multiple H···F bonds were formed between layers around 2.22. to 2.52 Å, leading to the relatively open structures observed for **2.9** and **2.13**.

Table 2.5 Hydrogen bonding parameters measured from solvent crystal structures of the fluoroalkyl aminomaleimide series. **2.2;** i: 1-X,2-Y,-Z, **2.4;** i: -1+X,+Y,+Z, **2.6; i:** 2-X,-Y,1-Z, ii: 1-X,-Y,1-Z, **2.7;** i: +X,1+Y,+Z, **2.9;** i: 1-X,1-Y,1-Z, ii: 1-X,-Y,1-Z, **2.13;** i: 1-X,-1/2+Y,1/2-Z; ii: 1-X,1/2+Y,1/2-Z; iii: 1-X,1-Y,1-Z; , iv: +X,3/2-Y,1/2+Z , v: 1-X,1-Y,-Z.

Compound	Bonds	Bond Length d(H-A) (Å)	Angle (°)	Form
Fluoroalkyl aminochloromaleimides (ACMs)				
2.2	N2−H2···O1^{i}	2.13(2)	150.6(17)	Dimer
2.4	N2−H2···O2^{i}	2.12(19)	139.6(16)	Chain
2.6	N2−H2···O1^{i}	2.14(2)	152(2)	Dimer
	C5−H5A···F3^{ii}	2.52	128.9	Interlayer
2.7	N2−H2···O2^{i}	2.10(6)	146(5)	Chain
	N102−H102···O102^{i}	2.14(7)	140(6)	Chain
Fluoroalkyl monoaminomaleimides (MAMs)				
2.9	N102−H102···O2	2.15(4)	143(5)	Chain
	H3···O101	2.42	146.3	Chain
	C7−H7B···F102^{i}	2.40	157.3	Interlayer
	C107−H10F···F3^{ii}	2.51	140.2	Interlayer
2.13	N2−H2···O2^{i}	2.10(4)	147(6)	Chain
	H3···O1^{ii}	2.44	139.0	Chain
	C7−H7A···F2A^{iii}	2.22	148.6	Interlayer
	C7−H7B···F6^{iv}	2.31	149.9	Interlayer
	C5−H5A···F5^{v}	2.52	156.5	Interlayer

It was hypothesized that the high solid-state fluorescence efficiency was attributed by the more distant π-π stacking, which prevents the maleimide rings from coming in close proximity, thus reducing the intermolecular π-π interactions which can result in fluorescence quenching of the fluorophores.[67] The formation of interlayer H-F bonds were suggestive of the further separation in the rings. In order to further quantify this, the ring distances, which serve as an indication of π-π interactions, were measured. These distances reflect the distribution of electronic density that reduces the π-electrons.[69] The distance between ring centroids was in the range of 5.4993 to 6.0630 Å for the fluoroalkyl substituted aminochloromaleimides (**2.2**, **2.4** and **2.6**), and was associated with higher solid-state ϕ_f (30- 53 %). In comparison, for **2.7** the shortest ring centroid distance of 3.69 Å was indicative of typical π-π interactions. Thus, a ring centroid distance >4 Å observed for the fluorinated ACMs was in accordance with the higher solid-state fluorescence efficiency. For the fluorinated monoaminomaleimide **2.9**, the relatively lower solid-state ϕ_f (11%) was associated with reduced ring centroid distance of 4.937 Å. In case of **2.13**, the decrease in the inter-plane shift to 2.634 Å with a ring centroid distance of 4.304 Å, implies an off-center nature of the π-π interactions (Table 2.6). The observed molecular conformation of the fluorinated maleimide motifs in the solid-state blocks the non-radiative relaxation, by suppressing π-π stacking, and results in high solid-state fluorescence efficiency.[70]

Table 2.6 Solid-state ϕ_f and maleimide crystal packing distances for crystals of the fluoroalkyl ACM and MAM series. †Measured distance between ring centroid of N1C1C2C3C4 and $N1^iC1^iC2^iC3^iC4^i$. ‡Distance between ring centroid of N1C1C2C3C4 and plane of $N1^iC1^iC2^iC3^iC4^i$. §Distance in horizontal shift between ring centroids of N1C1C2C3C4 and $N1^iC1^iC2^iC3^iC4^i$. *No single crystals were obtained, so lacks crystallographic data.

Compound	Solid-state ϕ_f (%)	Ring centroid distance† (Å)	Inter plane distance‡ (Å)	Plane to plane shift§ (Å)
Fluoroalkyl aminochloromaleimides (ACMs)				
2.2	36 (± 0.34)	5.4993 (±0.001)	3.497 (±0.004)	4.244 (±0.003)
2.4	30 (± 0.77)	6.0630 (±0.001)	5.2467 (±0.003)	3.038 (±0.004)
2.6	53 (± 0.18)	5.6672 (±0.002)	3.455 (±0.006)	4.492 (±0.004)
2.7	36 (± 0.34)	3.694 (±0.003)	3.064 (±0.006)	2.063 (±0.008)
Fluoroalkyl monoaminomaleimides (MAMs)				
2.9	11 (± 2.00)	4.937 (±0.003)	3.481 (±0.007)	3.501 (±0.007)
2.11*	12 (± 1.08)	-	-	-
2.13	50 (± 0.90)	4.304 (±0.002)	3.224 (±0.002)	2.634 (±0.01)
2.14*	2 (± 1.58)	-	-	-

To further explain the origins of the solid-state fluorescence efficiencies for the fluoroalkyl substituted aminomaleimide derivatives, the visualization of noncovalent interactions (NCI) was obtained from the X-Ray crystal structures displayed at the CAM-B3LYP-D3BJ/6-311G(d,p) level of theory (Fig. 2.19; 2.20). Clear π-π stacking interactions were observed in all the dimers for aminochloromaleimides (**2.2**, **2.4**, **2.6**, and **2.7**), and monoaminomaleimides (**2.9**, **2.11**, and **2.13**). The largest π-π stacking was observed for **2.7**, which was also correlated to the shortest ring centroid distance of 3.694 Å (for **2.14**, a similar scenario was expected, as the crystal structure has not been obtained). The attached trifluoroethyl (CH_2CF_3) groups are aligned in zigzag arrangements and induce steric hindrance which reduces the steric repulsion. On the other hand, **2.13** displayed more diffuse π-π interaction. Moreover, the ring centroid distances from 4.2 Å to 5.2 Å, indicated that these intermolecular interactions were moderate-weak. Therefore, the highest solid-state ϕ_f obtained for **2.6** (53%) and **2.13** (50%) was attributed to the electron-withdrawing substituents (chlorine and CH_2CF_3 groups). This signifies the decrease of inter- and intramolecular π-π interactions, making these fluorophores to be dual state emission (DSE) dyes.

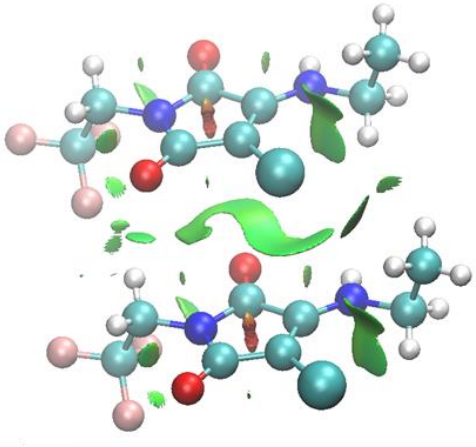

2.2

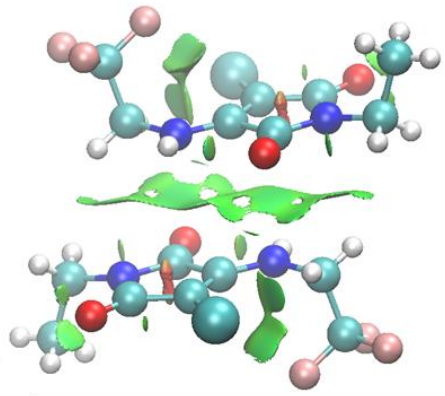

2.4

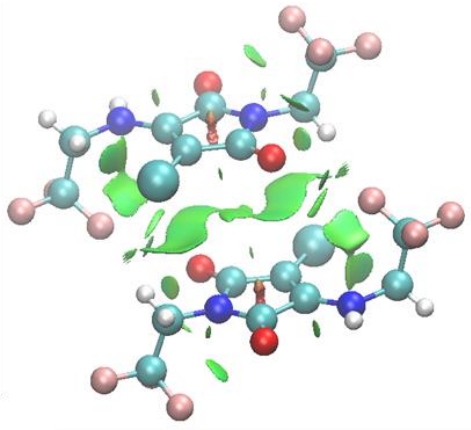

2.6

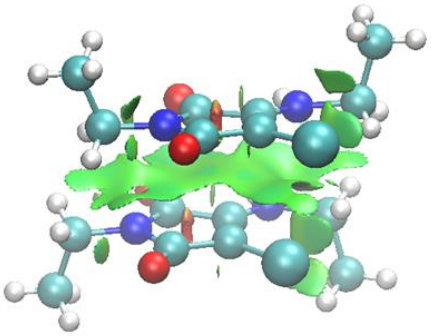

2.7

Fig. 2.19 CAM-B3LYP/6-311G(d,p) gradient isosurfaces with s=0.5 for the crystal structures of aminochloromaleimides, **2.2**, **2.4**, **2.6**, and **2.7**, with a blue-green-red color scale from -0.05 < sign(λ_2) < 0.05 au.

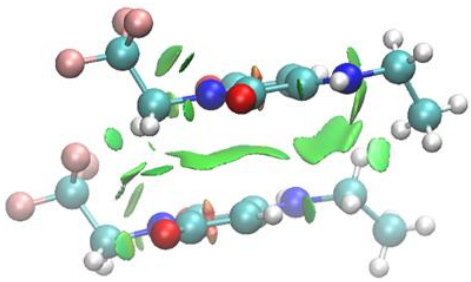

2.9

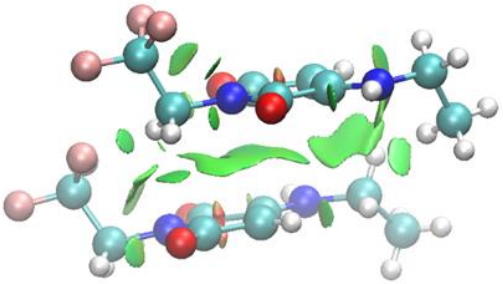

2.11

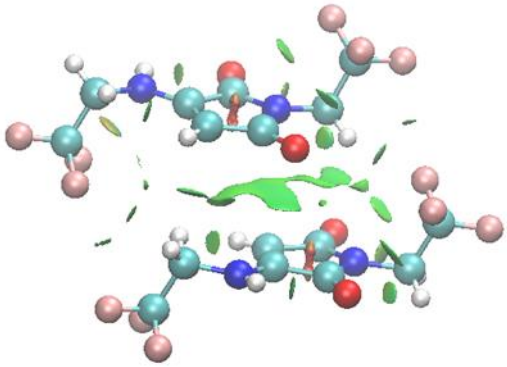

2.13

Fig. 2.20 CAM-B3LYP/6-311G(d,p) gradient isosurfaces with s=0.5 for the crystal structures of monoaminomaleimides, **2.9, 2.11**, and **2.13**, with a blue-green-red color scale from -0.05 < sign(λ_2) < 0.05 au.

2.3.3.3 Dual state emission (DSE) behavior

To investigate the potential of the synthesized fluoroalkyl substituted maleimides for dual state emission (DSE), **2.6** was used as a model compound. In order to ensure that the higher fluorescence quantum efficiencies (ϕ_f) displayed by the fluoroalkyl maleimide dyes in polar solvents, was not caused by aggregation (stemming from the hydrophobicity of the attached fluoroalkyl groups), the emission scans for **2.6** in different solvents (particularly in methanol) and solid-state were compared. Notably, the emission maxima (λ_{max}) observed for the solid-state varied completely when compared to methanol. In the solid-state, compound **2.6** displayed an emission maximum around 475 nm, but a bathochromic shift was observed in methanol (503 nm) (Fig. 2.21). This suggests that these fluorinated dyes were soluble in methanol, and the observed $\phi_f \approx 6–10\%$, has not been caused by the aggregation, thus rules out the possibility of precipitation of **2.6** in polar solvent, i.e., methanol.

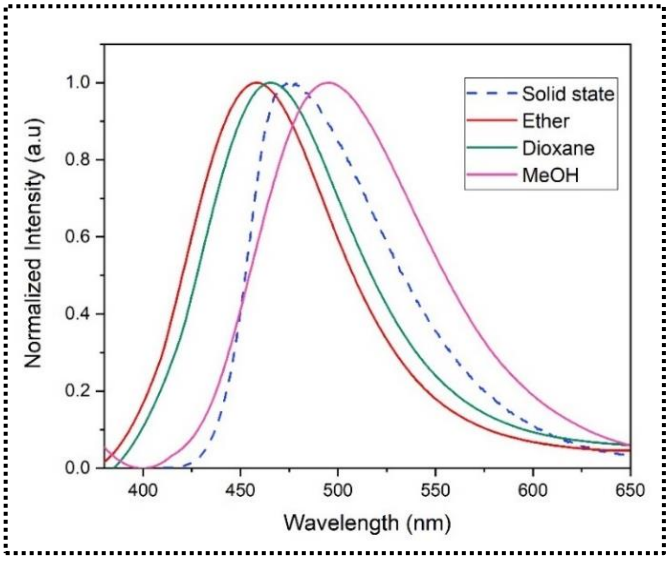

Fig. 2.21 Normalized emission spectra of **2.6** in different solvents (diethyl ether, dioxane and methanol) and solid-state (10 μM; slit width: ex 1.0 nm, em 1.0 nm).

To ascertain the DSE phenomenon of the fluoroalkyl substituted maleimide, a solution of **2.6** in methanol was titrated with water. The weak emission peak in methanol at 503 nm gradually decreased in intensity along with a slight red shift, with a progressive increase in water content (f_w) from 10-40% (Fig. 2.22), possibly originating from the twisted intramolecular charge transfer (TICT) effect.[11] Upon further increase in water content, a slight blue shift (514 to 510 nm) was observed, indicative of the onset of aggregation (Fig. 2.22). This further signifies the complete dissolution of the trifluoroethyl maleimide derivatives in protic polar solvents, and consequently implies the existence of dual state emission behavior.

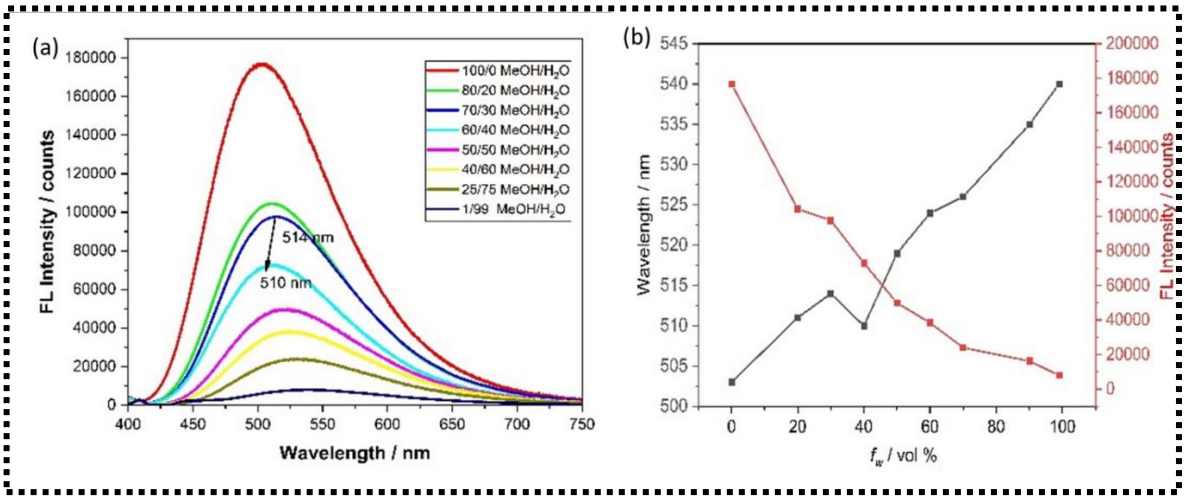

Fig. 2.22 a) Emission spectra of **2.6** in various ratios of methanol and water (left); b) Plot showing intensity and wavelength changes against water fraction for **2.6** (right) (10 μM, λ_{ex} 359 nm, slit width: ex 2.0 nm, em 2.0 nm).

2.4 Summary

To summarize, a library of single and double substituted fluoroalkyl maleimide fluorophores have been prepared by attaching trifluoroethyl groups at the imide and amine positions of aminomaleimide derivatives, utilizing a straightforward synthetic methodology. The effect of the substituted fluoro groups on the optical properties of the maleimide derivatives has been investigated. In general, all fluorinated maleimide derivatives showed bright blue-green emissions, with quantum yields up to 60% in the solution-state, and 53% in the aggregated state, compared to their non-fluorinated benchmark molecules. The di-CH_2CF_3 substituted aminochloromaleimide and monoaminomaleimide showed the highest quantum yields in comparison to their respective single substituted derivatives. The suppression of π-π stacking interactions in the solid-state, and molecular conformational changes inhibiting the electron driven proton transfer (EDPT) caused by polar protic solvents during excitation, contributes to their intense fluorescence in both states. These effects were further explored by analyzing the crystallographic parameters, and modelling the electronic distributions in the HOMO-LUMO isosurfaces, and NCI plots using density functional theory (DFT) simulation theory. These results indicated the rational design of maleimide-based molecular structures, exhibiting dual state emissions (DSE), was successful. Thus, this chapter provides a rational design strategy for maleimide-based dual-state luminophores for various biochemical applications.

2.5 Experimental

2.5.1 Materials and instrumentation

All chemicals were obtained from Alfa Aesar, Fisher Chemicals, Fluorochem, or Sigma Aldrich and used as received.

NMR spectra were recorded on a Bruker Advance 300, a Bruker Advance III HD 400 or a Bruker Advance III HD 500 spectrometer at 300, 400 and 500 MHz respectively. Shifts are quoted in δ in parts per million (ppm) and quoted relative to the internal standard tetramethylsilane (TMS) for ^{1}H; ^{13}C and $CFCl_3$ (for ^{19}F NMR)[71] or the solvent peak.

High Resolution Mass Spectra (HR-MS) were conducted by Dr Christopher Williams (University of Birmingham) on a Bruker UHR-Q-ToF MaXis spectrometer with electrospray ionization.

FTIR spectroscopy was carried out on neat samples using Agilent Technologies Cary 630 FTIR spectrometer. The spectra were corrected for background absorbance and 16 Scans were taken from 600 to 4000 cm^{-1} at a resolution of 4 cm^{-1}.

UV-Vis spectroscopy was carried out at room temperature on Evolution 350 UV-Vis spectrophotometer, equipped with Xenon Flash lamp light source, and silicon photodiode detectors. Quartz cells (3.5 mL; 170 - 2000 nm) from Hellma with two polished sides were used for examining the absorption spectral data, by using Thermo INSIGHT software.

Fluorescence emission and excitation spectra were obtained with an Agilent Cary Eclipse Fluorescence spectrophotometer or an Edinburgh Instruments FS5

Spectrofluorometer in quartz 3.5 mL cuvettes (Starna Cell, Type: 3/Q/10), for liquid samples (10–20 μM, 25°C). The data was analyzed in Fluoracle (Edinburgh Instruments), and Origin 2019 (Origin Labs). For the evaluation of solution-state quantum yield analysis, a solution of quinine sulfate dihydrate in 0.105 M perchloric acid was used as the standard (ϕ_{st} = 59%), based on a previously reported literature procedure.[65] For solid-state samples the SC-30 integrating sphere module of the FS5 was used to calculate absolute quantum yield. The mean of three to six replicate measurements was recorded. Fluorescence lifetime spectra were obtained by time correlated single photon counting (TCSPC). These experiments were done with Edinburgh Instruments FS5 spectrofluorometer, equipped with 375±10 nm pulsed diode laser source (PicoQuant). Instrument response functions (IRF) were determined from the scatter signal solution of Ludox HS-40 colloidal silica (10% particles in water w/w). The data was simulated using “Reconvolution fit” model to eliminate both the noise and the effects of the exciting light pulse. The reduced chi square χ^2 has been evaluated using Fluoroacle (software) and is used to assess the data fitting.

Crystals were grown for the samples by multi-solvent and hot filtration recrystallization techniques using hexane-dichloromethane. The datasets were collected on an Agilent Technologies SuperNova single crystal X-ray diffractometer, with dual wavelength microfocus X-ray sources (Mo and Cu), and an Atlas detector. The system is complemented by an Oxford Cryosystems Cryostream to collect data at temperatures as low as 100 K.

2.5.2 Synthesis of aminochloromaleimides *via* route-I

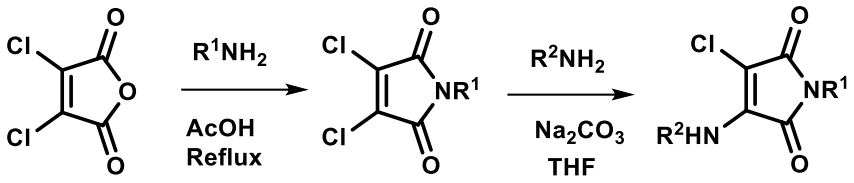

R^1 R^2 = CH_2CH_3, CH_2CF_3

Step-I: *N*-functionalization of dichloromaleimide was carried out according to the protocol established by a previous paper.[72] 1.0 equiv. of 3,4-dichloromaleic anhydride was dissolved in 20 mL of acetic acid, followed by the dropwise addition of 1.0 equiv. of the required amine. The solution was then refluxed at 80℃ for 4 – 6 h. After 6 h, solvent was evaporated under reduced pressure. The white solid was obtained after purification *via* column chromatography using *n*-hexane/ethyl acetate.

Step-II: Amine substitution of the maleimide was achieved following the previously reported protocol.[16] 1.0 equiv. of *N*-functionalized 3,4-dichloromaleimide, obtained from Step-I, was dissolved in 20–25 mL THF and mixed with 2.5 equiv. of sodium carbonate. The mixture was allowed to react with 1.0–1.5 equiv. of the targeted amine at room temperature. Reaction progress was monitored by TLC and was completed within 30 min to 1 h. The solvent was evaporated under reduced pressure and the residue was taken up with 150 mL of CH_2Cl_2, washed with 2×150 mL of water, and dried over magnesium sulfate. Purification *via* column chromatography on silica gel with *n*-hexane/ethyl acetate resulted in a yellow fluorescent solid.

3,4-dichloro-1-(2,2,2-trifluoroethyl)-1*H*-pyrrole-2,5-dione (2.1)

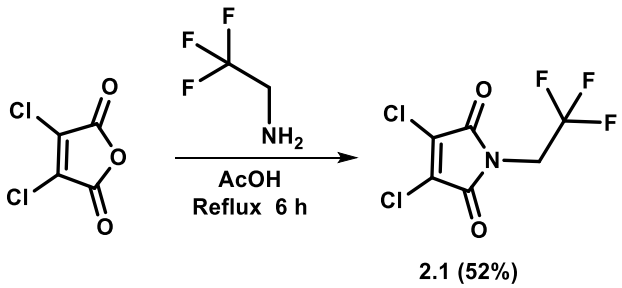

2.1 (52%)

R_f = 0.50 (hexane: ethyl acetate 3:1), Yield = 772 mg, 52%.

^{1}H NMR (400 MHz, $CDCl_3$, 25°C TMS) δ [ppm] =4.24 – 4.17 (q, 2H, H2).

^{13}C NMR (101 MHz, $CDCl_3$, 25°C, TMS) δ [ppm] = 161.7 (C=O), 134.2 (C=C), 126.9–18.5 (C1), 40.5–39.4 (C2).

^{19}F NMR (400 MHz, $CDCl_3$, 25°C, $CFCl_3$) δ [ppm] = -70.90.

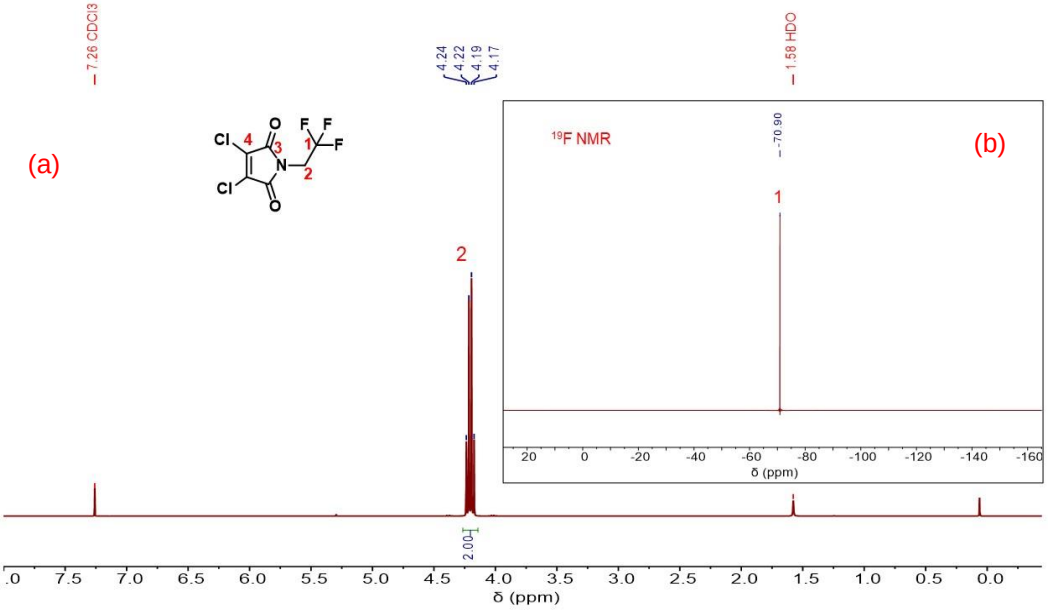

Fig. 2.23 ^{1}H (a) and ^{19}F (b) NMR spectra of **2.1** (400 and 300 MHz respectively, $CDCl_3$).

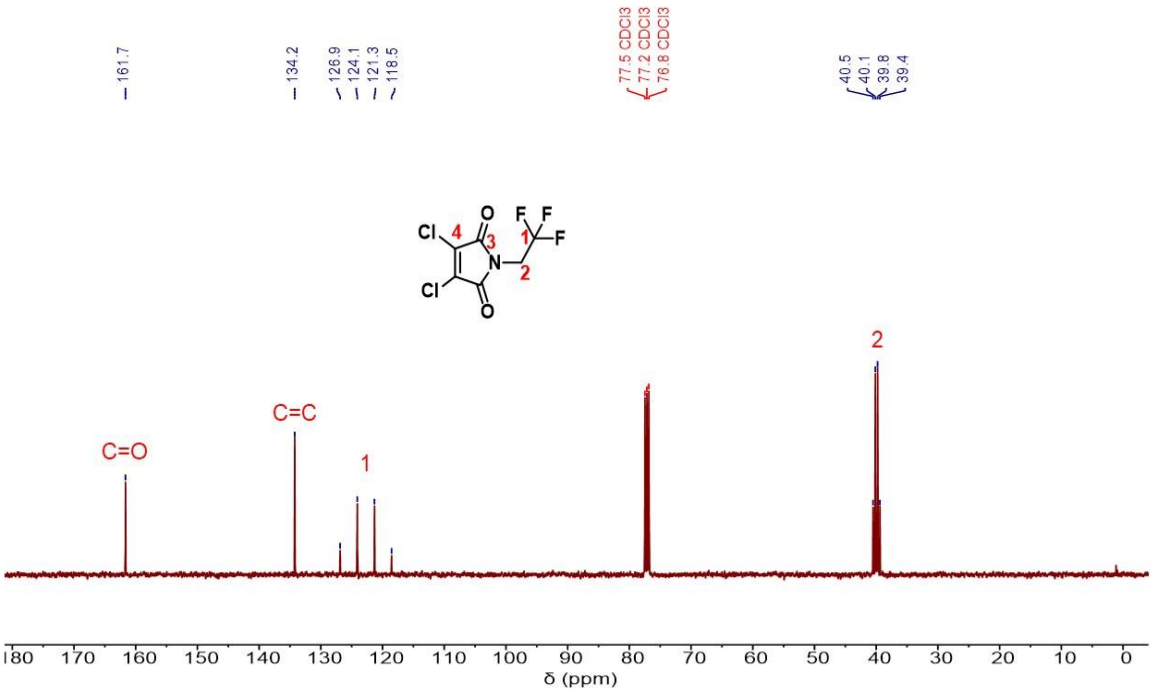

Fig. 2.24 ^{13}C NMR spectrum of **2.1** (101 MHz , $CDCl_3$).

3-chloro-4-(ethylamino)-1-(2,2,2-trifluoroethyl)-1*H*-pyrrole-2,5-dione (2.2)

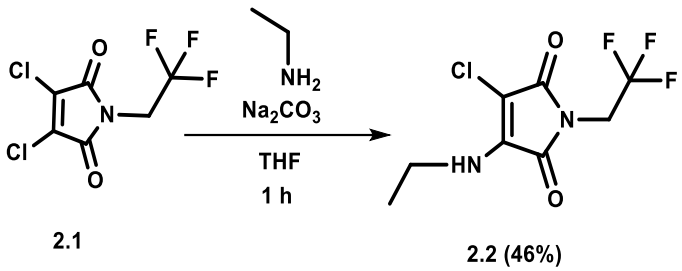

2.1 **2.2 (46%)**

R_f = 0.63 (hexane: ethyl acetate 2:1), Yield = 340 mg, 46%.

^{1}H NMR (400 MHz, $CDCl_3$, 25°C, TMS) δ [ppm] =5.43 (s, 1H, H5), 4.14 – 4.05 (q, 2H, H2), 3.74 –3.65 (m, 2H, H6), 1.34 –1.29 (t, 3H, H7).

^{13}C NMR (101 MHz, $CDCl_3$, 25°C, TMS) δ [ppm] = 165.7, 164.6 (C=O), 140.5 (C=C), 127.1–118.8 (C1), 39.7–38.6 (C2), 38.3 (C6), 16.1 (C7).

^{19}F NMR (400 MHz, $CDCl_3$, 25°C, $CFCl_3$) δ [ppm] = -71.02.

HR-MS (MaXis) $[M+Na]^+$ - *m/z* found 279.0227; *m/z* calculated 279.0226.

FTIR (cm^{-1}): ν = 3337 (N-H), 2964 (C-H), 1770,1720 (C=O), 1649 (C=C).

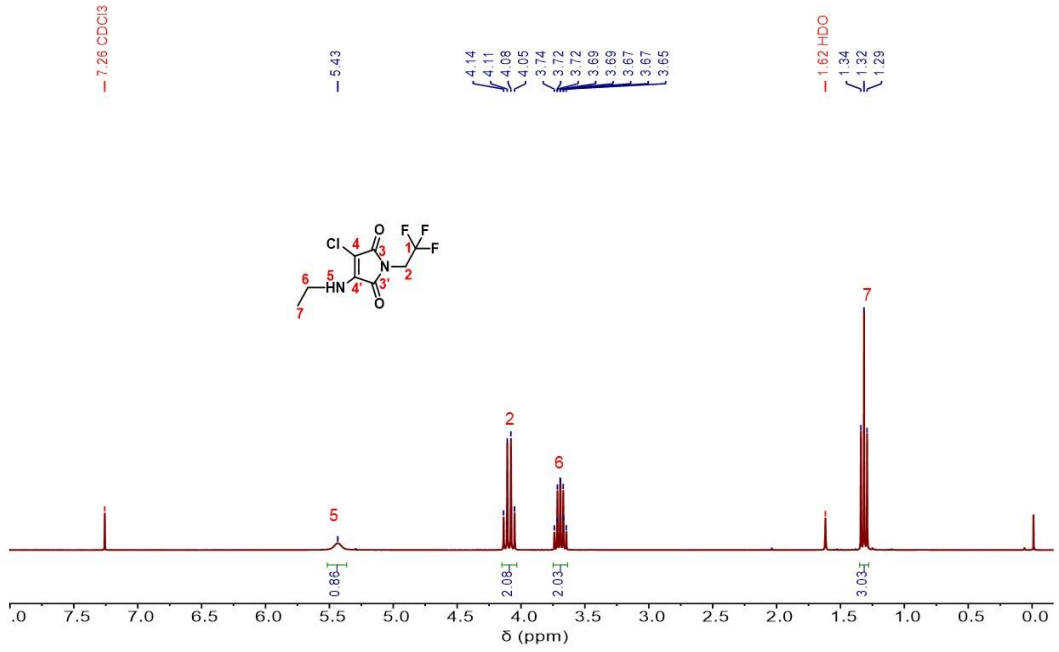

Fig. 2.25 ^{1}H NMR spectrum of **2.2** (400 MHz, $CDCl_3$).

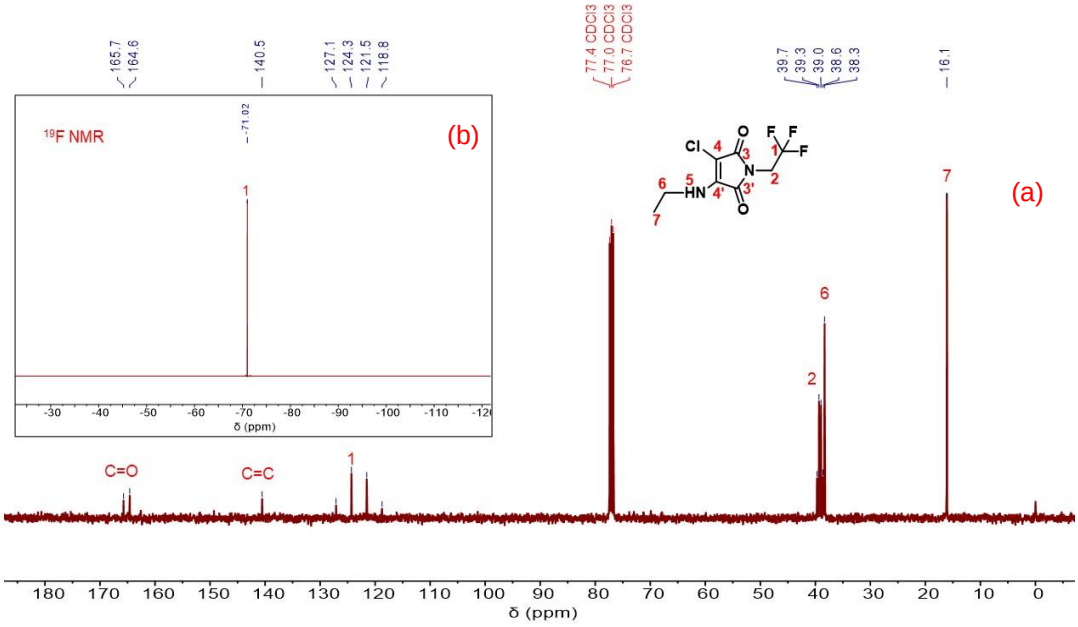

Fig. 2.26 ^{13}C (a) and ^{19}F (b) NMR spectra of **2.2** (101 and 300 MHz respectively, $CDCl_3$).

3,4-dichloro-1-ethyl-1*H*-pyrrole-2,5-dione (2.3)

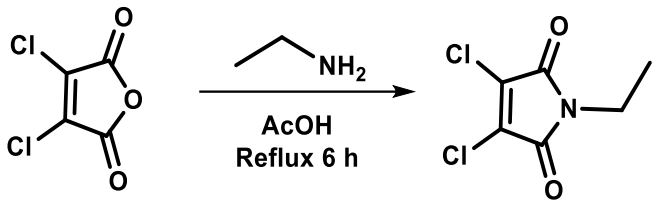

2.3 (70%)

R_f = 0.56 (hexane: ethyl acetate 3:1), Yield = 813 mg, 70%.

^1H NMR (400 MHz, $CDCl_3$, 25°C, TMS) δ [ppm] = 3.70 – 3.63 (q, 2H, H2), 1.23 - 1.21 (t, 3H, H1).

^{13}C NMR (101 MHz, $CDCl_3$, 25°C, TMS) δ [ppm] = 162.7 (C=O), 133.1 (C=C), 34.2 (C2), 13.6 (C1).

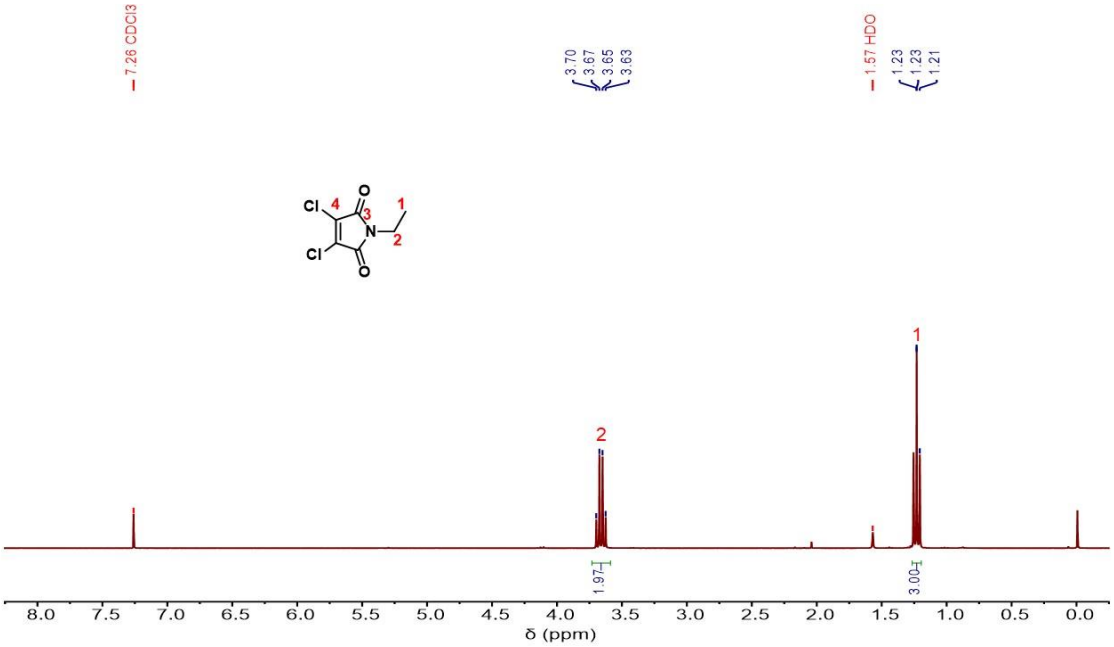

Fig. 2.27 ^{1}H NMR spectrum of **2.3** (400 MHz, $CDCl_3$).

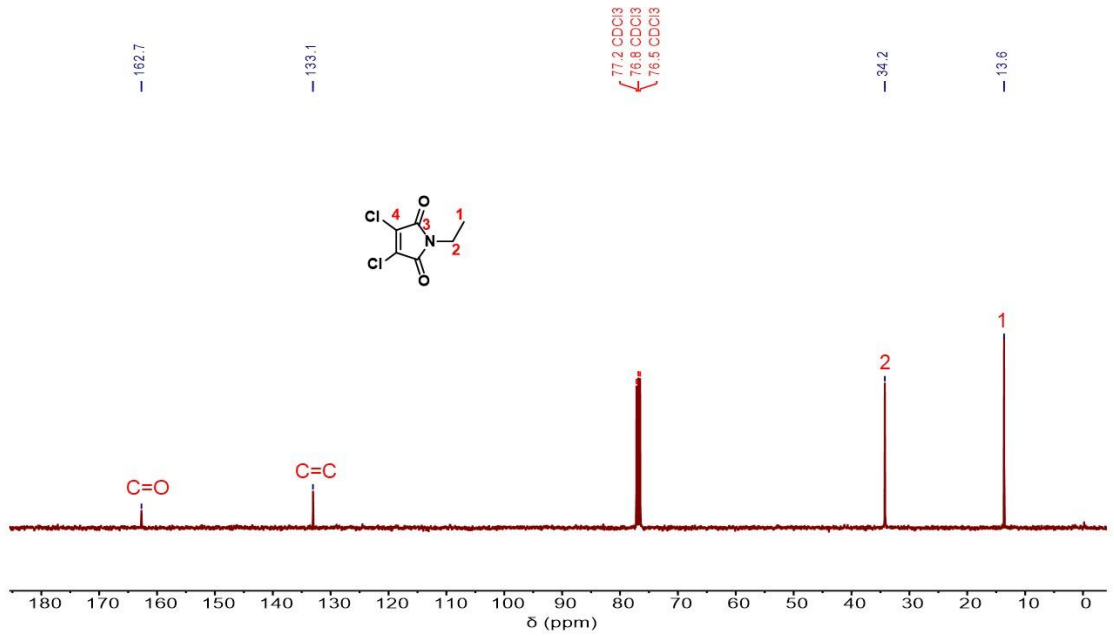

Fig. 2.28 ^{13}C NMR spectrum of **2.3** (101 MHz, $CDCl_3$).

3-chloro-1-ethyl-4-((2,2,2-trifluoroethyl)amino)-1*H*-pyrrole-2,5-dione (2.4)

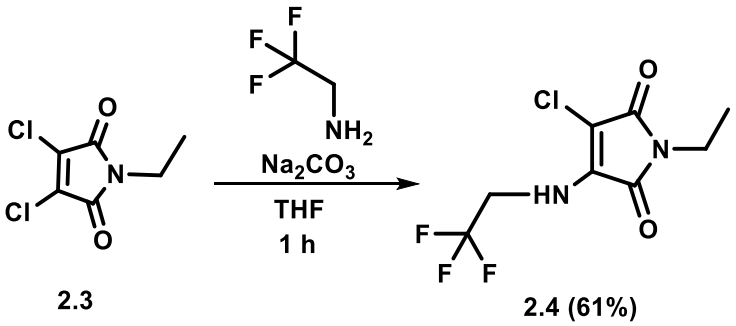

2.3 2.4 (61%)

R_f = 0.60 (hexane: ethyl acetate 2:1), Yield = 646 mg, 61%.

^{1}H NMR (400 MHz, $CDCl_3$, 25°C, TMS) δ [ppm] =5.45 (s, 1H, H5), 4.27 - 4.19 (m, 2H, H6), 3.59–3.54 (q, 2H, H2), 1.21–1.17 (t, 3H, H1).

^{13}C NMR (101 MHz, $CDCl_3$, 25°C, TMS) δ [ppm] = 166.8, 165.1 (C=O), 138.7 (C=C), 127.7 - 119.3 (C7), 44.6 – 43.5 (C6), 33.6 (C2), 13.9 (C1).

^{19}F NMR (400 MHz, $CDCl_3$, 25°C, $CFCl_3$) δ [ppm] = -72.90.

HR-MS (MaXis) $[M+Na]^+$ - *m/z* found 279.0225; *m/z* calculated 279.0226.

FTIR (cm^{-1}): ν = 3336 (N-H), 2942 (C-H), 1770,1714 (C=O), 1649 (C=C).

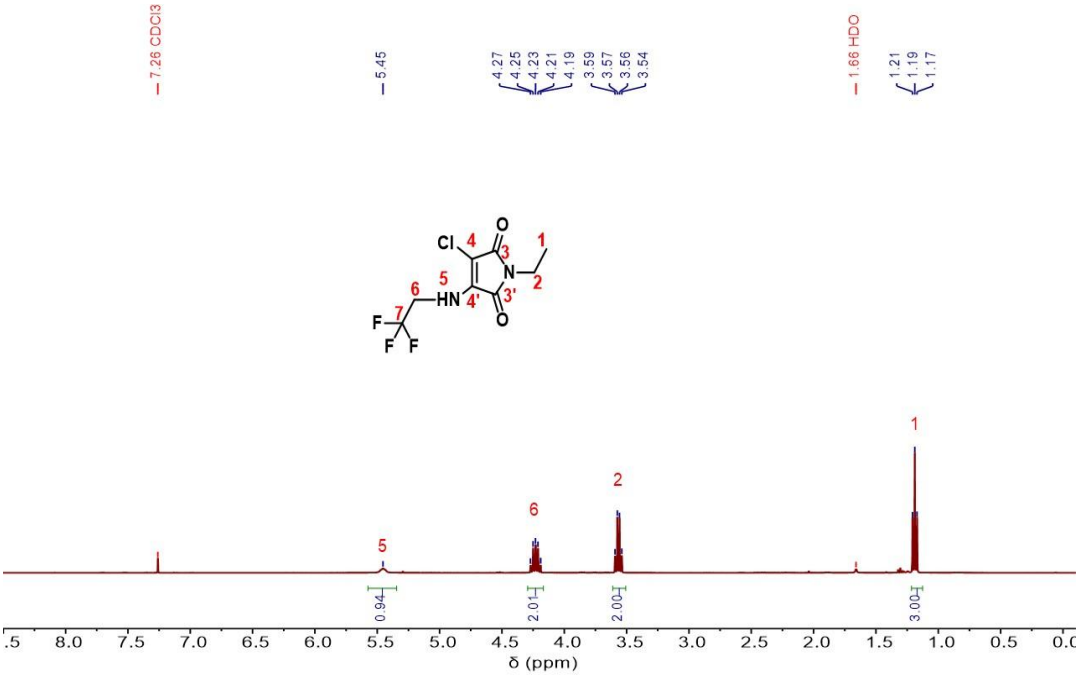

Fig 2.29 ^{1}H NMR spectrum of **2.4** (400 MHz, $CDCl_3$).

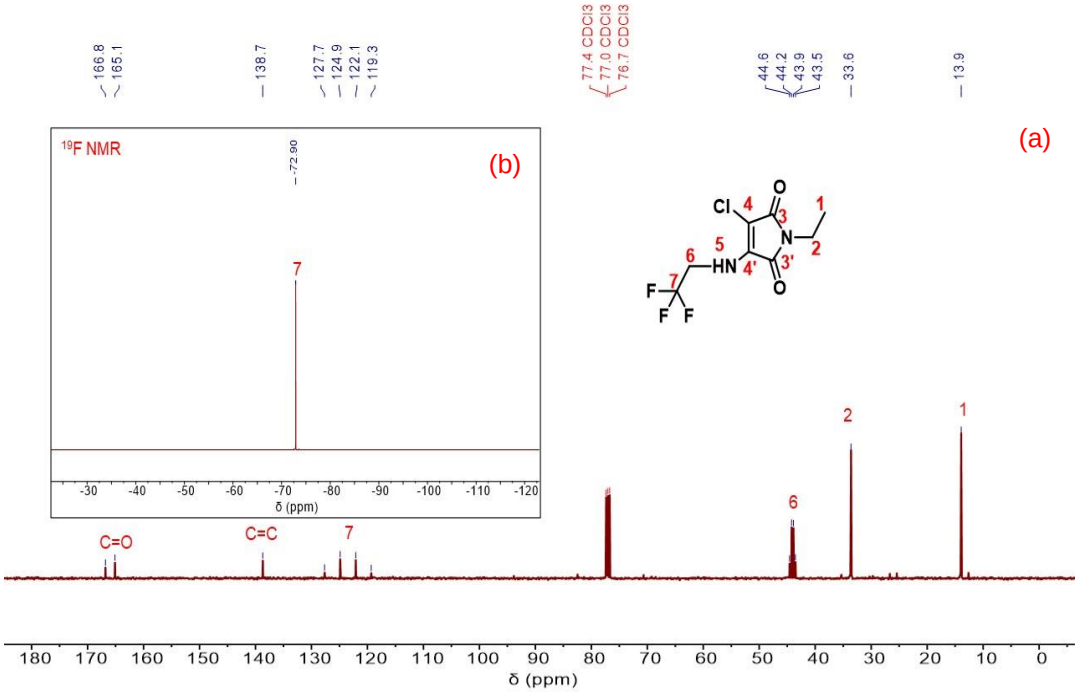

Fig. 2.30 ^{13}C (a) and ^{19}F (b) NMR spectra of **2.4** (101 and 300 MHz respectively, $CDCl_3$).

3-chloro-4-(isopropylamino)-1-(2,2,2-trifluoroethyl)-1*H*-pyrrole-2,5-dione (2.5)

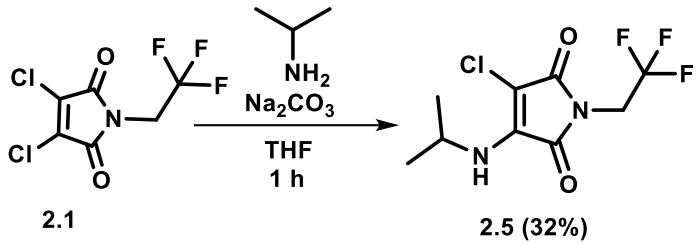

2.1 2.5 (32%)

R_f = 0.65 (hexane: ethyl acetate 2:1), Yield = 450 mg, 32%.

^{1}H NMR (400 MHz, $CDCl_3$, 25°C, TMS) δ [ppm] = 4.36 – 4.30 (m, 1H, H6), 4.13 – 4.06 (q, 2H, H2), 1.32–1.30 (d, 6H, H7).

^{13}C NMR (101 MHz, $CDCl_3$, 25°C, TMS) δ [ppm] = 165.8, 164.7 (C=O), 140.5 (C=C), 127.1–118.8 (C1), 45.3 (C6), 39.7–38.6 (C2), 23.8 (C7).

^{19}F NMR (400 MHz, $CDCl_3$, 25°C, $CFCl_3$) δ [ppm] = -71.01.

HR-MS (MaXis) $[M+Na]^+$ - *m/z* found 292.9422; *m/z* calculated 292.9423.

FTIR (cm^{-1}): ν = 3268 (N-H), 2977 (C-H), 1766,1714 (C=O), 1628 (C=C).

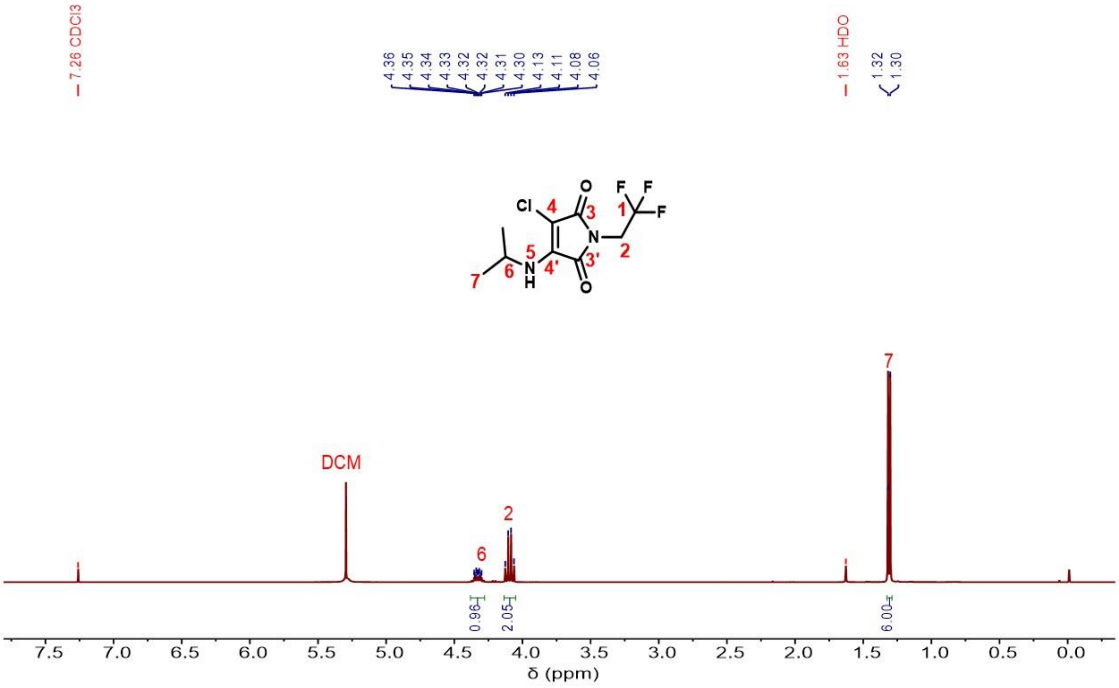

Fig. 2.31 ^{1}H NMR spectrum of **2.5** (400 MHz, $CDCl_3$).

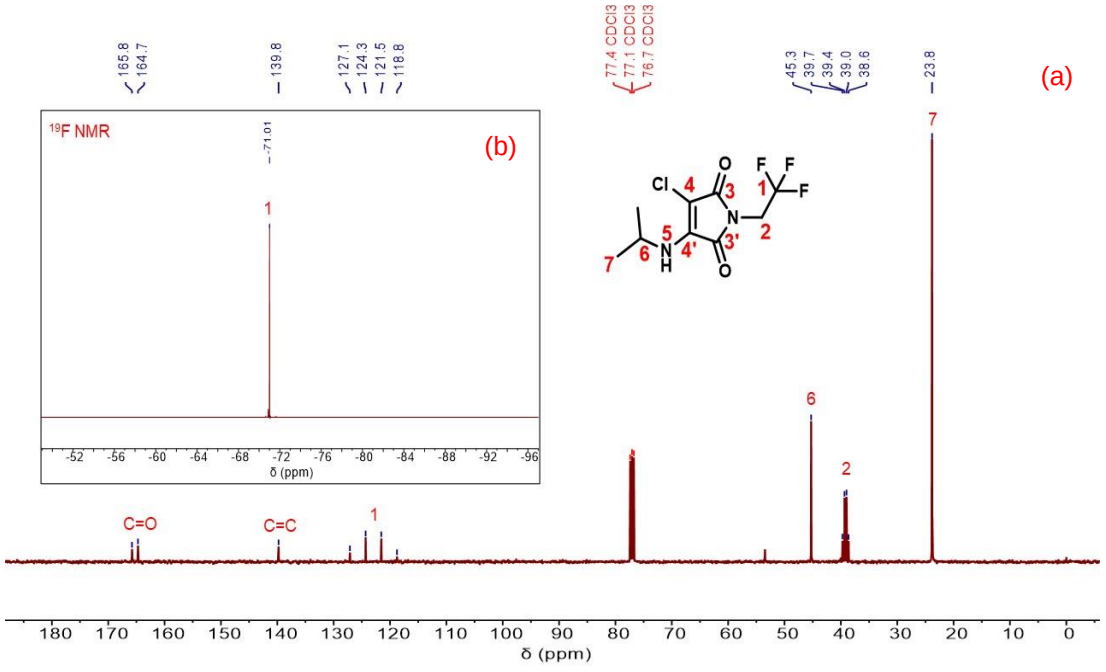

Fig. 2.32 ^{13}C (a) and ^{19}F (b) NMR spectra of **2.5** (101 and 300 MHz respectively, $CDCl_3$).

2.5.3 Synthesis of aminochloromaleimides *via* route-II

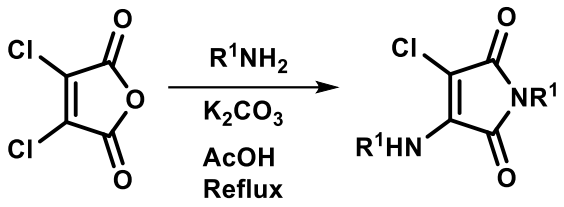

$R^1 = CH_2CH_3, CH_2CF_3$

Double substitution of dichloromaleic anhydride was achieved in single step, with a slight divergence from the previously reported protocol.[16] 2.0 equiv. of the targeted amine was added to a solution of acetic acid (20–25 mL) containing 1.0 equiv. of 3,4-dichloromaleic anhydride and 1.5 equiv. of potassium carbonate. The reaction mixture was stirred for 4–6 h at reflux temperature (80°C). After 6 h, the solvent was evaporated under reduced pressure and the residue was taken up with 150 mL of CH_2Cl_2. The resultant mixture was washed with 2×150 mL of water, and dried with magnesium sulfate. A yellow solid was obtained after purification *via* column chromatography on silica gel using *n*-hexane /ethyl acetate.

3-chloro-1-(2,2,2-trifluoroethyl)-4-((2,2,2-trifluoroethyl)amino)-1*H*-pyrrole-2,5-dione (2.6)

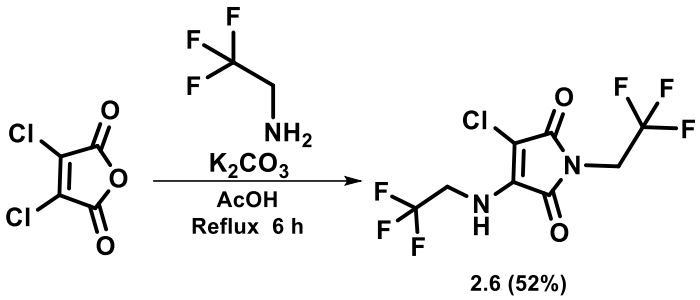

2.6 (52%)

R_f = 0.55 (hexane: ethyl acetate 2:1), Yield = 967 mg, 52%.

^{1}H NMR (400 MHz, $CDCl_3$, 25°C, TMS) δ [ppm] =5.46 (s, 1H, H5), 4.30 – 4.24 (m, 2H, H6), 4.15 – 4.10 (q, 2H, H2).

^{13}C NMR (101 MHz, $CDCl_3$, 25°C, TMS) δ [ppm] = 165.3, 164.5 (C=O), 139.6 (C=C), 127.9 – 119.0 (C7,C1), 45.1 – 44.0 (C2), 40.3 – 39.2 (C6).

^{19}F NMR (300 MHz, $CDCl_3$, 25°C, $CFCl_3$) δ [ppm] = -71.00, -72.83.

HR-MS (MaXis) $[M+Na]^+$ - *m/z* found 333.5104; *m/z* calculated 333.5103.

FTIR (cm^{-1}): ν = 3267 (N-H), 2976 (C-H), 1765, 1718 (C=O), 1627 (C=C).

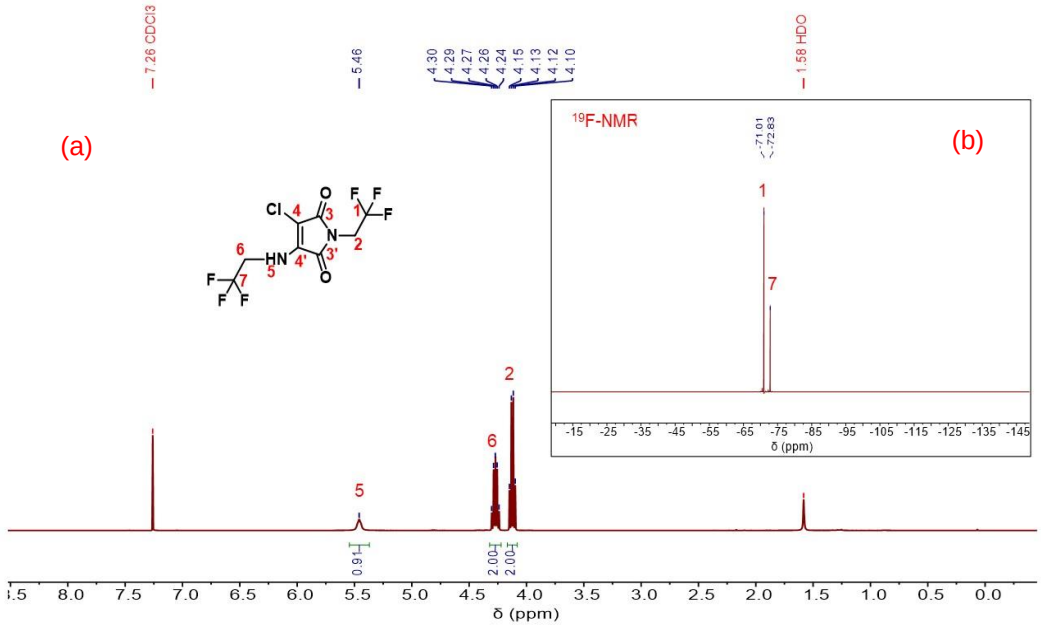

Fig. 2.33 ^{1}H (a) and ^{19}F (b) NMR spectra of **2.6** (400 and 300 MHz respectively, $CDCl_3$).

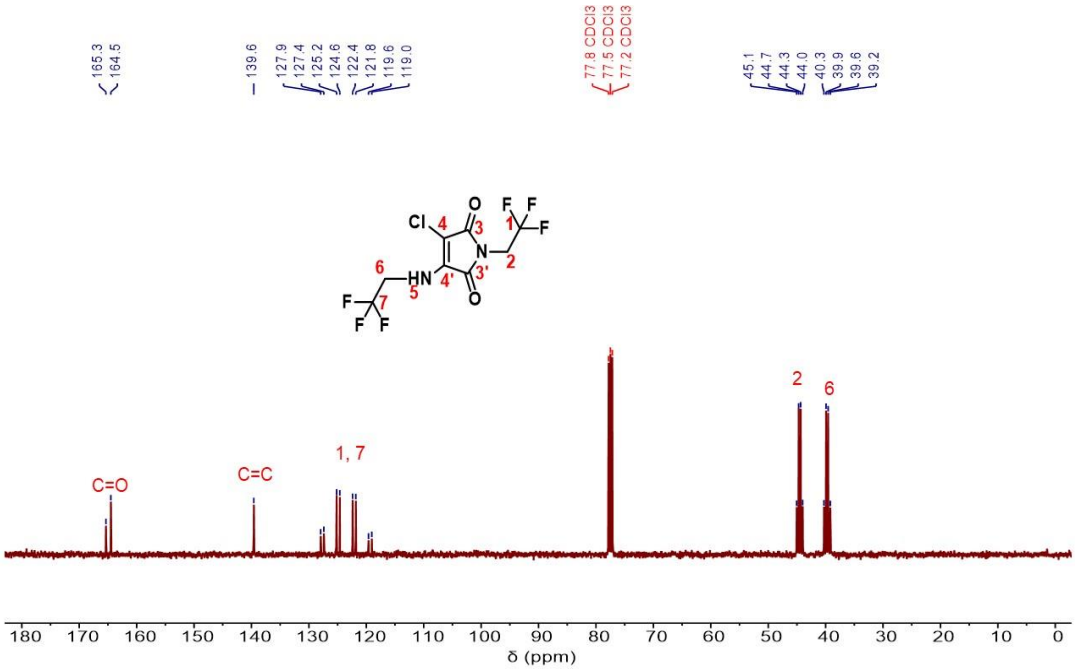

Fig. 2.34 ^{13}C NMR spectrum of **2.6** (101 MHz, $CDCl_3$).

3-chloro-1-ethyl-4-(ethylamino)-1*H*-pyrrole-2,5-dione (2.7)

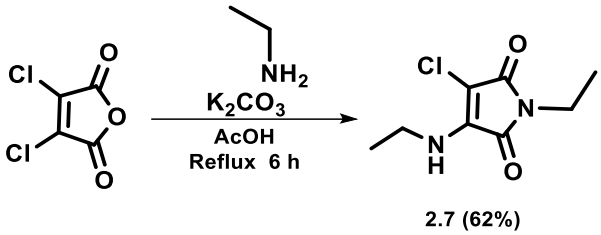

2.7 (62%)

R_f = 0.56 (hexane: ethyl acetate 2:1), Yield = 750 mg, 62%.

^{1}H NMR (400 MHz, $CDCl_3$, 25°C, TMS) δ [ppm] = 5.37 (s, 1H, H5), 3.67 – 3.60 (m, 2H, H6), 3.55 – 3.50 (q, 2H, H2), 1.30 – 1.26 (t, 3H, H1), 1.17 – 1.14 (t, 3H, H7).

^{13}C NMR (101 MHz, $CDCl_3$, 25°C, TMS) δ [ppm] = 167.8, 165.6 (C=O), 140.3 (C=C), 38.1 (C2), 33.3 (C6), 16.1 (C1), 14.0 (C7).

HR-MS (MaXis) $[M+Na]^+$ - *m/z* found 225.6403, *m/z* calculated 225.6402.

FTIR (cm^{-1}): ν = 3324 (N-H), 2964 (C-H), 1766, 1710 (C=O), 1636 (C=C).

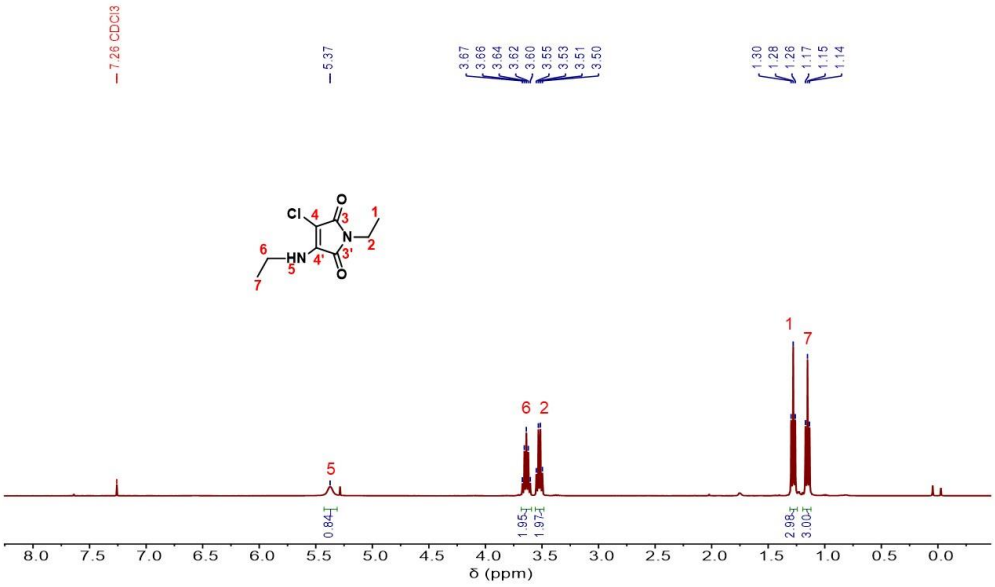

Fig. 2.35 ^{1}H NMR spectrum of **2.7** (400 MHz, $CDCl_3$).

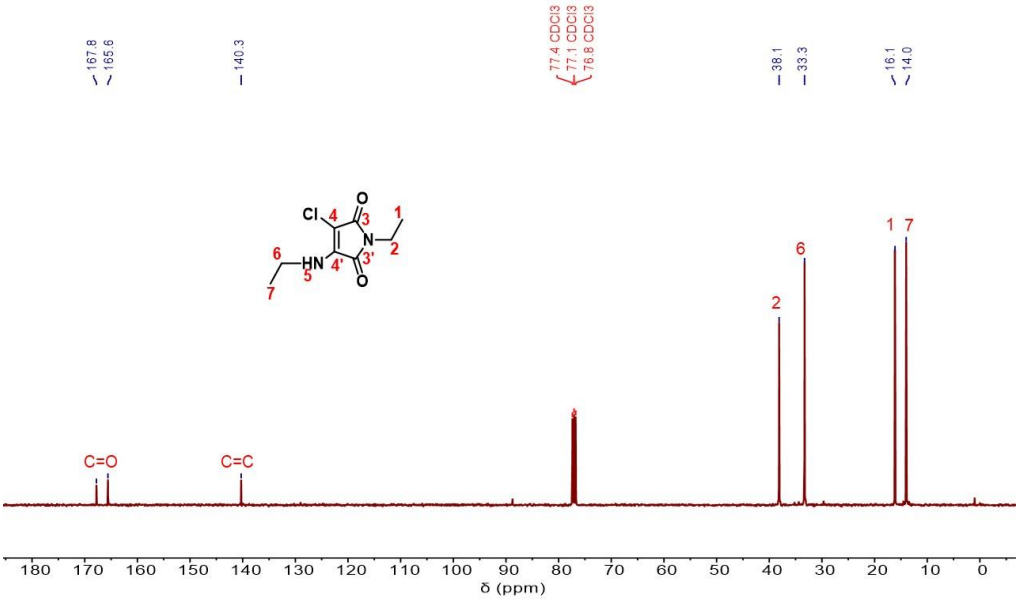

Fig. 2.36 ^{13}C NMR spectrum of **2.7** (101 MHz, $CDCl_3$).

2.5.4 Synthesis of monoaminomaleimides *via* route-I

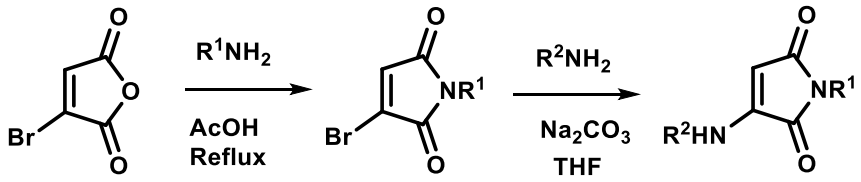

R^1 R^2 = CH_2CH_3, CH_2CF_3

Step-I: *N*-functionalization of monobromomaleimide was carried out according to the protocol established by a previous paper.[72] 1.0 equiv. of 3-bromomaleic anhydride was dissolved in 20 mL of acetic acid, followed by the dropwise addition of 1.0 equiv. of the required amine. The solution was then refluxed at 110℃ for 12 h. After 12 h, the solvent was evaporated under reduced pressure. The white solid was obtained after purification *via* column chromatography using *n*-hexane/ethyl acetate.

Step-II: In the next step, amine substitution of the bromomaleimide was achieved, following the previously reported protocol.[16] 1.0 equiv. of *N*-functionalized 3-bromomaleimide, obtained from Step-I, was dissolved in 20–25 mL THF and mixed with 2.5 equiv. of sodium carbonate. The mixture was allowed to react with 1.0–1.5 equiv. of the targeted amine at room temperature. Reaction progress was monitored by TLC and was complete within 2–3 h. The solvent was evaporated under reduced pressure and the residue was taken up with ~150 mL of CH_2Cl_2, washed with 2×150 mL of water, and dried over magnesium sulfate. Purification *via* column chromatography on silica gel with n-hexane/ethyl acetate resulted in a yellow fluorescent solid.

3-bromo-1-(2,2,2-trifluoroethyl)-1*H*-pyrrole-2,5-dione (2.8)

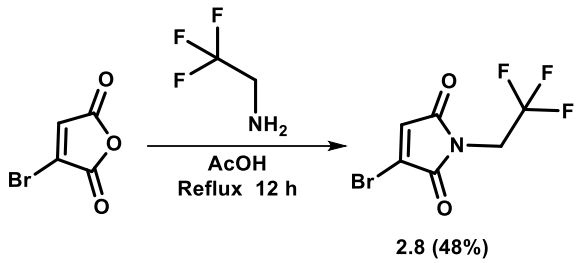

2.8 (48%)

R_f = 0.45 (hexane: ethyl acetate 3:1), Yield = 700 mg, 48%.

^{1}H NMR (400 MHz, $CDCl_3$, 25°C, TMS) δ [ppm] = 7.00 (s, 1H, H4), 4.22 – 4.13 (q, 2H, H2).

^{13}C NMR (101 MHz, $CDCl_3$, 25°C, TMS) δ [ppm] = 167.1 , 164.4 (C=O; 3,3'), 132.8 (C4), 132.4 (C4'), 127.4 – 119.0 (C1), 40.5 – 39.4 (C2).

^{19}F NMR (400 MHz, $CDCl_3$, 25°C, $CFCl_3$) δ [ppm] = -70.91.

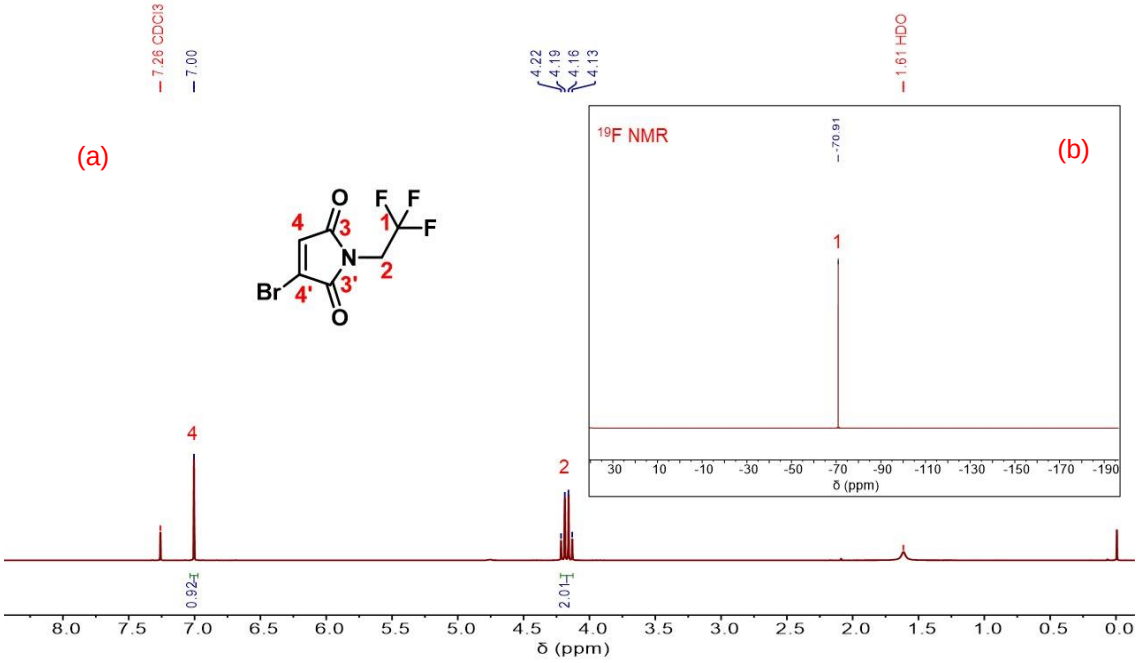

Fig. 2.37 ^{1}H (a) and ^{19}F (b) NMR spectra of **2.8** (400 and 300 MHz respectively, $CDCl_3$).

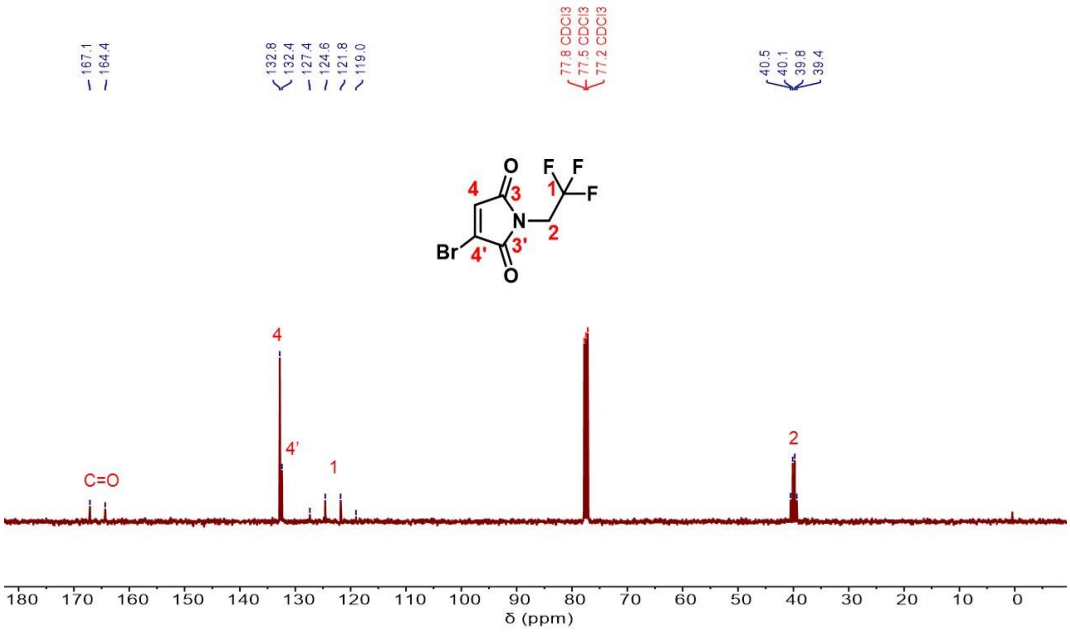

Fig. 2.38 ^{13}C NMR spectrum of **2.8** (101 MHz, CDCl3).

3-(ethylamino)-1-(2,2,2-trifluoroethyl)-1*H*-pyrrole-2,5-dione (2.9)

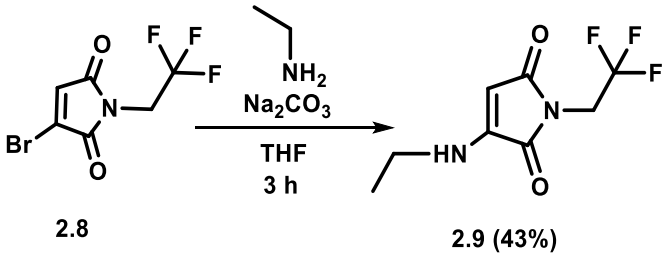

2.8 2.9 (43%)

R_f = 0.51 (hexane: ethyl acetate 2:1), Yield = 400 mg, 43%.

^{1}H NMR (400 MHz, $CDCl_3$, 25°C, TMS) δ [ppm] =5.52 (s, 1H, H5), 4.91 (s, 1H, H4), 4.12 – 4.03 (q, 2H, H2), 3.30 - 3.20 (m, 2H, H6), 1.32 - 1.27 (t, 3H, H7).

^{13}C NMR (101 MHz, $CDCl_3$, 25°C, TMS) δ [ppm] = 170.0, 166.5 (C=O; 3,3'), 149.1 (C4'), 127.4 – 119.0 (C1), 84.6 (C4), 39.2 (C6), 39.1 – 38.0 (C2), 13.7 (C7).

^{19}F NMR (400 MHz, $CDCl_3$, 25°C, $CFCl_3$) δ [ppm] = -71.03.

HR-MS (MaXis) $[M+Na]^+$ - *m/z* found 245.1712; *m/z* calculated 245.1710.

FTIR (cm^{-1}): ν = 3263 (N-H), 2957 (C-H), 1761,1702 (C=O), 1613 (C=C).

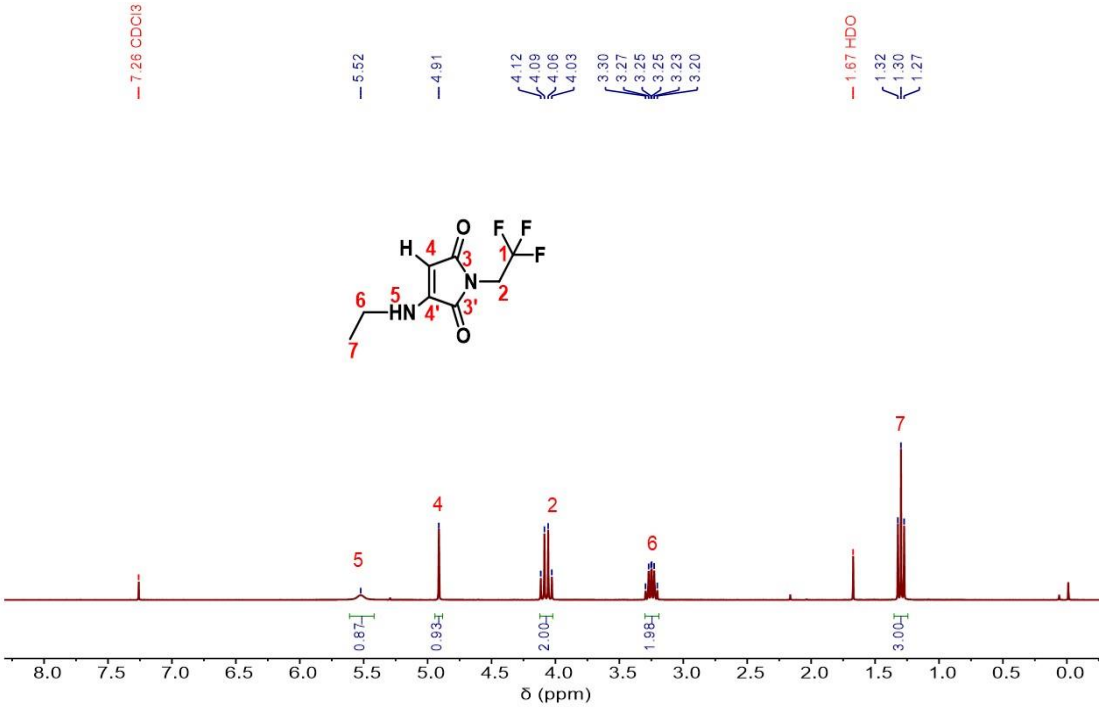

Fig. 2.39 ^{1}H NMR spectrum of **2.9** (400 MHz, $CDCl_3$).

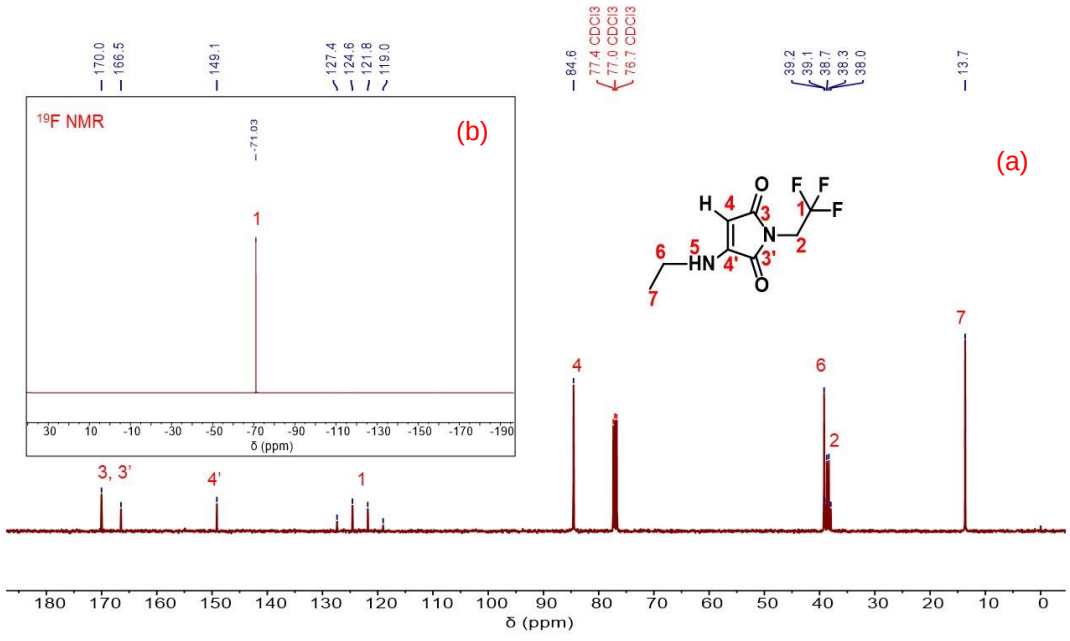

Fig. 2.40 ^{13}C (a) and ^{19}F (b) NMR spectra of **2.9** (101 and 300 MHz respectively, $CDCl_3$).

3-bromo-1-ethyl-1*H*-pyrrole-2,5-dione (2.10)

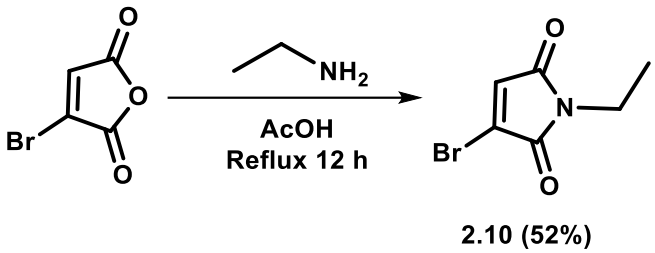

2.10 (52%)

R_f = 0.58 (hexane: ethyl acetate 3:1), Yield =600 mg, 52%.

^{1}H NMR (400 MHz, $CDCl_3$, 25°C, TMS) δ [ppm] = 6.83 (s, 1H, H4), 3.60 – 3.55 (q, 2H, H2), 1.17 - 1.14 (t, 3H, H1).

^{13}C NMR (101 MHz, $CDCl_3$, 25°C, TMS) δ [ppm] = 168.4 , 165.2 (C=O; 3,3'), 131.9 (C4), 131.3 (C4'), 33.8 (C2), 13.8 (C1).

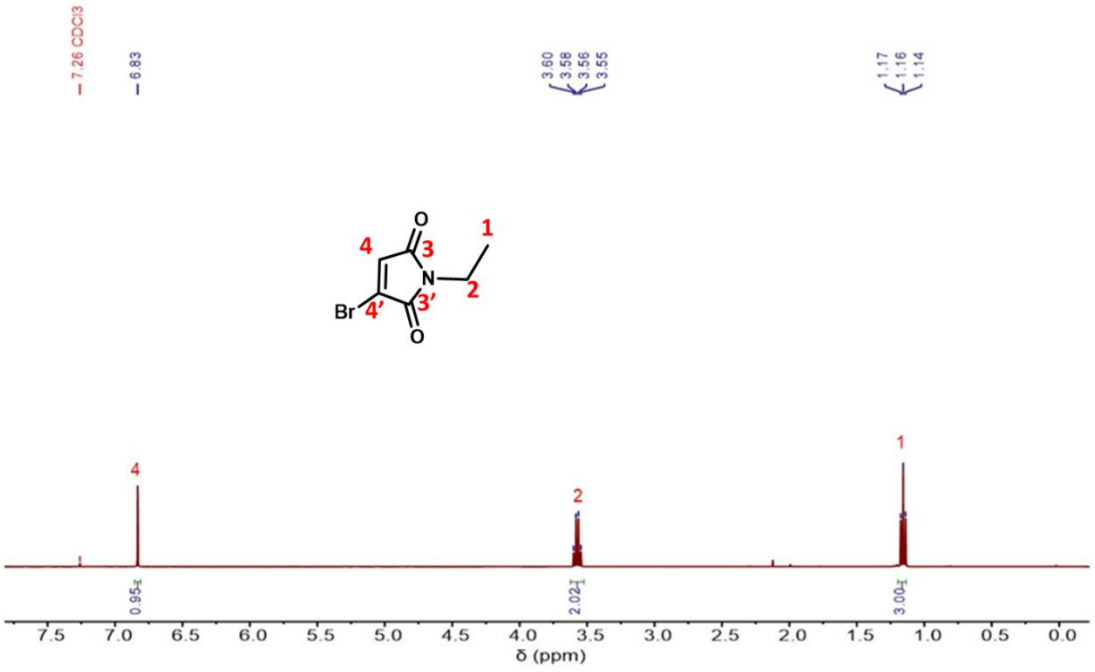

Fig. 2.41 ^{1}H NMR spectrum of **2.10** (400 MHz, $CDCl_3$).

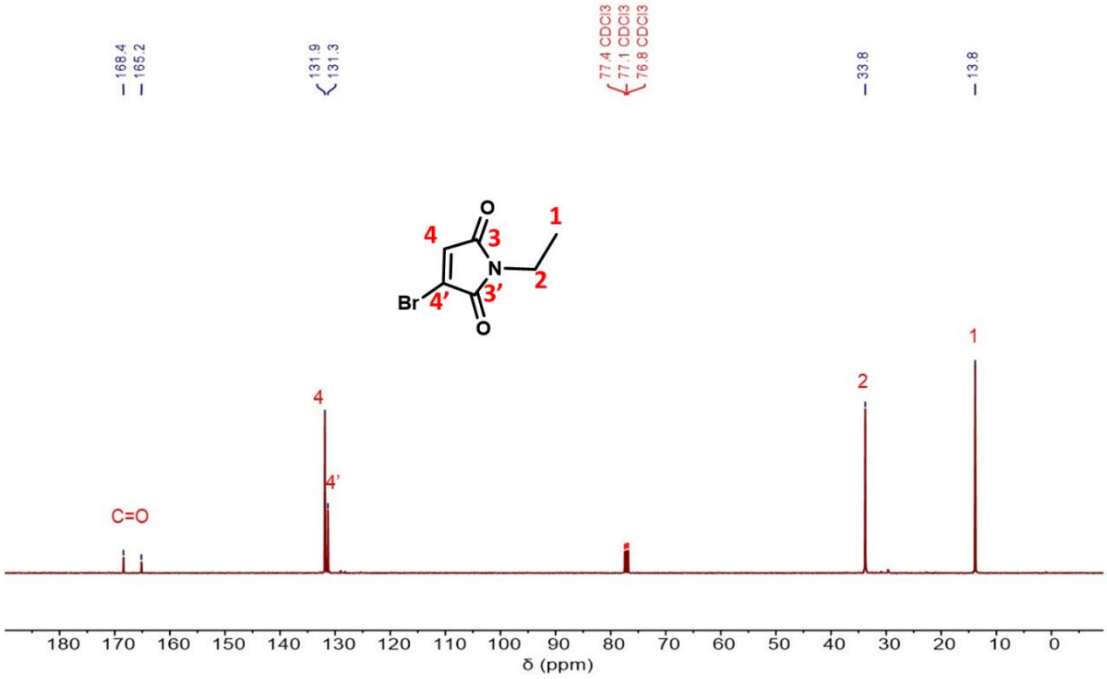

Fig. 2.42 ^{13}C NMR spectrum of **2.10** (101 MHz, $CDCl_3$).

1-ethyl-3-((2,2,2-trifluoroethyl)amino)-1*H*-pyrrole-2,5-dione (2.11)

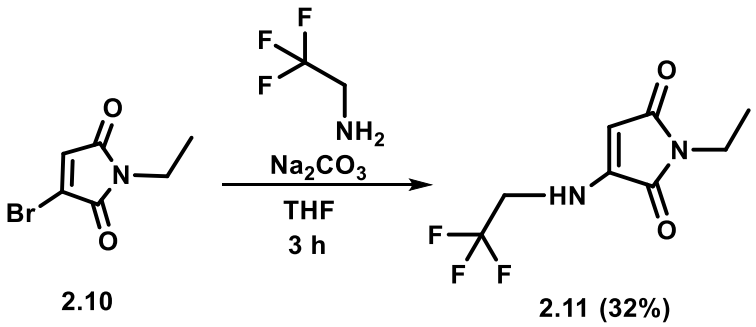

R_f = 0.49 (hexane: ethyl acetate 2:1), Yield =350 mg, 32%.

^{1}H NMR (400 MHz, $CDCl_3$, 25°C, TMS) δ [ppm] = 5.55 (s, 1H, H5), 5.03 (s, 1H, H4), 3.81 – 3.70 (m, 2H, H6), 3.57 - 3.50 (q, 2H, H2), 1.20 - 1.16 (t, 3H, H1).

^{13}C NMR (101 MHz, $CDCl_3$, 25°C, TMS) δ [ppm] = 171.8, 167.1 (C=O, 3,3'), 148.3 (C4'), 128.2 – 119.2 (C7), 88.2 (C4), 46.5 – 45.5 (C6), 32.8 (C2), 14.1 (C1).

^{19}F NMR (300 MHz, $CDCl_3$, 25°C, $CFCl_3$) δ [ppm] = -71.57.

HR-MS (MaXis) $[M+Na]^+$ - *m/z* found 245.1310; *m/z* calculated 245.1312.

FTIR (cm^{-1}): ν = 3254 (N-H), 2914 (C-H), 1770, 1698 (C=O), 1629 (C=C).

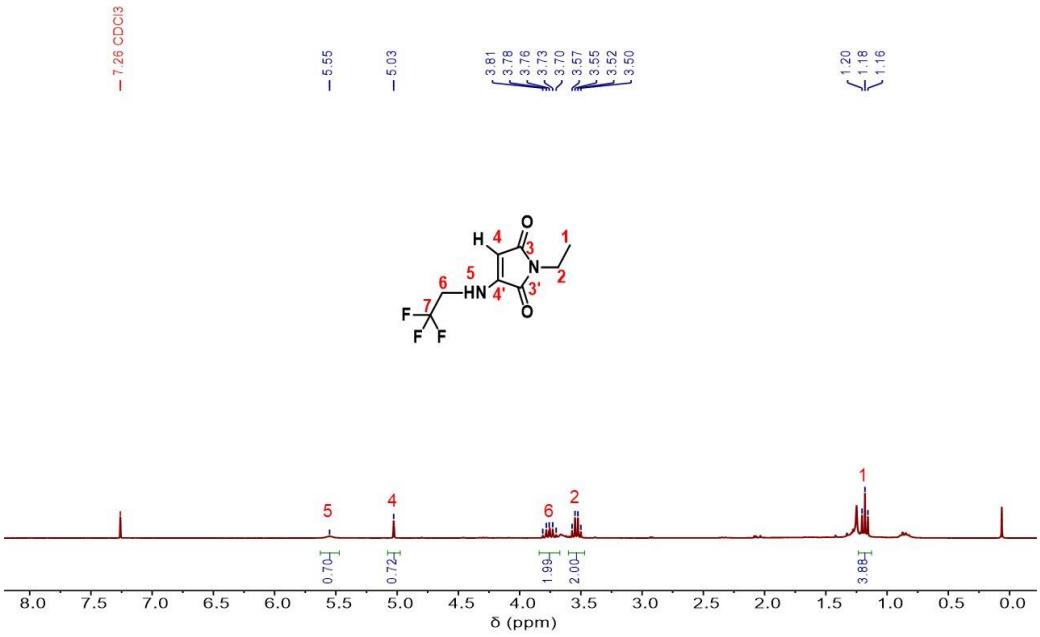

Fig. 2.43 ^{1}H NMR spectrum of **2.11** (400 MHz, $CDCl_3$).

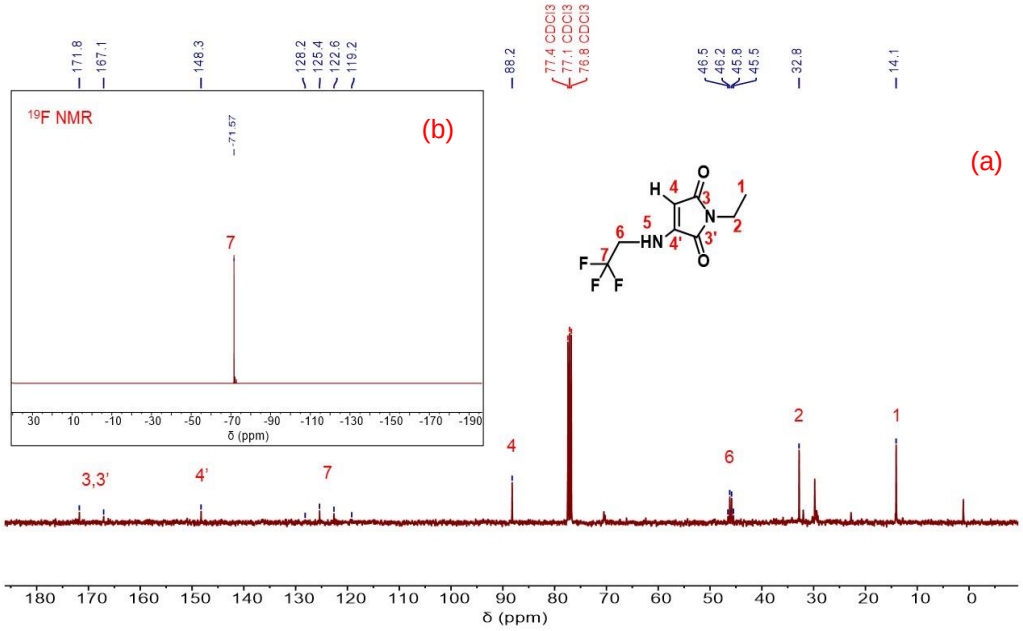

Fig. 2.44 ^{13}C (a) and ^{19}F (b) NMR spectra of **2.11** (101 and 300 MHz respectively, $CDCl_3$).

3-(isopropylamino)-1-(2,2,2-trifluoroethyl)-1*H*-pyrrole-2,5-dione (2.12)

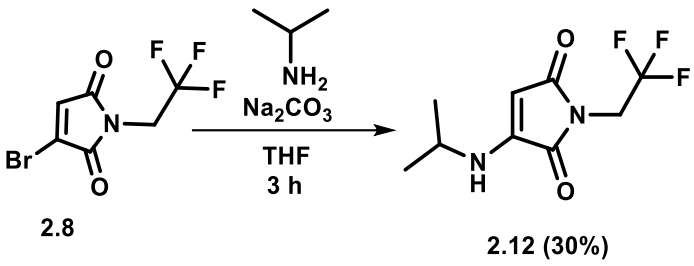

R_f = 0.51 (hexane: ethyl acetate 2:1), Yield = 350 mg, 30%.

^1H NMR (400 MHz, $CDCl_3$, 25°C, TMS) δ [ppm] = 5.50 (s, 1H, H5), 4.88 (s, 1H, H4), 4.10 – 4.02 (q, 2H, H2), 3.58 - 3.47 (m, 1H, H6), 1.28 - 1.26 (d, 6H, H7).

^{13}C NMR (101 MHz, $CDCl_3$, 25°C, TMS) δ [ppm] = 170.1, 166.7 (C=O, 3,3'), 148.1 (C4'), 127.4 – 119.0 (C1), 84.3 (C4), 46.5 (C6), 39.1 – 38.0 (C2), 21.7 (C7).

^{19}F NMR (300 MHz, $CDCl_3$, 25°C, $CFCl_3$) δ [ppm] = -70.99.

HR-MS (MaXis) $[M+Na]^+$ - *m/z* found 259.0802, *m/z* calculated 259.0806.

FTIR (cm^{-1}): ν = 3264 (N-H), 2969 (C-H), 1762, 1697 (C=O), 1610 (C=C).

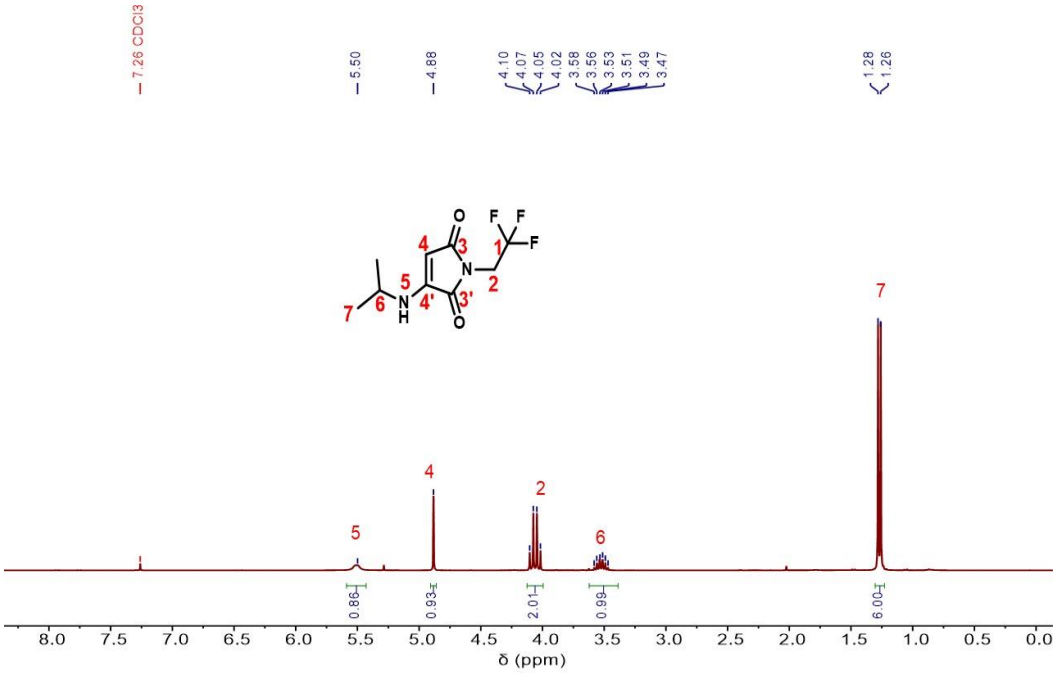

Fig. 2.45 ^{1}H NMR spectrum of **2.12** (400 MHz, $CDCl_3$).

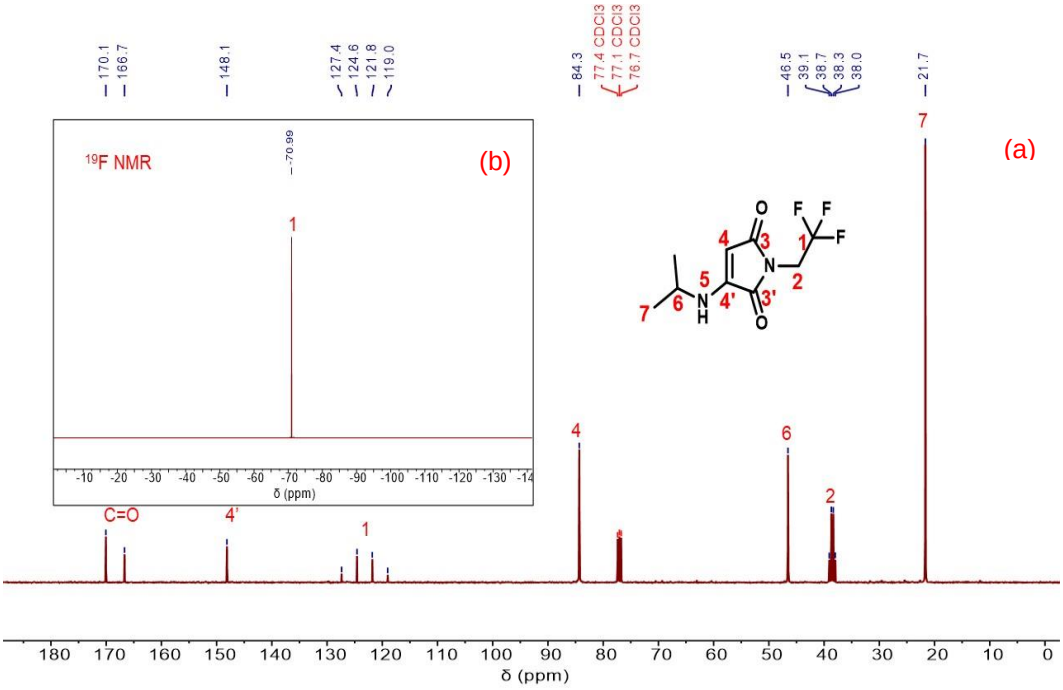

Fig. 2.46 ^{13}C (a) and ^{19}F (b) NMR spectra of **2.12** (101 and 300 MHz respectively, $CDCl_3$).

2.5.5 Synthesis of monoaminomaleimides *via* route-II

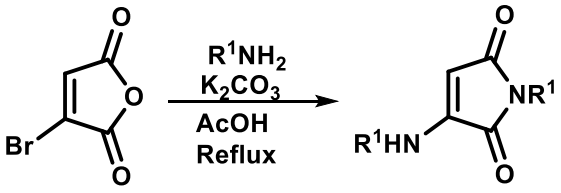

$R^1 = CH_2CH_3, CH_2CF_3$

Double substitution of monobromomaleic anhydride was achieved in single step, with a slight divergence from the previously reported protocol.[16] 2.0 equiv. of the targeted amine was added to a solution of acetic acid (20–25 mL) containing 1.0 equiv. of 3-bromomaleic anhydride and 1.5 equiv. of potassium carbonate. The reaction mixture was stirred for 12 h at reflux temperature (110℃). After 12 h, the solvent was

evaporated under reduced pressure, and the residue was taken up with 150 mL of CH_2Cl_2. The resultant mixture was washed with 2×150 mL of water, and dried over magnesium sulfate. A yellow-orange solid was obtained after purification *via* column chromatography on silica gel using *n*-hexane /ethyl acetate.

1-(2,2,2-trifluoroethyl)-3-((2,2,2-trifluoroethyl)amino)-1*H*-pyrrole-2,5-dione (2.13)

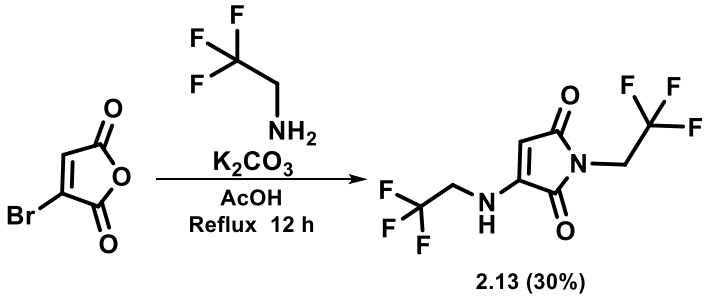

2.13 (30%)

R_f = 0.48 (hexane: ethyl acetate 2:1), Yield = 500 mg, 30%.

^{1}H NMR (400 MHz, $CDCl_3$, 25°C, TMS) δ [ppm] = 5.71 (s, 1H, H5), 5.18 (s, 1H, H4), 4.14 – 4.05 (q, 2H, H2), 3.85 – 3.74 (m, 2H, H6)

^{13}C NMR (101 MHz, $CDCl_3$, 25°C, TMS) δ [ppm] = 169.3, 166.0 (C=O, 3,3'), 148.3 (C4'), 128.0 - 119.6 (C7, C1), 88.8 (C4), 46.5 - 45.4 (C2), 39.3 - 38.2 (C6).

^{19}F NMR (300 MHz, $CDCl_3$, 25°C, $CFCl_3$) δ [ppm] = -71.00, -71.45.

HR-MS (MaXis) $[M+Na]^+$ - *m/z* found 299.0302; *m/z* calculated 299.0305.

FTIR (cm^{-1}): ν = 3256 (N-H), 3043 (C-H), 1766, 1705 (C=O), 1628 (C=C).

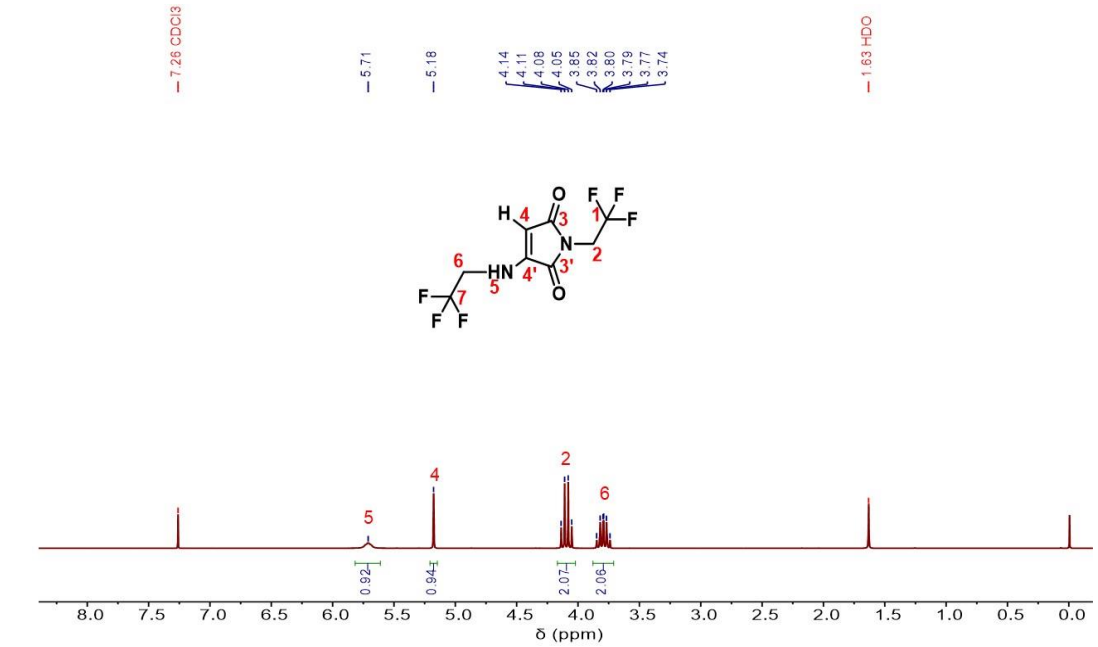

Fig. 2.47 ^{1}H NMR spectrum of **2.13** (400 MHz, $CDCl_3$).

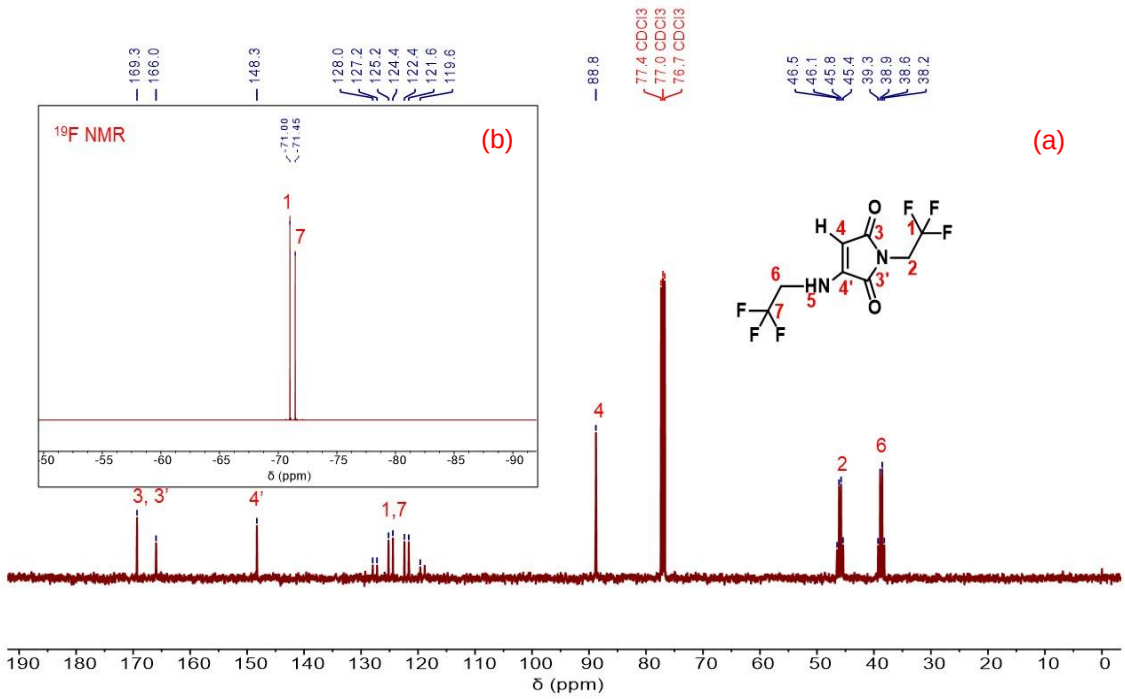

Fig. 2.48 ^{13}C (a) and ^{19}F (b) NMR spectra of **2.13** (101 and 300 MHz respectively, $CDCl_3$).

1-ethyl-3-(ethylamino)-1*H*-pyrrole-2,5-dione (2.14)

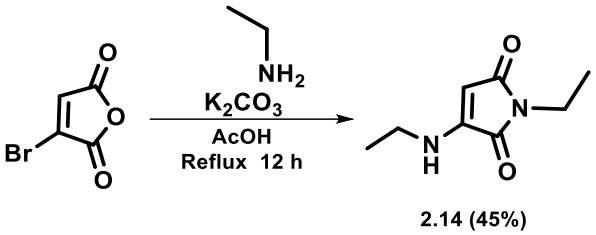

2.14 (45%)

R_f = 0.51 (hexane: ethyl acetate 2:1), Yield = 430 mg, 45%.

^{1}H NMR (400 MHz, $CDCl_3$, 25°C, TMS) δ [ppm] = 5.41 (s, 1H, H5), 3.72 – 3.65 (m, 2H, H6), 3.58 – 3.53 (q, 2H, H2), 2.17 (s, 1H, H4), 1.31 – 1.28 (t, 3H, H1), 1.19 – 1.15 (t, 3H, H7).

^{13}C NMR (101 MHz, $CDCl_3$, 25°C, TMS) δ [ppm] = 168.3, 166.4 (C=O, C3,3'), 143.5 (C4'), 123.8 (C4), 38.5 (C2), 34.0 (C6), 16.4 (C1), 14.4 (C7).

HR-MS (MaXis) $[M+Na]^+$ - *m/z* found 191.2012; *m/z* calculated 191.2011.

FTIR (cm^{-1}): ν = 3020 (N-H), 2932 (C-H),1690 (C=O), 1617 (C=C).

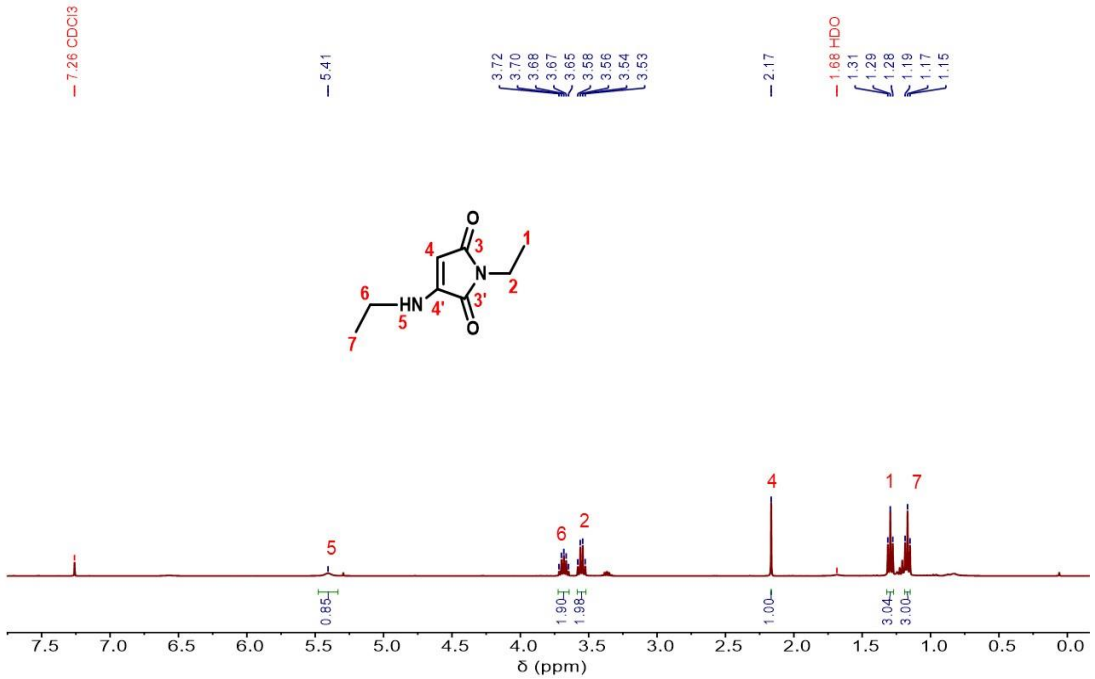

Fig. 2.49 ^{1}H NMR spectrum of **2.14** (400 MHz, $CDCl_3$).

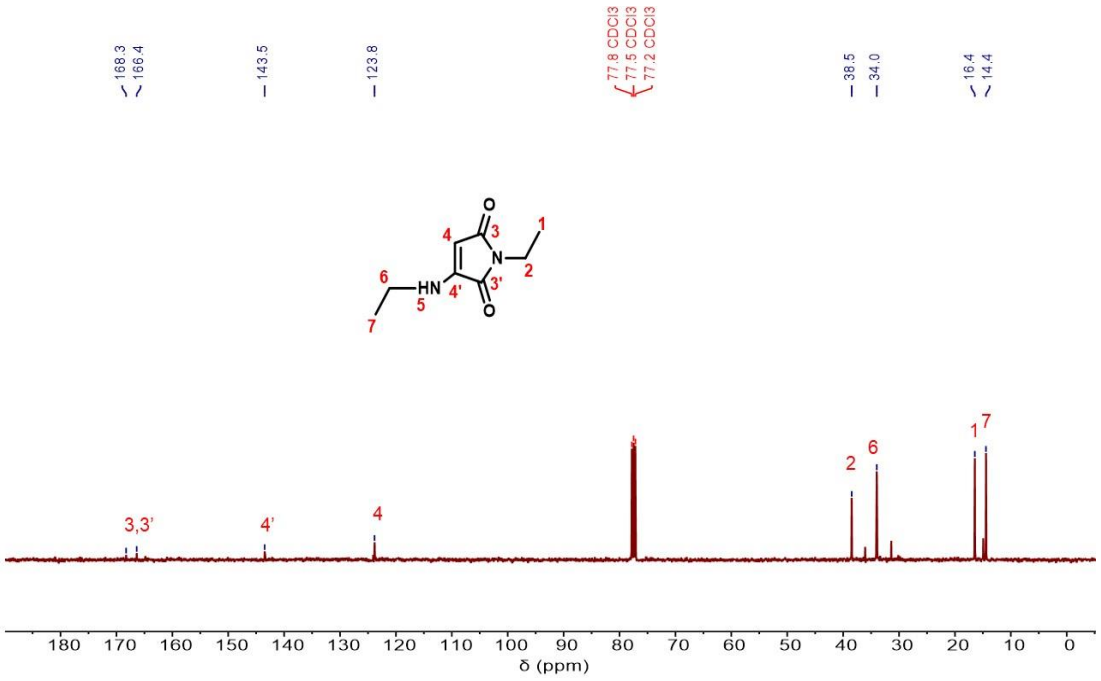

Fig. 2.50 ^{13}C NMR spectrum of **2.14** (101 MHz, $CDCl_3$).

2.5.6 Computational Details*

The geometries for all studied systems in the ground state were fully optimized with the CAM-B3LYP functional[73] and the 6-311G(d,p) basis set.[74, 75] The dispersion effects and the solvent were included in the optimization process. The D3-Grimme's dispersion[76] with Becke-Johnson damping factor[77, 78] was used to evaluate the dispersion effects. The solvent was considered using the polarization continuum model (PCM).[79, 80] The calculations were performed using the same solvents as in the experiments; i.e., 1,4-dioxane (ε=2.2099), toluene (ε=2.3741), diethyl ether (ε=4.24), tetrahydrofuran (ε=7.4257), methanol (ε=32.613), and dimethyl sulfoxide (ε=46.826). The harmonic vibrational frequencies were also calculated at the same level of theory in order to verify that all the stationary points are minima of their potential energy surface. Additionally, in the protic solvents (methanol and dimethyl sulfoxide), two explicit solvent molecules have been added. In all the systems, several conformers have been studied, but only the lowest minima have been reported.

The time-dependent density functional theory (TD-DFT)[81, 82] was applied to compute the absorption and emission (fluorescence) spectra. In the TD-DFT calculations, the first 40 excited states have been considered, although only the results of the first excitation have been displayed, which correspond to HOMO → LUMO transitions ($\pi \rightarrow \pi^*$). The charge distribution was obtained following the natural bond orbital (NBO) partition scheme by Weinhold and co-workers.[83] All geometry optimizations, frequencies, and TD-DFT calculations were calculated using the Gaussian 09 program package.[84]

*These studies were conducted by Dr. Miquel Torrent-Sucarrat.

To quantify the electron redistribution of the different substituents in the aminomaleimide derivative rings, two indices Q_{NBO1} and Q_{NBO2} have been defined, based on the sum of the natural population charges (see Eq. 2.1 and 2.2).

In the systems with two explicit solvent molecules, an additional third index has been evaluated, the sum of all natural population charges in the aminomaleimide molecule.

$$Q_{NBO3} = \sum_{i=1}^{Natoms} q_{NBO,Xi} \qquad \textbf{(Eq. 2.3)}$$

Finally, the non-covalent interactions (NCI) descriptor has been used to plot the π −stacking interactions. The NCI is a well-established methodology that allows the visualization of both attractive (van der Waals and hydrogen bonding) and repulsive (steric) interactions.[85] The NCI index is based on the electron density, $\rho\left(\vec{r}\right)$, and the reduced density gradient, $s\left(\vec{r}\right)$, which is defined as:

$$s\left(\vec{r}\right) = \frac{\left|\nabla\rho\left(\vec{r}\right)\right|}{2\left(3\pi^2\right)^{1/3}\rho\left(\vec{r}\right)^{4/3}} \qquad \textbf{(Eq. 2.4)}$$

The 3D representation of the isosurfaces was colorized according to a Red-Blue-Green scheme over the range of the second eigenvalue of the electron-density Hessian, λ_2, showing van der Waals interactions, hydrogen bonds, steric repulsions, and covalent bonds. Negative values of λ_2 are characteristic of hydrogen bonds (strong attractions

are indicated in the NCI plots by the blue color). On the other hand, nonbonding interactions (steric repulsions) are represented by positive values (and red color in the NCI plots). Finally, weak interactions (π stacking) show small λ_2 values (and represented in the NCI plots by the green color). Taking into account all these aspects, for the crystal structures, the NCI analysis has been performed using the NCIPLOT program.[86] The wave functions have been obtained at CAM-B3LYP-D3BJ/6-311G(d,p) level of theory in the gas phase from the X-Ray crystal structures.

The photophysical parameters of the absorption and emission spectra of the fluoroalkyl aminomaleimide compounds (Tables 2.7–2.14) were computed at CAM-B3LYP-D3BJ/6-311G(d,p) level of theory in solution, using the PCM methodology of six solvents (diethyl ether, toluene, tetrahydrofuran, 1,4-dioxane, dimethyl sulfoxide and methanol). All the excitation energies correspond the HOMO → LUMO transitions, while the emission energies denote the LUMO → HOMO transitions.

Although, the TD-DFT results predict lower absorption (λ_{ex}) and emission (λ_{em}) values than the experimental ones, the theoretical values of λ_{ab} and λ_{em} are in good agreement with the experimental ones. When two explicit solvent molecules (e.g., dimethyl sulfoxide and methanol) were studied, the difference of 25 nm was observed between experimental and theoretical λ_{em} and λ_{ex} values, while the average difference measured was 14 nm (Table 2.15).

Table 2.7 TD-DFT excitation and emission energies and their corresponding oscillator strengths of **2.2** using six different solvents (PCM model).[a,b] Charge descriptors along the π-conjugated structure of the aminomaleimide ring are also included.

Solvent	λ_{ex}[c]	f_{ex}[d]	λ_{em}[e]	f_{em}[d]	$\Delta\lambda$[f]	Q_{NBO1}	Q_{NBO2}
Diethyl Ether	335.3	0.110	445.6	0.093	110.4	0.168	-0.915
Toluene	334.2	0.115	437.7	0.080	103.5	0.176	-0.913
Tetrahydrofuran	336.9	0.113	450.8	0.102	113.9	0.162	-0.916
1,4-Dioxane	333.4	0.112	436.5	0.079	103.1	0.178	-0.912
DMSO	338.4	0.115	457.5	0.115	119.1	0.155	-0.918
Methanol	337.7	0.110	456.9	0.114	119.2	0.156	-0.917

[a]All excitation and emission energies correspond to the first excited state ($\pi \rightarrow \pi^*$ and $\pi^* \rightarrow \pi$ transitions, respectively). [b]All values computed at CAM-B3LYP-D3BJ/6-311G(d,p) level of theory in solution using the PCM model. [c]Excitation wavelength in nm. [d]Oscillator strength. [e]Emission wavelength in nm. [f]Stokes shift (λ_{em} - λ_{ex}).

Table 2.8 TD-DFT excitation and emission energies and their corresponding oscillator strengths of **2.4** using six different solvents (PCM model).[a,b] Charge descriptors along the π-conjugated structure of the aminomaleimide ring are also included.

Solvent	λ_{ex}[c]	f_{ex}[d]	λ_{em}[e]	f_{em}[d]	$\Delta\lambda$[f]	Q_{NBO1}	Q_{NBO2}
Diethyl Ether	330.6	0.073	452.7	0.060	122.1	0.170	-0.924
Toluene	329.2	0.077	446.1	0.051	116.9	0.177	-0.921
Tetrahydrofuran	332.2	0.075	457.0	0.066	124.8	0.165	-0.925
1,4-Dioxane	328.5	0.074	445.2	0.049	116.6	0.178	-0.921
DMSO	334.1	0.077	463.0	0.076	128.9	0.158	-0.926
Methanol	333.4	0.074	462.5	0.075	129.0	0.159	-0.926

[a]All excitation and emission energies correspond to the first excited state ($\pi \rightarrow \pi^*$ and $\pi^* \rightarrow \pi$ transitions, respectively). [b]All values computed at CAM-B3LYP-D3BJ/6-311G(d,p) level of theory in solution using the PCM model. [c]Excitation wavelength in nm. [d]Oscillator strength. [e]Emission wavelength in nm. [f]Stokes shift (λ_{em} - λ_{ex}).

Table 2.9 TD-DFT excitation and emission energies and their corresponding oscillator strengths of **2.6** using six different solvents (PCM model).[a,b] Charge descriptors along the π-conjugated structure of the aminomaleimide ring are also included.

Solvent	λ_{ex}[c]	f_{ex}[d]	λ_{em}[e]	f_{em}[d]	$\Delta\lambda$[f]	Q_{NBO1}	Q_{NBO2}
Diethyl Ether	326.5	0.097	434.9	0.086	108.5	0.209	-0.890
Toluene	325.3	0.102	427.8	0.074	102.5	0.216	-0.888
Tetrahydrofuran	328.1	0.100	439.7	0.095	111.7	0.204	-0.890
1,4-Dioxane	324.6	0.099	426.8	0.073	102.2	0.217	-0.888
DMSO	329.7	0.101	446.1	0.107	116.5	0.198	-0.891
Methanol	329.0	0.097	445.6	0.106	116.6	0.199	-0.891

[a]All excitation and emission energies correspond to the first excited state ($\pi \rightarrow \pi^*$ and $\pi^* \rightarrow \pi$ transitions, respectively). [b]All values computed at CAM-B3LYP-D3BJ/6-311G(d,p) level of theory in solution using the PCM model. [c]Excitation wavelength in nm. [d]Oscillator strength. [e]Emission wavelength in nm. [f]Stokes shift (λ_{em} - λ_{ex}).

Table 2.10 TD-DFT excitation and emission energies and their corresponding oscillator strengths of **2.7** using six different solvents (PCM model).[a,b] Charge descriptors along the π-conjugated structure of the aminomaleimide ring are also included.

Solvent	λ_{ex}[c]	f_{ex}[d]	λ_{em}[e]	f_{em}[d]	$\Delta\lambda$[f]	Q_{NBO1}	Q_{NBO2}
Diethyl Ether	338.7	0.087	460.8	0.069	122.1	0.129	-0.949
Toluene	337.4	0.091	453.3	0.059	115.9	0.138	-0.946
Tetrahydrofuran	340.5	0.090	465.6	0.076	125.2	0.123	-0.951
1,4-Dioxane	336.7	0.088	452.2	0.057	115.6	0.139	-0.946
DMSO	342.2	0.091	471.9	0.087	129.7	0.116	-0.953
Methanol	341.5	0.088	471.4	0.086	129.9	0.116	-0.952

[a]All excitation and emission energies correspond to the first excited state ($\pi \rightarrow \pi^*$ and $\pi^* \rightarrow \pi$ transitions, respectively). [b]All values computed at CAM-B3LYP-D3BJ/6-311G(d,p) level of theory in solution using the PCM model. [c]Excitation wavelength in nm. [d]Oscillator strength. [e]Emission wavelength in nm. [f]Stokes shift (λ_{em} - λ_{ex}).

Table 2.11 TD-DFT excitation and emission energies and their corresponding oscillator strengths of **2.9** using six different solvents (PCM model).[a,b] Charge descriptors along the π-conjugated structure of the aminomaleimide ring are also included.

Solvent	λ_{ex}[c]	f_{ex}[d]	λ_{em}[e]	f_{em}[d]	$\Delta\lambda$[f]	Q_{NBO1}	Q_{NBO2}
Diethyl Ether	317.1	0.116	416.8	0.090	99.8	-0.028	-1.122
Toluene	315.0	0.121	408.8	0.076	93.9	-0.016	-1.115
Tetrahydrofuran	319.3	0.121	422.1	0.100	102.8	-0.037	-1.127
1,4-Dioxane	314.1	0.117	407.6	0.074	93.6	-0.014	-1.114
DMSO	321.8	0.123	429.0	0.114	107.2	-0.047	-1.133
Methanol	320.9	0.118	428.4	0.112	107.5	-0.046	-1.132

[a]All excitation and emission energies correspond to the first excited state ($\pi \rightarrow \pi^*$ and $\pi^* \rightarrow \pi$ transitions, respectively). [b]All values computed at CAM-B3LYP-D3BJ/6-311G(d,p) level of theory in solution using the PCM model. [c]Excitation wavelength in nm. [d]Oscillator strength. [e]Emission wavelength in nm. [f]Stokes shift (λ_{em} - λ_{ex}).

Table 2.12 TD-DFT excitation and emission energies and their corresponding oscillator strengths of **2.11** using six different solvents (PCM model).[a,b] Charge descriptors along the π-conjugated structure of the aminomaleimide ring are also included.

Solvent	λ_{ex}[c]	f_{ex}[d]	λ_{em}[e]	f_{em}[d]	$\Delta\lambda$[f]	Q_{NBO1}	Q_{NBO2}
Diethyl Ether	314.5	0.071	429.4	0.046	114.8	-0.023	-1.127
Toluene	312.3	0.073	423.7	0.036	111.5	-0.012	-1.120
Tetrahydrofuran	316.7	0.074	433.3	0.052	116.7	-0.030	-1.131
1,4-Dioxane	311.5	0.070	422.9	0.035	111.4	-0.010	-1.119
DMSO	319.1	0.076	438.8	0.062	119.7	-0.039	-1.136
Methanol	318.4	0.073	438.3	0.061	119.9	-0.038	-1.136

[a]All excitation and emission energies correspond to the first excited state ($\pi \rightarrow \pi^*$ and $\pi^* \rightarrow \pi$ transitions, respectively). [b]All values computed at CAM-B3LYP-D3BJ/6-311G(d,p) level of theory in solution using the PCM model. [c]Excitation wavelength in nm. [d]Oscillator strength. [e]Emission wavelength in nm. [f]Stokes shift (λ_{em} - λ_{ex}).

Table 2.13 TD-DFT excitation and emission energies and their corresponding oscillator strengths of **2.13** using six different solvents (PCM model).[a,b] Charge descriptors along the π-conjugated structure of the aminomaleimide ring are also included.

Solvent	λ_{ex}[c]	f_{ex}[d]	λ_{em}[e]	f_{em}[d]	$\Delta\lambda$[f]	Q_{NBO1}	Q_{NBO2}
Diethyl Ether	309.0	0.097	408.1	0.073	99.1	0.021	-1.089
Toluene	306.9	0.101	401.4	0.061	94.5	0.032	-1.083
Tetrahydrofuran	311.1	0.101	412.8	0.082	101.6	0.014	-1.092
1,4-Dioxane	306.1	0.098	400.5	0.059	94.4	0.033	-1.082
DMSO	313.5	0.103	419.2	0.095	105.7	0.005	-1.097
Methanol	312.7	0.099	418.6	0.094	105.9	0.006	-1.097

[a]All excitation and emission energies correspond to the first excited state ($\pi \rightarrow \pi^*$ and $\pi^* \rightarrow \pi$ transitions, respectively). [b]All values computed at CAM-B3LYP-D3BJ/6-311G(d,p) level of theory in solution using the PCM model. [c]Excitation wavelength in nm. [d]Oscillator strength. [e]Emission wavelength in nm. [f]Stokes shift (λ_{em} - λ_{ex}).

Table 2.14 TD-DFT excitation and emission energies and their corresponding oscillator strengths of **2.14** using six different solvents (PCM model).[a,b] Charge descriptors along the π-conjugated structure of the aminomaleimide ring are also included.

Solvent	λ_{ex}[c]	f_{ex}[d]	λ_{em}[e]	f_{em}[d]	$\Delta\lambda$[f]	Q_{NBO1}	Q_{NBO2}
Diethyl Ether	322.1	0.090	434.3	0.061	112.2	-0.071	-1.160
Toluene	319.8	0.093	427.1	0.050	107.4	-0.058	-1.152
Tetrahydrofuran	324.4	0.093	439.1	0.069	114.7	-0.080	-1.165
1,4-Dioxane	318.9	0.090	426.1	0.049	107.2	-0.056	-1.151
DMSO	326.9	0.096	445.4	0.081	118.5	-0.091	-1.171
Methanol	326.2	0.092	444.8	0.080	118.6	-0.090	-1.171

[a]All excitation and emission energies correspond to the first excited state ($\pi \rightarrow \pi^*$ and $\pi^* \rightarrow \pi$ transitions, respectively). [b]All values computed at CAM-B3LYP-D3BJ/6-311G(d,p) level of theory in solution using the PCM model. [c]Excitation wavelength in nm. [d]Oscillator strength. [e]Emission wavelength in nm. [f]Stokes shift (λ_{em} - λ_{ex}).

Table 2.15 TD-DFT excitation and emission energies and their corresponding oscillator strengths of the studied aminomaleimides using two different solvents (methanol and dimethyl sulfoxide) and considering two explicit solvent molecules.[a,b] Three different charge descriptors are also included.

Solvent	λ_{ex}[c]	f_{ex}[d]	λ_{em}[e]	f_{em}[d]	$\Delta\lambda$[f]	Q_{NBO1}	Q_{NBO2}	Q_{NBO3}
2.2_2MeOH	359.2	0.121	511.6	0.109	152.4	0.126	-0.945	-0.010
2.4_2MeOH	355.7	0.085	515.2	0.078	159.5	0.136	-0.951	-0.009
2.6 _2MeOH	349.7	0.109	495.9	0.105	146.2	0.170	-0.923	-0.020
2.7_2MeOH	364.5	0.098	529.0	0.085	164.4	0.092	-0.973	0.001
2.9_2MeOH	341.5	0.130	475.2	0.112	133.7	-0.071	-1.152	0.001
2.11_2MeOH	340.2	0.083	484.0	0.068	143.8	-0.067	-1.162	0.007
2.13 _2MeOH	333.2	0.110	463.4	0.096	130.2	-0.029	-1.131	-0.010
2.14_2MeOH	348.1	0.097	493.1	0.080	145.0	-0.119	-1.191	0.018
2.2_2DMSO	356.1	0.133	495.3	0.117	139.1	0.101	-0.972	-0.053
2.4_2DMSO	351.8	0.093	497.9	0.082	146.1	0.116	-0.981	-0.050
2.6 _2DMSO	346.7	0.121	480.8	0.112	134.1	0.152	-0.949	-0.060
2.7_2DMSO	360.8	0.106	510.2	0.091	149.4	0.065	-1.003	-0.042
2.9_2DMSO	339.6	0.142	464.8	0.120	125.3	-0.105	-1.190	-0.048
2.11_2DMSO	339.1	0.085	479.8	0.075	140.7	-0.105	-1.220	-0.058
2.13 _2DMSO	333.6	0.113	462.3	0.104	128.8	-0.063	-1.184	-0.063
2.14_2DMSO	350.1	0.103	494.3	0.088	144.2	-0.167	-1.255	-0.042

[a]All excitation and emission energies correspond to the first excited state ($\pi \rightarrow \pi^*$ and $\pi^* \rightarrow \pi$ transitions, respectively). [b]All values computed at CAM-B3LYP-D3BJ/6-311G(d,p) level of theory in solution using the PCM model. [c]Excitation wavelength in nm. [d]Oscillator strength. [e]Emission wavelength in nm. [f]Stokes shift (λ_{em} - λ_{ex}).

2.6 References

1. Yu, J.; Rong, Y.; Kuo, C. T.; Zhou, X. H.; Chiu, D. T., Recent Advances in the Development of Highly Luminescent Semiconducting Polymer Dots and Nanoparticles for Biological Imaging and Medicine. *Anal. Chem.* **2017,** *89* (1), 42-56.

2. Kenry; Chen, C.; Liu, B., Enhancing the performance of pure organic room-temperature phosphorescent luminophores. *Nat. Commun.* **2019,** *10* (1), 2111.

3. Feng, S.; Gong, S.; Feng, G., Aggregation-induced emission and solid fluorescence of fluorescein derivatives. *Chem. Commun.* **2020,** *56* (16), 2511-2513.

4. Zheng, Q.; Juette, M. F.; Jockusch, S.; Wasserman, M. R.; Zhou, Z.; Altman, R. B.; Blanchard, S. C., Ultra-stable organic fluorophores for single-molecule research. *Chem. Soc. Rev.* **2014,** *43* (4), 1044-1056.

5. Sippel, T. O., New fluorochromes for thiols: maleimide and iodoacetamide derivatives of a 3-phenylcoumarin fluorophore. *J. Histochem. Cytochem.* **1981,** *29* (2), 314-316.

6. Kand, D.; Kalle, A. M.; Talukdar, P., Chromenoquinoline-based thiol probes: a study on the quencher position for controlling fluorescent Off–On characteristics. *Org. Biomol. Chem.* **2013,** *11* (10), 1691-1701.

7. Youziel, J.; Akhbar, A. R.; Aziz, Q.; Smith, M. E. B.; Caddick, S.; Tinker, A.; Baker, J. R., Bromo- and thiomaleimides as a new class of thiol-mediated fluorescence ‘turn-on’ reagents. *Org. Biomol. Chem.* **2014,** *12* (4), 557-560.

8. Prasanna de Silva, A.; Nimal Gunaratne, H. Q.; Gunnlaugsson, T., Fluorescent PET(Photoinduced Electron Transfer) reagents for thiols. *Tetrahedron Lett.* **1998,** *39* (28), 5077-5080.

9. Robin, M. P.; Wilson, P.; Mabire, A. B.; Kiviaho, J. K.; Raymond, J. E.; Haddleton, D. M.; O'Reilly, R. K., Conjugation-Induced Fluorescent Labeling of Proteins and Polymers Using Dithiomaleimides. *J. Am. Chem. Soc.* **2013,** *135* (8), 2875-2878.

10. Heindel, N. D., Maleimide syntheses by amine reaction with acetylenedicarboxylate esters. *J. Org. Chem.* **1970,** *35* (9), 3138-3140.

11. Zhu, Q.; Ye, Z.; Yang, W.; Cai, X.; Tang, B. Z., One-Pot Synthesis and Structure–Property Relationship of Aminomaleimides: Fluorescence Efficiencies in Monomers and Aggregates Easily Tuned by Switch of Aryl and Alkyl. *J. Org. Chem.* **2017,** *82* (2), 1096-1104.

12. Fletcher, S. A.; Sin, P. K. B.; Nobles, M.; Årstad, E.; Tinker, A.; Baker, J. R., A dual optical and nuclear imaging reagent for peptide labelling via disulfide bridging. *Org. Biomol. Chem.* **2015,** *13* (37), 9559-9563.

13. Onimura, K.; Matsushima, M.; Yamabuki, K.; Oishi, T., Synthesis and properties of N-substituted maleimides conjugated with 1,4-phenylene or 2,5-thienylene polymers. *Polym. J.* **2010,** *42* (4), 290-297.

14. Ambrogi, M.; Ciogli, A.; Mancinelli, M.; Ranieri, S.; Mazzanti, A., Atropisomers of Arylmaleimides: Stereodynamics and Absolute Configuration. *J. Org. Chem.* **2013,** *78* (8), 3709-3719.

15. Robin, M. P.; O'Reilly, R. K., Fluorescent and chemico-fluorescent responsive polymers from dithiomaleimide and dibromomaleimide functional monomers. *Chem. Sci.* **2014,** *5* (7), 2717-2723.

16. Mabire, A. B.; Robin, M. P.; Quan, W.-D.; Willcock, H.; Stavros, V. G.; O'Reilly, R. K., Aminomaleimide fluorophores: a simple functional group with bright, solvent dependent emission. *Chem. Commun.* **2015,** *51* (47), 9733-9736.

17. Yeh, H.-C.; Wu, W.-C.; Chen, C.-T., The colourful fluorescence from readily-synthesised 3,4-diaryl-substituted maleimide fluorophores. *Chem. Commun.* **2003,** (3), 404-405.

18. Mabire, A. B.; Robin, M. P.; Willcock, H.; Pitto-Barry, A.; Kirby, N.; O'Reilly, R. K., Dual effect of thiol addition on fluorescent polymeric micelles: ON-to-OFF emissive switch and morphology transition. *Chem. Commun.* **2014,** *50* (78), 11492-11495.

19. Imoto, H.; Nohmi, K.; Kizaki, K.; Watase, S.; Matsukawa, K.; Yamamoto, S.; Mitsuishi, M.; Naka, K., Effect of alkyl groups on emission properties of aggregation induced emission active N-alkyl arylaminomaleimide dyes. *RSC Adv.* **2015,** *5* (114), 94344-94350.

20. Bouissane, L.; Sestelo, J. P.; Sarandeses, L. A., Synthesis of 3,4-Disubstituted Maleimides by Selective Cross-Coupling Reactions Using Indium Organometallics. *Org. Lett.* **2009,** *11* (6), 1285-1288.

21. Xie, Y.; Husband, J. T.; Torrent-Sucarrat, M.; Yang, H.; Liu, W.; O'Reilly, R. K., Rational design of substituted maleimide dyes with tunable fluorescence and solvafluorochromism. *Chem. Commun.* **2018,** *54* (27), 3339-3342.

22. Richards, D. A.; Fletcher, S. A.; Nobles, M.; Kossen, H.; Tedaldi, L.; Chudasama, V.; Tinker, A.; Baker, J. R., Photochemically re-bridging disulfide bonds and the discovery of a thiomaleimide mediated photodecarboxylation of C-terminal cysteines. *Org. Biomol. Chem.* **2016,** *14* (2), 455-459.

23. Hull, E. A.; Livanos, M.; Miranda, E.; Smith, M. E. B.; Chester, K. A.; Baker, J. R., Homogeneous Bispecifics by Disulfide Bridging. *Bioconjug. Chem.* **2014,** *25* (8), 1395-1401.

24. Chan, L.-H.; Lee, Y.-D.; Chen, C.-T., Achieving saturated red photoluminescence and electroluminescence with readily synthesized maleimide-arylamine copolymers. *Tetrahedron* **2006,** *62* (41), 9541-9547.

25. Gu, G.; Wang, H.; Liu, P.; Fu, C.; Li, Z.; Cao, X.; Li, Y.; Fang, Q.; Xu, F.; Shen, J.; Wang, P. G., Discovery and structural insight of a highly selective protein kinase inhibitor hit through click chemistry. *Chem. Commun.* **2012,** *48* (22), 2788-90.

26. Ghosh, A. K.; Samanta, S.; Ghosh, P.; Neogi, S.; Hajra, A., Regioselective hydroarylation and arylation of maleimides with indazoles via a Rh(iii)-catalyzed C–H activation. *Org. Biomol. Chem.* **2020,** *18* (16), 3093-3097.

27. Nakamura, M.; Yamabuki, K.; Oishi, T.; Onimura, K., Synthesis and fluorescent properties of conjugated co-oligomers containing maleimide and carbazole units at the main chain. *Polym. J.* **2014,** *46* (2), 94-103.

28. Xie, H. D.; Ho, L. A.; Truelove, M. S.; Corry, B.; Stewart, S. G., Fluorescent triphenyl substituted maleimide derivatives: synthesis, spectroscopy and quantum chemical calculations. *J. Fluoresc.* **2010,** *20* (5), 1077-85.

29. Li, T.-T.; Jia, Y.-H.; Huang, M.-H.; Wang, Y.; Luo, Y., A crystalline bisindolylmaleimide with strong solid-state fluorescence of red color and its analogous cross-linked polymer without fluorescence. *Des. Monomers Polym.* **2016,** *19* (2), 172-179.

30. Nacheva, K. P.; Maza, W. A.; Myers, D. Z.; Fronczek, F. R.; Larsen, R. W.; Manetsch, R., Fluorescent properties and resonance energy transfer of 3,4-bis(2,4-difluorophenyl)-maleimide. *Org. Biomol. Chem.* **2012,** *10* (38), 7840-7846.

31. Cui, J.; Wang, S.; Huang, K.; Li, Y.; Zhao, W.; Shi, J.; Gu, J., Conjugation-induced fluorescence labelling of mesoporous silica nanoparticles for the sensitive and selective detection of copper ions in aqueous solution. *New J. Chem.* **2014,** *38* (12), 6017-6024.

32. Gil Alvaradejo, G.; Glassner, M.; Hoogenboom, R.; Delaittre, G., Maleimide end-functionalized poly(2-oxazoline)s by the functional initiator route: synthesis and (bio)conjugation. *RSC Adv.* **2018,** *8* (17), 9471-9479.

33. Wu, X.; Wang, R.; Kwon, N.; Ma, H.; Yoon, J., Activatable fluorescent probes for in situ imaging of enzymes. *Chem. Soc. Rev.* **2022,** *51* (2), 450-463.

34. Alkilany, A. M.; Rachid, O.; Alkawareek, M. Y.; Billa, N.; Daou, A.; Murphy, C. J., PLGA-Gold Nanocomposite: Preparation and Biomedical Applications. *Pharmaceutics* **2022,** *14* (3), 660.

35. Guy, J.; Caron, K.; Dufresne, S.; Michnick, S. W.; Skene; Keillor, J. W., Convergent Preparation and Photophysical Characterization of Dimaleimide Dansyl Fluorogens: Elucidation of the Maleimide Fluorescence Quenching Mechanism. *J. Am. Chem. Soc.* **2007,** *129* (39), 11969-11977.

36. Wu, C.-W.; Yarbrough, L. R.; Wu, F. Y. H., *N*-(1-Pyrene)maleimide: a fluorescent crosslinking reagent. *Biochem.* **1976,** *15* (13), 2863-2868.

37. Sasaki, S.; Drummen, G. P. C.; Konishi, G.-i., Recent advances in twisted intramolecular charge transfer (TICT) fluorescence and related phenomena in materials chemistry. *J. Mater. Chem. C* **2016,** *4* (14), 2731-2743.

38. Haberhauer, G.; Gleiter, R.; Burkhart, C., Planarized Intramolecular Charge Transfer: A Concept for Fluorophores with both Large Stokes Shifts and High Fluorescence Quantum Yields. *Chem. Eur. J.* **2016,** *22* (3), 971-978.

39. Husband, J. T. The development of maleimide derived fluorophores for peptide-based applications. University of Birmingham, 2020.

40. Staniforth, M.; Quan, W.-D.; Karsili, T. N. V.; Baker, L. A.; O'Reilly, R. K.; Stavros, V. G., First Step toward a Universal Fluorescent Probe: Unravelling the Photodynamics of an Amino–Maleimide Fluorophore. *J. Phys. Chem. A* **2017,** *121* (34), 6357-6365.

41. Kumar, N. S. S.; Gujrati, M. D.; Wilson, J. N., Evidence of preferential π-stacking: a study of intermolecular and intramolecular charge transfer complexes. *Chem. Commun.* **2010,** *46* (30), 5464-5466.

42. Ma, X.; Sun, R.; Cheng, J.; Liu, J.; Gou, F.; Xiang, H.; Zhou, X., Fluorescence Aggregation-Caused Quenching versus Aggregation-Induced Emission: A Visual Teaching Technology for Undergraduate Chemistry Students. *J. Chem. Educ.* **2016,** *93* (2), 345-350.

43. Mei, J.; Leung, N. L. C.; Kwok, R. T. K.; Lam, J. W. Y.; Tang, B. Z., Aggregation-Induced Emission: Together We Shine, United We Soar! *Chem. Rev.* **2015,** *115* (21), 11718-11940.

44. Nicol, A.; Qin, W.; Kwok, R. T. K.; Burkhartsmeyer, J. M.; Zhu, Z.; Su, H.; Luo, W.; Lam, J. W. Y.; Qian, J.; Wong, K. S.; Tang, B. Z., Functionalized AIE nanoparticles with efficient deep-red emission, mitochondrial specificity, cancer cell selectivity and multiphoton susceptibility. *Chem. Sci.* **2017,** *8* (6), 4634-4643.

45. Wang, D.; Su, H.; Kwok, R. T. K.; Shan, G.; Leung, A. C. S.; Lee, M. M. S.; Sung, H. H. Y.; Williams, I. D.; Lam, J. W. Y.; Tang, B. Z., Facile Synthesis of Red/NIR AIE Luminogens with Simple Structures, Bright Emissions, and High Photostabilities, and Their Applications for Specific Imaging of Lipid Droplets and Image-Guided Photodynamic Therapy. *Adv. Funct. Mater.* **2017,** *27* (46), 1704039.

46. Chen, G.; Li, W.; Zhou, T.; Peng, Q.; Zhai, D.; Li, H.; Yuan, W. Z.; Zhang, Y.; Tang, B. Z., Conjugation-Induced Rigidity in Twisting Molecules: Filling the Gap Between Aggregation-Caused Quenching and Aggregation-Induced Emission. *Adv. Mater.* **2015,** *27* (30), 4496-4501.

47. Liu, Y.; Zhang, Y.; Wu, X.; Lan, Q.; Chen, C.; Liu, S.; Chi, Z.; Jiang, L.; Chen, X.; Xu, J., Deep-blue luminescent compound that emits efficiently both in solution and solid state with considerable blue-shift upon aggregation. *J. Mater. Chem. C* **2014,** *2* (6), 1068-1075.

48. Zhang, X.; Zhou, Y.; Wang, M.; Chen, Y.; Zhou, Y.; Gao, W.; Liu, M.; Huang, X.; Wu, H., Metal-Free Facile Synthesis of Multisubstituted 1-Aminoisoquinoline Derivatives with Dual-State Emissions. *Chem. Asian J* **2020,** *15* (11), 1692-1700.

49. Mei, X.; Wang, J.; Zhou, Z.; Wu, S.; Huang, L.; Lin, Z.; Ling, Q., Diarylmaleic anhydrides: unusual organic luminescence, multi-stimuli response and photochromism. *J. Mater. Chem. C* **2017,** *5* (8), 2135-2141.

50. Wang, J.; Liu, Z.; Yang, S.; Lin, Y.; Lin, Z.; Ling, Q., Large Changes in Fluorescent Color and Intensity of Symmetrically Substituted Arylmaleimides Caused by Subtle Structure Modifications. *Chem. Eur. J.* **2018,** *24* (2), 322-326.

51. Price, J.; Albright, E.; Decken, A.; Eisler, S., Thioarylmaleimides: accessible, tunable, and strongly emissive building blocks. *Org. Biomol. Chem.* **2019,** *17* (44), 9562-9566.

52. Lei, Y.; Liu, Q.; Dong, L.; Cai, Z.; Shi, J.; Zhi, J.; Tong, B.; Dong, Y., The Dual-State Luminescent Mechanism of 2,3,4,5-Tetraphenyl-1*H*-pyrrole. *Chem. Eur. J.* **2018,** *24* (53), 14269-14274.

53. Ramamurthy, K.; Malar, E. J. P.; Selvaraju, C., Hydrogen bonded dimers of ketocoumarin in the solid state and alcohol:water binary solvent: fluorescence spectroscopy, crystal structure and DFT investigation. *New J. Chem.* **2019,** *43* (23), 9090-9105.

54. Wu, H.; Chen, Z.; Chi, W.; Bindra, A. K.; Gu, L.; Qian, C.; Wu, B.; Yue, B.; Liu, G.; Yang, G.; Zhu, L.; Zhao, Y., Structural Engineering of Luminogens with High Emission Efficiency Both in Solution and in the Solid State. *Angew. Chem. Int. Ed.* **2019,** *58* (33), 11419-11423.

55. Xu, Y.; Ren, L.; Dang, D.; Zhi, Y.; Wang, X.; Meng, L., A Strategy of “Self-Isolated Enhanced Emission” to Achieve Highly Emissive Dual-State Emission for Organic Luminescent Materials. *Chem. Eur. J.* **2018,** *24* (41), 10383-10389.

56. Yu, Z.; Duan, Y.; Cheng, L.; Han, Z.; Zheng, Z.; Zhou, H.; Wu, J.; Tian, Y., Aggregation induced emission in the rotatable molecules: the essential role of molecular interaction. *J. Mater. Chem.* **2012,** *22* (33), 16927-16932.

57. Zhang, Y.; Qu, Y.; Wu, J.; Rui, Y.; Gao, Y.; Wu, Y., Naphthalimide end-capping molecular rotors with different donor cores: Tuning emission in wide gamut and cell imaging. *Dyes Pigm.* **2020,** *179*, 108431.

58. Qiu, Q.; Xu, P.; Zhu, Y.; Yu, J.; Wei, M.; Xi, W.; Feng, H.; Chen, J.; Qian, Z., Rational Design of Dual-State Emission Luminogens with Solvatochromism by Combining a Partially Shared Donor–Acceptor Pattern and Twisted Structures. *Chem. Eur. J.* **2019,** *25* (70), 15983-15987.

59. Kumar, S.; Singh, P.; Kumar, P.; Srivastava, R.; Pal, S. K.; Ghosh, S., Exploring an Emissive Charge Transfer Process in Zero-Twist Donor–Acceptor Molecular Design as a Dual-State Emitter. *J. Phys. Chem. C* **2016,** *120* (23), 12723-12733.

60. Jian, N.; Qu, K.; Gu, H.; Zou, L.; Liu, X.; Hu, F.; Xu, J.; Yu, Y.; Lu, B., Highly fluorescent triazolopyridine–thiophene D–A–D oligomers for efficient pH sensing both in solution and in the solid state. *Phys. Chem. Chem. Phys.* **2019,** *21* (13), 7174-7182.

61. Singh, V. D.; Kushwaha, A. K.; Singh, R. S., Achieving flexibility/rigidity balance through asymmetric Donor−Acceptor scaffolds in pursuit of dual state emission with application in acidochromism. *Dyes Pigm.* **2021,** *187*, 109117.

62. Ni, Y.; Zhang, S.; He, X.; Huang, J.; Kong, L.; Yang, J.; Yang, J., Dual-state emission difluoroboron derivatives for selective detection of picric acid and reversible acid/base fluorescence switching. *Anal. Methods* **2021,** *13* (25), 2830-2835.

63. Sletten, E. M.; Swager, T. M., Fluorofluorophores: fluorescent fluorous chemical tools spanning the visible spectrum. *J. Am. Chem. Soc.* **2014,** *136* (39), 13574-7.

64. Jones, M. W.; Strickland, R. A.; Schumacher, F. F.; Caddick, S.; Baker, J. R.; Gibson, M. I.; Haddleton, D. M., Polymeric dibromomaleimides as extremely efficient disulfide bridging bioconjugation and pegylation agents. *J. Am. Chem. Soc.* **2012,** *134* (3), 1847-52.

65. Würth, C.; Grabolle, M.; Pauli, J.; Spieles, M.; Resch-Genger, U., Relative and absolute determination of fluorescence quantum yields of transparent samples. *Nat. Protoc.* **2013,** *8* (8), 1535-1550.

66. Eaton, D. F., Recommended methods for fluorescence decay analysis. *Pure Appl. Chem.* **1990,** *62* (8), 1631-1648.

67. Husband, J. T.; Xie, Y.; Wilks, T. R.; Male, L.; Torrent-Sucarrat, M.; Stavros, V. G.; O'Reilly, R. K., Rigidochromism by imide functionalisation of an aminomaleimide fluorophore. *Chem. Sci.* **2021,** *12* (31), 10550-10557.

68. Quan, W.-D. The design, construction and characterisation of self-assembled biomimetic multi-chromophoric photosystems. University of Warwick, 2017.

69. Percino, M. J.; Cerón, M.; Rodríguez, O.; Soriano-Moro, G.; Castro, M. E.; Chapela, V. M.; Siegler, M. A.; Pérez-Gutiérrez, E., Conformational and Molecular Structures of α,β-Unsaturated Acrylonitrile Derivatives: Photophysical Properties and Their Frontier Orbitals. *Molecules* **2016,** *21* (4), 389.

70. Zheng, R.; Mei, X.; Lin, Z.; Zhao, Y.; Yao, H.; Lv, W.; Ling, Q., Strong CIE activity, multi-stimuli-responsive fluorescence and data storage application of new diphenyl maleimide derivatives. *J. Mater. Chem. C* **2015,** *3* (39), 10242-10248.

71. Harris, R. K.; Becker, E. D.; Cabral de Menezes, S. M.; Goodfellow, R.; Granger, P., NMR Nomenclature: Nuclear Spin Properties and Conventions for Chemical Shifts. IUPAC Recommendations 2001. *Solid State Nucl. Magn. Reson.* **2002,** *22* (4), 458-483.

72. Nirogi, R.; Dwarampudi, A.; Kambhampati, R.; Bhatta, V.; Kota, L.; Shinde, A.; Badange, R.; Jayarajan, P.; Bhyrapuneni, G.; Dubey, P. K., Rigidized 1-aryl

sulfonyl tryptamines: synthesis and pharmacological evaluation as 5-HT6 receptor ligands. *Bioorg. Med. Chem. Lett.* **2011,** *21* (15), 4577-4580.

73. Yanai, T.; Tew, D. P.; Handy, N. C., A new hybrid exchange-correlation functional using the Coulomb-attenuating method (CAM-B3LYP). *Chem. Phys. Lett.* **2004,** *393* (1-3), 51-57.

74. Hehre, W. J.; Ditchfield, R.; Pople, J. A., Self-consistent molecular-orbital methods. 12. Further extensions of gaussian-type basis sets for use in molecular-orbital studies of organic-molecules. *J. Chem. Phys.* **1972,** *56* (5), 2257-2261.

75. Hehre, W. J.; Random, L.; Schleyer, P. v. R.; Pople, J. A., *Ab initio Molecular Orbital Theory*. Wiley: New York, 1986.

76. Grimme, S.; Antony, J.; Ehrlich, S.; Krieg, H., A consistent and accurate ab initio parametrization of density functional dispersion correction (DFT-D) for the 94 elements H-Pu. *J. Chem. Phys.* **2010,** *132* (15), 154104.

77. Johnson, E. R.; Becke, A. D., A post-Hartree-Fock model of intermolecular interactions: Inclusion of higher-order corrections. *J. Chem. Phys.* **2006,** *124* (17).

78. Grimme, S.; Ehrlich, S.; Goerigk, L., Effect of the Damping Function in Dispersion Corrected Density Functional Theory. *J. Comput. Chem.* **2011,** *32* (7), 1456-1465.

79. Cossi, M.; Rega, N.; Scalmani, G.; Barone, V., Energies, structures, and electronic properties of molecules in solution with the C-PCM solvation model. *J. Comput. Chem.* **2003,** *24* (6), 669-681.

80. Tomasi, J.; Mennucci, B.; Cammi, R., Quantum mechanical continuum solvation models. *Chem. Rev.* **2005,** *105* (8), 2999-3093.

81. Adamo, C.; Jacquemin, D., The calculations of excited-state properties with Time-Dependent Density Functional Theory. *Chem. Soc. Rev.* **2013,** *42* (3), 845-856.

82. Laurent, A. D.; Adamo, C.; Jacquemin, D., Dye chemistry with time-dependent density functional theory. *Phys. Chem. Chem. Phys.* **2014,** *16* (28), 14334-14356.

83. Reed, A. E.; Curtiss, L. A.; Weinhold, F., Intermolecular interactions from a natural bond orbital, donor-acceptor viewpoint. *Chem. Rev.* **1988,** *88* (6), 899-926.

84. Frisch, M. J.; Trucks, G. W.; Schlegel, H. B.; Scuseria, G. E.; Robb, M. A.; Cheeseman, J. R.; Scalmani, G.; Barone, V.; Petersson, G. A.; Nakatsuji, H.; Li, X.; Caricato, M.; Marenich, A. V.; Bloino, J.; Janesko, B. G.; Gomperts, R.; Mennucci, B.; Hratchian, H. P.; Ortiz, J. V.; Izmaylov, A. F.; Sonnenberg, J. L.; Williams; Ding, F.; Lipparini, F.; Egidi, F.; Goings, J.; Peng, B.; Petrone, A.; Henderson, T.; Ranasinghe, D.; Zakrzewski, V. G.; Gao, J.; Rega, N.; Zheng, G.; Liang, W.; Hada, M.; Ehara, M.; Toyota, K.; Fukuda, R.; Hasegawa, J.; Ishida, M.; Nakajima, T.; Honda, Y.; Kitao, O.; Nakai, H.; Vreven, T.; Throssell, K.; Montgomery Jr., J. A.; Peralta, J. E.; Ogliaro, F.; Bearpark, M. J.; Heyd, J. J.; Brothers, E. N.; Kudin, K. N.; Staroverov, V. N.; Keith, T. A.; Kobayashi, R.; Normand, J.; Raghavachari, K.; Rendell, A. P.; Burant, J. C.; Iyengar, S. S.; Tomasi, J.; Cossi, M.; Millam, J. M.; Klene, M.; Adamo, C.; Cammi, R.; Ochterski, J. W.; Martin, R. L.; Morokuma, K.; Farkas, O.; Foresman, J. B.; Fox, D. J. *Gaussian 16 Rev. C.01*, Wallingford, CT, 2016.

85. Johnson, E. R.; Keinan, S.; Mori-Sánchez, P.; Contreras-García, J.; Cohen, A. J.; Yang, W., Revealing Noncovalent Interactions. *J. Am. Chem. Soc.* **2010,** *132* (18), 6498-6506.

86. Contreras-García, J.; Johnson, E. R.; Keinan, S.; Chaudret, R.; Piquemal, J. P.; Beratan, D. N.; Yang, W., NCIPLOT: a program for plotting non-covalent interaction regions. *J. Chem. Theory Comput.* **2011,** *7* (3), 625-632.

CHAPTER 3: DEVELOPMENT OF FLUORESCENT HALF-SANDWICH TRANSITION METAL BASED ORGANOMETALLIC COMPLEXES USING MALEIMIDE DERIVATIVES AS LIGANDS

3.1 Abstract

In this chapter, “three or four legged piano-stool” metallocarbonyl carbonyl maleimide complexes of (η^5-Cp)M(CO)$_x$L type were synthesized. These half-sandwich metallocarbonyl complexes contained aminobromo- (ABM), aminochloro- (ACM) and dithio- (DTM) maleimides as ligands, exhibiting bright emissions, and solvent-dependent fluorescence. Substituted maleimide is an interesting class of organic luminophores, as they are non-invasive, strongly emissive, and highly sensitive to the environment. Therefore, the effect of complexation on the fluorescence of maleimides was explored by investigating the optical properties of these half-sandwich metal-maleimide complexes. The switch on→off electrofluorochromic properties of these complexes were examined by cyclic voltammetry and fluorescence spectroscopy. Thus, the functionalization of the metallocarbonyl complexes with the maleimide derivatives increases their versatility in their use as fluorescent probes, in addition to the IR-markers, which opens fascinating opportunities for the development of maleimide-based probes.

3.2 Introduction

3.2.1 Luminescence in organometallic complexes

Over the years, there has been a tremendous interest in developing luminescent transition metal complexes for various applications, such as sensors,[1, 2] dye-sensitized solar cells (DSSCs),[3] organic light emitting diodes (OLEDs),[4] cell imaging,[5] and monitoring industrial reactions.[6] This is due to their high tunability, high photostability, and unique photophysical properties.[7] The photochemistry of the transition metal complexes made them ideal candidates for these applications owing to their controlled and specific response to external stimuli. This chapter focuses on developing new and fluorescent transition metal-based complexes and investigating their luminescent properties.

3.2.1.1 Electronic transitions in organometallic complexes

Organometallic complexes are well-known to exhibit different transitions based on energy levels of the ligand and metal orbitals and the interactions between these orbitals. These electronic transitions include ligand field (LF), intra-ligand (IL), metal-to-ligand charge-transfer (MLCT), ligand-to-metal charge transfer (LMCT), ligand-to-ligand charge transfer (LLCT), sigma-bond-to-ligand charge transfer (SBLCT), metal-to-metal charge transfer (MMCT), and metal-to-solvent metal charge transfer (MSCT) (Fig. 3.1).[8-10] Low-lying ligand field (LF) transitions are also referred to as d-d transitions or metal-centered transitions, and they arise from electronic promotion between the metal d-orbitals,[11] while on the other hand intraligand (IL) transitions

involves electronic transition between the ligand-centered orbitals, such as π- π *, and also termed as ligand centered (LC) transitions.[12, 13]

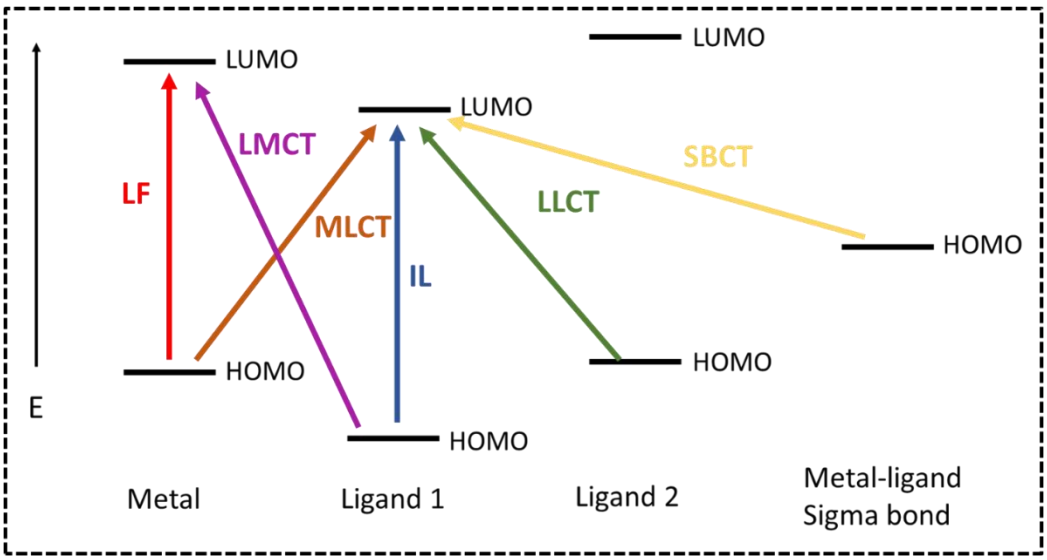

Fig. 3.1 Schematic illustrations of various electronic transitions in organometallic complexes.

The electronic transitions that involve both metal and ligand orbits are either MLCT, or LMCT.[14] MLCT excited states involve electronic transitions from the d-orbital of an electron-rich metal to ligands low-lying empty orbitals (e.g., CO or CN^-), and depends on both the solvent and the substituent. On the other hand, LMCT involves transitions from the fully occupied molecular orbitals of a ligand to the empty or partially filled metal d-orbitals. It is important to note that the occurrence of MLCT or LMCT transitions depends on the ligands being classified by their ability to donate or accept electrons in charge transfer (CT) transitions. Once classified, a ligand can be referred to as a CT donor, a CT acceptor or neutral. CT donors, such as allyl, cyclopentadienyl (Cp), are anionic in nature, whereas CT acceptors, like cyclohexadienyl, exhibit a cationic

nature. The Cp ligand can contribute as a CT donor not only for MLCT but also for LLCT and ILCT transitions. In comparison, neutral ligands, such as carbenes, arenes, etc., may behave as CT acceptors or donors depending on the metal atom involved.[15] Additionally, SBLCT occurs from the orbitals that possess metal-ligand sigma bonding character.[16-18] LLCT transitions occur in complexes that simultaneously contain a reducing and an oxidizing ligand,[19, 20] while MMCT includes the transitions between the orbitals of metal-to-metal bonded bi- or tri-nuclear complexes.[21, 22]

The intensities of the electronic transitions are determined by the “Spin rule” and the “Orbital rule (Laporte)”. According to the Laporte selection rule, if the complex is of centrosymmetric symmetry, transitions of the same parity, such as d- d transitions, are forbidden. However, due to the coupling of electronic wave functions of appropriate symmetry and energy, these transitions occur with molar extinction coefficient ε = 5–100 $M^{-1}cm^{-1}$, which is lower than IL/LC and CT transitions that display higher intensities where ε >> 10^3 $M^{-1}cm^{-1}$, and occur between states of different parity. However, if the centrosymmetric species undergo a distortion of the ground state geometry, such as deviation from the idealized O_h geometry as result of Jahn-Teller effect, it relaxes the “Laporte selection rule”.[23, 24] Furthermore, the “Spin selection rule” forbids the transitions between electronic states of different spin multiplicities. Because of that, second and third row transition metals experience more spin–orbit coupling, and have larger molar extinction coefficients.

Fig. 3.2 illustrates the simplified version of molecular orbital (MO) diagram for a transition metal complex in octahedral (O_h) symmetry, exhibiting some of its characteristic electronic transitions. These orbital parentages offered analytical insight into the photochemistry of the hexacoordinate complexes. In such complexes,

transitions such as MC and LMCT involve the electronic populations of the metal e_g MOs, that are antibonding (σ*) in nature, and as a consequence weakens the metal-ligand (M-L) bond. On the other hand, t_{2g} molecular orbitals are either antibonding (π*) or bonding (π_b), with reference to π -donor or π -acceptor ligands, and any change in the population of these orbitals results in M-L bond strengthening.[11, 23]

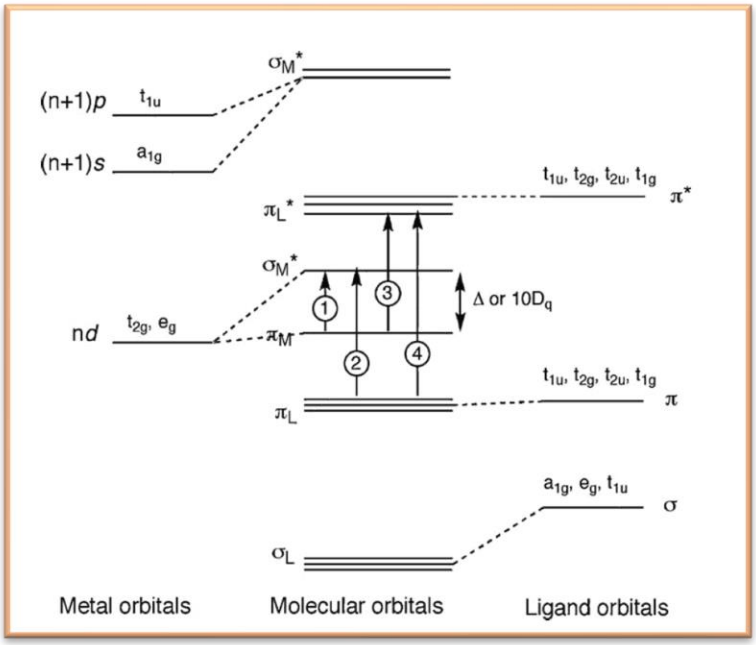

Fig. 3.2 Molecular orbital diagram for a transition metal complex in O_h symmetry. The arrows labeled 1–4 represent, a metal centered (MC) ligand field transition, a ligand to metal charge transfer (LMCT), a metal to ligand charge transfer (MLCT), and an intraligand or ligand centered (LC) band respectively. Adapted from the reference.[11] Copyright 2011 Elsevier.

3.2.2 Transition metal carbonyl complexes

Metallocarbonyl complexes are well-known for their intense and characteristic absorption band, in the mid-IR spectral region (2150-1800 cm^{-1}) and unique

luminescence characteristics.[25-27] In 1985, Jaouen's research group for the first time utilized the metallocarbonyl complexes to develop the carbonylmetalloimmunoassay (CMIA) method for the detection of biomolecules.[28, 29] They utilized the metal carbonyl complexes, such as $CO_2(CO)_6L$, $CpFe(CO)_2L$, and $CpMn(CO)_3L$, etc. (**1**–**4**), to label and trace an antigen (Fig. 3.3).[30, 31] The tailored tracer was separated after the treatment, either free or antibody-bound, and quantified by FT-IR spectroscopy. Furthermore, this method was extended to monitor the concentrations of multiple drugs simultaneously, and was named the multi-CMIA method.[32] Although, the significance of the CO group with respect to IR or Raman spectroscopy was reported by Leong's group in 2007.[33] In their work, water-soluble osmium carbonyl cluster derivatives (**5**) were utilized an IR-tag for the labelling of a fatty acid and phosphatidylcholine derivative (Fig. 3.3). In another report, a tris(pyrazolyl)methane (tpm) manganese tricarbonyl cationic complex (**6**) was employed, to investigate photoinduced cytotoxic activity against cancer cells by Raman microscopy.[34, 35] Recently, Policar and co-workers reported subcellular imaging of hydroxytamoxifen $CpRe(CO)_3$ derivative (**7**), using photothermal induced resonance (PTIR), in which atomic force microscopy (AFM) is combined with the chemical specificity of the infrared spectroscopy.[36]

3.2.3 Tailored half-sandwich metallocarbonyl maleimide complexes

Organometallic half-sandwich metal complexes is an emerging field of research, for promising applications such as catalysis,[37] therapeutics, and sensors.[38, 39] Generally, these complexes comprise of a metal atom surrounded by three or more ligands, one

of which is a cyclic aromatic ligand, i.e., arene or cyclopentadienyl (Cp), exhibiting "piano-stool" geometries.[40] These complexes can behave as Lewis bases and may react with a wide range of electrophilic species,[41] and thus considered as excellent precursors for a variety of reactions.

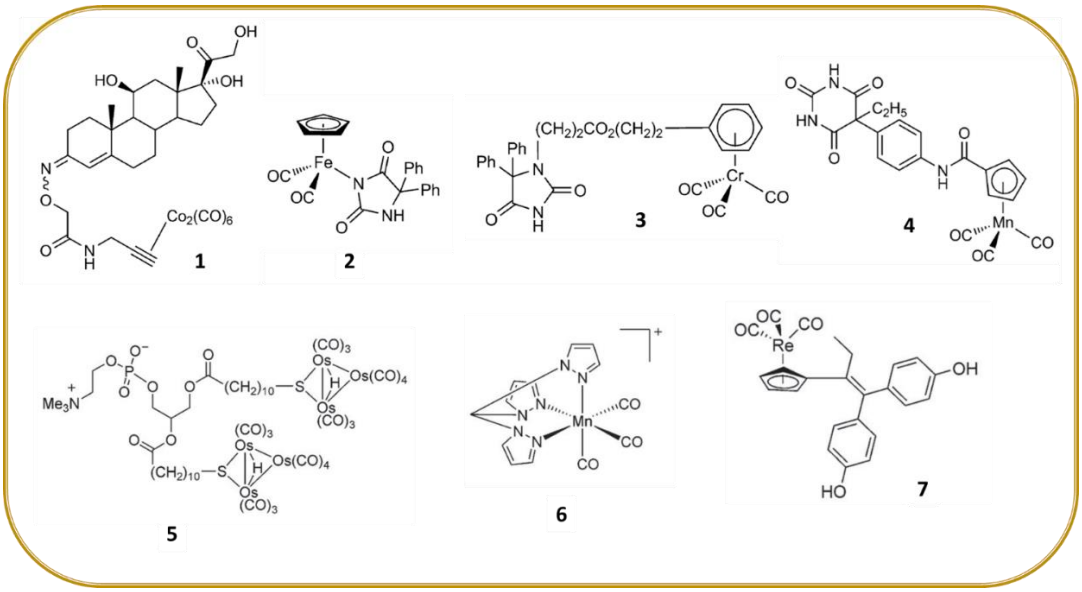

Fig. 3.3 Structures of metal-carbonyl-containing biomolecules (1 – 7) used for IR, Raman and PTIR imaging.[29, 31, 33-35]

Maleimide derivatives are known to be extremely reactive, and have been widely employed as a linker in the organometallic complexes to undergo facile conjugation with biomolecules.[42, 43] Rudolf and co-workers employed unfunctionalized maleimide derivatives, as a ligand to coordinate with transition metal atoms, for conjugation to the biomolecules, such as human serum albumin (HSA), bovine serum albumin (BSA), and glutathione.[44-46] Later, the (η^5-C_5H_5)Fe(CO)$_2$(η^1-*N*-maleimidato) complex and its tungsten and molybdenum analogues were employed as enzyme inhibitors, IR-

detectable markers and CO-releasing molecules.[47-50] Soon after Rudolf *et al*., reported reversible cleavage of half-sandwich monobromo- and dibromomaleimide metallocarbonyl complexes with tris(2-carboxyethyl)phosphine (TCEP) to regenerate catalytically active enzyme (Fig. 3.4).[51] Nevertheless, fluorescent properties of these half-sandwich metallocarbonyl complexes have not been explored so-far. Therefore, in this chapter the development of half-sandwich metallocarbonyl maleimides complexes has been discussed and their fluorochromic behavior has been investigated, especially with regards to the free maleimide fluorophores.

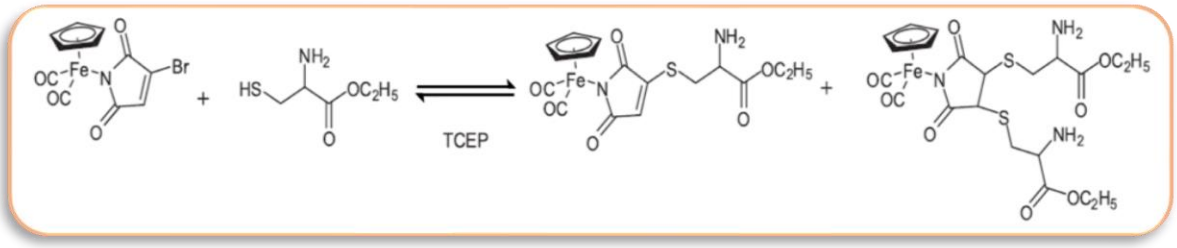

Fig. 3.4 Reaction of half-sandwich thiomaleimidato metallocarbonyl complex with cysteine residue and its cleavage. Adapted from the reference.[51] Copyright 2012 John Wiley & Sons, Ltd.

It is well-known that the cyclopentadienyl (Cp) ligand is inert to a large number of electrophiles and nucleophiles, thus engages in stabilizing of the organometallic complexes. Hence, in the tailored half-sandwich metallocarbonyl maleimide complexes, the cyclopentadienyl (Cp) moiety acts as “spectator” ligand, exhibiting “piano stool” geometries for $CpML_n$ (n = 2, 3 or 4) type structures. In these structures, the Cp ligand acts as the “seat”, while the remaining ligands are regarded as the “legs” of the piano-stool. Furthermore, these structures are extended to “metallocene” (Cp_2M)

or “bent metallocene” (Cp_2MX_n) structures. It is noteworthy that the Cp ligand mostly binds to a metal atom in pentahapto (η^5) mode, in contrast to rarely observed monohapto (η^1) and trihapto (η^3) ligands. Notably, in η^5 mode Cp behaves as an L_2X ligand type, therefore $CpML_3$ complexes where L = CO, or maleimide; are considered as pseudo-octahedral complexes of the ML_5X type.[24] These d^6-$CpML_3$ complexes most likely are classified as low spin complexes, owing to the presence of strong field ligands (i.e., CO) causing larger crystal field splitting (Δ) between the t_{2g} and e_g orbitals. The half-sandwich complexes depict the isolable analogy with the octahedral and tetrahedral fragments, which is shown in the Fig. 3.5. Theoretical parameters for determining the metal-ligand interactions in the tailored half-sandwich metallocarbonyl maleimide complexes have been given in Table 3.1.

Table 3.1 Theoretical parameters of the tailored half-sandwich metallocarbonyl maleimide complexes.

	(η^5-Cp)Fe(CO)$_2$(η^1-maleimidato)	**(η^5-Cp)Ru(CO)$_2$(η^1-maleimidato)**	**(η^5-Cp)Mo(CO)$_3$(η^1-maleimidato)**
Oxidation state	II	II	II
d- electronic configuration	d^6	d^6	d^4
# of unpaired electrons	0	0	0
18-electron rule	18 e^-	18 e^-	18 e^-
Coordination number	6	6	7
Low spin or high spin	Low spin	Low spin	High spin/ Low spin
Geometry	Pseudo-Octahedral	Pseudo-Octahedral	Pseudo-square bipyramidal

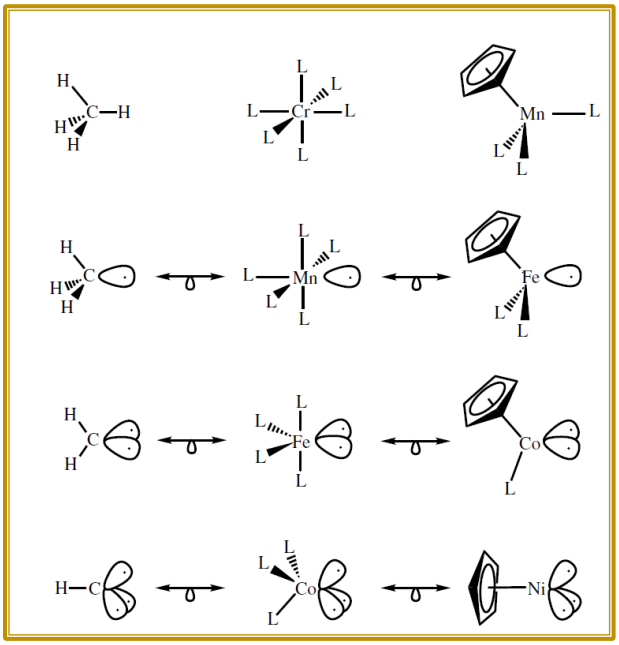

Fig. 3.5 Isolobal analogy between fragments of octahedral, pseudooctahedral and tetrahedral structures. Adapted from the reference.[52] Copyright 2005 Oxford University Press.

Notably, if different ligands are attached to the metal centre in the octahedral complex, the symmetry of the organometallic complexes reduces from O_h. Although, underlying σ-frameworks and the shape of molecular orbitals remains unchanged, the symmetry labels change slightly. Consequently, the MO diagram was achieved by dropping the symmetry of the fragment orbitals, followed by combining the orbitals of the same symmetry using the basic O_h MO diagram as reference.[52] Following on to that, $CpML_4$ complexes exhibit hepta-coordination leading to a pseudo-square-pyramidal or a capped-octahedron structures. The schematic MO diagram for the interaction between the central metal atom and ligands in $CpML_3$ and $CpML_4$ complexes is illustrated in Fig. 3.6. [53, 54]

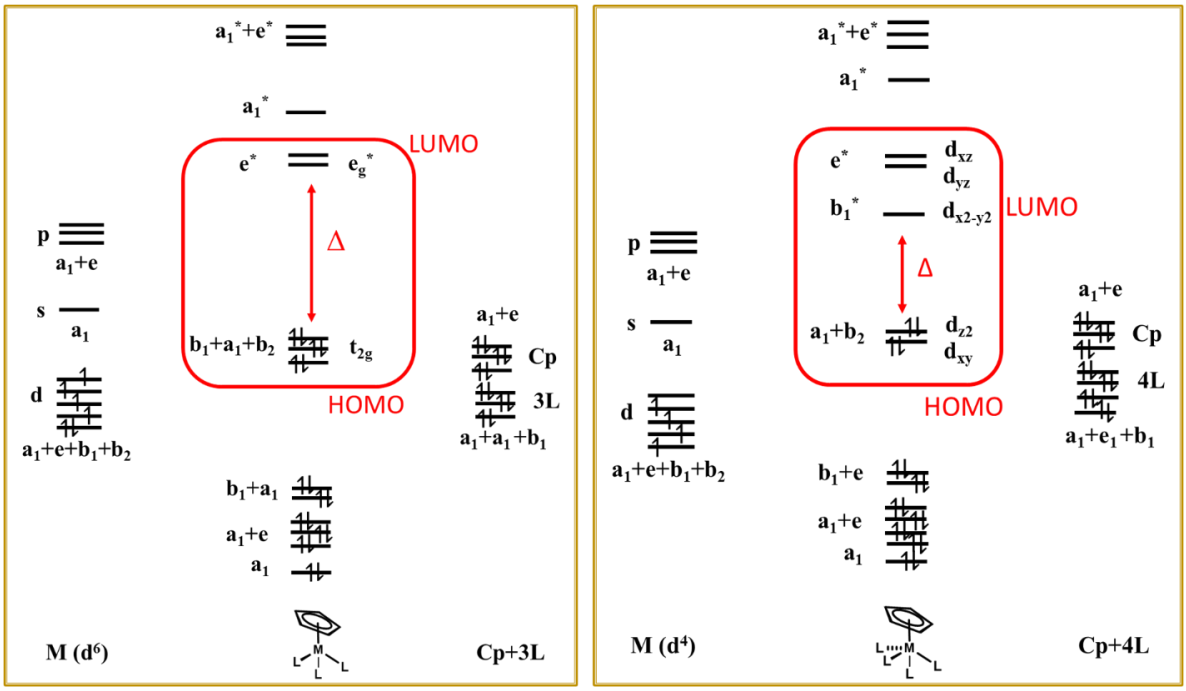

Fig. 3.6 Molecular orbital diagram for hexa-coordinated (left) and hepta-coordinated (right) half-sandwich metallocarbonyl complexes.

3.3 Results and Discussions

3.3.1 Metal-maleimide complexes

In the past, several organometallic complexes have been synthesized and used for various biochemical application, as discussed in Chapter 1. But there has been a negligible amount of work done to integrate the small-size, fluorescent maleimide-based ligands into organometallic complexes. In this chapter, we developed stable fluorescent ligands, coordinated them to the transition metals, and investigated the effect of complexation on their photophysical properties. Firstly, (η^5-cyclopentadienyl)M(CO)$_{2\text{-}3}$I (M = Fe: **3.7; 3.14**, Ru: **3.16**, and Mo: **3.18**). The metal iodide precursors were synthesized by the reaction of metallocarbonyl dimers [(η^5-C_5H_5)M(CO)$_{2\text{-}3}$]$_2$ with iodine (Scheme 3.1), as previously reported.[45, 48]

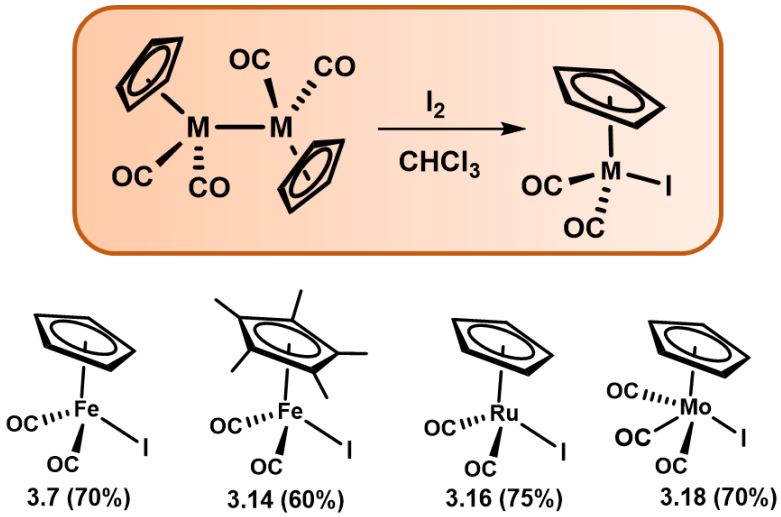

Scheme 3.1 Synthesis of metallocarbonyl iodide precursors.

Complexes **3.8**–**3.12** were synthesized by the photochemical reaction of (η^5-C_5H_5)Fe(CO)$_2$I (**3.7**) with different maleimide derivatives in the presence of diisopropyl amine under inert conditions (Scheme 3.2). Owing to their ease of synthesis and availability, 2,3-dibromomaleimide (DBM) and 3-bromo-4-(ethylamino)-1*H*-pyrrole-2,5-dione (ABM) (**3.1**) were chosen as the ligands to begin with, to obtain complexes (η^5-C_5H_5)Fe(CO)$_2$(η^1-*N*-dibromomaleimidato) (**3.8**; CpFe(CO)$_2$DBM) and (η^5-C_5H_5)Fe(CO)$_2$(η^1-*N*-3-bromo-4-ethylaminomaleimidato) (**3.9**; CpFe(CO)$_2$ABM), respectively.

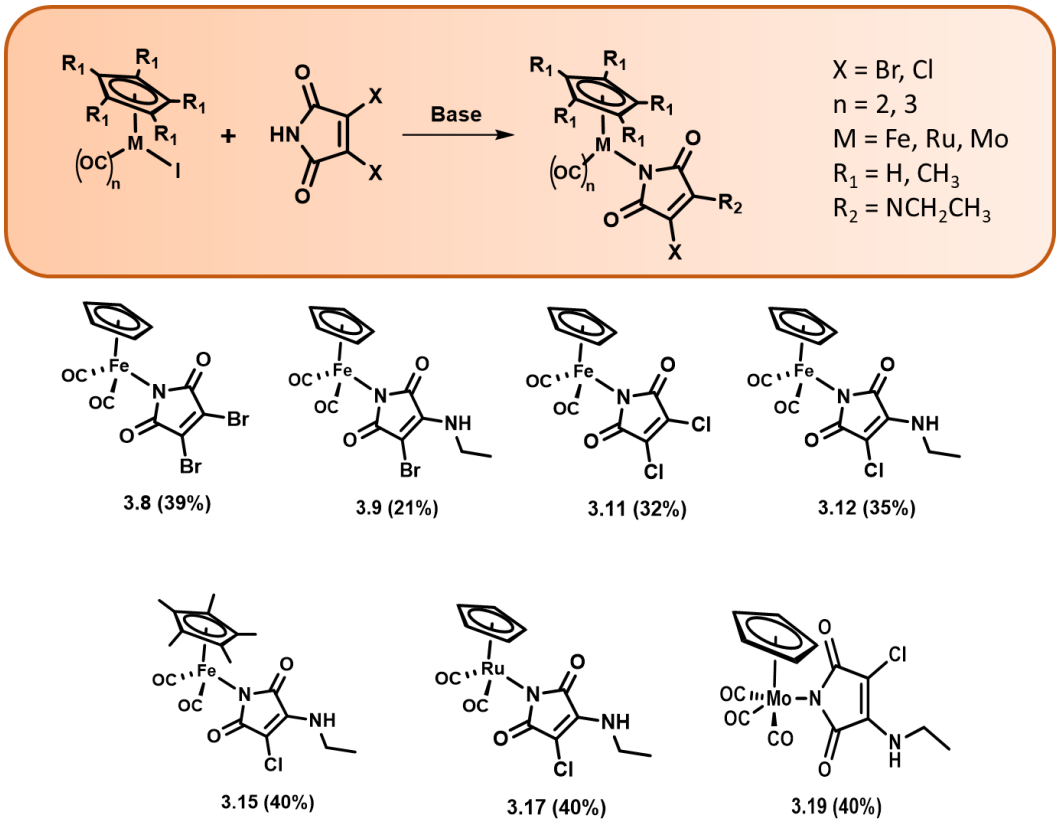

Scheme 3.2 Synthesis of metallocarbonyl maleimide complexes *via* the reaction metallocarbonyl iodide precursors with maleimide derived ligands.

Two synthetic approaches were identified to obtain the iron half-sandwich complex (η^5-C_5H_5)Fe(CO)$_2$(ABM) (Scheme 3.3). Route A involves the photochemical reaction of CpFe(CO)$_2$I with previously synthesized aminobromomaleimide ligand (**3.1**).[51] On the other hand, route B comprises of two steps. In first step, iron half-sandwich complex bearing the dibromomaleimide ligand (**3.8**) was obtained similar to the route A, while the second step involves the amine substitution of the dibromomaleimide moiety coordinated to the metal center. Owing to the better yields achieved, route A was chosen as a preferred method for the synthesis of these half-sandwich metallocarbonyl complexes.

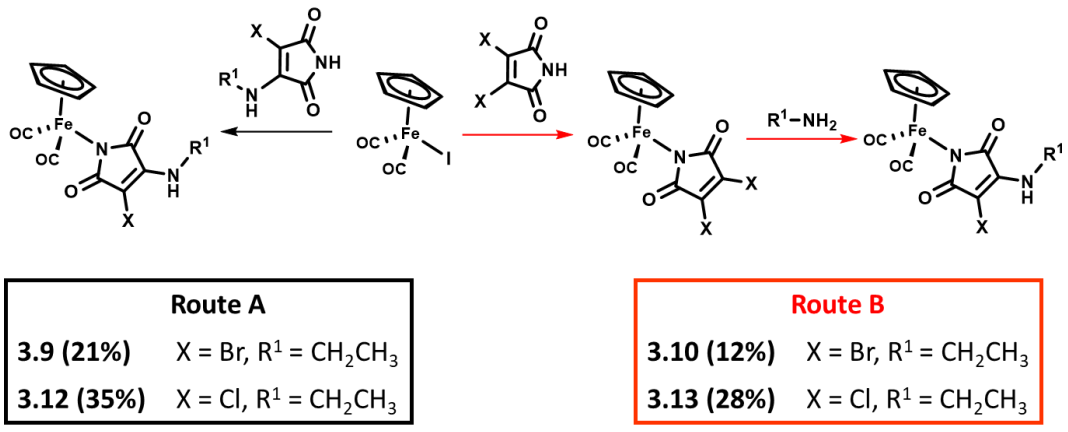

Scheme 3.3 Synthesis of η^5-cyclopentadienyldicarbonyliron aminohalomaleimide complexes *via* two routes.

Regardless of the choice of synthetic route, poor yields were observed for the synthesized (η^5-C_5H_5)Fe(CO)$_2$(ABM) complexes. It was hypothesized that (η^5-C_5H_5)Fe(CO)$_2$(ABM) complex may decompose to its respective aminomaleimide components when photoirradiated for longer durations. In ^{1}H-NMR spectra, complex

3.9 , displayed upfield signals for H2 (3.26-3.19 ppm) and H3 (4.82 ppm), compared to the ABM ligand **3.1** (H2 = 3.75– 3.66 ppm and H3 = 5.41 ppm), suggesting the formation of a complex. However, for **3.9,** a downfield but weak signal corresponding to the Cp ring was observed at 5.30 ppm, compared to the strong Cp peak at 5.08 ppm for complex **3.8**, which is an indicative of instability of iron aminobromomaleimide complex in solvents for longer periods (Fig. 3.7).

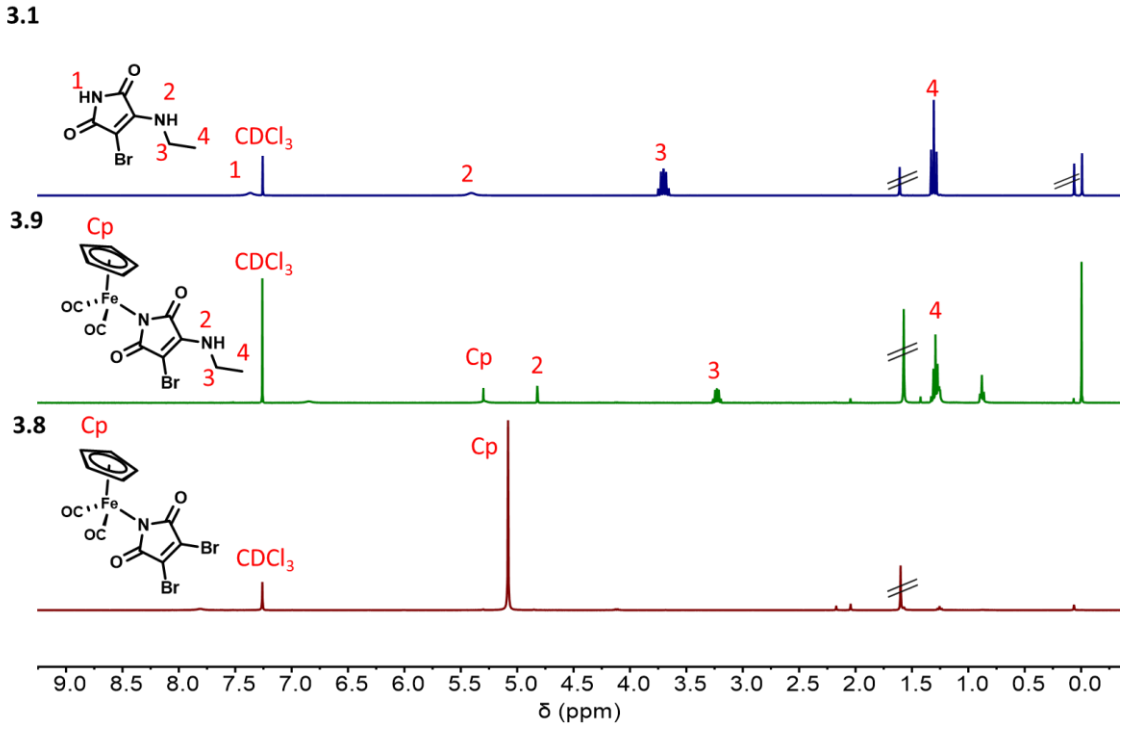

Fig. 3.7 ^{1}H NMR (400 MHz, $CDCl_3$) spectrum for **3.1**, **3.8**, and **3.9**.

This was further proved by the light-induced degradation process of (η^5-C_5H_5)$Fe(CO)_2$(ABM) complex. The half-sandwich complex **3.9** in methanol was illuminated with $h\nu$ = 365 nm for 48 h. The change in color and formation of brown precipitate is an indication of photodegradation.[55] The filtrate was collected and evaporated to obtain pale yellow crystals. APCI-MS displaying major peak $[M+H]^+$ at

141.05, as well as single crystal analysis of the acquired solid, corresponds to the aminomaleimide based side-product (Fig. 3.8), suggesting that aminobromomaleimide complex of iron is not stable. The carbonyl containing organometallic complexes containing in low oxidation-state are known to be light sensitive. Light could cause decoordination of the attached ligands, and results in the coordinatively unsaturated intermediates.[47] This explains the loss of Cp ring, metal atom and carbonyl groups from the synthesized organometallic complex, leading to a formation of aminomaleimide derivatives, as an indicative of the instability of half-sandwich iron bromomaleimide complexes.

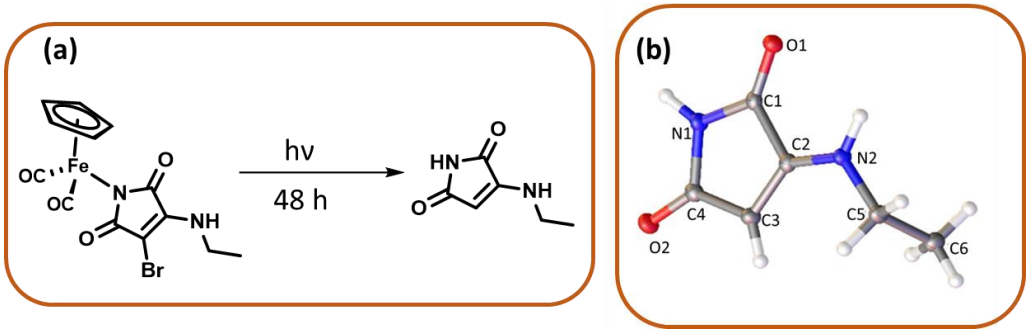

Fig. 3.8 Schematic illustration of photodegradation of metallocarbonyl complex **3.9** (**a**); and molecular structure of product obtained from degradation in crystal state (**b**).

Previously our group has reported that chloro-substituted maleimides are more stable relative to the bromo-substituted maleimides,[56] which encouraged developing chloro-substituted maleimides as ligands to form the half-sandwich metallocarbonyl complexes. Henceforth, applying the same method, (η^5-C_5H_5)Fe(CO)$_2$(η^1-*N*-dichloromaleimidato) (**3.11**; CpFe(CO)$_2$DCM) and (η^5-C_5H_5)Fe(CO)$_2$(η^1-*N*-3-chloro-4-ethylaminomaleimidato) (**3.12**; CpFe(CO)$_2$ACM) were synthesized by the reaction of

$CpFe(CO)_2I$ (**3.7**) with 2,3-dichloromaleimide (**3.2**) and 3-chloro-4-(ethylamino)-1*H*-pyrrole-2,5-dione (**3.3**), respectively (Scheme 3.2). The synthesized half-sandwich complexes were purified by column chromatography and characterized by ^{1}H, ^{13}C NMR, APCI-MS, FTIR and single crystal analysis (Fig. 3.13 & 3.30–3.33, experimental section 3.5.3). It is noteworthy that the selection of light source of a suitable wavelength, and that for an appropriate duration are important parameters for these reactions. Higher yields were obtained when the reaction mixtures were illuminated with ultraviolet light while the illumination by visible light (Table 3.2; entry no. 1) didn't lead to satisfactory conversions of the products. Furthermore, longer exposure to the light source resulted into the formation of photodegraded side-products, thus lowers the yield. Therefore, a couple of reactions were performed to optimize the reaction conditions for the synthesis of targeted half-sandwich complexes (Table 3.2).

Table 3.2 Summary of conditions attempted for the synthesis of half-sandwich iron aminochloromaleimide complex **3.12.**

#	**Reactants**	**Conditions**	**Duration**	**Light source**	**Yield (%)**
1	$CpFe(CO)_2I$ (**3.7**) & ACM (**3.3**)	N_2, DIPEA, Benzene	2.5 h	Visible light	2%
2	$CpFe(CO)_2I$ (**3.7**) & ACM (**3.3**)	N_2, DIPEA, Benzene	2.5 h	$h\nu$ = 365 nm	~20%
3	$CpFe(CO)_2I$ (**3.7**) & ACM (**3.3**)	N_2, Na_2CO_3, Benzene	2.5 h	$h\nu$ = 365 nm	<12%
4	$CpFe(CO)_2I$ (**3.7**) & ACM (**3.3**)	N_2, DIPEA, Benzene	4.5 h	$h\nu$ = 365 nm	35-40%
5	$CpFe(CO)_2I$ (**3.7**) & ACM (**3.3**)	N_2, DIPEA, Toluene	4.5 h	$h\nu$ = 365 nm	15%

It was observed that using a strong inorganic base resulted in the formation of significant side product (Table 3.2; entry no. 3), and using toluene as solvent led to very slow conversion (Table 3.2; entry no. 5). However, illuminating the reaction mixture with appropriate wavelength is the most significant requirement (Table 3.2; entry 4).

Subsequently, the appropriate metal iodide complexes Cp*Fe(CO)$_2$I (**3.14**), CpRu(CO)$_2$I (**3.16**), and CpMo(CO)$_3$I (**3.18**) were synthesized, by applying the same method as for **3.7**. These metal iodide precursors reacted with aminochloromaleimide (**3.3**) upon irradiation with $h\nu$ = 365 nm in the presence of diisopropylamine to produce (η^5-C$_5$(CH$_3$)$_5$Fe(CO)$_2$(η^1-*N*-3-chloro-4-ethylaminomaleimidato) (**3.15**), (η^5-C$_5$H$_5$)Ru(CO)$_2$(η^1-*N*-3-chloro-4-ethylaminomaleimidato) (**3.17**), and (η^5-C$_5$H$_5$)Mo(CO)$_3$(η^1-*N*-3-chloro-4-ethylaminomaleimidato) (**3.19**) complexes.[49, 57] These half-sandwich complexes were characterized by ^{1}H, ^{13}C NMR, APCI-MS, and single crystal XRD analysis (Fig. 3.13 & 3.34–3.45, experimental section 3.5.3). All the metallocarbonyl maleimide complexes displayed a downfield signal, for the Cp ring (**3.12**: 85.8 ppm; **3.15**: 96.5 ppm; **3.17**: 88.4 ppm; and **3.19**: 95.7 ppm), relative to their respective metal iodide precursors (**3.7**: 84.0 ppm; **3.14**: 96.0 ppm; **3.16**: 87.1 ppm; and **3.18**: 94.3 ppm). All these complexes are sufficiently stable and can be stored for months, except **3.19.** Notably, **3.19** decomposed relatively quickly compared to the other metal-maleimide complexes. When exposed to light and air for a prolonged period of time, the color changes from orange to green, which is caused by the light-induced degradation process. Upon analysis of the photodegraded product (of the complex **3.19**) using ^{1}H, ^{13}C NMR spectroscopy and APCI-mass spectrometry, there was no observed difference for the samples displaying different colors. However,

single crystal XRD analysis yielded a different result. Interestingly, single crystal XRD analysis indicated the presence of polymorph structures originating from the complex (Fig. 3.9). These structures have the same chemical formula (of the decomposition product, i.e., ACM) but different structural orientations within the unit cell. The color change from orange to green corresponds to the change in oxidation state of molybdenum atoms from +2 to +3, as a result of photodegradation.[58]

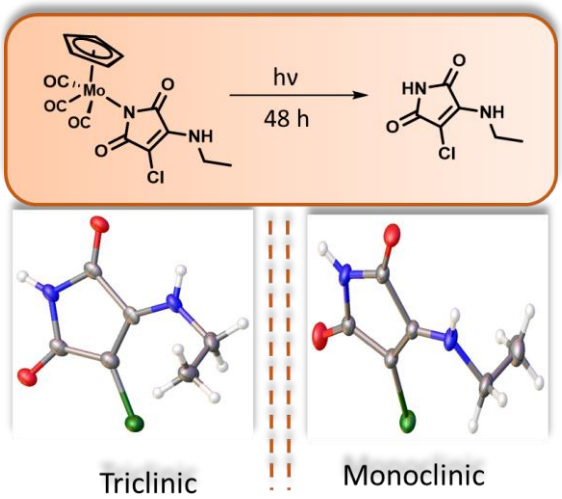

Fig. 3.9 Schematic illustration of photodegradation of **3.19** and molecular structure of observed polymorphs in crystal state.

In order to obtain another complex η^5-$C_5H_5Co(CO)IACM$, η^5-$C_5H_5Co(CO)I_2$ (**3.21**) was synthesized and characterized successfully, following an established protocol (Fig. 3.48–3.49).[59] Several attempts were made to obtain the complex CpCo(CO)ACM, by reacting **3.21** with the aminomaleimide ligand**,** although none of them were successful. Comparison of the ^{13}C NMR spectra, recorded before and after reaction, displayed a lot of unidentified peaks along with multiple Cp peaks, indicating the decomposition

and instability of the targeted complex. Unfortunately, due to the unavailability of more dimer precursors, we were unable to target more metals to develop the half-sandwich metallocarbonyl complexes.

Additionally, another dithiomaleimide (DTM) based fluorescent half-sandwich complex was synthesized, using the approach similar to the $CpFe(CO)_2ACM$ complex. Using this approach, the pre-synthesized DTM derivative **3.4** was employed as a ligand, and reacted with **3.7** in the presence of a base under inert conditions (Scheme 3.4). The complex η^5-$C_5H_5Fe(CO)_2$(DTM) (**3.20**) was purified *via* column chromatography and characterized by ^1H, ^{13}C NMR, APCI-MS and IR spectroscopy (Fig. 3.46–3.47). The brown complex obtained product was viscous in nature, and we were unable to grow crystals for this compound. In ^{13}C NMR spectra (Fig. 3.10), **3.20** appearance of Cp and C≡O peaks at 85.6 ppm and 213.5 ppm, respectively, and a downfield signal for C=C at 138.7 relative to **3.4**, which displayed C=C peak at 136.8, suggest the successful synthesis of complex **3.20**. Furthermore, the peak for [M^+] observed at *m/z* = 449.96 in AP-MS, confirmed the complex **3.20** has been synthesized successfully.

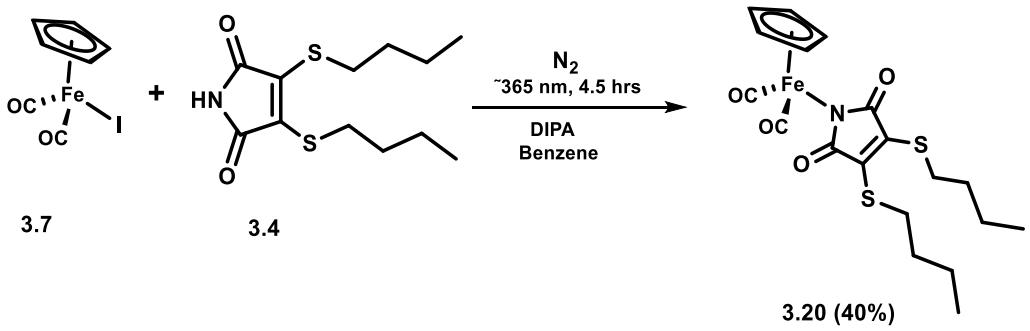

Scheme 3.4 Synthesis of half-sandwich iron dithiomaleimide complex **3.20**.

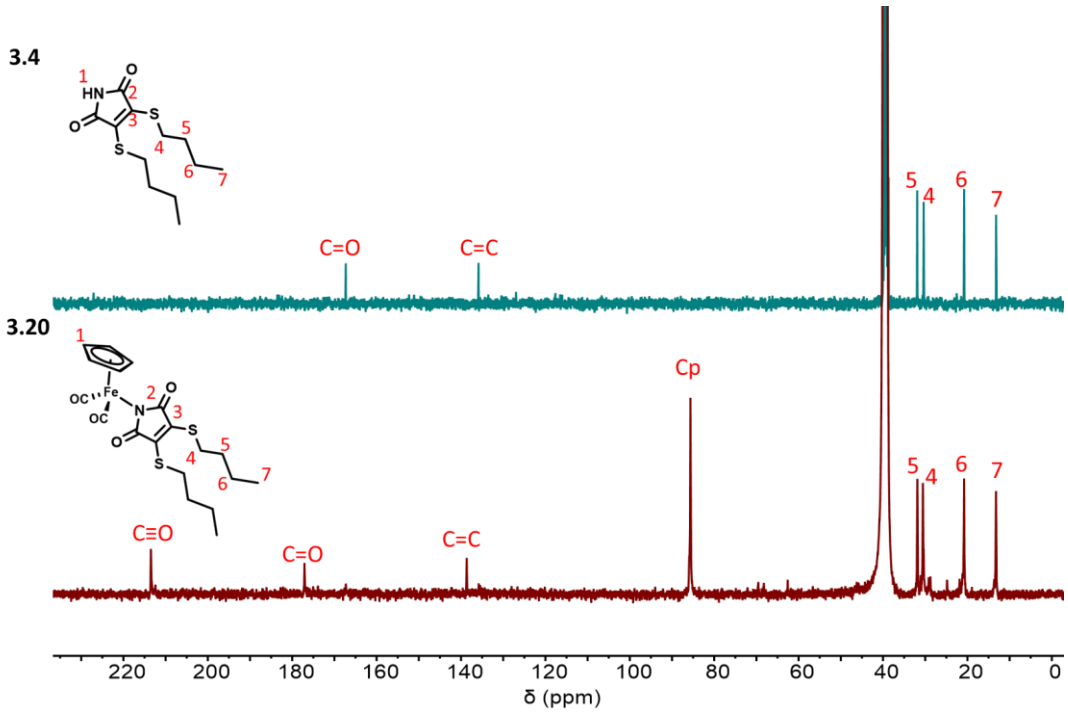

Fig. 3.10 ^{1}H NMR (400 MHz, $CDCl_3$) spectrum for DTM (**3.4**), and $CpFe(CO)_2$DTM (**3.20**).

In order to explore the potential use of half-sandwich complexes containing maleimides as ligands, maleimide coordination to the metal atom at amine position was investigated (Scheme 3.5). The synthesis of the complex $CpFe(CO)_2$(Me-ACM) was targeted through three different routes *via* cationic complex of iron as an intermediate. The cationic complexes of metal such as iron, $[CpM(CO)_2L]^+$ are an important class which have been significantly utilized for the applications, such as synthesis and catalysis.[60, 61] Reaction of $CpFe(CO)_2I$ (**3.7**) with a large excess of anhydrous diethyl ether in dichloromethane and in the presence of silver tetrafluoroborate under inert atmosphere, produced red color compound $[CpFe(CO)_2(OEt_2)]^+$ (**3.23**) (Scheme 3.5). The moisture sensitive, cationic complex **3.23** is formed as a result of halide abstraction from **3.7** by $AgBF_4$,[62] and is partially soluble in chloroform but highly soluble in

dichloromethane. The characteristic peak of Cp at 5.36 ppm in ^{1}H NMR spectrum as well as at 85.6 ppm in ^{13}C NMR spectrum, confirms the successful synthesis of diethyl ether complex of iron.

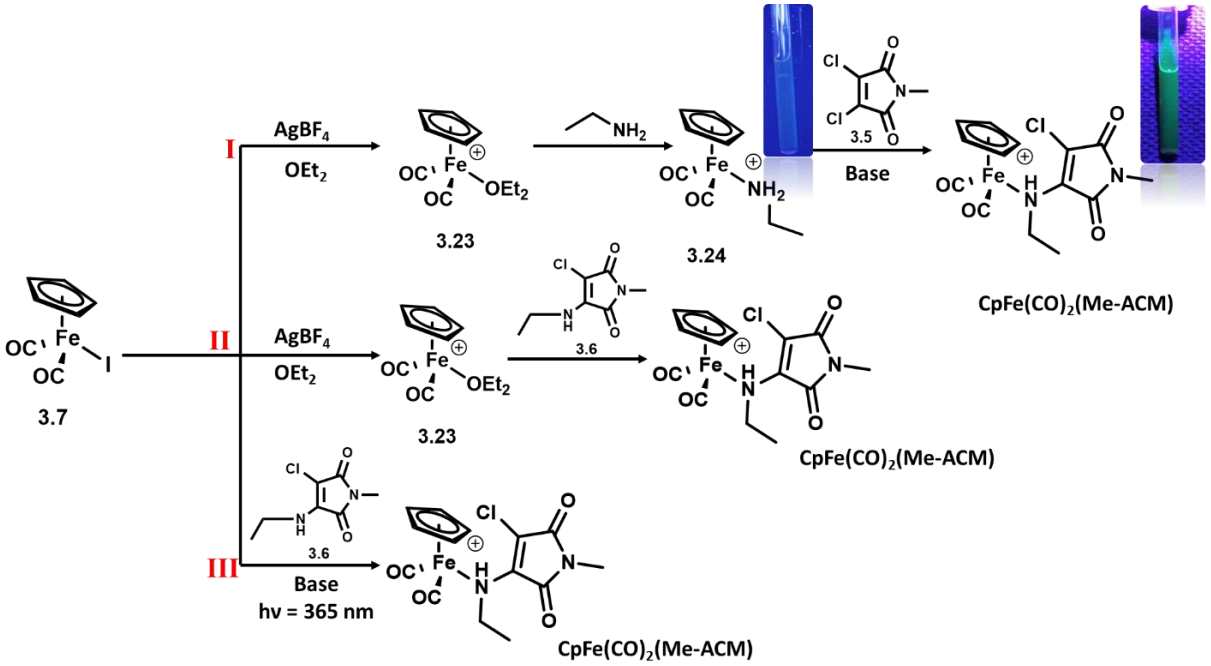

Scheme 3.5 Scheme for the synthesis of **CpFe(CO)$_2$(Me-ACM)** complex.

The diethyl ether ligand is very labile in the complex [CpFe(CO)$_2$(OEt$_2$)]BF$_4$ (**3.23**), and can be replaced easily when reacted with ethylamine in dry dichloromethane, to form yellow crystals of amine containing cyclopentadienyldicarbonyl complex of iron (**3.24**). The aminoalkane complex has been characterized by ^{1}H and ^{13}C NMR spectroscopy. In ^{1}H NMR spectrum, **3.24** shows a singlet at 2.90 ppm assignable to the two amine protons, which is a downfield shift relative to free amine (1.50 ppm). Additionally, an upfield signal for Cp ring at 5.27 ppm relative to **3.23** and a quartet 2.57–2.44 at ppm and a triplet at 0.99–0.95 ppm corresponding to -CH$_2$ and -CH$_3$, respectively, confirms

the synthesis of $CpFe(CO)_2(NH_2CH_2CH_3)$ (**3.24**) successfully (experimental section 3.5.3).

For a final step, the non-fluorescent complex **3.24** reacted with methylated dichloromaleimide (**3.5**; Me-DCM) in the presence of a base. The onset of fluorescence was an indication of the formation of the desired complex. The fluorescent product was purified and analyzed by NMR spectroscopy. The ^{13}C NMR spectrum, indicated the presence of decomposed product, which is methylated aminochloromaleimide (Me-ACM), instead of the targeted complex ($CpFe(CO)_2$(Me-ACM)). Additionally, AP-MS spectrum showed a peak at *m/z* = 189.04, corresponding to the Me-ACM (Fig. 3.11), which explains the fluorescence noted for the reaction mixture. We also attempted precipitation/ recrystallization to obtain the purified product but it was ineffective due to the similar solubilities of Me-DCM and desired product. Then again, the ^{13}C NMR spectra of crude product was analyzed and compared with the reactants $CpFe(CO)_2(NH_2CH_2CH_3)$ (**3.24**) and Me-DCM (**3.5**). The downfield signals displayed for Me and CH_2 groups, suggested the possibility of a reaction happening, although the rate of the desired reaction is very slow, as the peaks (such as C=O and C=C at 162.8 and 133.1 ppm, respectively) for the unreacted Me-DCM can be noticed (Fig. 3.12). Additionally, extremely weak signal for Cp ring suggested that the compound is either not stable or the reaction conditions were not very feasible. It was hypothesized that the desired reaction is possibly in competition with the formation of Me-ACM product, as confirmed by AP-MS and NMR spectroscopy.

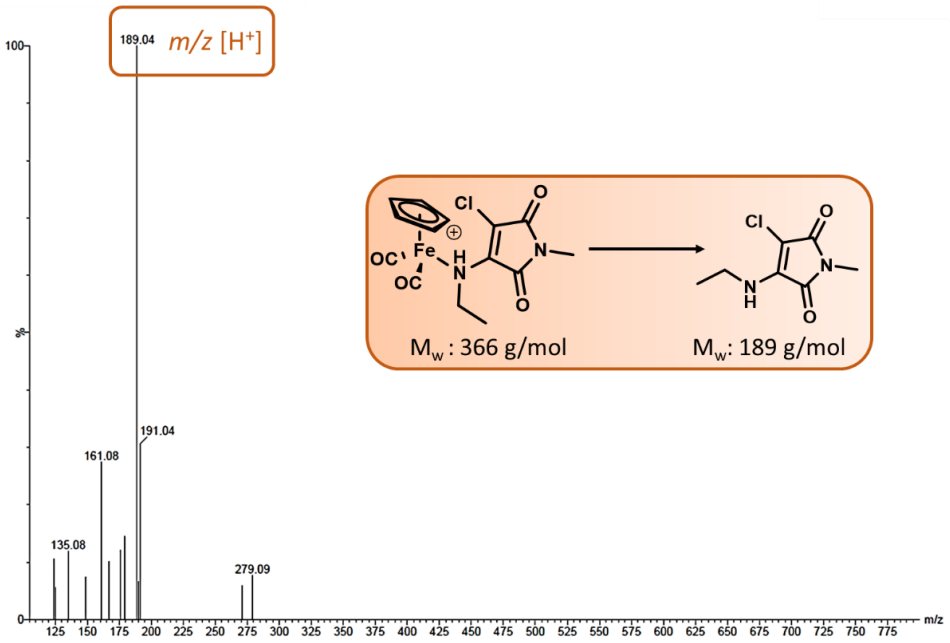

Fig. 3.11 APCI-MS spectrum for the product obtained by reacting **3.24** with **3.5**.

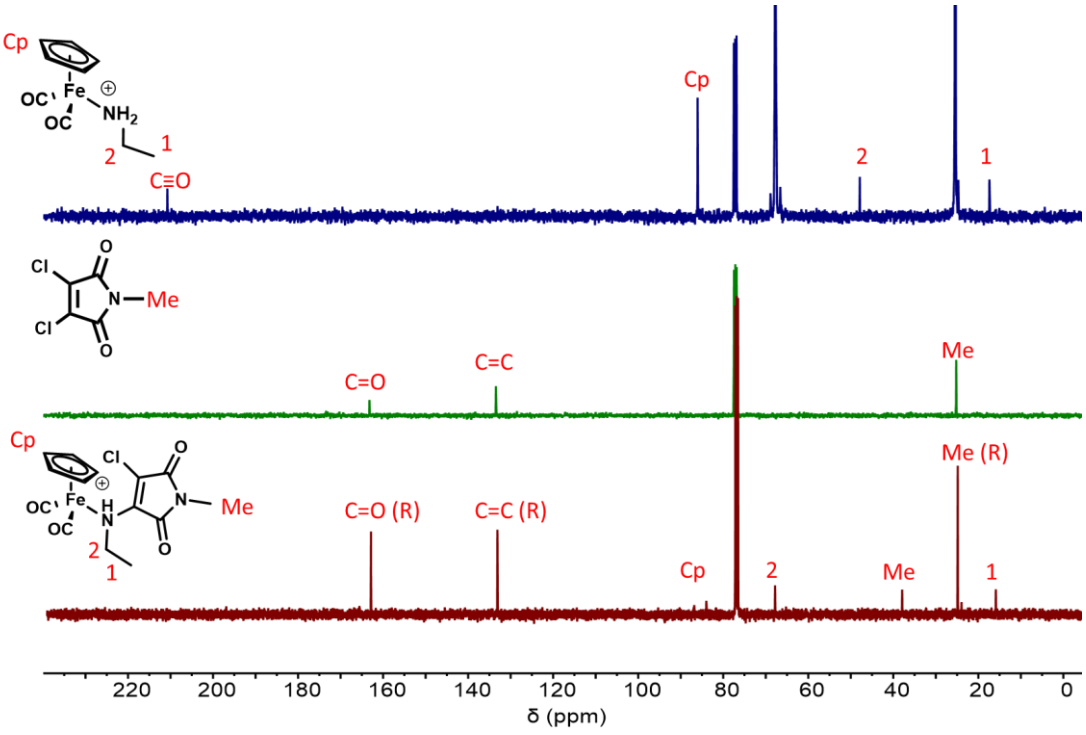

Fig. 3.12 Comparison of ^{13}C NMR spectra for the crude reaction mixture with **3.24** and **3.5**.

In the second approach (approach-II) to the synthesis of metal-maleimide complex $[CpFe(CO)_2(Me\text{-}ACM)]^+$, the diethyl ether complex $[CpFe(CO)_2(OEt_2)]^+$ (**3.23**) was synthesized in the first step, similarly to the approach-I (described above), which was then allowed to react with pre-synthesized Me-ACM ligand (**3.6**) (Scheme 3.5). Although, the time duration for this reaction was doubled, no physical changes were observed. This is contrary to the reaction of $[CpFe(CO)_2(OEt_2)]^+$ with ethyl amine (from approach-I) where immediate color change of reaction mixture from red to brown occurred, followed by the formation of fluorescent yellow crystalline solid. Furthermore, when analyzed by NMR spectroscopy, the results obtained are similar to the ones observed in the former case (approach-I), i.e., degradation.

In the final attempt, approach-III, the $CpFe(CO)_2I$ (**3.7**) was photochemically reacted with the Me-ACM (**3.6**), using the conditions optimized for the half-sandwich complexes mentioned previously (Scheme 3.5).[51] The reaction was carried out for 6 h, along with the progress of reaction monitored by TLC. It was noticed that the concentration of iron iodide precursor (**3.7**) decreased over time, however no other spot beside the reactants was observed. This led to the two possibilities: either the base is not strong enough to activate the nitrogen or reaction is not feasible to obtain the, possibly air sensitive, compound. In order to prove the former statement, sodium carbonate (a stronger base than diisopropyl amine) was used, though there was no luck with synthesis of the targeted complex. Despite a lot of efforts, the synthesis of the targeted complex $CpFe(CO)_2(Me\text{-}ACM)$ remained unsuccessful.

3.3.2 Crystal structure description

The molecular structures of complexes $CpFe(CO)_2DCM$ (**3.11**); $CpFe(CO)_2ACM$ (**3.12**); $Cp^*Fe(CO)_2ACM$ (**3.15**); $CpRu(CO)_2ACM$ (**3.17**); and $CpMo(CO)_3ACM$ (**3.19**) were determined by single crystal XRD analysis and are presented in Fig. 3.13.

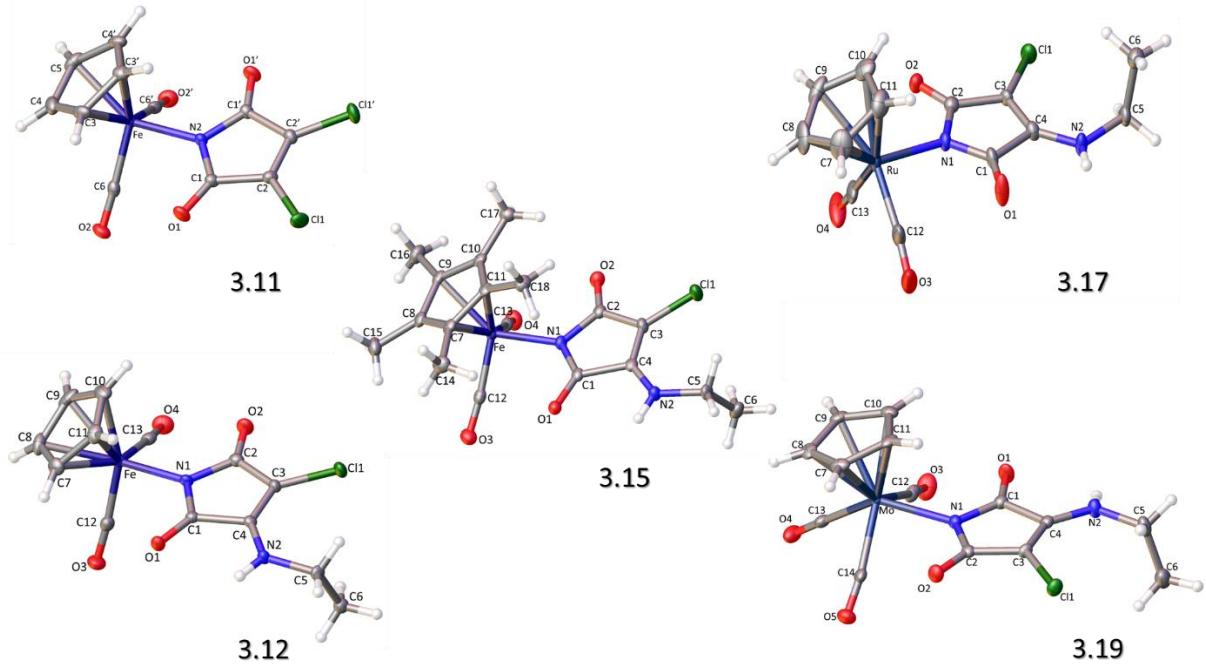

Fig. 3.13 Molecular structures of complexes **3.11**, **3.12**, **3.15**, **3.17** and **3.19** in the single crystal state.

Complexes **3.12**, **3.15**, and **3.17** crystallized in centrosymmetric space group P-1 triclinic, while **3.11** and **3.19** crystallized in Cmce orthorhombic and $P2_1$ monoclinic, respectively, space groups. In all the complexes, the metal atom is bonded to the cyclopentadienyl ring (C7-C8-C9-C10-C11; Cg referred to as center of gravity of the cyclopentadienyl ring), nitrogen atom (N1) of the maleimide moiety, and two carbonyl ligands (C12-O3, and C13-O4), with **3.19** as exception which contains three carbonyl

ligands (C12-O3, C13-O4, and C14-O5). The distance between the iron atom and centroid of the cyclopentadienyl ring (Fe-Cg) for complexes **3.11**, **3.12** and **3.15** were 1.7129 (13), 1.7170 (12) and 1.7263 (10) Å, respectively. These bond lengths were slightly shorter than the distance between the carbonyl ligands and iron atoms (Fe-C12, and Fe-C13) and are in the range of 1.780 (3) – 1.789 (2) Å. In comparison, the corresponding distances were longer for **3.17** (Ru-Cg: 1.8840 Å, Ru-C12: 1.872 (3) Å and Ru-C13: 1.878 (4) Å), which in turn were shorter than the **3.19** (Mo-Cg: 1.9950 (17) Å, Mo-C12: 2.018(4) Å, Mo-C13: 2.005 (4) Å, and Mo-C14: 2.039 (3) Å).

Furthermore, the Fe-N1 bond was observed to be 1.965(2) Å, 1.9646(16) Å, and 1.9743(18) Å for **3.11**, **3.12** and **3.15**, whereas for Ru-N1 in **3.17** and Mo-N1 in **3.19**, it corresponded to 2.073(2) Å and 2.176(3) Å. The distances C1-O1 and C2-O2 of maleimide coordinated to metal are shortest for **3.19**, equals to 1.212 (5) Å and 1.219 (4) Å, respectively, compared to rest of the complexes for which they are in the range of 1.214 (3) – 1.230 (3) Å. The half-sandwich complexes (**3.11**, **3.12**, **3.15**, and **3.17**) exhibited pseudo-octahedral “three legged piano-stool” geometry, where the cyclopentadienyl moiety occupies facially three coordinated sites,[63] while the maleimide acts as a monodentate ligand, in addition to the two carbonyl atoms. On the other hand, complex **3.19**, showed capped octahedron structure (coordination no. 7) as “four legged piano-stool” geometry. Some of the previous works had also reported these type of complexes as tetrahedron strongly deformed in the direction of trigonal pyramidal structures.[51, 64-66] This was vindicated by considering the centroid of the cyclopentadienyl ring (Cg) occupying one coordination site instead of three, which makes the overall coordination number of 4 to 5 (depending on the number of other ligands attached), and was justified by the valence angles around metal to be 90° and

120° in the crystal state (Table 3.3). Hence, these complexes are not considered as ideal octahedral complexes, despite being 18-electron saturated,[67] and acquiring six coordination number.

Table 3.3 Intermolecular contacts measured from solvent crystal structures of the half-sandwich metallocarbonyl maleimide complexes. **3.12** i: 1-X,1-Y,1-Z; **3.15** i: -X,1-Y,-Z; **3.17**i: 1-X,1-Y,-Z; ii: -X,-Y,2-Z; **3.19** i: +X,+Y,1+Z; ii: 1-X,1/2+Y,1-Z.

Compound	**Bond D-H···A**	**Bond Length d(H-A) / Å**	**Angle D-H-A / °**	**Form**
3.12	N2−H2···O101	2.08(2)	147(2)	Chain
	N102−H102···O1	2.19(3)	150(2)	
	C9−H9···O104^{i}	2.64	126.3	
3.15	N2−H2···O1^{i}	2.116(19)	155 (2)	Dimer
3.17	N2−H2···O1^{i}	2.18(4)	150(3)	Dimer
	N102−H102···O101^{ii}	2.18 (5)	145 (5)	
3.19	N2−H2···O2^{i}	2.10(5)	150(4)	Chain
	C9−H9···O1^{ii}	2.60	168.4	
	C5−H5A···Cl^{ii}	2.85	121.0	

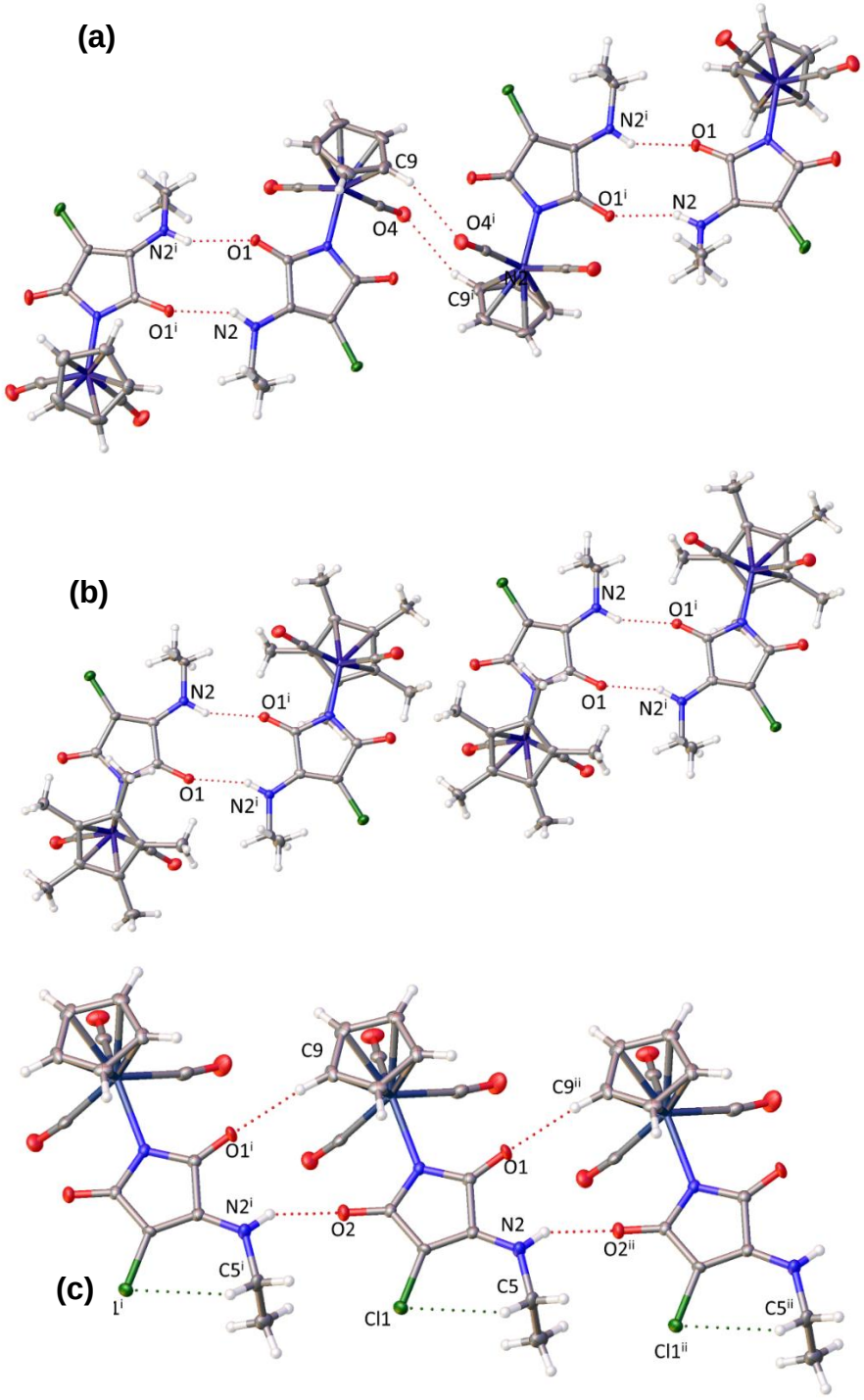

Fig. 3.14 Intermolecular interactions shown by dotted line in **3.12** (**a**), **3.15** (**b**), and **3.19** (**c**).

The packing modes of the complexes (Fig. 3.14) showed the intermolecular N−H···O interactions, leading to the formation of a one-dimensional chain of molecules in **3.12** and **3.19,** whereas dimers were observed for **3.15** and **3.17** packed as parallel layers (Table 3.3). The molecules are oriented in the same direction within each layer for **3.19**, while for **3.12**, **3.15**, and **3.17** in the opposite direction, in order to minimize steric repulsion. Notably, **3.12** exhibited additional C9-H9···O4^{i} (~C9^{i}-H9^{i}···O4) forming intermolecular contacts between the inverted dimers, leading to the zigzag arrangements stacked as parallel layers. In addition to the N−H···O hydrogen bonds, **3.19** exhibited intramolecular C5-H5A···Cl1 distances, and intermolecular C9−H9···O1^{i} (C9 ^{ii}−H9 ^{ii}···O1) distances, through carbonyl (C=O) of the maleimide and hydrogen of the cyclopentadienyl ring equals to 2.85 Å and 2.60 Å, respectively (Table 3.3).

3.3.3 Photophysical properties

To gain the insight into the influence of complexation on the optical properties of maleimides, quantum yields of acquired half-sandwich metallocarbonyl maleimide complexes were evaluated. No fluorescence was observed for the complex **3.11**; CpFe(CO)$_2$DCM, containing the di-halogenated maleimide ligand (**3.2**), which lacks the essential push-pull mechanism required for fluorescence, due to the absence of electron-donating groups on the maleimide moiety. Alternatively, upon complexation of the metals with aminochloromaleimide derivatives, blue-green emissions were observed. The emission properties of the acquired half-sandwich complexes (**3.12**, **3.15**, **3.17**, **3.19** and **3.20**) synthesized in section 3.3.1 were evaluated and compared with their respective maleimide ligands (**3.3** and **3.4**). The absorption and emission spectra of these half-sandwich complexes were equated at the same concentration

(10 µM) using a range of solvents with different polarities (Table 3.4). All the complexes, analogous to non-coordinated ligand, exhibited solvatochromic behavior when dissolved in polar solvent, resulting in the stabilization of ground and excited states due to the solute-solvent interactions (Fig. 3.15; Table 3.4).

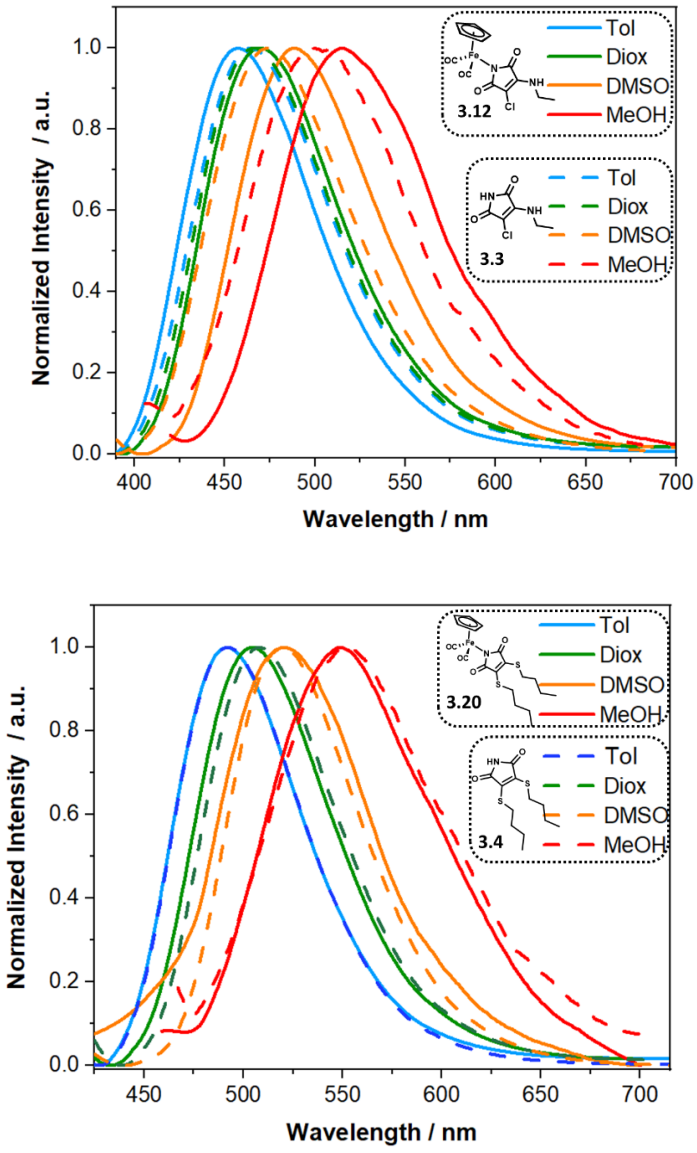

Fig. 3.15 Comparison of the normalized emission spectra of the half-sandwich complexes **3.12** and **3.20** *vs* the ligands **3.3** and **3.4** in different solvents (10 µM).

Table 3.4 Fluorescent properties of the half-sandwich metallocarbonyl maleimide complexes (**3.12**, **3.15**, **3.17**, **3.19**, and **3.20**) and their respective ligands (**3.3** and **3.4**) in solution-state (10 μM) and in solid-state (ϕ_f = relative quantum yield in different solvents using quinine sulfate as reference, and absolute quantum yield in solid-state using integrating sphere; λ_{max} = maximum absorption wavelength; ε_{max} = molar absorption coefficient; B = Brightness; λ_{ex} = excitation wavelength ; λ_{em} = maximum emission wavelength; $\Delta\lambda$ = Stokes shift ; slit width ex 1.0 nm, em 1.0 nm; 25°C).

Compound	Solvent	ϕ_f (%)	ε_{max} ($M^{-1}cm^{-1}$)	B ($M^{-1}cm^{-1}$)	λ_{max} (nm)	λ_{ex} (nm)	λ_{em} (nm)	$\Delta\lambda$ (nm)
3.3	Ether	48	5916	284006	363	359	458	99
	Toluene	41	4538	186082	360	363	461	98
	THF	37	5553	205494	361	363	471	108
	Dioxane	31	3893	120704	368	363	471	108
	DMSO	17	4783	81312	376	369	486	117
	Methanol	<1	4419	4535	368	366	517	151
	Powder	15	-	-	-	360	491	-
3.4	Ether	11	3519	98532	396	396	492	95
	Toluene	10	3171	66591	400	399	500	99
	THF	6	2984	44760	401	401	501	102
	Dioxane	5	2304	23040	404	401	501	97
	DMSO	<1	1619	4857	405	401	521	120
	Methanol	<1	1230	615	400	397	551	154
3.12	Ether	36	5954	214358	362	359	459	100
	Toluene	32	4271	136675	361	361	462	101
	THF	24	4522	108537	360	363	466	103
	Dioxane	30	3893	116811	361	363	469	106
	DMSO	11	4677	51451	365	370	490	120
	Methanol	<1	4494	2247	367	373	519	146
	Powder	<1	-	-	-	361	495	-

3.15	Ether	33	5228	172543.8	359	357	459	102
	Toluene	30	5345	160365	360	359	465	106
	THF	24	5464	131145	361	360	469	109
	Dioxane	25	4118	102965	362	363	472	109
	DMSO	8	5227	41816	370	368	489	121
	Methanol	<1	5622	1686	368	370	516	146
	Powder	<1	-	-	-	361	493	-
3.17	Ether	11	8092	89013	363	345	455	110
	Toluene	10	6570	65697	365	349	458	109
	THF	8	8026	64205	366	350	460	110
	Dioxane	5	7698	34891	367	351	464	113
	DMSO	3	9862	29585	376	357	476	119
	Methanol	<1	8340	4170	379	359	502	143
	Powder	<1	-	-	-	362	491	-
3.19	Ether	50	4434	221725	356	360	463	103
	Toluene	45	3714	167166	358	362	465	103
	THF	41	3603	147743	362	364	468	104
	Dioxane	47	4214	198086	363	365	471	106
	DMSO	19	4409	83786	375	372	489	117
	Methanol	1	2852	3422	369	370	515	145
	Powder	<1	-	-	-	365	495	-
3.20	Ether	15	3553	106590	397	397	491	94
	Toluene	11	3092	77300	399	399	502	99
	THF	4	2784	27840	400	404	505	103
	Dioxane	3	2180	17440	401	404	507	103
	DMSO	<1	1453	2179.5	404	405	521	117
	Methanol	<1	1124	449.6	406	405	545	144

The brightness B of the fluorophore determines its analytical sensitivity, and can be calculated by the product of ϕ_f and the molar absorption coefficient at the excitation wavelength (ε_{max}) (Table 3.4). For this purpose, molar absorption coefficient for the synthesized half-sandwich maleimide complexes ACM was calculated by dilution method. The solutions of six different concentrations were made (5 μM, 7.5 μM, 10 μM, 12.5 μM, 15 μM and 20 μM); each in six different solvents and run their absorptions spectra. The plot of concentration *vs* absorption followed a linear equation, and molar absorption coefficient was identified as a slope. Organometallic complexes tend to exhibit various electronically excited state upon coordination, as explained in section 3.2. Molar absorptivities observed in the range of 10^3 – 10^4 $M^{-1}cm^{-1}$, suggested the observed transitions are attributed to the intraligand (IL) excited states.

To quantify this further, reference quantum yields[68] of aminochloromaleimide containing complexes (**3.12**, **3.15**, **3.17, 3.19**), against the ligand (**3.3**), were investigated, to explore the effect of coordinating different metal centers to the maleimide (Fig. 3.16). Amongst all the acquired complexes, $CpMo(CO)_3ACM$ (**3.19**) demonstrated highest ϕ_f (50% in diethyl ether), along with largest Stokes shift in the range of 103 – 145 nm. This is slightly higher than ϕ_f recorded for the ACM ligand (48% in diethyl ether), while on the other hand $CpFe(CO)_2ACM$ (**3.12**) showed ϕ_f lower than the ACM (36% in diethyl ether). It was hypothesized that coordinating the metal with maleimide pushes the electron density away from the ring, thus reduces the twisted intramolecular charge transfer (TICT) between the maleimide and the solvent molecules. The higher ϕ_f observed for **3.19**, corresponds to the higher electronegativity of the Mo atom, that minimized TICT by pulling electron density away from the maleimide ring, and establishing back bonding between the metal atom and the

aminochloromaleimide ligand. However, no significant red shift in the emission maxima, for the half-sandwich complexes was observed on attaching the metal center to the maleimide derivatives. Although, an iron metal center, possessing the electronegativity value lower than molybdenum atom but higher than hydrogen atom, showed ϕ_f comparable to the aminochloromaleimide ligand. Based on the electronegativity trend, another complex $CpRu(CO)_2ACM$ (**3.17**) was targeted and evaluated its ϕ_f to test the hypothesis further. Interestingly, the introduction of ruthenium metal which is more-electronegative than molybdenum, depicting the electronegativity trend: Fe (1.83) < Mo (2.16) < Ru (2.20), quenched the fluorescence instead of increasing the ϕ_f, by facilitating the non-radiative decay and switching off the fluorescence. This can be further explained on the basis of bond strengths, and interactions between ligands and metal atoms, assessed by the FTIR spectroscopy, and also mirrored by the single crystal XRD data.

In order to investigate the contribution of other ligands coordinated to the metal (i.e. cyclopentadienyl in this case) on the optical properties of maleimide, ϕ_f of the $Cp^*Fe(CO)_2ACM$ complex (**3.15**) was evaluated. Compared with quantum efficiency of the $CpFe(CO)_2ACM$ (**3.12**), $Cp^*Fe(CO)_2ACM$ (**3.15**) showed slightly lower emissions (33% in diethyl ether; 8% in dimethyl sulfoxide) (Fig. 3.16). The substitution of the cyclopentadienyl (Cp) ring with methyl groups, increases the electrophilicity of ligand coordinated to the metal atom. However, no significant effect on ϕ_f, indicates that changing the metal center attached to maleimide is more effective than altering the electronics of the auxiliary ligands.

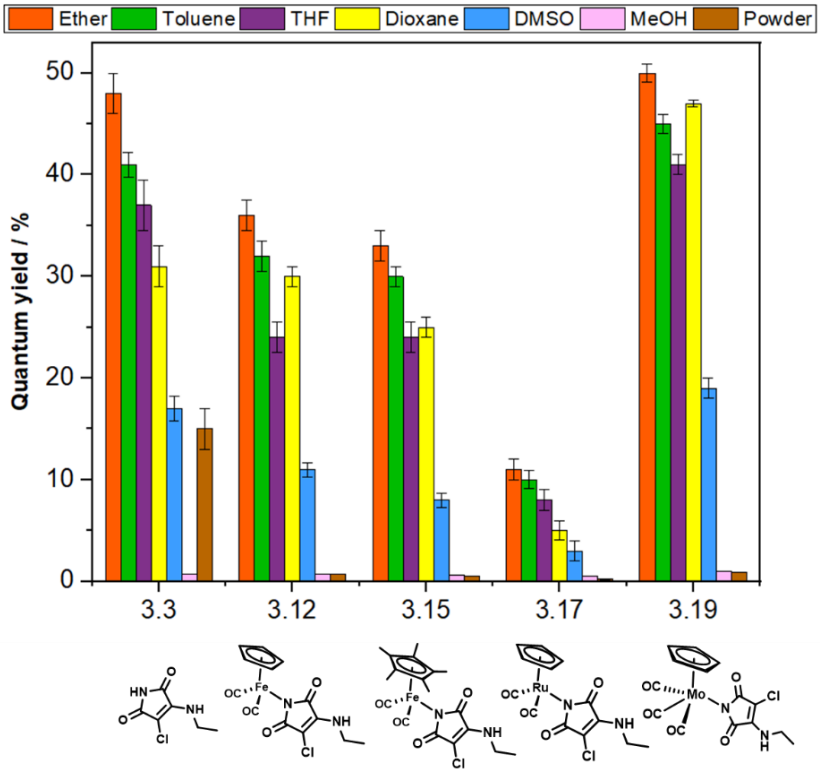

Fig. 3.16 Comparison of the solution and solid-state ϕ_f for the complexes, **3.12**, **3.15**, **3.17**, and **3.19**, and the ligand **3.3**, in six different solvents (diethyl ether, toluene, tetrahydrofuran, dioxane, dimethyl sulfoxide and methanol), using the reference and absolute methods, respectively.

Following on the analysis, solid-state quantum yields (ϕ_f) of **3.12**; $CpFe(CO)_2ACM$, **3.15**; $Cp^*Fe(CO)_2ACM$, **3.17**; $CpRu(CO)_2ACM$, **3.19**; $CpMo(CO)_3ACM$, and **3.3**; ACM was evaluated by the absolute method.[68] The solid-state ϕ_f (%) for all the complexes containing an aminochloromaleimide ligand were observed to be <1, while the reference ligand (**3.3**) gave a value of 15% (Fig. 3.16). This might be due to the π-π stacking interactions and the intermolecular hydrogen bonds in the solid-state, resulting in the aggregation caused quenching (ACQ) behavior for these complexes. Moreover, the fluorescence efficiencies for the complexes with the same metal atom but different maleimide derived ligands $CpFe(CO)_2ACM$ (**3.12**) and $CpFe(CO)_2DTM$

(**3.20**) were compared. For **3.20**, ϕ_f was calculated to be 11% in diethyl ether and 0.43% in methanol, which is significantly lower in comparison to the complex **3.12** (36% in diethyl ether and ~1% in methanol) (Fig. 3.17). The molar extinction coefficient (ε_{max}) and brightness (B) of **3.20** were calculated to be 3553 $M^{-1}cm^{-1}$ and 106590 $M^{-1}cm^{-1}$, respectively, while for **3.12**, ε_{max} and brightness were found to be 5954 $M^{-1}cm^{-1}$ and 214358 $M^{-1}cm^{-1}$, respectively (Table 3.4). This illustrates that aminochloromaleimide derived complexes are brighter than the dithiomaleimide based complexes, associated with the small charge differences between C=C atoms of the aminochloromaleimide moiety,[69] thus emphasizing the strong push–pull mechanism for the enhanced fluorescence. Though, the evaluated ϕ_f for **3.20** was quite comparable to its uncoordinated ligand DTM (**3.4**), with some exceptions (for example, in diethyl ether, for **3.20** ϕ_f = 15%, and for **3.4** ϕ_f = 11%). For **3.20**, an increase in solvent polarity also generated a red-shift in the fluorescence emission maximum, from 459 nm in cyclohexane to 519 nm in methanol. Unfortunately, the solid-state ϕ_f could not be measured for the complex **3.20** and the ligand **3.4**, as the final products obtained were oily in nature.

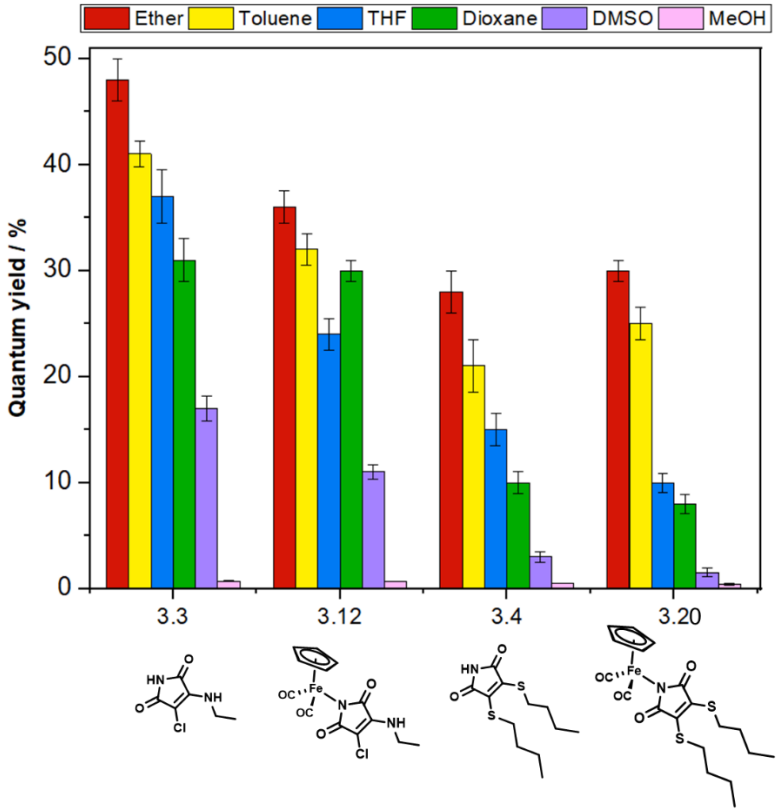

Fig. 3.17 Fluorescence ϕ_f of the ligands, **3.3** and **3.4**, and the complexes, **3.12**, and **3.20**, in six different solvents (diethyl ether, toluene, tetrahydrofuran, dioxane, dimethyl sulfoxide and methanol) using quinine sulfate (ϕ_{st} = 59% in 0.105 M $HClO_4$) as the reference. Error bars represent standard deviation over three repeats.

In order to check the relationship between electron density of the maleimide and its optical properties, FTIR spectra of these complexes were compared. The functionalities of interest and their corresponding frequencies (ν) are tabulated and correlated with the fluorescence efficiency (Table 3.5). The normal range of the M-CO stretching frequency, ν(C≡O) is 1820 –2150 cm^{-1}. The band position can tell how good the metal is, as a π-base. The greater the ability of a metal to donate electrons to the π^* orbitals of carbonyl ligand, the lower the energy of the C-O stretching vibrations. Complex **3.19** presented lower -C≡O stretching vibration frequencies (i.e., 2043 and

1933 cm^{-1}) associated with higher ϕ_f (58%). This signifies the increased sigma donating capability of the maleimide ring, which means the electron density has been pulled away from the maleimide ring due to the increased back-bonding to the carbonyl ligands, resulting in higher N-C=O stretching vibration frequency. These results are in agreement with the solution-state ϕ_f analysis, where relatively more electronegative metal (Mo) exhibited higher ϕ_f. This was also reflected through the data from the NMR spectroscopy (Table 3.5).

Table 3.5 Correlation of FTIR and NMR spectroscopic data with optical properties of half-sandwich metallocarbonyl complexes.

Compound	**FTIR ν of designated functionalities**		**^{13}C NMR data**	**ϕ_f in diethyl ether**
	-C≡O stretching (cm^{-1})	**-C=O stretching (cm^{-1})**	**δ for C≡O (ppm)**	**(%)**
3.12	2038, 1988	1620	213.8	36
3.15	2023, 1955	1623	214.9	33
3.17	2047, 1974	1629	198.8	11
3.19	2043, 1933	1636	228.8	50
3.20	2025, 1960	1610	213.5	15

Unfortunately, we did not get any information about M-N bonds directly as they lie between 200–300 cm^{-1}. Also, the instrument noise at low wavenumbers prevented any accurate measurements in this region. The metal aminochloromaleimide complexes also showed a medium split absorption band, in the range of 3250–3315 cm^{-1}, assignable to the -N–H stretching of the amine group attached to the maleimide, which was absent in the metal dithiomaleimide complex.

^{13}C NMR spectra of these half-sandwich metallocarbonyl-maleimide complexes, demonstrated the relationship between bond electron density and the fluorescence efficiency. A more downfield signal for C≡O was observed for Mo- complex (**3.19**) (δ = 228.8 ppm), due to its small size and electronegative nature, thus pushing the electron density away from the ligands, and in turn also associated with higher fluorescence efficiency (ϕ_f) (Table 3.5).

The lifetime studies of the synthesized complexes, **3.12**; $CpFe(CO)_2ACM$, **3.15**; $Cp^*Fe(CO)_2ACM$, **3.17;** $CpRu(CO)_2ACM$, **3.19**; $CpMo(CO)_3ACM$, **3.20**; $CpFe(CO)_2DTM$, and reference dyes, **3.3**; ACM and **3.4**; DTM, was also analyzed using 1,4-dioxane as solvent. The λ_{em} pre-recorded in solution-state for these compounds was used to observe the fluorescence decay. The fluorescent lifetime measurements for the metal-aminochloromaleimide complexes (**3.12**, **3.15**, **3.17**, and **3.19**) gave two lifetimes while iron-dithiomaleimide complex (**3.20**) displayed three life times. Although, high reduced chi-squared values (χ^2 >1.3) were observed for all the fluorophores (Table 3.6). This indicates high deviations from the degree of exponentially fitted data,[70] and the fitting of additional decay components did not yield any improvement. All the metal maleimide complexes gave lifetimes slightly higher than their individual ligands (Table 3.6). **3.17** showed longest lifetime (2.57 ns and

15.18 ns), compared to **3.12**, **3.15**, and **3.19,** and especially w.r.t ligand **3.3** (1.22 ns and 14.04 ns), whereas complex **3.20** showed lifetimes (1.55 ns, 4.31 ns and 10.75 ns) similar to **3.4** (1.31 ns and 4.35 ns).

Table 3.6 Fluorescence life time decay measurements by Time-Correlated Single-Photon Counting (TCSPC) of the half-sandwich metallocarbonyl complexes (**3.12**, **3.15**, **3.17**, **3.19**, and **3.20**) and their respective ligands (**3.3** and **3.4**) in 1,4-dioxane. Data was simulated using "Reconvolution Fit" model; and Instrument response function (IRF) was determined using 10% w/w Ludox in water (10 μM; λ_{ex} = 375 nm; 25°C).

Compound	τ_1 (ns)	Rel. (%)	τ_2 (ns)	Rel. (%)	τ_3 (ns)	Rel. (%)	χ^2
CpM(CO)$_n$(ACM) complexes							
3.3	1.22	0.69	14.04	99.31	-	-	2.719
3.12	1.8	0.78	15.21	99.22	-	-	2.505
3.15	2.12	0.64	14.56	99.36	-	-	1.789
3.17	2.57	4.92	15.18	95.08	-	-	1.772
3.19	2.12	1.27	14.48	98.73	-	-	2.427
CpM(CO)$_n$(DTM) complex							
3.4	1.31	5.33	4.35	94.67	-	-	1.739
3.20	1.55	5.28	4.31	91.6	10.75	3.12	1.364

It has been observed that the emissive behaviour and fluorescence parameters of the half-sandwich metallocarbonyl maleimide complexes are quite comparable. There is a

slight increase in solution state ϕ_f for the molybdenum-maleimide complex than its iron-analogue. However, their solid-state ϕ_f identified these complexes as aggregation caused quenching (ACQ) dyes. The fluorescence lifetime decay of these complexes were higher compared to the uncoordinated maleimide-based ligands. All these properties expand the scope of use for these complexes as organic-inorganic hybrid probes.

3.3.4 Chemical oxidation of (η^5- $C_5H_5Fe(CO)_2$(ACM) complex

In order to expand the scope of these half-sandwich metallocarbonyl maleimide complexes, their redox properties were explored. For this purpose, the oxidation of the synthesized half-sandwich iron(II)-ACM complex (**3.12**) was achieved, and the effect of oxidation on the fluorescence behavior was examined, by modifying an already established protocol.[71] The oxidation of iron(II) complex by hydrogen peroxide occurred in the presence of triflic acid (HOTf) in acetonitrile (MeCN) (Eq. 3.1).

$$2Fe^{2+} + H_2O_2 + 2H^+ \rightarrow 2Fe^{3+} + 2H_2O \qquad \textbf{Eq. 3.1}$$

Changes in the UV-Vis absorption and fluorescence spectra are shown in Fig. 3.18, where the absorption band at 380 nm and emission maxima at 489 nm decreased over time, as a result of oxidation. The observed bands corresponds to the ligand-based transition (LFT) primarily, but may contains a mixture of LFT and metal-to-ligand charge transfer (MLCT).[72] It was observed that approximately 70% of the fluorescence

was quenched in the first 4 h, which reached completion after 14–16 h (Fig. 3.18). In order to confirm, that this decrease in fluorescence was caused by the oxidation of complex and not because of photobleaching, a control experiment was conducted. For which, instead of the complex **3.12**, the aminochloromaleimide ligand **3.3**, was subjected to the similar conditions for oxidation. The presence of fluorescence even after 16 h in the solution suggested that the fluorescence quenching, in case of **3.12,** was primarily caused by the oxidation of Fe(II) to Fe(III). The ligand ACM (**3.3**), exhibited blue shifted absorption and emission maxima at 365 nm and 482 nm, respectively (Fig. 3.18). There was no significant decrease in absorption change for 5 h, though a slight decrease (~30%) was observed after 16 h, while the fluorescence was not affected even after 16–20 h. These results confirm that the fluorescence switch-off observed for the complex **3.12**, was due to the oxidation of Fe(II) to Fe(III), and not because of the photobleaching of the dye over time.

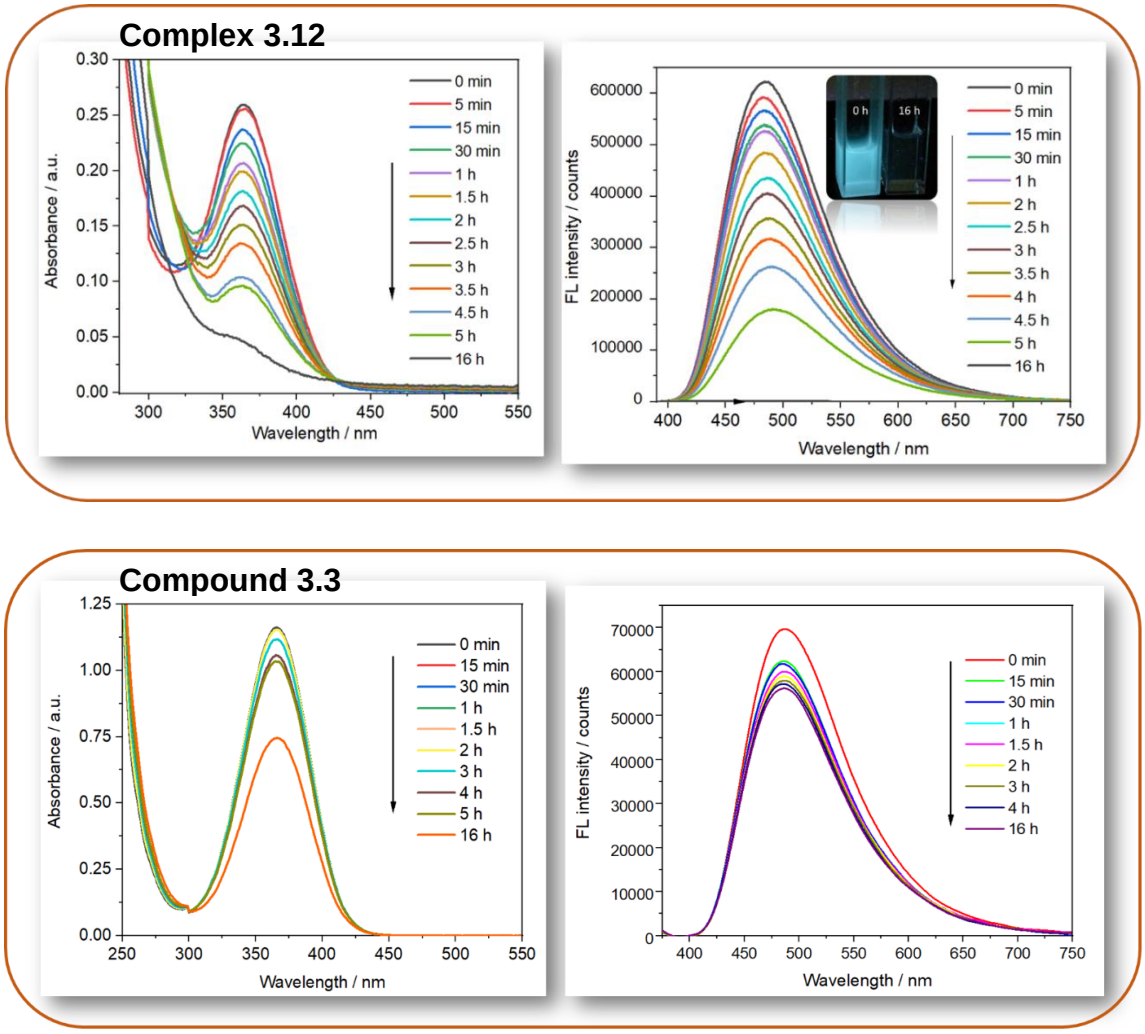

Fig. 3.18 Changes in the UV-Vis absorption (left), and fluorescence emission (right) spectra, by the oxidation of $CpFe^{II}(CO)_2ACM$ (**3.12**) (top) and ACM (**3.3**) (bottom) (2.0×10^{-4} M) using H_2O_2 in MeCN containing HOTf (5.0×10^{-2} M).

3.3.5 Electrochemical studies*

Owing to the growing interest in exploiting redox properties, the half-sandwich metal maleimide complexes exhibiting electrofluorochromic properties was investigated by cyclic voltammetry and fluorescence spectroelectrochemistry. Complex **3.12** ($CpFe(CO)_2ACM$) and it's precursor **3.7** ($CpFe(CO)_2I$) were investigated, owing to its

* These studies were carried out in collaboration with Dr. Paramaconi Rodriguez Perez.

good fluorescence and stability, to probe the electrochemical and spectroscopic properties using a bench-top set-up for cyclic voltammetry followed by the fluorescence analysis. Tetrabutylammonium perchlorate (0.1 M in MeCN) was used as the ionic conducting liquid instead of 1-butyl-3-methylimidazolium hexafluorophosphate, to avoid the poor convection in the electrolyte, observed for the latter, due to which the fluorescence emission showed abnormal trend over time. The external voltage applied to the established electrochemical cell at the specified higher and lower potentials was -2.5 and +2.0 V, respectively. The potential window depends on many factors like conducting liquid and electrode etc., so it may or may not be symmetrical.[73-75] Choosing the right scan rate for the experiment is quite crucial. It controls how fast the applied potential is scanned for cyclic voltammetry. With a slower scan rate there is a risk of missing a redox event for a system, that possess consecutive redox processes. On the other hand, faster scan rates lead to a decrease in the size of the diffusion layer, and resultantly higher currents are observed. Therefore, the scan rates between 50–100 mV/s are usually suitable to "probe" the electrochemical behavior, depending on the type of required information.[75]

The electrochemical behaviour of complex **3.12** was investigated by cyclic voltammetry. No solvent effect was detected on the position of the analyte peaks. Fig. 3.19a, presents a cyclic voltammogram for the complex **3.12**, which displayed occurrence of four redox events, with peak-to-peak separation measured as: ΔEp_{I} = 270 mV ; ΔEp_{II} =177 mV; ΔEp_{III} = 240 mV; and ΔEp_{IV} = 210 mV, indicating them to be quasireversible processes. The half wave potential around 810 mV observed as a result of electrolysis, corresponds to the oxidation of Fe^{II} to Fe^{III}. The redox process at -1.8 V was assigned to the formation of dimer ([η^5-$CpFe^{I}(CO)_2]_2$; Fp_2), as a result of

reduction of [η^5-CpFe^{I}(CO)$_2$L]$^-$ accompanied by a loss of ligand.[72] The cyclic voltammogram for the precursor CpFe(CO)$_2$I (**3.7**) was also observed to be in agreement with previously published report.[76] The precursor CpFe(CO)$_2$I exhibited redox chemistry similar to the complex **3.12** (Fig. 3.19d). with relatively larger peak-to-peak separations, i.e., ΔEp_{I} = 185 mV; ΔEp_{II} =270 mV; ΔEp_{III} = 174 mV; and ΔEp_{IV} = 97 mV. This difference was associated with the stability of excited state of the complex **3.12**. It is well-established that the reduction potential of a compound is correlated with the energy level of a LUMO. The higher the energy levels of the LUMO, the more vulnerable the complex is to the decomposition.[72, 74] For the maleimide ligand (**3.3**), voltammogram did not show any response under similar conditions (Fig. 3.19c).

Subsequently, the effect of redox process on the fluorescence emission for the complex **3.12** was evaluated. In the absence of applied potential, complex **3.12** displayed a fluorescence peak at 489 nm. After applying the potential of +0.89 V for 30 min, the fluorescence emission intensity decreased along with red-shifted in emission maxima (from 489 nm to 505 nm), due to the oxidation of Fe^{II} to Fe^{III}. Unexpectedly, after 1 h of electrolysis the fluorescence emission intensity abnormally rises, along with the formation of precipitates. It was hypothesized that the sudden increase in fluorescence intensity was triggered due to the precipitate formation that caused scattering while measuring the fluorescence, and results in poor convection in the electrochemical cell as well. Therefore, to chose the optimal concentration of the complex, cyclic voltammograms were recorded and compared for the complex **3.12** for different concentrations (0.2 µM, 2.0 µM, 4.0 µM and 10 µM) in MeCN/[TBA][BF$_4$](0.1 M), under inert atmosphere at scan rate of 50 mV/s (Fig. 3.20a). Based on these

measurements, the concentration 10 µM displaying the most prominent peaks, was chosen to perform the next spectroelectrochemical experiment.

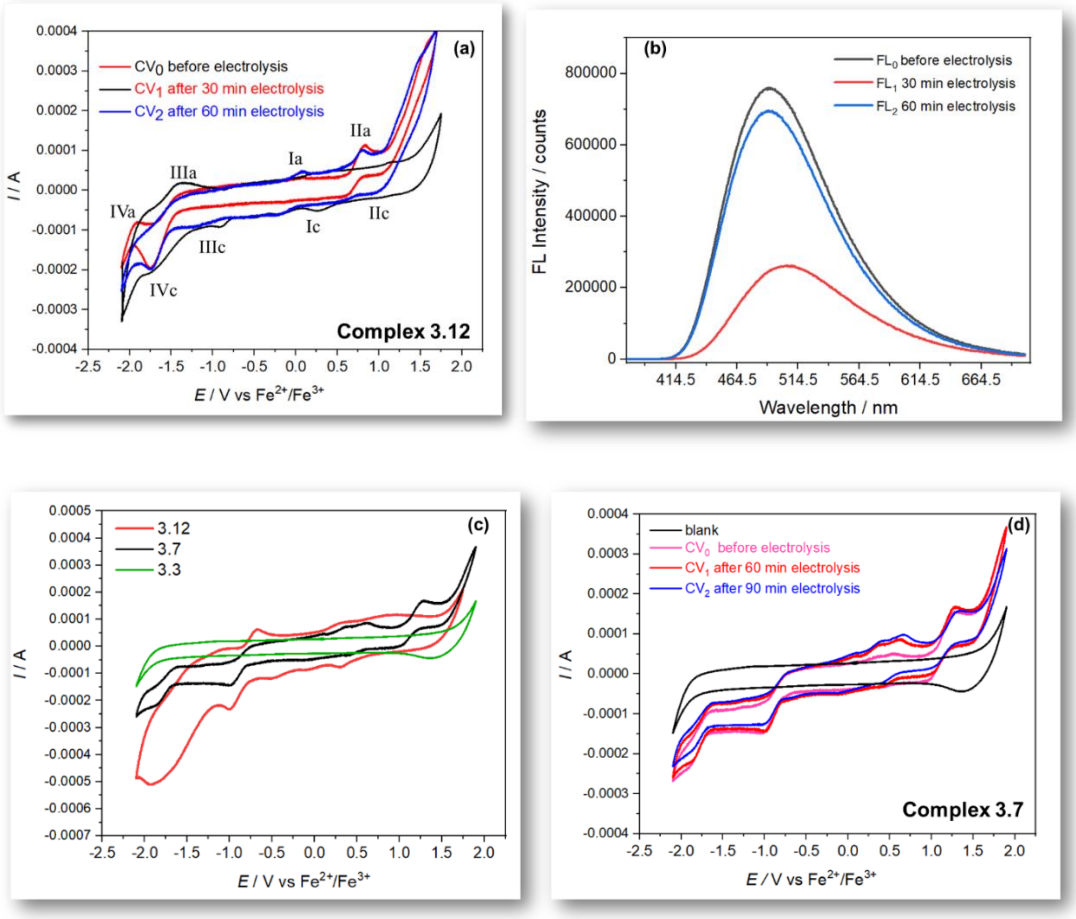

Fig. 3.19 Cyclic voltammogram of **3.12** (10 mM) in MeCN/[TBA][BF_4](0.1 M), performed at a scan rate of 50 mV/s (**a**); fluorescence emission spectra recorded in MeCN/[TBA][BF_4] before and after 30 and 60 min of electrolysis (10 mM, λ_{ex} = 369 nm) (**b**); comparing the cyclic voltammograms of the complex **3.12** (CpFe(CO)$_2$ACM) with the iron(II) precursor **3.7** (CpFe(CO)$_2$I), and the ligand **3.3** (ACM) (**c**); and cyclic voltammogram of **3.7** (10 mM) in MeCN/[TBA][BF_4](0.1 M), performed at a scan rate of 50 mV/s (**d**).

Following on the study, the cyclic voltammogram (CV) of the complex **3.12**, at the concentration of 10 µM was analyzed. As illustrated in Fig. 3.20c, an anodic peak observed at 850 mV, which is a characteristic of oxidation of Fe^{II} to Fe^{III}, and was higher than reported for Fe^{II}/Fe^{III}, suggesting greater stabilization of Fe^{II} with the attached ligands.[77] The CV further displayed the occurrence of four redox events with peak-to-peak separation measured as: ΔEp_{I} = 111 mV; ΔEp_{II} =101 mV; ΔEp_{III} = 198 mV; and ΔEp_{IV} = 55 mV, suggesting the first three processes to be quasireversible process (>59 mV), while the fourth one represented a reversible one-electron wave process. Additionally, the redox process at about -1.4 V is assigned to the reduction of Fe^{II} to Fe^{I}, while the redox process at -1.8 V is assigned to the formation of a dimer ([η^5-$CpFe^{I}(CO)_2]_2$; Fp_2), through the reduction of [η^5-$CpFe^{I}(CO)_2X]^-$.[72] The fluorescence spectrum displayed an emission peak at 489 nm (λ_{ex} = 369 nm) corresponds to the π-π* transitions. A decrease in fluorescence was observed as a result of applying the electrolysis for 3 h, indicating that electrogenerated species were non-fluorescent (Fig. 3.20d).[78] It was hypothesized that the observed electrochemical switching on→off fluorescence was triggered by the oxidation of **3.12** to its corresponding non-fluorescent radical. However, the fluorescence recovery upon switching was difficult as the precipitates started to form causing poor convection in the electrochemical cell.

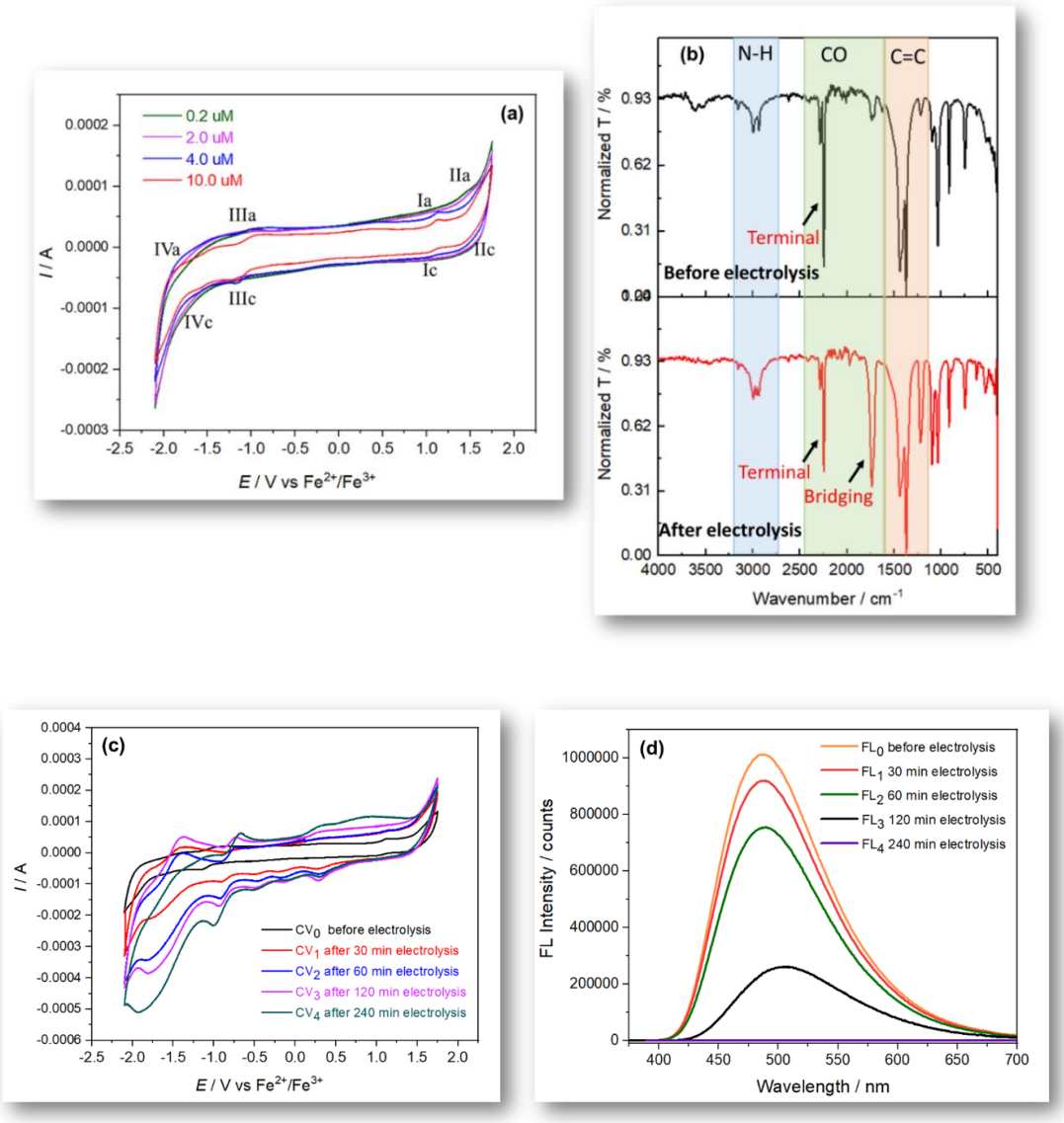

Fig. 3.20 Cyclic voltammogram of **3.12** for different concentrations (0.2 µM, 2.0 µM, 4.0 µM and 10 µM) in MeCN/[TBA][BF_4](0.1 M) at a scan rate of 50 mV/s (**a**); FTIR spectra of the complex **3.12** before electrolysis compared with the solid extracted after electrolysis (**b**); cyclic voltammogram of **3.12** (10 µM) in MeCN/[TBA][BF_4](0.1 M), before and after electrolysis at a scan rate of 50 mV/s (**c**); and fluorescence emission spectra of **3.12** (10 µM) recorded in MeCN/[TBA][BF_4](0.1 M), before and after electrolysis (λ_{ex} = 369 nm) (**d**).

The stability of the complex was also examined by using the same concentration in MeCN/[TBA][BF_4] without any potential. No precipitates were formed for more than 2 days, though after two days some solid particles started to appear, which suggested that electrolysis had just escalated the precipitation process. The precipitates extracted from the solution were analyzed by FTIR spectroscopy, and compared with the IR spectrum of a fresh sample (Fig. 3.20b). Upon comparison, no significant peak shift was observed for C=C stretching, and terminal M-CO stretching. However, a strong peak at 1734 cm^{-1} was observed after electrolysis, in addition to the 2232 cm^{-1} and 2275 cm^{-1}, corresponding to the symmetric and asymmetric CO stretching vibrations. The peak displayed at 1734 cm^{-1} is assignable to the bridging CO or semi-bridging CO, in which carbonyl is neither fully terminal not fully bridged but intermediate between the two.[79] This is the characteristic of the [η^5-$CpFe^I(\mu^2$-CO)(CO)]$_2$ dimer, formed as a result of a reduction during the electrolysis process.

3.4 Summary

In this chapter, half-sandwich metallocarbonyl complexes were successfully synthesized *via* the photochemical reaction of transition metal iodide precursors with maleimide based derivatives. The reaction conditions were optimized for the synthesis of fluorescent half-sandwich metal-maleimide complexes. Aminochloromaleimides were found to be better candidates for the complexation, in comparison to the aminobromomaleimides. The complexes were characterized by NMR, MS, FTIR spectroscopy and Single crystal X-Ray diffraction.

The optical properties of these half-sandwich metal-maleimide complexes were investigated. The complexes exhibited fluorescence efficiencies comparable to the free maleimide fluorophores in solution-state, while the fluorescence in solid-state was quenched, thus classified them as aggregation caused quenching dyes. The fluorescence parameters were also correlated with the data obtained from ^{13}C-NMR and FTIR spectroscopy. Moreover, the fluorescence lifetime decay of these complexes were also explored, which expands the potential of these complexes as organic-inorganic hybrid probes.

Significantly, fluorescence quenching of a half-sandwich iron-maleimide complex was observed upon chemical oxidation with hydrogen peroxide, and was also compared to the free maleimide fluorophore. Next, the electrofluorochromic properties of the half-sandwich iron-maleimide complex was investigated by cyclic voltammetry, followed by the fluorescence analysis. Interestingly, the complex exhibited electrochemical fluorescence on→off switching, as a result of the oxidation. Some traces of the reduced

species precipitated out during the electrolysis process, and was analyzed by FTIR spectroscopy.

Based on this chapter, the fluorescent properties of metallocarbonyl complexes, along with IR-tagging, were explored for the first time and investigated their electrofluorochromic behavior, which made them excellent candidates for applications, such as labelling or catalysis, etc.

3.5 Experimental

3.5.1 Materials and instrumentation

All chemicals were obtained from either: Sigma Aldrich, Acros Chemicals, Alfa Aesar, or Fisher Chemicals, and used as received.

NMR spectra were recorded on a Bruker Advance 300 or a Bruker Advance III HD 400 at 300 and 400 MHz respectively. Shifts are quoted in δ in parts per million (ppm) and quoted relative to the internal standard tetramethylsilane (TMS).

High Resolution Mass Spectra (HR-MS) were conducted by Dr Christopher Williams (University of Birmingham) on a Bruker UHR-Q-ToF MaXis spectrometer with electrospray ionization. Atmospheric Pressure Chemical Ionization (APCI) was performed on Waters Xevo-G2-XS to analyze organometallic compounds.

FTIR spectroscopy was carried out on neat samples using Agilent Technologies Cary 630 FTIR spectrometer. The spectra were corrected for background absorbance and 16 Scans were taken from 600 to 4000 cm^{-1} at a resolution of 4 cm^{-1}.

UV-Vis spectroscopy was carried out at room temperature on Evolution 350 UV-Vis spectrophotometer, equipped with Xenon Flash lamp light source, and silicon photodiode detectors. Quartz cells (3.5 mL; 170 - 2000 nm) from Hellma with two polished sides were used for examining the absorption spectral data by using Thermo INSIGHT software.

Fluorescence emission and excitation spectra were obtained with Agilent Cary Eclipse Fluorescence spectrophotometer or an Edinburgh Instruments FS5 Spectrofluorometer in quartz 3.5 mL cuvettes (Starna Cell, Type: 3/Q/10), for liquid

samples (10–20 μM, 25 °C). The data was analyzed in Fluoracle (Edinburgh Instruments) and Origin 2019 (Origin Labs). A solution of quinine sulfate dihydrate in 0.105 M perchloric acid was used as standard (ϕ_{st} = 59%), for the evaluation of solution-state quantum yield analysis, according to previously reported literature procedure.[68] The absolute quantum yield in solid state is evaluated as an average of six replicate measurements, using the SC-30 integrating sphere module. Fluorescence lifetime spectra were obtained by time correlated single photon counting (TCSPC). These experiments were done with Edinburgh Instruments FS5 spectrofluorometer, equipped with 375±10 nm pulsed diode laser source (PicoQuant). Instrument response functions (IRF) were determined from the scatter signal solution of Ludox HS-40 colloidal silica (10% particles in water w/w). The data was simulated using "Reconvolution fit" model to eliminate both the noise and the effects of the exciting light pulse. The reduced chi square χ^2 has been evaluated using Fluoroacle (software) and is used to assess the data fitting.

Crystals were grown for the complexes using multisolvent recrystallization approach using hexane-methanol. The datasets were collected on Agilent Technologies SuperNova single crystal X-ray diffractometer with dual wavelength microfocus X-ray sources (Mo and Cu) and an Atlas detector. The system is complemented by an Oxford Cryosystems Cryostream to collect data at temperatures as low as 100 K.

Electrochemical studies were carried out, under argon, in acetonitrile using 0.1 M tetrabutylammonium perchlorate as the supporting electrolyte, and 10 μM to 10 mM of the sample. HOPG (highly oriented pyrolytic graphite) was used as the working electrode, glassy carbon (GC), with gold as the auxiliary electrode and Fe(II)/Fe(III) redox couple as the reference electrode, along with purging an inert gas through the

cell. CV experiments were measured after at least 10 min of argon purging, at room temperature.

3.5.2 Synthesis of ligands

3-bromo-4-(ethylamino)-1*H*-pyrrole-2,5-dione (3.1)

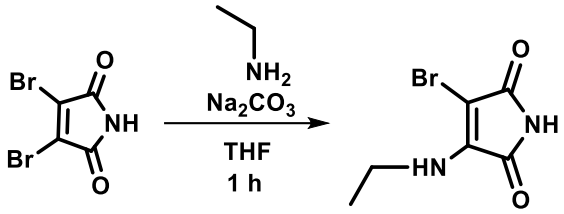

3.1 (39%)

Reactions were performed according to the protocol established by a previous paper.[56] 1.5 g of 2,3-dibromomaleimide (1.0 equiv.) was dissolved in 10 mL THF followed by the addition of 1.55 g of sodium carbonate (2.5 equiv.). A slight excess of ethylamine (360 µL, 1.1 equiv.) was added to the reaction mixture dropwise and stirred for 30–60 min. The progress of the reaction was monitored through TLC. The obtained yellow product was dried under the vacuum and further dissolved in 20 mL CH_2Cl_2. The resultant mixture was washed with 3×20 mL of water and pure product was obtained after purification by column chromatography.

R_f = 0.65 (hexane: ethyl acetate = 6:1); Yield = 502 mg, 39%.

^{1}H NMR (400 MHz, $CDCl_3$, 25°C, TMS) δ [ppm] = 7.37 (1H, s, H1), 5.41 (1H, s, H4), 3.75– 3.66 (2H, q, H5), 1.33-1.28 (3H, t, H6).

^{13}C NMR (101 MHz, $CDCl_3$, 25°C, TMS) δ [ppm] = 167.0, 165.5 (C=O), 143.4 (C=C), 37.8 (C5), 15.8 (C6).

FTIR (cm^{-1}): ν = 3321 (N-H amine), 3189 (N-H imide), 1764, 1708 (C=O), 1610 (C=C).

HR-MS (MaXis) $[M+H]^+$ - *m/z* found 219.9018; *m/z* calculated 219.9090.

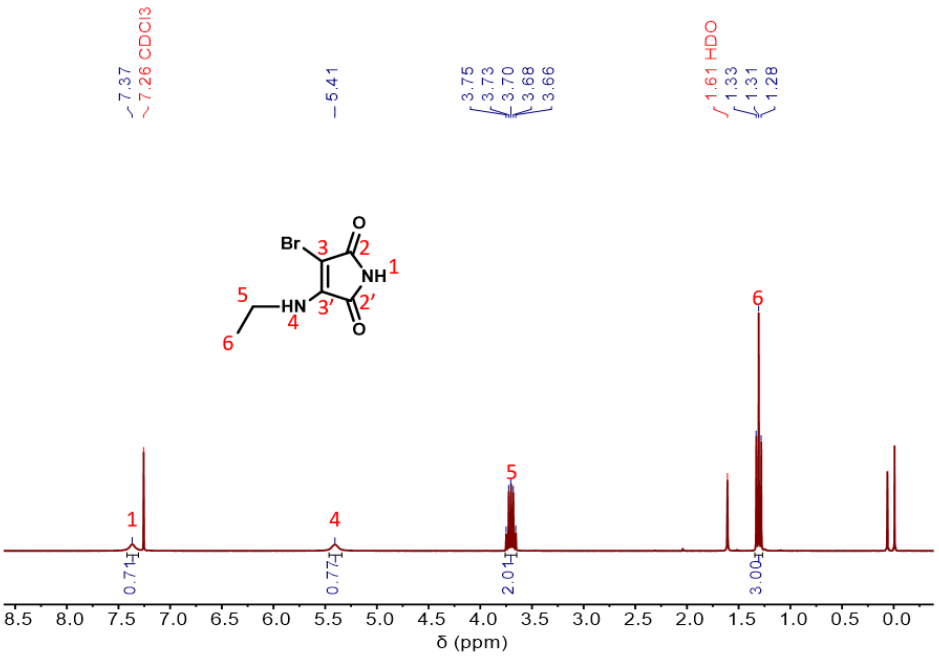

Fig. 3.21 ^{1}H NMR spectrum of **3.1** (400 MHz, $CDCl_3$).

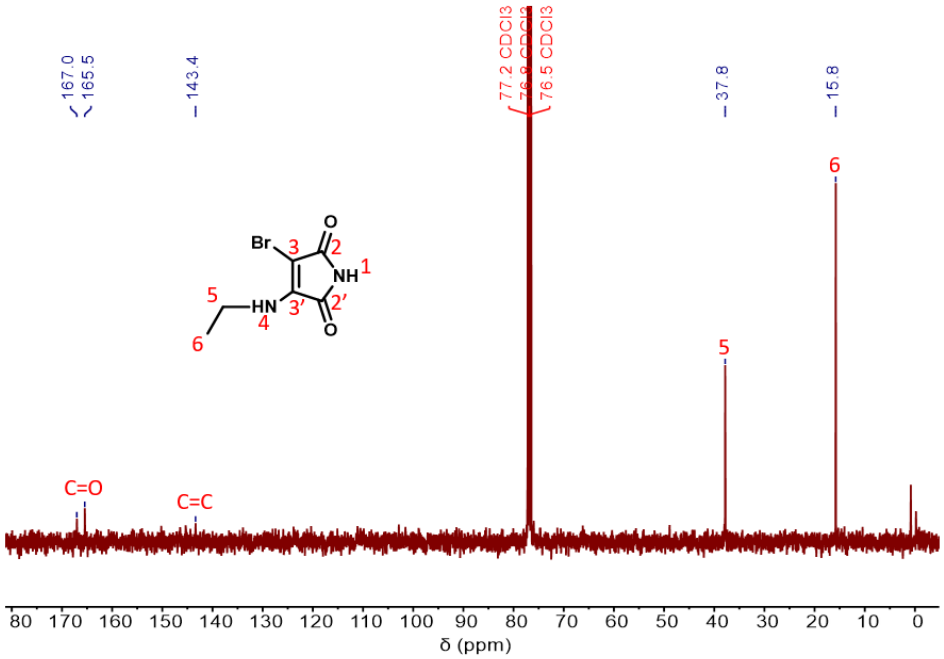

Fig. 3.22 ^{13}C NMR spectrum of **3.1** (101 MHz, $CDCl_3$).

3,4-dichloro-1*H*-pyrrole-2,5-dione (3.2)

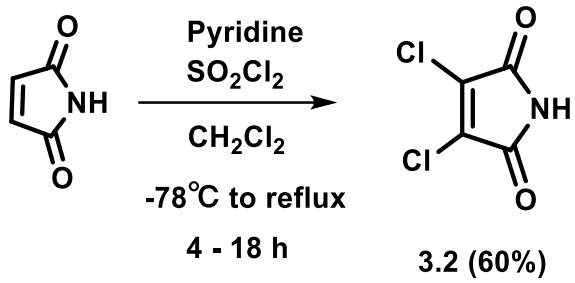

3.2 (60%)

Synthesis of 3,4-dichloromalemide was achieved, following a previously reported protocol.[80] 15 g of maleimide (1.0 equiv.) was added to 150 mL freshly distilled thionyl chloride and the solution was put onto a dry ice/acetone bath to cool to -78℃. To this, a solution of pyridine in dichloromethane (28 mL pyridine in 50 mL CH_2Cl_2) was added dropwise over 30–60 min. and was left for another 60 min on the dry ice bath and allowed it to warm to the room temperature. The solution was then refluxed at 80℃

overnight. After being left to cool, volatiles were removed *in vacuo* and then washed with ethyl acetate and brine three times. The organic layer was collected and dried *in vacuo*. The solid was recrystallized in hot toluene to produce beige colored crystals.

Yield = 14 g, 60%.

^{1}H NMR (400 MHz, $CDCl_3$, 25°C, TMS) δ [ppm] = 5.75 (1H, s, H1)

^{13}C NMR (101 MHz, $CDCl_3$, 25°C, TMS) δ [ppm] = 164.5 (C=O), 134.1 (C=C).

FTIR (cm^{-1}): ν = 3215 (N-H), 1784, 1735 (C=O), 1610 (C=C).

HR-MS $[M+H]^+$ – *m/z* found 165.9470; *m/z* calculated 165.9463.

Matches literature data.[80]

3-chloro-4-(ethylamino)-1*H*-pyrrole-2,5-dione (3.3)

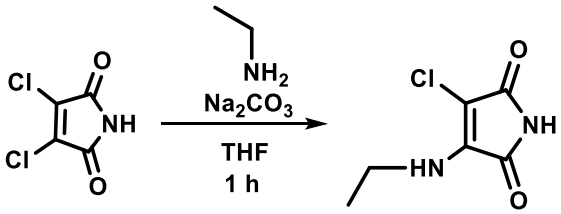

3.2 3.3 (38%)

Reaction was carried out according to already reported protocol.[56] 1.0 g of 2,3-dichloromaleimide (1.0 equiv.) was dissolved in 20 mL THF and mixed with 1.6 g of sodium carbonate (2.5 equiv.). 242 µL of ethylamine (1.1 equiv.) was dropwise added to the reaction mixture and stirred for 30–60 min at room temperature. The solvent was evaporated *in vacuo* and the residue was taken up with 50 mL of CH_2Cl_2, washed with 3×50 mL of water, and dried over magnesium sulfate. The residue was purified by column chromatography to obtain yellow solid product.

R_f = 0.65 (hexane: ethyl acetate = 6:1); Yield = 410 mg, 38%.

^{1}H NMR (400 MHz, $CDCl_3$, 25°C, TMS) δ [ppm] = 7.56 (1H, s, H1), 5.37 (1H, s, H4), 3.71– 3.63 (2H, q, H5), 1.32-1.28 (3H, t, H6).

^{13}C NMR (101 MHz, $CDCl_3$, 25°C, TMS) δ [ppm] = 167.0, 165.4 (C=O), 140.8 (C=C), 38.1 (C5), 16.1 (C6).

FTIR (cm^{-1}): ν = 3322 (N-H amine), 3189 (N-H imide), 1766, 1711 (C=O), 1649 (C=C).

HR-MS (MaXis)) $[M+H]^+$ - *m/z* found 174.5871; *m/z* calculated 174.5802.

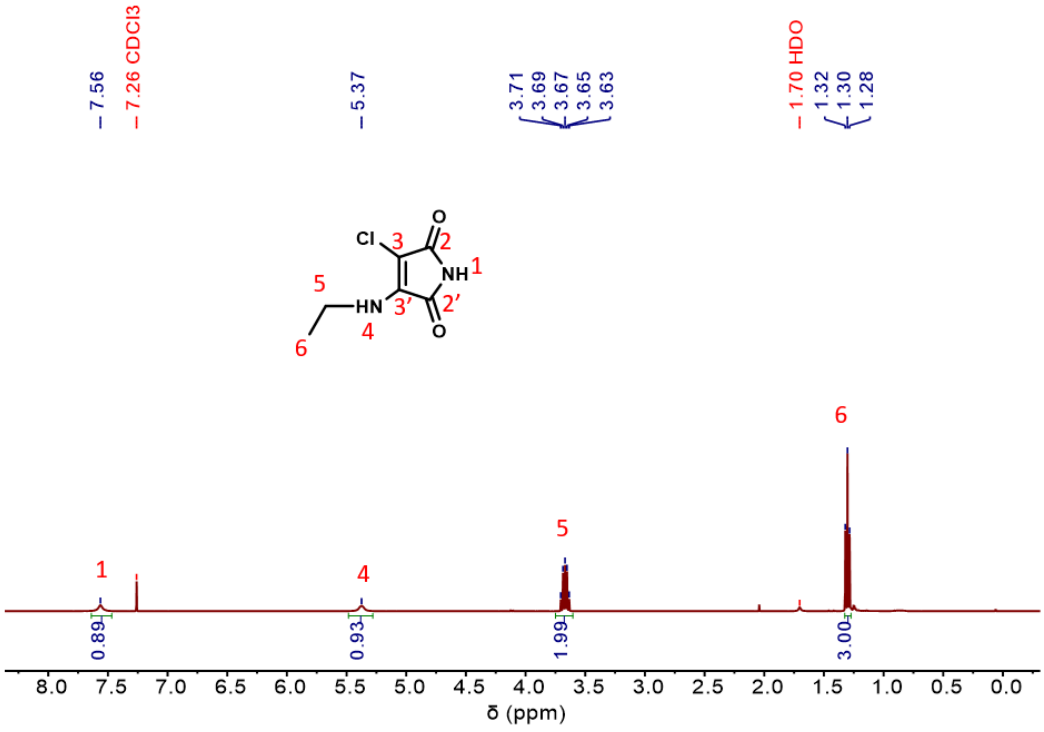

Fig. 3.23 ^{1}H NMR spectrum of **3.3** (400 MHz, $CDCl_3$).

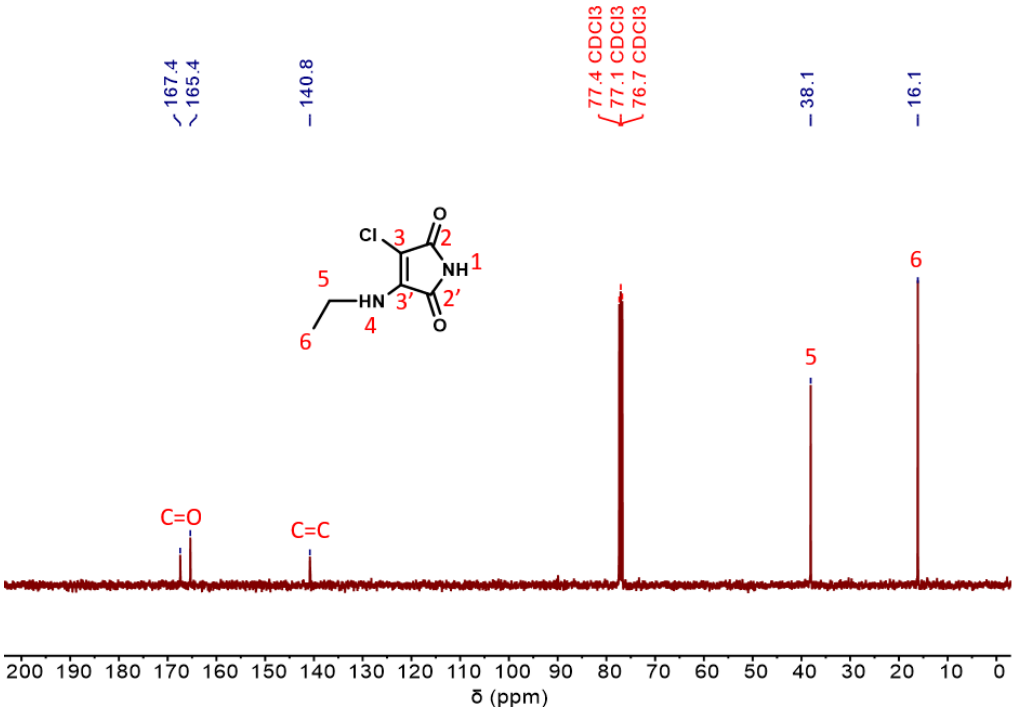

Fig. 3.24 ^{13}C NMR spectrum of **3.3** (101 MHz, $CDCl_3$).

3,4-bis(butylthio)-1*H*-pyrrole-2,5-dione (3.4)

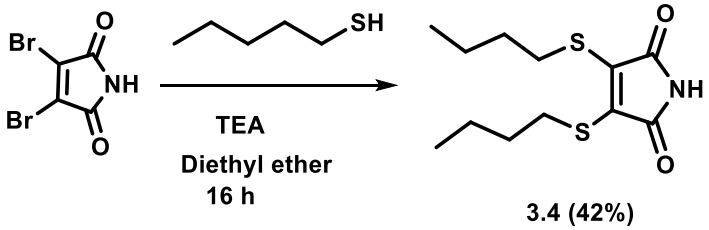

3.4 (42%)

1.0 g of 2,3-dibromomaleimide (1.0 equiv.) was dissolved in 30 mL diethyl ether and cooled to 0°C in an ice bath. To the cooled solution, 0.818 g butanethiol (2.0 equiv.) was added and stirred for 5 minutes. 576 µL of triethylamine (2.0 equiv.) was added dropwise to the cooled solution, whereby an immediate yellow color was observed. The solution was allowed to warm to room temperature and left to stir for 16 hours. Next, 70 mL of diethyl ether was added, and the organic solution washed with water

(150 mL), brine (150 mL) and dried over anhydrous magnesium sulfate. The crude mixture was purified *via* column chromatography to yield the product as an orange oil.

R_f = 0.31 (hexane : ethyl acetate = 9:1), Yield = 450 mg, 42%.

^{1}H NMR (400 MHz, $CDCl_3$, 25°C, TMS) δ [ppm] = 11.12 (1H, s, H1), 3.24-3.20 (4H,t, H4), 1.57-1.50 (4H, m, H5), 1.40-1.31 (4H, m, H6), 0.88-0.84 (6H, t, H7).

^{13}C NMR (101 MHz, $CDCl_3$, 25°C, TMS) δ [ppm] = 166.1 (C=O), 136.8 (C=C), 32.5 (C5), 31.5 (C4), 21.7 (C6), 13.6 (C7).

FTIR (cm^{-1}): ν = 3282 (N-H), 1770, 1704 (C=O), 1548 (C=C).

HR-MS (MaXis) $[M+H]^+$ - *m/z* found 274.0926; *m/z* calculated 274.0930.

Matches literature data.[81]

3,4-dichloro-1-methyl-1*H*-pyrrole-2,5-dione (3.5)

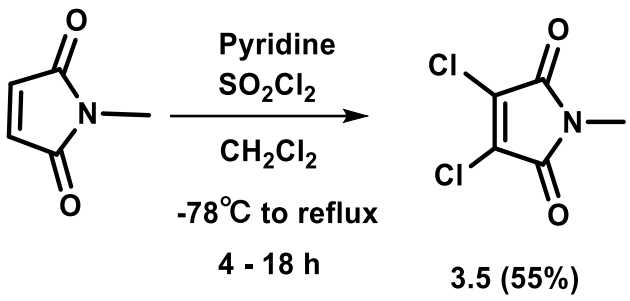

The reaction was carried out following a previously reported protocol.[80] 7.0 g of maleimide (1.0 equiv.) was added to 100 mL freshly distilled thionyl chloride and the solution was put onto a dry ice/acetone bath to cool to -78°C To this, a solution of pyridine in dichloromethane (14 mL pyridine in 50 mL CH_2Cl_2) was added dropwise over 30–60 min. and was left for another 60 min on the dry ice bath and allowed to warm to room temperature. The solution was then refluxed at 80°C overnight. After

being left to cool, volatiles were removed *in vacuo* and then washed with ethyl acetate and brine three times. The organic layer was collected and dried *in vacuo*. The solid was recrystallized in hot toluene to produce beige colored crystals.

Yield = 6.42 g, 55%.

^{1}H NMR (400 MHz, $CDCl_3$, 25°C, TMS) δ [ppm] = 3.16 (3H, s, Me)

^{13}C NMR (101 MHz, $CDCl_3$, 25°C, TMS) δ [ppm] = 163.1 (C=O), 133.4 (C=C), 25.1 (CH_3).

FTIR (cm^{-1}): ν = 3215 (N-H), 1784, 1735 (C=O), 1610 (C=C).

HR-MS $[M+H]^+$ – *m/z* found 179.9618; *m/z* calculated 179.9619

Matches literature data.[80]

3-chloro-4-(ethylamino)-1*H*-pyrrole-2,5-dione (3.6)

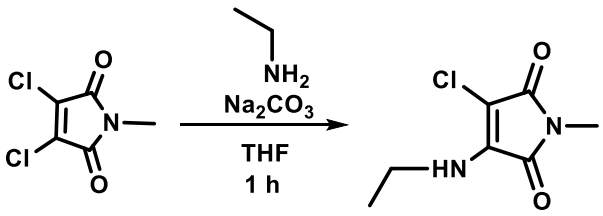

3.5 (38%) **3.6 (35%)**

The reaction was developed according to a reported protocol.[56] 1.0 g of **3.5** (1.0 equiv.) was dissolved in 20 mL THF and mixed with 1.5 g of sodium carbonate (2.5 equiv.). 405 µL of ethylamine (1.1 equiv.) was dropwise added to the reaction mixture and stirred for 30–60 min at room temperature. The solvent was evaporated *in vacuo* and the residue was taken up with 50 mL of CH_2Cl_2, washed with 3×50 mL of water, and

dried over magnesium sulfate. The residue was purified by column chromatography to obtain yellow solid product.

R_f = 0.70 (hexane: ethyl acetate = 6:1); Yield = 367 mg, 35%.

^{1}H NMR (400 MHz, $CDCl_3$, 25°C, TMS) δ [ppm] = 5.31 (1H, s, H4), 3.69– 3.62 (2H, m, H5), 2.99 (3H, s, H1), 1.31-1.27 (3H, t, H6).

^{13}C NMR (101 MHz, $CDCl_3$, 25°C, TMS) δ [ppm] = 168.4, 166.3 (C=O), 140.9 (C=C), 38.6 (C5), 24.6 (C1), 16.5 (C6).

HR-MS (MaXis)) $[M+H]^+$ - *m/z* found 189.5341; *m/z* calculated 189.5302

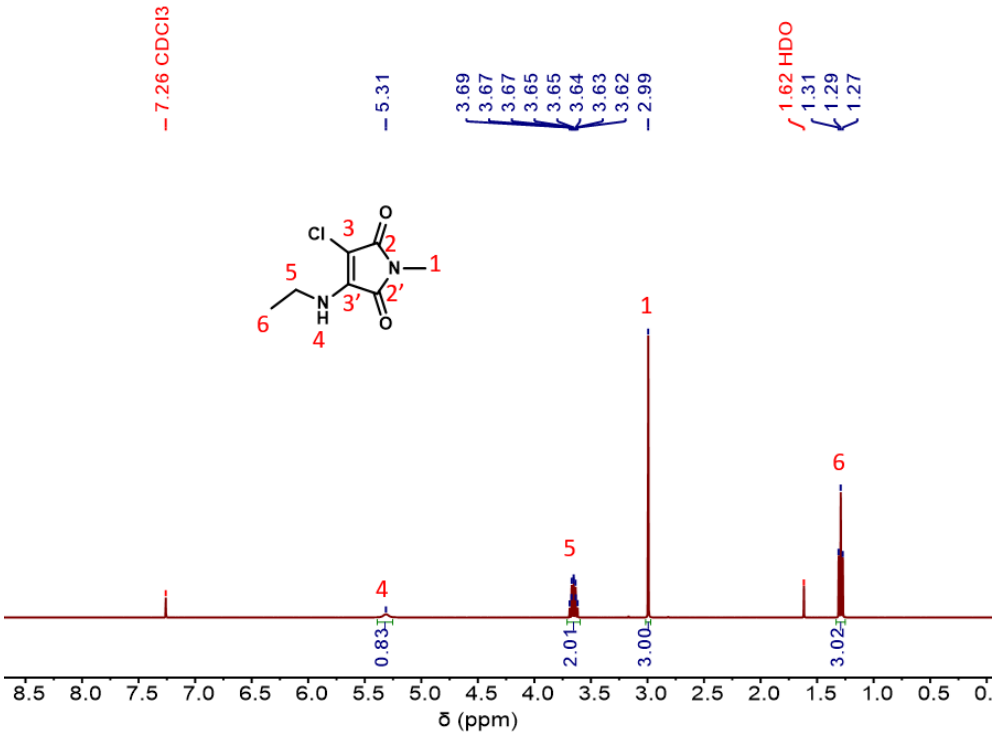

Fig. 3.25 ^{1}H NMR spectrum of **3.6** (400 MHz, $CDCl_3$).

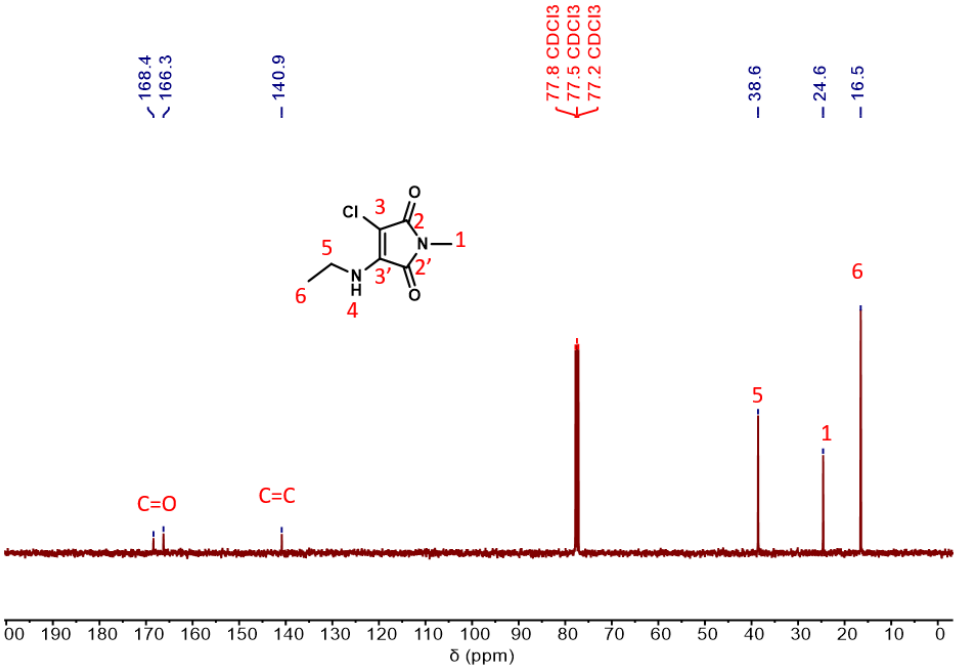

Fig. 3.26 ^{13}C NMR spectrum of **3.6** (101 MHz, $CDCl_3$).

3.5.3 Synthesis of metallocarbonyl maleimidato complexes

η^5-$C_5H_5Fe(CO)_2I$ (3.7; $CpFe(CO)_2I$)

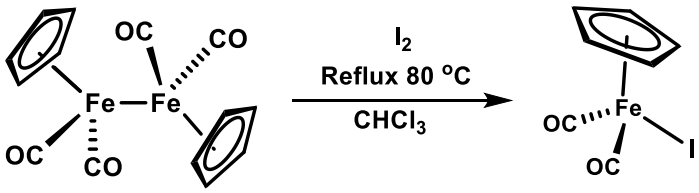

3.7 (70%)

Reaction was carried out according to the established protocol.[82] 1.5 g of cyclopentadienyl iron(II) dicarbonyl dimer (4.24 mmol, 1.0 equiv.) was dissolved in 25 mL of chloroform, and followed by the addition of 1.6 g iodine granules (6.36 mmol, 1.5 equiv.). The reaction mixture was refluxed at 80°C for 30 min. After 30 min, the reaction

mixture was extracted with $Na_2S_2O_3.5H_2O$ solution (3×100 mL, 1 M). The black color organic layer was collected and filtered. The solvent is removed *in vacuo* to obtain the black crystals of cyclopentadienyl iron(II) dicarbonyl iodide.

Yield = 1.8 g, 70%.

^{1}H NMR (400 MHz, $CDCl_3$, 25°C, TMS) δ [ppm] = 5.05 (5H, s, Cp).

^{13}C NMR (101 MHz, $CDCl_3$, 25°C, TMS) δ [ppm] = 212.5 (C≡O), 84.0 (Cp).

FTIR (cm^{-1}): ν = 2020, 1957(C≡O).

Matches literature data.[82]

(η^5-C_5H_5)Fe(CO)$_2$(η^1-*N*-dibromomaleimidato) (3.8; CpFe(CO)$_2$DBM)

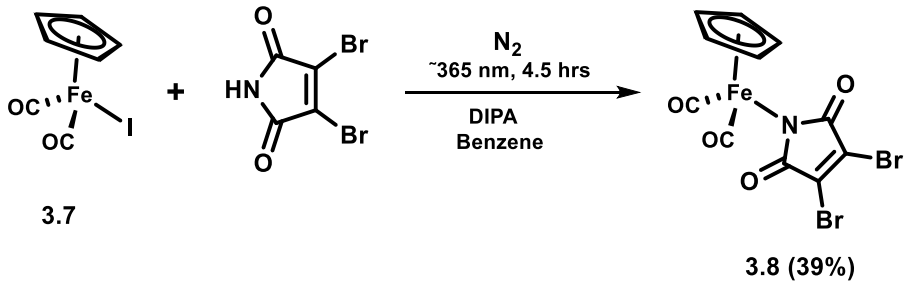

The complex was prepared by modifying the already established protocol.[44, 45] 500 mg of **3.7** (1.65 mmol, 1.0 equiv.) and 500 mg 2,3-dibromomaleimide (1.96 mmol, 1.1 equiv.) was dissolved in 15 mL of ice-cooled anhydrous benzene. The solution was transferred to ice-cooled 100 mL 2-neck round bottom flask under nitrogen, followed by the addition of 1.5 mL diisopropylamine at 0°C. The nitrogen-saturated reaction mixture was then illuminated with UV-light 365 nm for 4.5 hours. The solid was filtered

off and the filtrate was evaporated to dryness. The orange-brown residue was purified by column chromatography to obtain brown color solid product.

R_f = 0.47 (hexane : ethyl acetate = 2 :1), Yield = 280 mg, 39%.

^{1}H NMR (400 MHz, $CDCl_3$, 25°C, TMS) δ [ppm] = 5.08 (5H, s, Cp).

^{13}C NMR (101 MHz, $CDCl_3$, 25°C, TMS) δ [ppm] = 211.5 (C≡O), 175.1 (C=O), 131.8 (C=C), 84.7 (Cp).

FTIR (cm^{-1}): ν = 2050, 1996 (C≡O), 1655 (C=O).

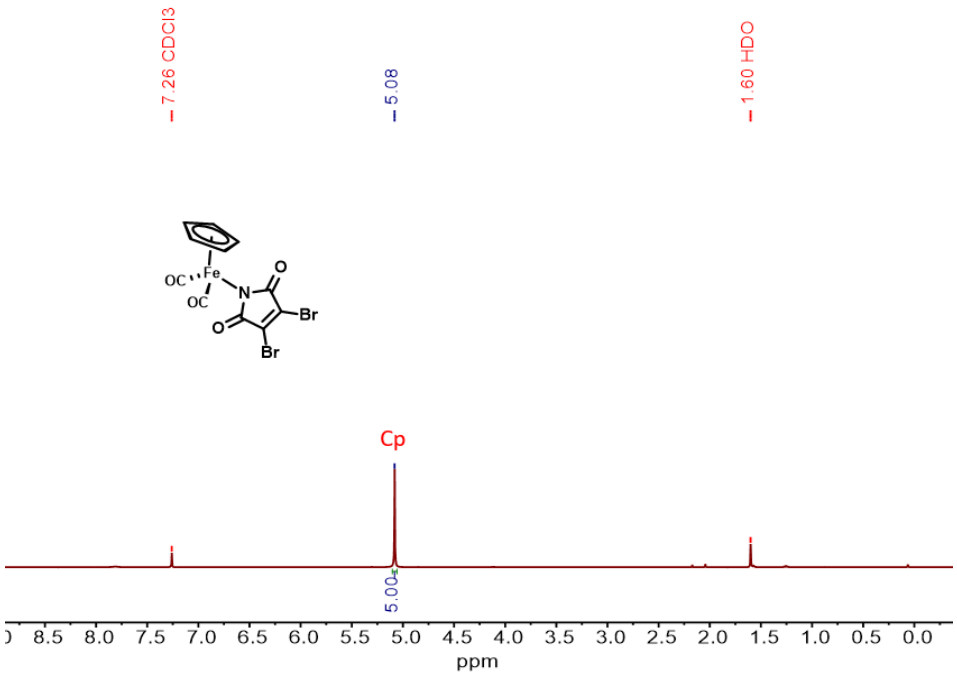

Fig. 3.27 ^{1}H NMR spectrum of **3.8** (400 MHz, $CDCl_3$).

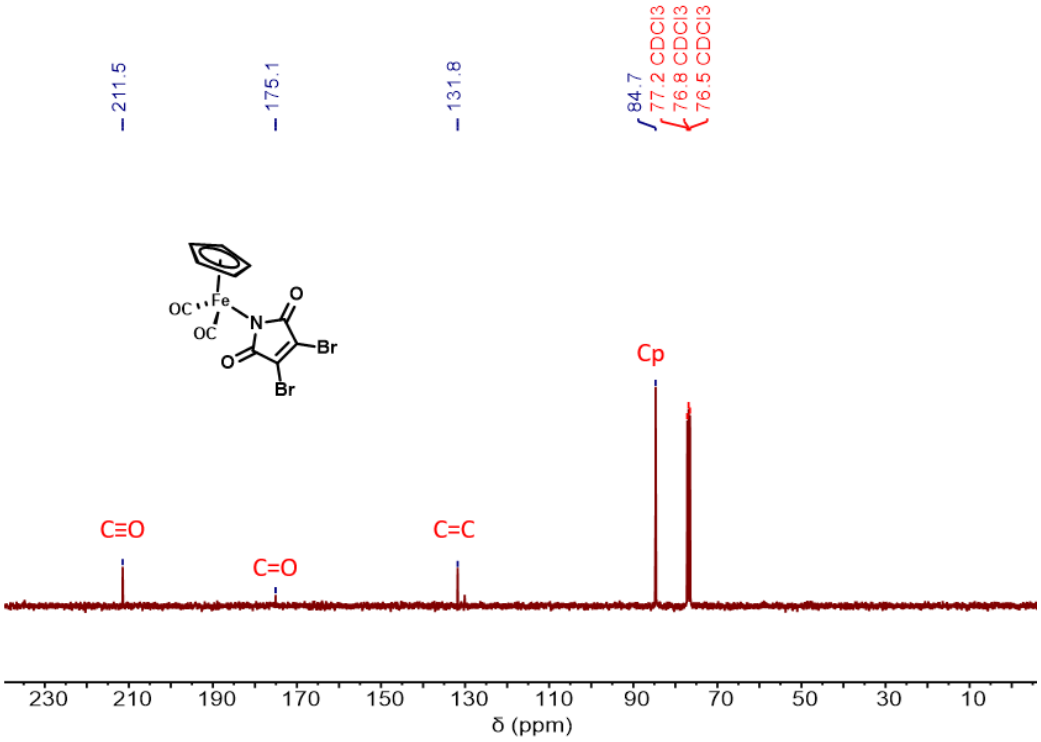

Fig. 3.28 ^{13}C NMR spectrum of **3.8** (101 MHz, $CDCl_3$).

(η^5-C_5H_5)Fe(CO)$_2$(η^1-*N*-3-bromo-4-ethylaminomaleimidato) (3.9; CpFe(CO)$_2$ABM)

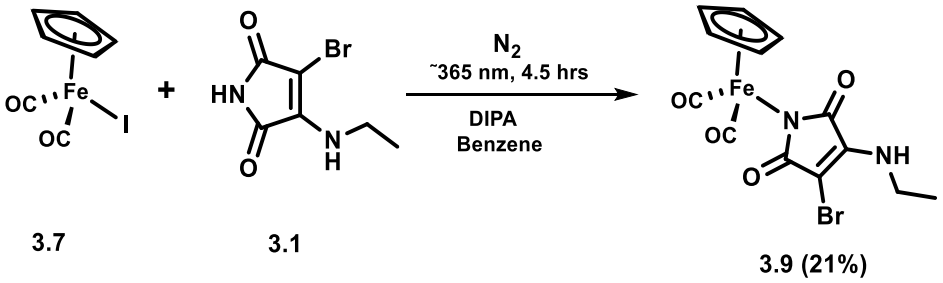

3.7 3.1 3.9 (21%)

The reaction was carried out by modifying the already established protocol.[44, 45] 700 mg of **3.7** (2.30 mmol, 1.0 equiv.) and 505 mg of **3.1** (2.30 mmol, 1.0 equiv.) was dissolved in 15 mL of ice-cooled anhydrous benzene. The solution was transferred to ice-cooled 100 mL 2-neck round bottom flask under nitrogen, followed by the addition

of 2.0 mL diisopropylamine at 0°C. The nitrogen-saturated reaction mixture was then illuminated with UV-light 365 nm for 4.5 hours. The solid was filtered off and the filtrate was evaporated to dryness. The orange-brown residue was purified by column chromatography to obtain light brown solid product.

R_f = 0.40 (hexane : ethyl acetate = 2:1), Yield = 140 mg, 21%.

^{1}H NMR (400 MHz, DMSO-d_6, 25°C, TMS) δ [ppm] = 5.30 (5H, s, Cp), 3.26-3.19 (2H, m, H5), 1.31-1.27 (3H, t, H6).

^{13}C NMR (101 MHz, DMSO-d_6, 25°C, TMS) δ [ppm] = 173.3, 168.5 (C=O), 150.4 (C=C), 83.3 (Cp), 38.5 (C5), 13.3 (C6).

FTIR (cm^{-1}): ν = 3250 (N-H), 2052, 2000 (C≡O), 1658 (C=O).

^{1}H NMR spectra shown in Fig. 3.7.

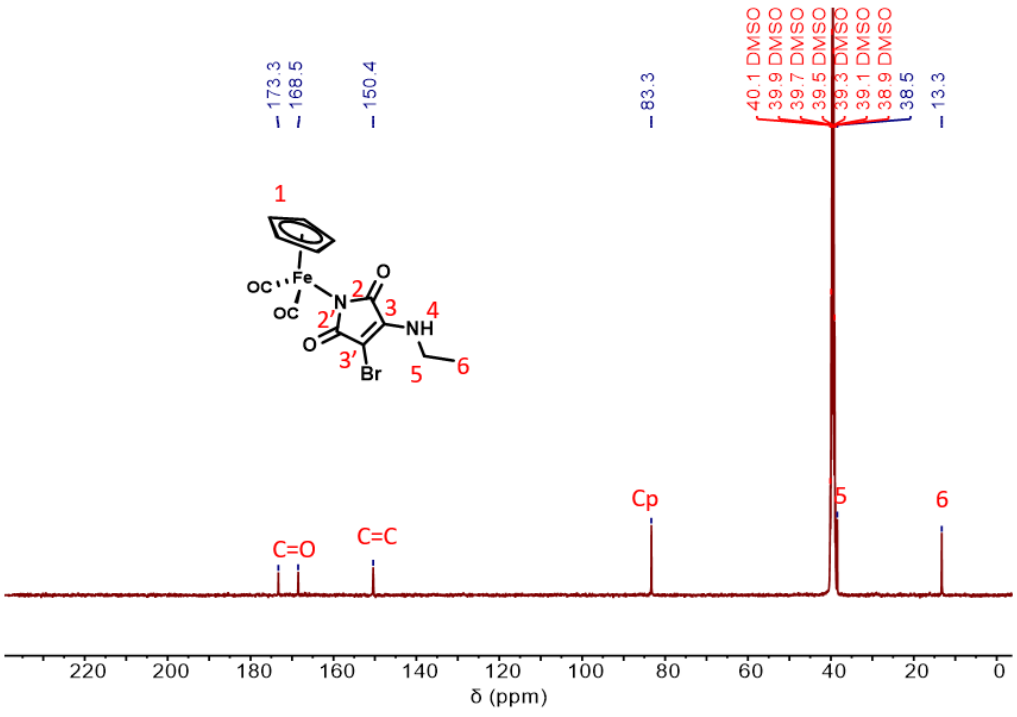

Fig. 3.29 ^{13}C NMR spectrum of **3.9** (101 MHz, DMSO-d_6).

(η^5-C_5H_5)Fe(CO)$_2$(η^1-*N*-dichloromaleimidato) (3.10; CpFe(CO)$_2$DCM)

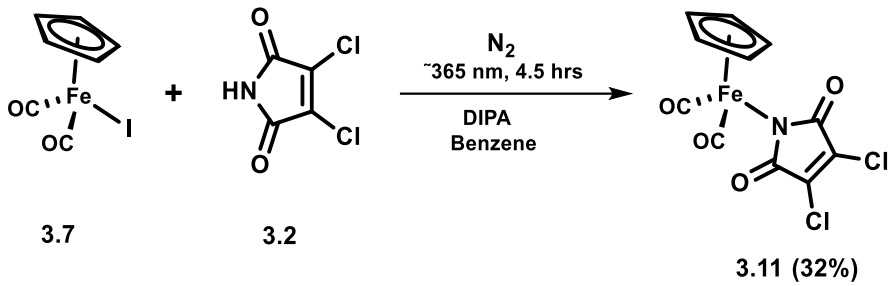

3.7 3.2 3.11 (32%)

The reaction was carried out by modifying the already established protocol.[44, 45] 1.0 g of **3.7** (3.29 mmol, 1.0 equiv.) and 546 mg of **3.2** (3.29 mmol, 1.0 equiv.) was dissolved in 15 mL of ice-cooled anhydrous benzene. The solution was transferred to ice-cooled 100 mL 2-neck round bottom flask under nitrogen, followed by the addition of 2.0 mL diisopropylamine at 0°C. The nitrogen-saturated reaction mixture was then illuminated with UV-light 365 nm for 4.5 hours. The solid was filtered off and the filtrate was evaporated to dryness. The residue was purified by column chromatography to obtain brown solid product.

R_f = 0.39 (hexane : ethyl acetate = 2:1), Yield = 365 mg, 32%.

^{1}H NMR (400 MHz, DMSO-d_6, 25°C, TMS) δ [ppm] = 5.35 (5H, s, Cp).

^{13}C NMR (101 MHz, DMSO-d_6, 25°C, TMS) δ [ppm] = 213. 1 (C≡O), 173.1 (C=O), 134.4 (C=C), 85.8 (Cp).

AP$^+$-MS: *m/z* [M]$^+$: 341.86

FTIR (cm^{-1}): ν = 2030, 1994 (C≡O), 1618 (C=O).

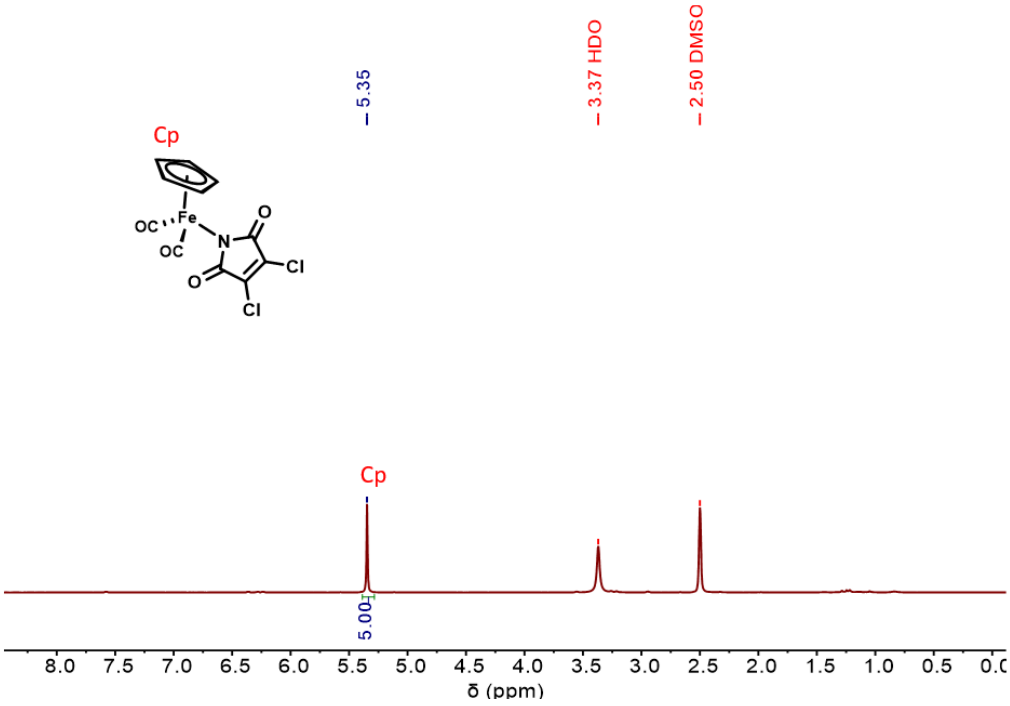

Fig. 3.30 ^{1}H NMR spectrum of **3.11** (400 MHz, DMSO-d_6).

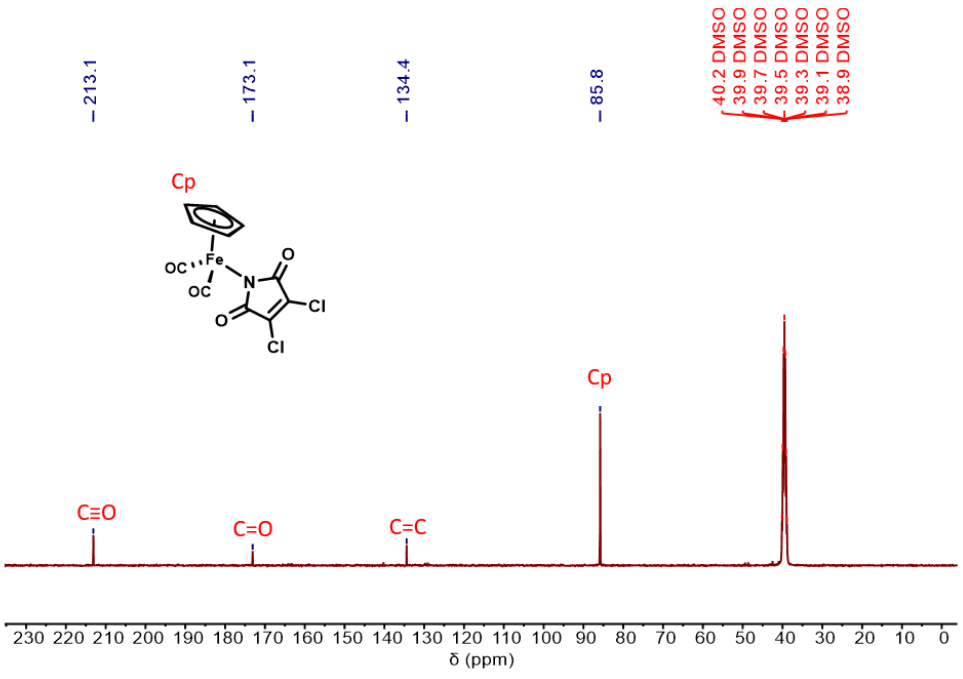

Fig. 3.31 ^{13}C NMR spectrum of **3.11** (101 MHz, DMSO-d_6).

(η^5-C_5H_5)Fe(CO)$_2$(η^1-*N*-3-chloro-4-ethylaminomaleimidato) (3.12; CpFe(CO)$_2$ACM)

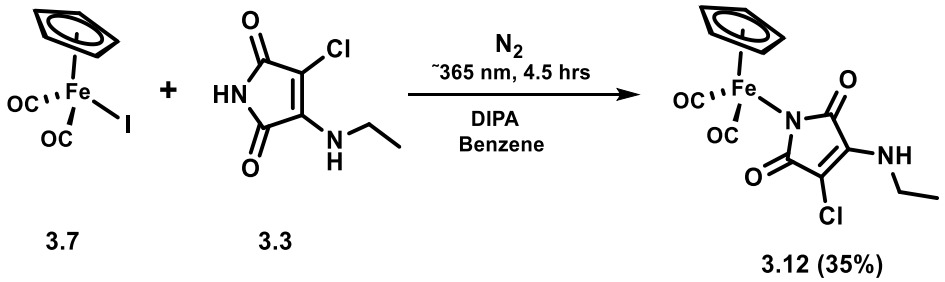

3.7 3.3 3.12 (35%)

The complex was prepared by modifying the already established protocol.[44, 45] 1.0 g of **3.7** (3.29 mmol, 1.0 equiv.) and 574 mg of **3.3** (3.29 mmol, 1.0 equiv.) was dissolved in 15 mL of ice-cooled anhydrous benzene. The solution was transferred to ice-cooled 100 mL 2-neck round bottom flask under nitrogen, followed by the addition of 1.5 mL diisopropylamine at 0°C. The nitrogen-saturated reaction mixture was then illuminated with UV-light 365 nm for 4.5 hours. The solid was filtered off and the filtrate was evaporated to dryness. The orange-brown residue was purified by column chromatography to obtain brown solid product.

R_f = 0.32 (hexane : ethyl acetate = 1.5:1), Yield = 404 mg, 39%.

^{1}H NMR (400 MHz, DMSO-d_6, 25°C, TMS) δ [ppm] = 6.99 (1H, s, H4), 5.28 (5H, s, Cp), 3.37 (2H, m, H5), 1.12-1.08 (3H, t, H6).

^{13}C NMR (101 MHz, DMSO-d_6, 25°C, TMS) δ [ppm] = 213.8 (C≡O), 177.9, 176.0 (C=O), 144.3 (C=C), 85.8 (Cp), 36.8 (C5), 16.4 (C6).

AP$^+$-MS: *m/z* [M]$^+$: 350.9

FTIR (cm^{-1}): ν = 3299 (N-H), 2038, 1988 (C≡O), 1620 (C=O).

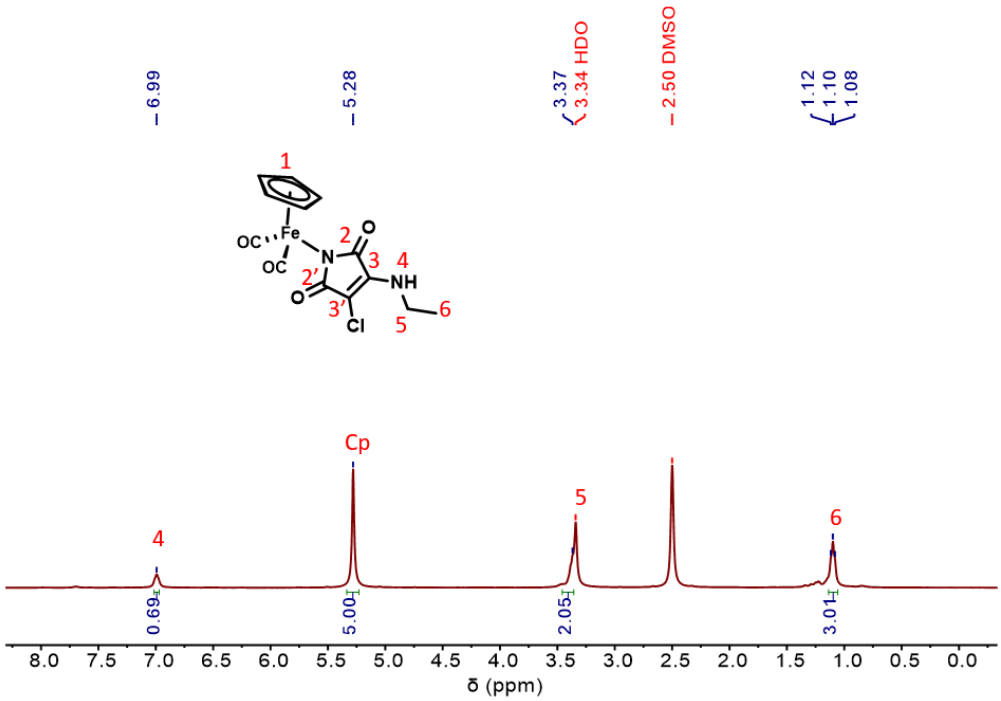

Fig. 3.32 ^{1}H NMR spectrum of **3.12** (400 MHz, DMSO-d_6).

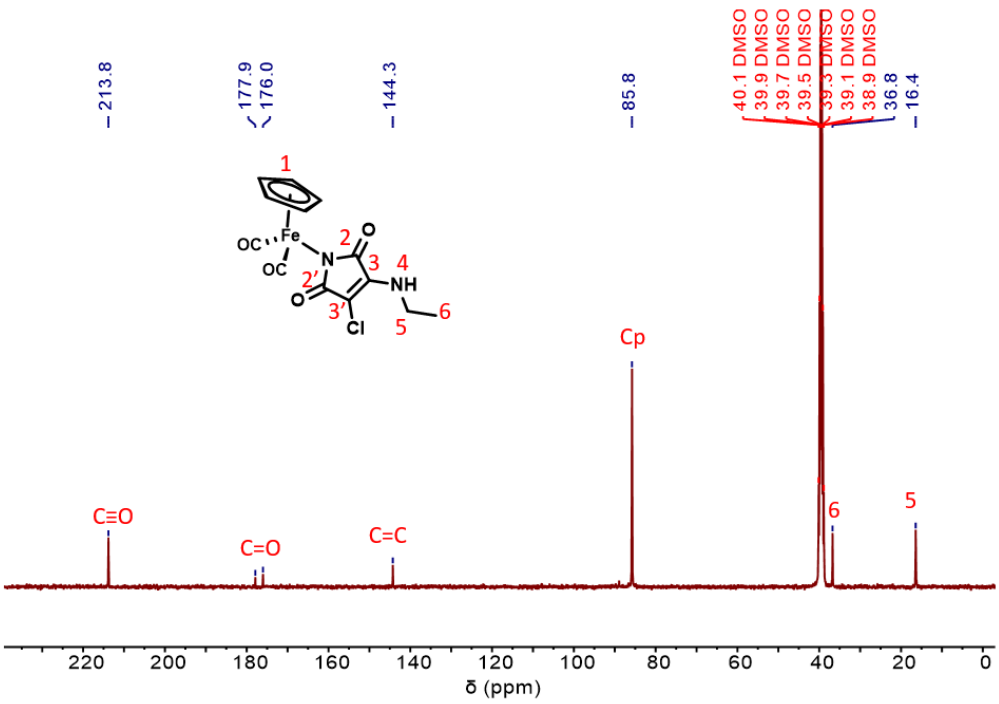

Fig. 3.33 ^{13}C NMR spectrum of **3.12** (101 MHz, DMSO-d_6).

η^5-$C_5(CH_3)_5Fe(CO)_2I$ (3.14; Cp*$Fe(CO)_2I$)

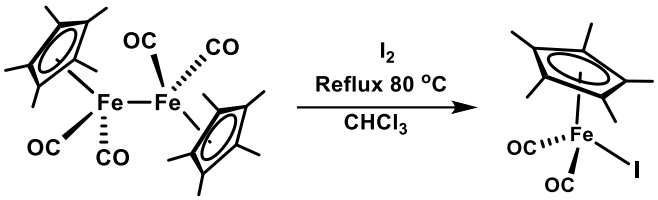

3.14 (60%)

Reaction was carried out according to the established protocol.[82] 2.0 g of pentamethylcyclopentadiene iron(II) dicarbonyl dimer (4.05 mmol, 1.0 equiv.) was dissolved in 25 mL of chloroform, and followed by the addition of 1.5 g iodine granules (6.07 mmol, 1.5 equiv.). The reaction mixture was refluxed at 80℃ for 60 min. After 60 min, the reaction mixture was extracted with $Na_2S_2O_3.5H_2O$ solution (3×100 mL, 1 M). The black color organic layer was collected and filtered. The solvent is removed *in vacuo* to obtain the black crystals of pentamethylcyclopentadienyl iron(II) dicarbonyl iodide.

Yield = 1.8 g, 60%.

^{1}H NMR (400 MHz, $CDCl_3$, 25°C, TMS) δ [ppm] = 1.98 (15H, s, H1).

^{13}C NMR (101 MHz, $CDCl_3$, 25°C, TMS) δ [ppm] = 215.4 (C≡O), 96.0 (Cp), 10.6 (C1).

FTIR (cm^{-1}): ν = 2001, 1941 (C≡O).

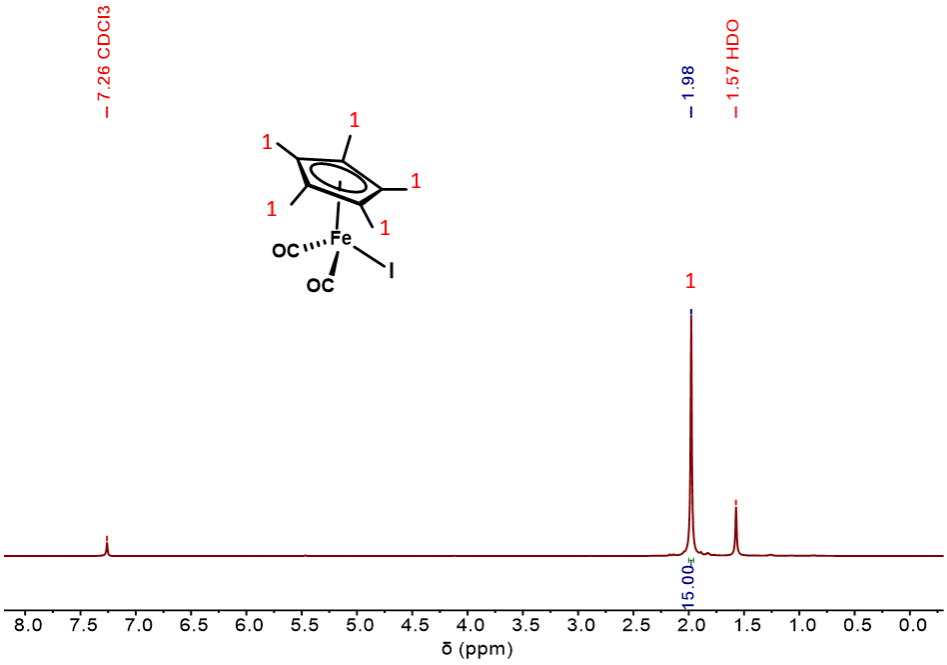

Fig. 3.34 ^{1}H NMR spectrum of **3.14** (400 MHz, $CDCl_3$).

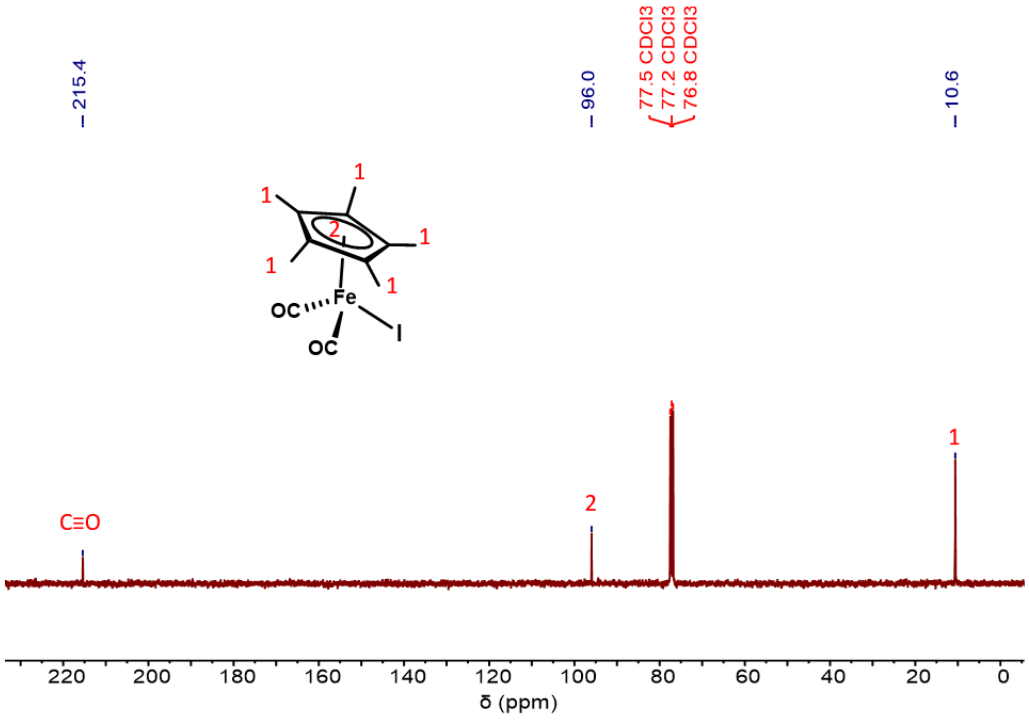

Fig. 3.35 ^{13}C NMR spectrum of **3.14** (101 MHz, $CDCl_3$).

(η^5- $C_5(CH_3)_5Fe(CO)_2$(η^1-*N*-3-chloro-4-ethylaminomaleimidato) (3.15; Cp*Fe(CO)$_2$ACM)

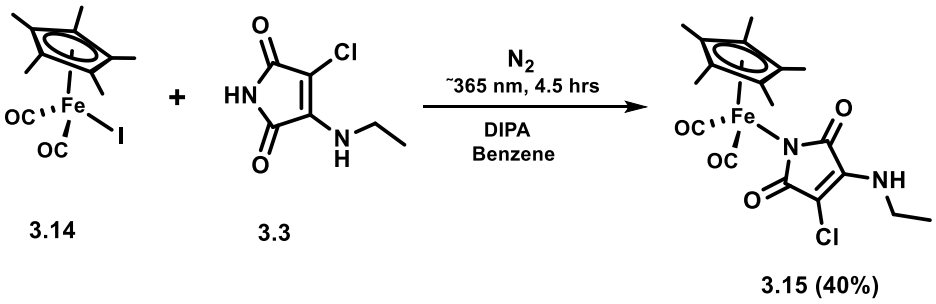

Reaction was carried out by modifying the already established protocol.[44, 45] 1.0 g of **3.14** (2.67 mmol, 1.0 equiv.) and 466 mg of **3.3** (2.67 mmol, 1.0 equiv.) was dissolved in 15 mL of ice-cooled anhydrous benzene. The solution was transferred to ice-cooled 100 mL 2-neck round bottom flask under nitrogen, followed by the addition of 1.5 mL diisopropylamine at 0°C. The nitrogen-saturated reaction mixture was then illuminated with UV-light 365 nm for 4.5 hours. The solid was filtered off and the filtrate was evaporated to dryness. The residue was purified by column chromatography to obtain brown solid product.

R_f = 0.46 (hexane : ethyl acetate = 1.5:1), Yield = 450 mg, 40%.

^{1}H NMR (400 MHz, $CDCl_3$, 25°C, TMS) δ [ppm] = 4.94 (1H, H4), 3.35 (2H, H5), 1.05 (18H, H1 & H6).

^{13}C NMR (101 MHz, $CDCl_3$, 25°C, TMS) δ [ppm] = 214.9 (C≡O), 179.0, 177.0 (C=O), 143.7 (C=C), 96.5 (C7), 37.7 (C5), 16.1 (C6), 9.6 (C1).

AP$^+$-MS: *m/z* $[M]^+$: 432.9

FTIR (cm^{-1}): ν = 3315 (N-H), 2023, 1955 (C≡O), 1623 (C=O).

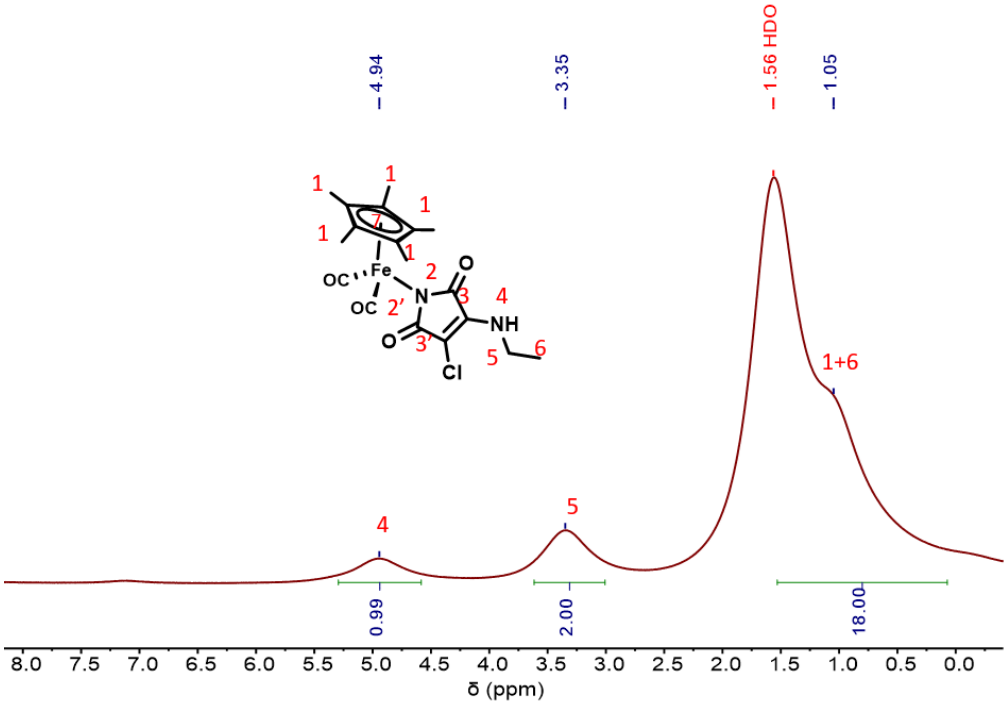

Fig. 3.36 ^{1}H NMR spectrum of **3.15** (400 MHz, $CDCl_3$).

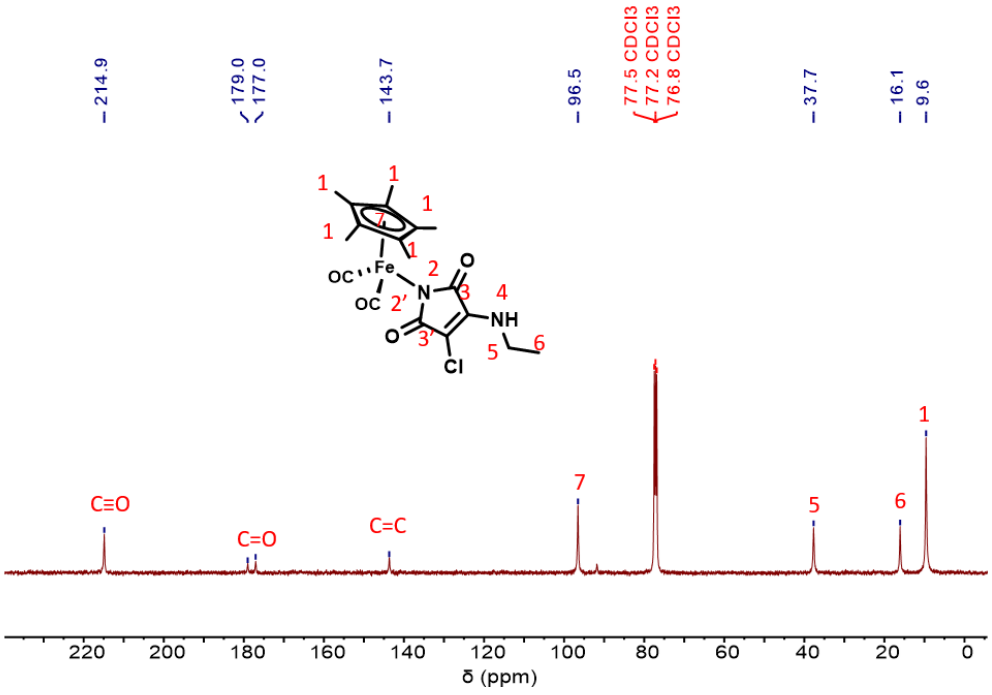

Fig. 3.37 ^{13}C NMR spectrum of **3.15** (101 MHz, $CDCl_3$).

η^5-$C_5H_5Ru(CO)_2I$ (3.16; $CpRu(CO)_2I$)

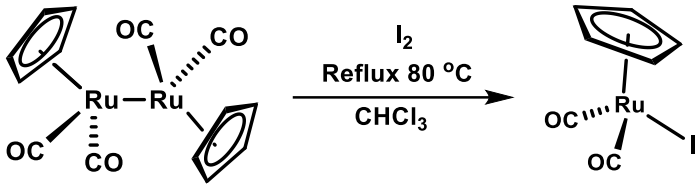

3.16 (75%)

Synthesis of the precursor was carried out according to the established protocol.[83] 1.5 g of cyclopentadienyl ruthenium(II) dicarbonyl dimer (3.37 mmol, 1.0 equiv.) was dissolved in 25 mL of chloroform, and followed by the addition of 1.3 g iodine granules (5.05 mmol, 1.5 equiv.). The reaction mixture was refluxed at 80°C for 60 min. After 1 h, the reaction mixture was extracted with $Na_2S_2O_3.5H_2O$ solution (3 × 100 mL, 1 M). The black color organic layer was collected and filtered. The solvent is removed in vacuo to obtain the orange crystals of cyclopentadienyl ruthenium(II) dicarbonyl iodide.

Yield = 2.3 g, 75%.

^{1}H NMR (400 MHz, $CDCl_3$, 25°C, TMS) δ [ppm] = 5.46 (5H, s, Cp).

^{13}C NMR (101 MHz, $CDCl_3$, 25°C, TMS) δ [ppm] = 195.3 (C≡O), 87.1 (Cp).

FTIR (cm^{-1}): ν = 2033, 1940 (C≡O).

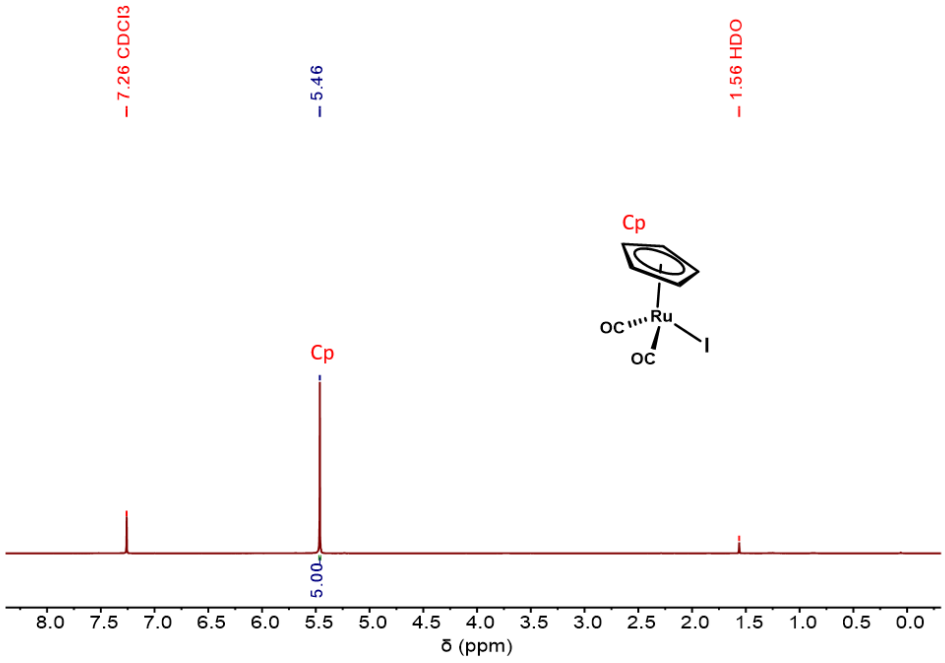

Fig. 3.38 ^{1}H NMR spectrum of **3.16** (400 MHz, $CDCl_3$).

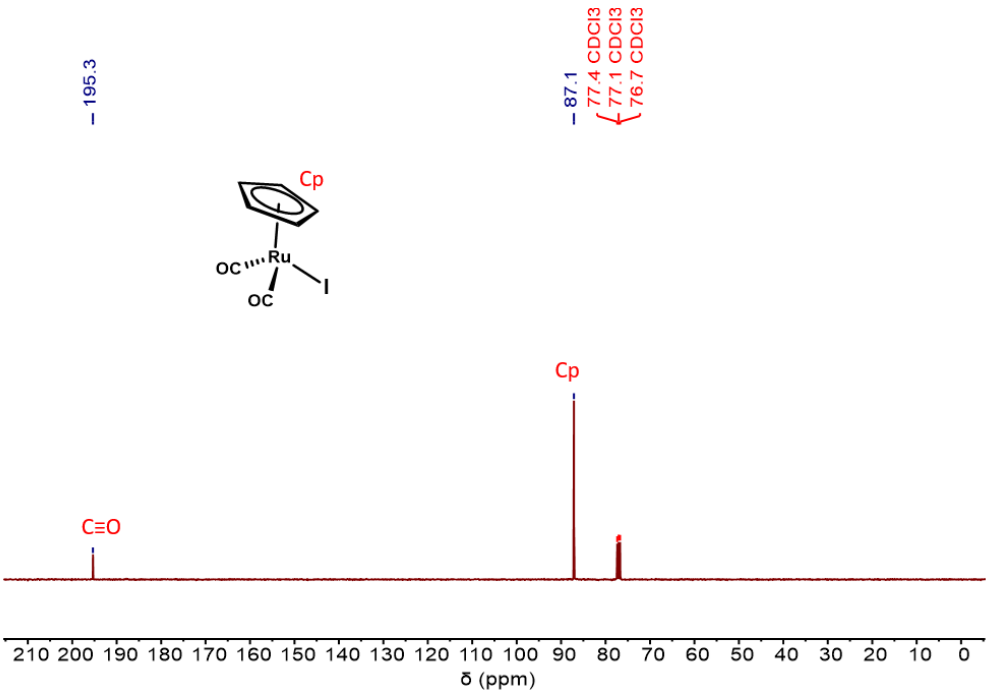

Fig. 3.39 ^{13}C NMR spectrum of **3.16** (101 MHz, $CDCl_3$).

(η^5-C_5H_5)Ru(CO)$_2$(η^1-*N*-3-chloro-4-ethylaminomaleimidato) (3.17; CpRu(CO)$_2$ACM)

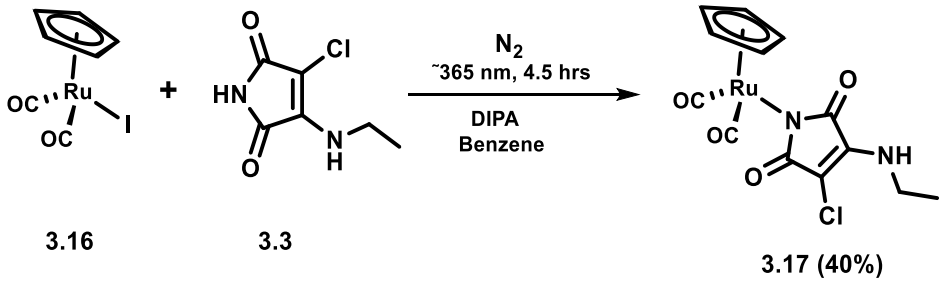

3.16 3.3 3.17 (40%)

The ruthenium maleimide complex was prepared by modifying the already established protocol.[57] 1.0 g of **3.16** (2.86 mmol, 1.0 equiv.) and 500 mg of **3.3** (2.86 mmol, 1.0 equiv.) was dissolved in 15 mL of ice-cooled anhydrous benzene. The solution was transferred to ice-cooled 100 mL 2-neck round bottom flask under nitrogen, followed by the addition of 1.5 mL diisopropylamine at 0°C. The nitrogen-saturated reaction mixture was then illuminated with UV-light 365 nm for 4.5 hours. The solid was filtered off and the filtrate was evaporated to dryness. The residue was purified by column chromatography to obtain bright orange color solid product.

R_f = 0.30 (hexane : ethyl acetate = 1.5:1), Yield = 455 mg, 40%.

^{1}H NMR (400 MHz, DMSO-d_6, 25°C, TMS) δ [ppm] = 7.08 (1H, s, H4), 5.69 (5H, s, Cp), 3.43-3.36 (2H, m, H5), 1.14-1.10 (3H, t, H6).

^{13}C NMR (101 MHz, DMSO-d_6, 25°C, TMS) δ [ppm] = 198.8 (C≡O), 177.6, 175.4 (C=O), 144.0 (C=C), 88.4 (Cp), 37.2 (C5), 16.9 (C6).

AP$^+$-MS: *m/z* [M]$^+$: 395.57

FTIR (cm^{-1}): ν = 3311 (N-H), 2047, 1974 (C≡O), 1629 (C=O).

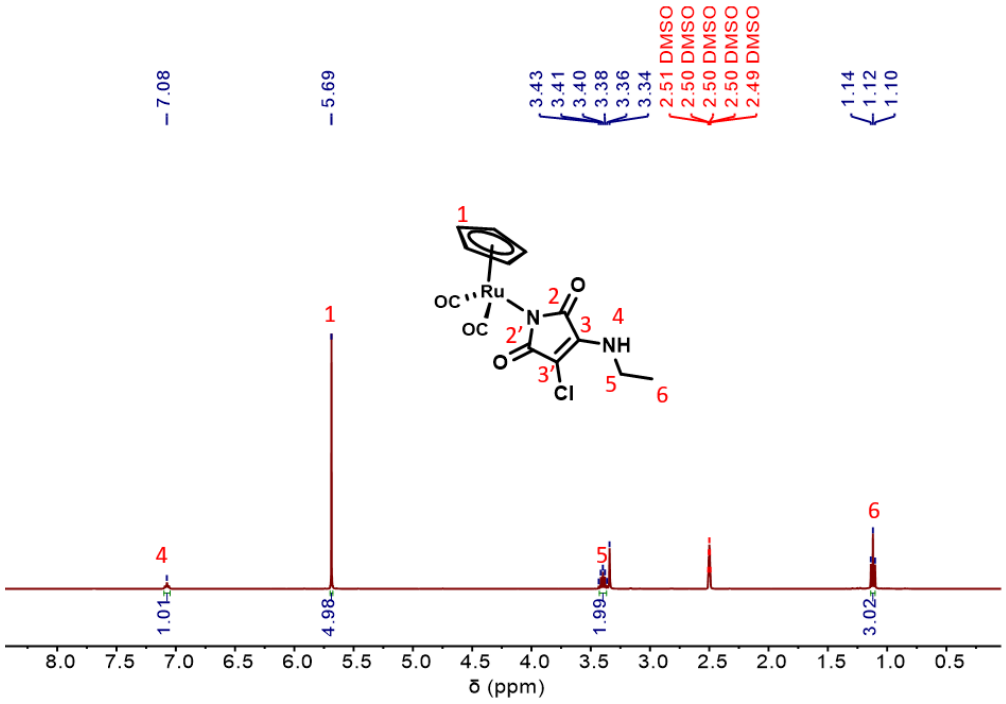

Fig. 3.40 ^{1}H NMR spectrum of **3.17** (400 MHz, DMSO-d_6).

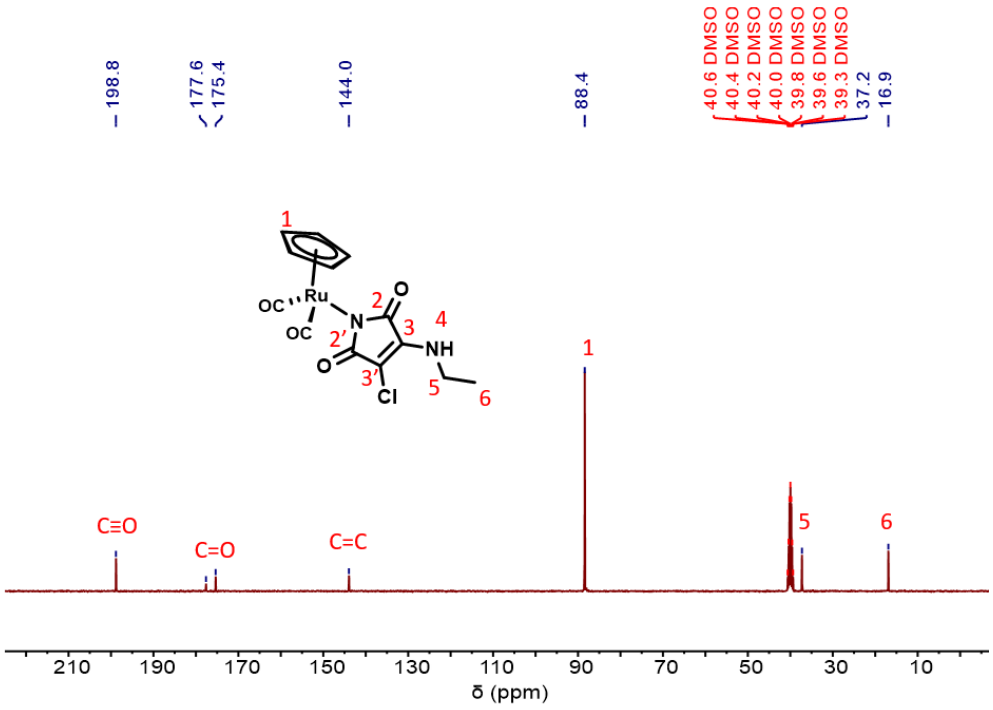

Fig. 3.41 ^{13}C NMR spectrum of **3.17** (101 MHz, DMSO-d_6).

η^5-$C_5H_5Mo(CO)_3I$ (3.18; $CpMo(CO)_3I$)

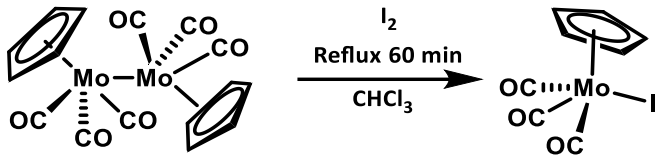

3.18 (70%)

Synthesis of the precursor was carried out according to the established protocol.[84] 1.5 g of cyclopentadienyl molybdenum(II) tricarbonyl dimer (3.06 mmol, 1.0 equiv.) was dissolved in 25 mL of chloroform, and followed by the addition of 1.2 g iodine granules (4.59 mmol, 1.5 equiv.). The reaction mixture was refluxed at 80°C for 60 min. After 1 h, the reaction mixture was extracted with $Na_2S_2O_3.5H_2O$ solution (3×100 mL, 1 M). The black color organic layer was collected and filtered. The solvent is removed in vacuo to obtain the orange crystals of cyclopentadienyl molybdenum(II) tricarbonyl iodide.

Yield = 1.6 g, 70%.

^{1}H NMR (400 MHz, $CDCl_3$, 25°C, TMS) δ [ppm] = 5.62 (5H, s, Cp).

^{13}C NMR (101 MHz, $CDCl_3$, 25°C, TMS) δ [ppm] = 220.3 (C≡O), 94.3 (Cp).

FTIR (cm^{-1}): ν = 2029, 1927 (C≡O).

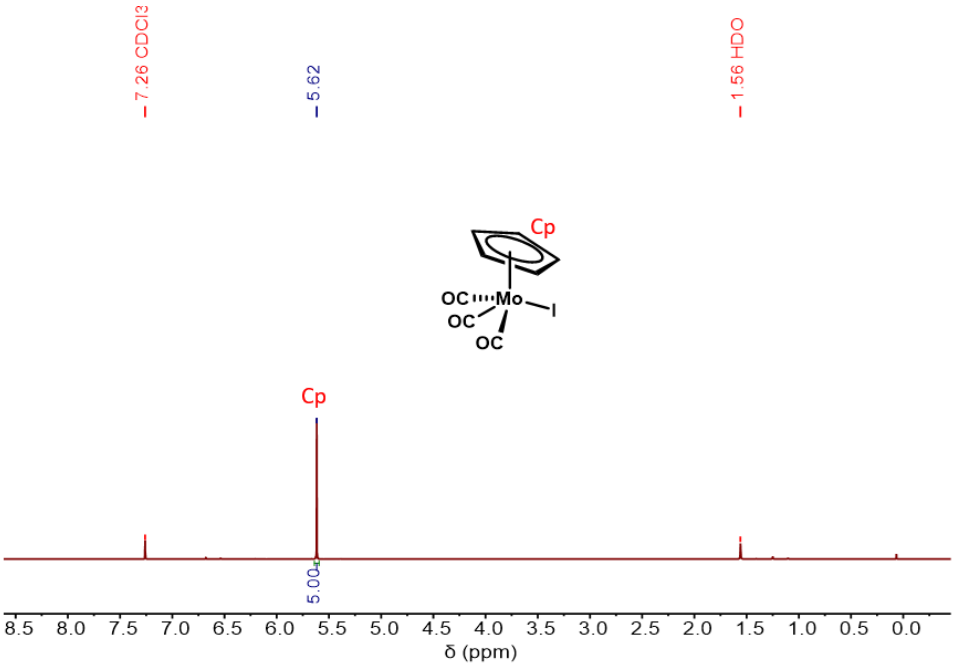

Fig. 3.42 ^{1}H NMR spectrum of **3.18** (400 MHz, $CDCl_3$).

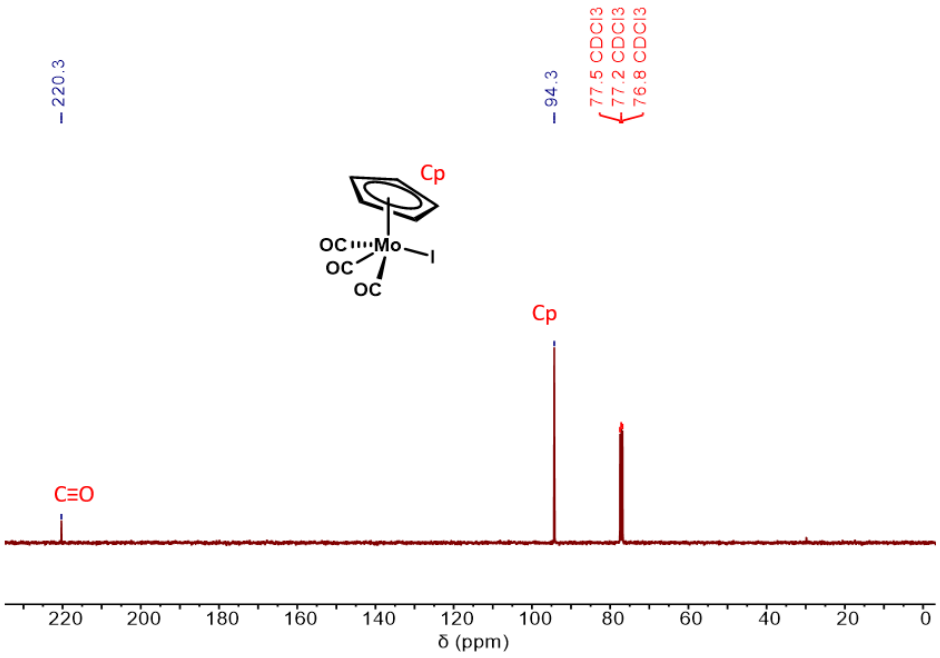

Fig. 3.43 ^{13}C NMR spectrum of **3.18** (400 MHz, $CDCl_3$).

(η^5-C_5H_5)Mo(CO)$_3$(η^1-*N*-3-chloro-4-ethylaminomaleimidato) (3.19; CpMo(CO)$_3$ACM)

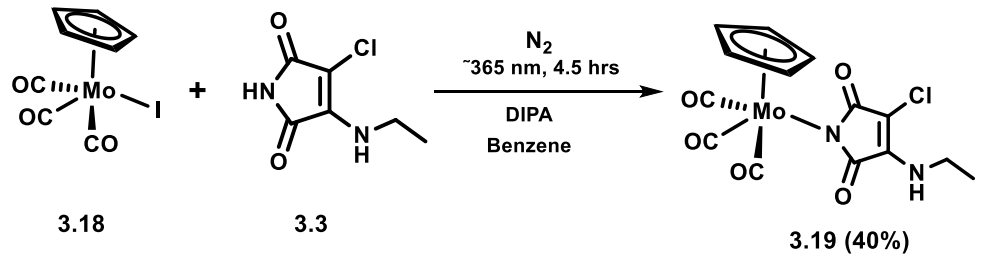

3.18 3.3 3.19 (40%)

The molybdenum maleimide complex was prepared by modifying the already established protocol.[48] 875 mg of **3.18** (2.35 mmol, 1.0 equiv.) and 410 mg of **3.3** (2.35 mmol, 1.0 equiv.) was dissolved in 15 mL of ice-cooled anhydrous benzene. The solution was transferred to ice-cooled 100 mL 2-neck round bottom flask under nitrogen, followed by the addition of 1.5 mL diisopropylamine at 0°C. The nitrogen-saturated reaction mixture was then illuminated with UV-light 365 nm for 4.5 hours. The solid was filtered off and the filtrate was evaporated to dryness. The residue was purified by column chromatography to obtain orange color solid product.

R_f = 0.35 (hexane : ethyl acetate = 1.5:1), Yield = 395 mg, 40%.

^{1}H NMR (400 MHz, DMSO-d_6, 25°C, TMS) δ [ppm] = 7.21 (1H, s, H4), 5.77 (5H, s, Cp), 3.46 (2H, m, H5), 1.14-1.10 (3H, t, H6).

^{13}C NMR (101 MHz, DMSO-d_6, 25°C, TMS) δ [ppm] = 228.8 (C≡O), 177.3, 175.1 (C=O), 144.0 (C=C), 95.7 (Cp), 36.9 (C5), 16.4 (C6).

AP$^+$-MS: *m/z* [M]$^+$: 418.49.

FTIR (cm^{-1}): ν = 3311 (N-H), 2034, 1933 (C≡O), 1636 (C=O).

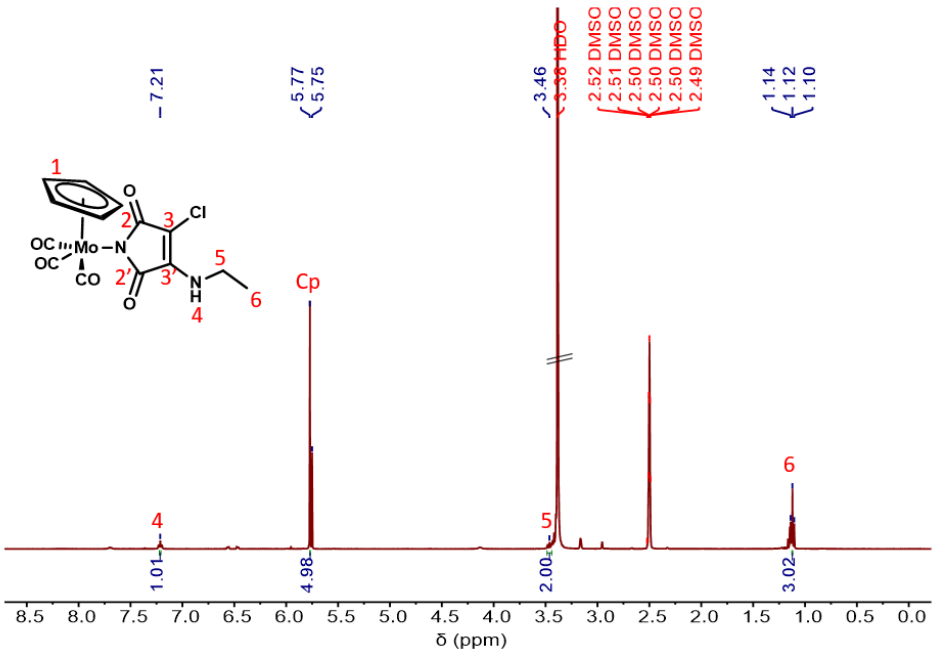

Fig. 3.44 ^{1}H NMR spectrum of **3.19** (400 MHz, DMSO-d_6).

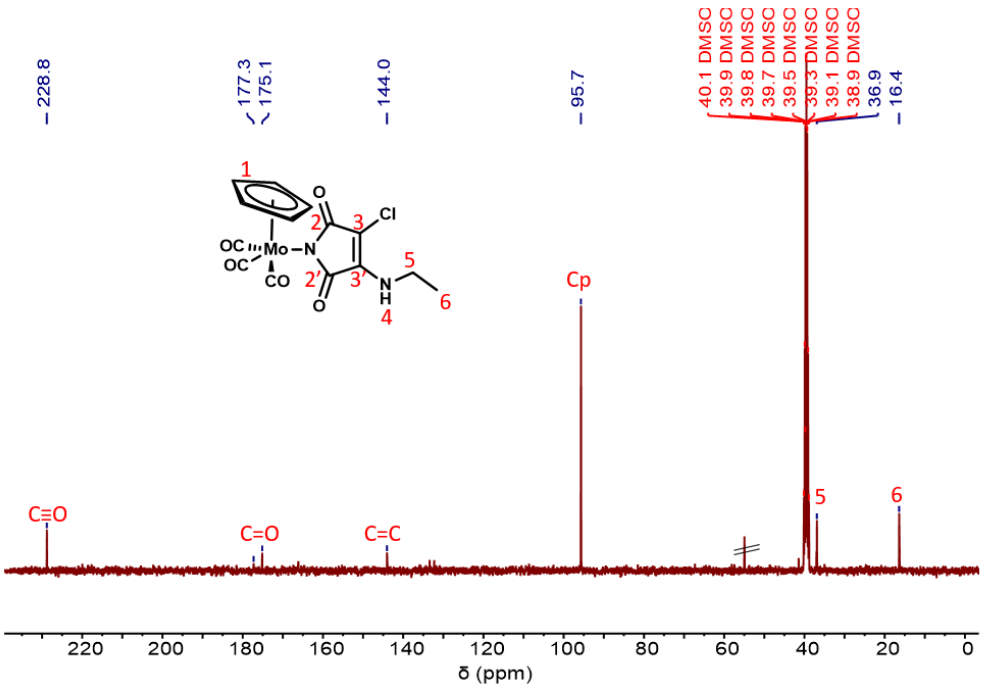

Fig. 3.45 ^{13}C NMR spectrum of **3.19** (101 MHz, DMSO-d_6).

(η^5-C_5H_5)Fe(CO)$_2$(η^1-*N*-3,4-bis(butylthiol)maleimidato) (3.20; CpFe(CO)$_2$DTM)

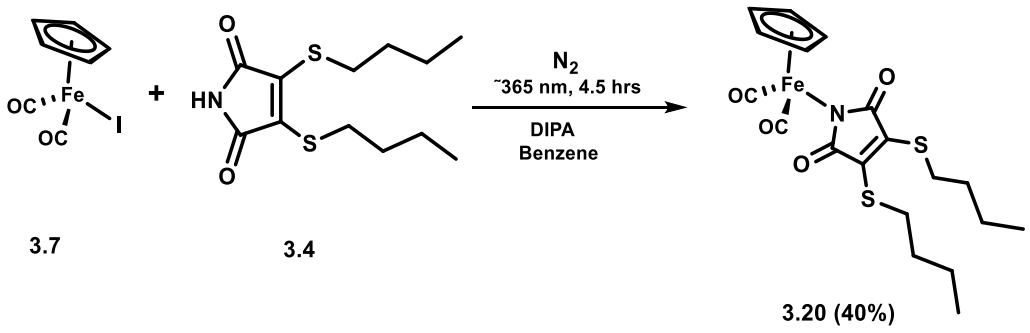

3.7 3.4 3.20 (40%)

The complex was prepared by modifying the already established protocol.[44, 45] 700 mg of **3.7** (2.30 mmol, 1.0 equiv.) and 628 mg of **3.4** (2.30 mmol, 1.0 equiv.) was dissolved in 15 mL of ice-cooled anhydrous benzene. The solution was transferred to ice-cooled 100 mL 2-neck round bottom flask under nitrogen, followed by the addition of 1.5 mL diisopropylamine at 0°C. The nitrogen-saturated reaction mixture was then illuminated with UV-light 365 nm for 4.5 hours. The solid was filtered off and the filtrate was evaporated to dryness. The residue was purified by column chromatography to obtain brown oil as product.

R_f = 0.41 (n-hexane : ethyl acetate = 2:1), Yield = 345 mg, 40%.

^{1}H NMR (400 MHz, DMSO-d_6, 25°C, TMS) δ [ppm] = 5.28 (5H, Cp), 3.17 (4H, H4), 1.49-1.32 (8H, t, H5&6), 0.85 (6H, H7).

^{13}C NMR (101 MHz, DMSO-d_6, 25°C, TMS) δ [ppm] = 213.5 (C≡O), 177.1 (C=O), 138.7 (C=C), 85.6 (Cp), 31.9 (C5), 30.6 (C4), 20.8 (C6), 13.2 (C7).

AP$^+$-MS: *m/z* [M]$^+$: 449.96.

FTIR (cm^{-1}): ν = 2025, 1960 (C≡O), 1610 (C=O).

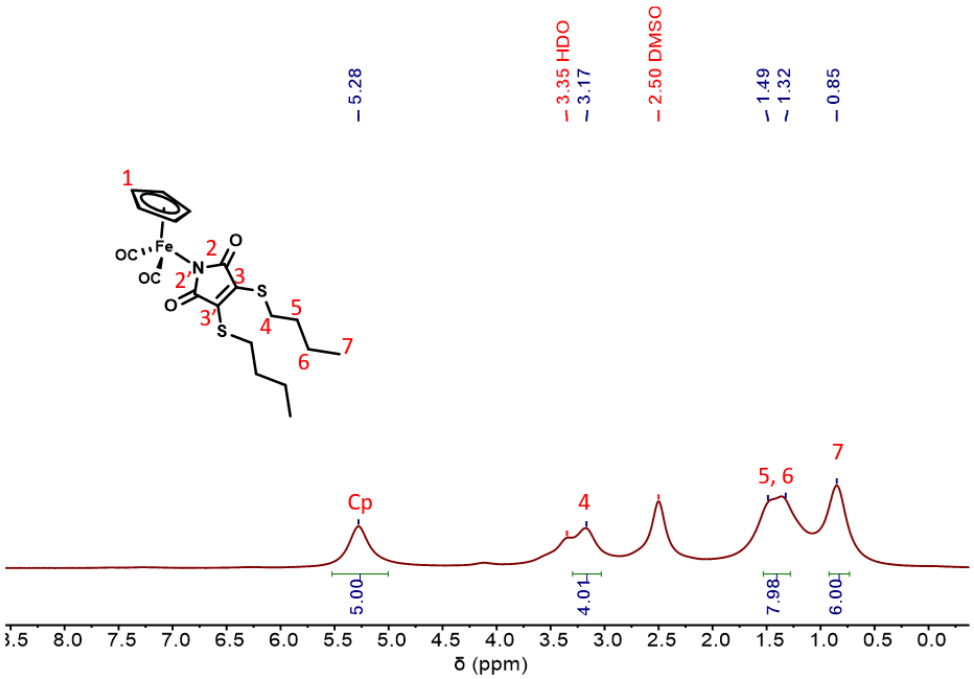

Fig. 3.46 ^{1}H NMR spectrum of **3.20** (400 MHz, DMSO-d_6).

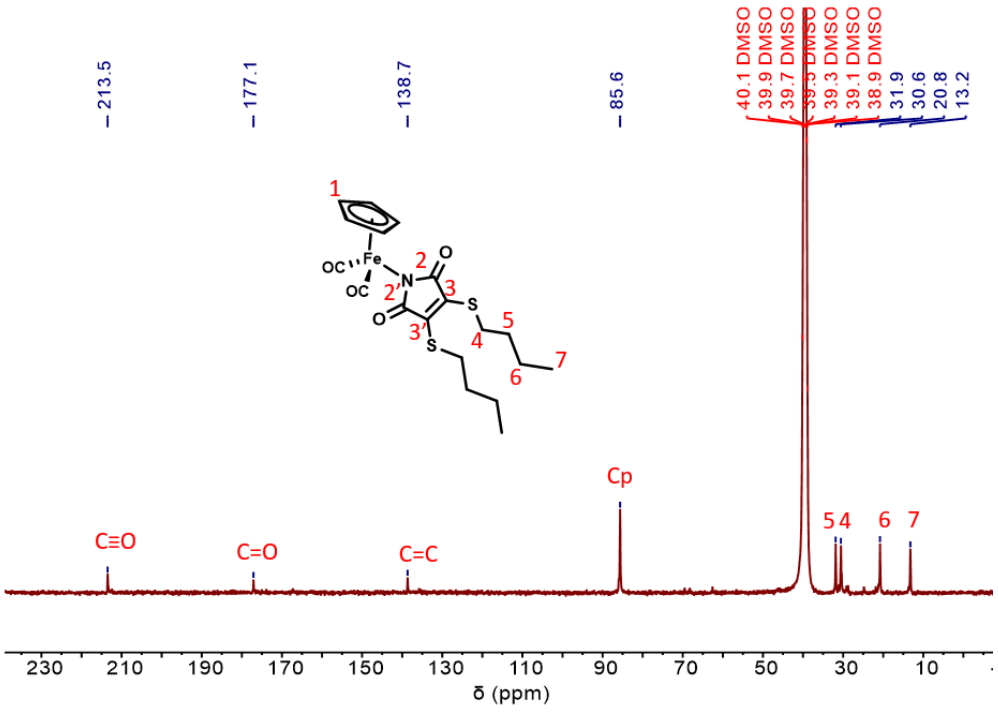

Fig. 3.47 ^{13}C NMR spectrum of **3.20** (101 MHz, DMSO-d_6).

η^5-$C_5H_5Co(CO)I_2$ (3.21; $CpCo(CO)I_2$)

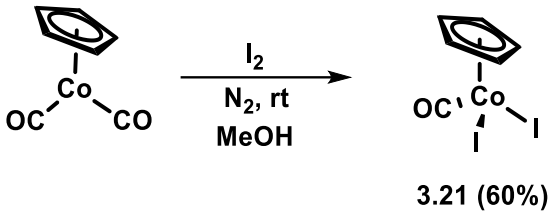

3.21 (60%)

Reaction was carried out according to the already reported protocol.[59] 1.0 g of $C_5H_5Co(CO)_2$ (5.55 mmol, 1.0 equiv.) was dissolved in anhydrous methanol under nitrogen, followed by the addition of 1.4 g of iodine (5.55 mmol, 1.0 equiv.). The formation of a black precipitate occurred immediately. After stirring for 24 h to assure complete reaction, the black crystalline precipitate was filtered, washed with diethyl ether, and dried to give purple black crystals of $CpCoCOI_2$.

Yield = 1.3 g, 60%.

^{1}H NMR (400 MHz, $CDCl_3$, 25°C, TMS) δ [ppm] = 5.69 (s, 5H).

^{13}C NMR (101 MHz, $CDCl_3$, 25°C, TMS) δ [ppm] = 89.6 (C_p).

AP$^+$-MS: *m/z* [M^+]: 405.94.

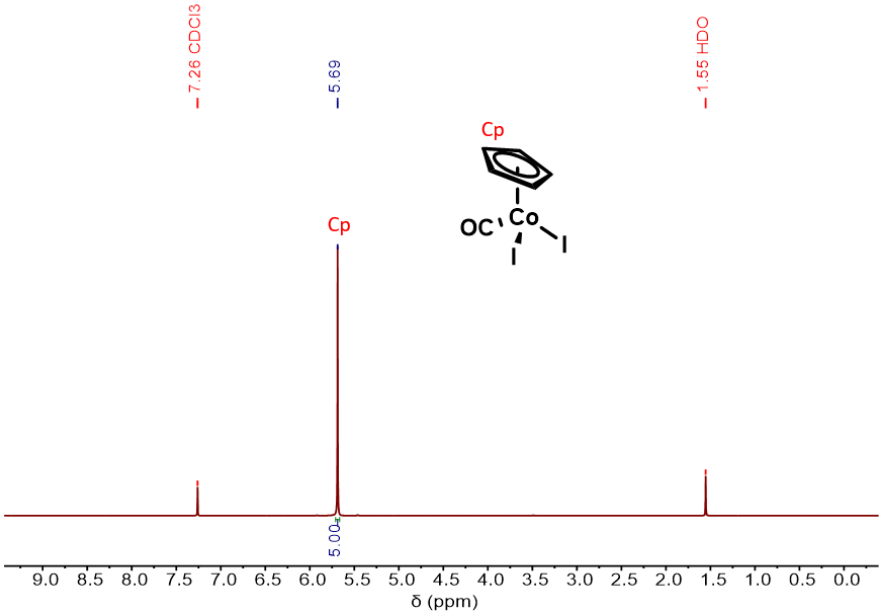

Fig. 3.48 ^{1}H NMR spectrum of **3.21** (400 MHz, $CDCl_3$).

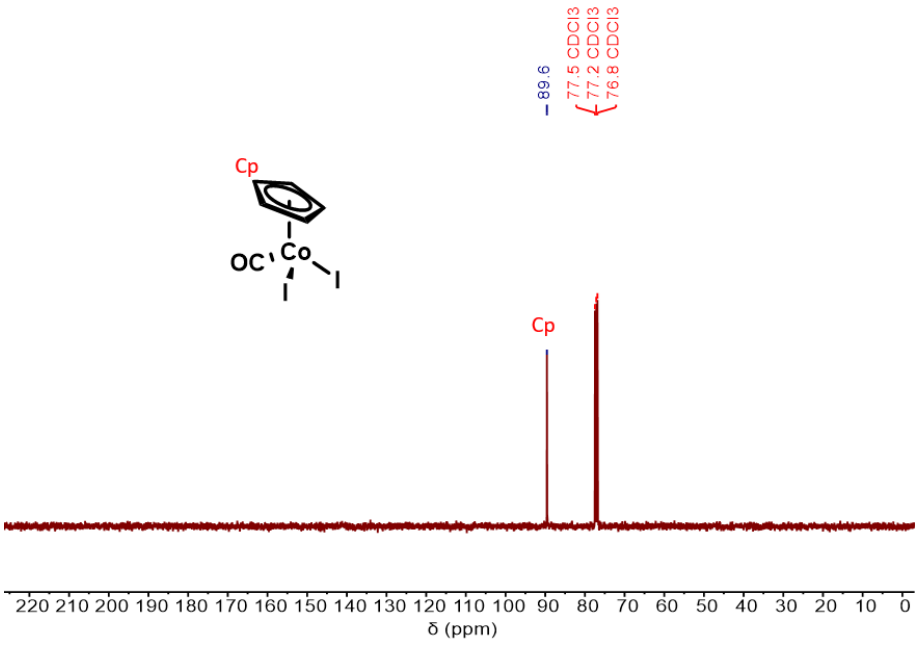

Fig. 3.49 ^{13}C NMR spectrum of **3.21** (101 MHz, $CDCl_3$).

$[\eta^5\text{-}C_5H_5Fe(CO)_2(Et_2O)]BF_4$ (3.23)

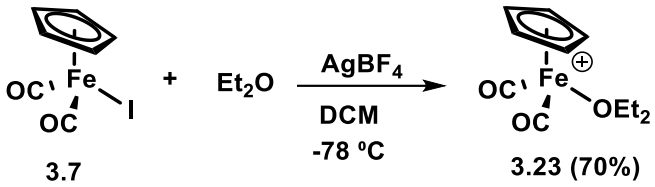

The diethyl ether complex, $[CpFe(CO)_2(Et_2O)]BF_4$ has been synthesized following the published protocol.[85] 547 mg of **3.7** (0.70 mmol) and 500 mg of $AgBF_4$ (1.00 mmol) were transferred to a foil-wrapped 100 mL Schleck ampoule and dried overnight under reduced pressure to remove any water absorbed. 30 mL of dichloromethane was added and stirred in the dark for 45 min. The reaction mixture was cooled to -78℃ and stirred for further 30 min. The resulting wine red-colored solution was canula filtered into another Schleck ampoule, already flushed with nitrogen and filled with ice-cooled dry nitrogen-saturated diethyl ether (80 mL). Immediately a red precipitate formed and the mixture was cooled to -78℃ and allowed to stand for 2 h. The mother liquor was removed under nitrogen to leave a red solid residue and dried under reduced pressure at 0°C to obtain red-orange crystalline solid.

Yield: 180 mg, 70%.

^{1}H NMR (400 MHz, CD_2Cl_2, 25 ℃, TMS) δ [ppm] = 5.36 (5H, s, Cp), 3.50-3.45 (4H, q, CH_2), 1.21-1.18 (6H, t, CH_3).

^{13}C NMR (101 MHz, CD_2Cl_2, 25 ℃, TMS) δ [ppm] = 209.8 (C≡O), 85.6 (Cp), 65.9 (CH_2), 15.2 (CH_3).

Matches literature data.[85]

[η^5-$C_5H_5Fe(CO)_2(NH_2CH_3CH_3)$] (3.24)

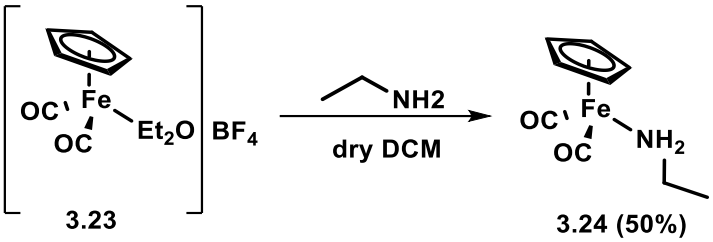

The synthesis of amine complex of the cyclopentadienyliron dicarbonyl complex cation was achieved according to the published protocol.[85] The diethyl ether iron complex **3.23** (200 mg, 0.59 mmol) was dissolved in 10mL anhydrous dichloromethane, followed by the dropwise addition of ethylamine (58 µL, 0.88 mmol). There is an immediate change of color from red to brown. The reaction mixture was stirred for 3 h and then anhydrous diethyl ether was added till the formation of yellow precipitates. The mixture was allowed to stand for 20 min. The mother liquid was removed and the complex [η^5-$C_5H_5Fe(CO)_2(NH_2CH_3CH_3)$] was obtained as yellow-orange crystalline solid.

Yield: 100 mg, 50%.

^{1}H NMR (400 MHz, CD_2Cl_2, 25 ˚C, TMS) δ [ppm] = 5.27 (5H, s, Cp), 2.95 (2H, s, –NH_2), 2.57-2.44 (2H, m, -CH_2), 0.99-0.95 (3H, t, CH_3).

^{13}C NMR (101 MHz, CD_2Cl_2, 25 ˚C, TMS) δ [ppm] = 210.0 (C≡O), 86.1 (Cp), 36.48 (CH_2), 19.1 (CH_3).

^{13}C NMR spectra shown in Fig. 3.12

3.6 References

1. Keefe, M. H.; Benkstein, K. D.; Hupp, J. T., Luminescent sensor molecules based on coordinated metals: a review of recent developments. *Coord. Chem. Rev.* **2000,** *205* (1), 201-228.

2. Lo, K. K.-W.; Li, S. P.-Y.; Zhang, K. Y., Development of luminescent iridium(iii) polypyridine complexes as chemical and biological probes. *New J. Chem.* **2011,** *35* (2), 265-287.

3. Zhao, Q.; Li, F.; Huang, C., Phosphorescent chemosensors based on heavy-metal complexes. *Chem. Soc. Rev.* **2010,** *39* (8), 3007-3030.

4. Gao, H.; Yu, R.; Ma, Z.; Gong, Y.; Zhao, B.; Lv, Q.; Tan, Z. a., Recent advances of organometallic complexes in emerging photovoltaics. *J. Polym. Sci,* **2022,** *60* (6), 865-916.

5. Thorp-Greenwood, F. L.; Balasingham, R. G.; Coogan, M. P., Organometallic complexes of transition metals in luminescent cell imaging applications. *J. Organomet. Chem.* **2012,** *714*, 12-21.

6. Lees, A. J., Organometallic complexes as luminescence probes in monitoring thermal and photochemical polymerizations. *Coord. Chem. Rev.* **1998,** *177* (1), 3-35.

7. Mauro, M.; Aliprandi, A.; Cebrián, C.; Wang, D.; Kübel, C.; De Cola, L., Self-assembly of a neutral platinum(ii) complex into highly emitting microcrystalline fibers through metallophilic interactions. *Chem. Commun.* **2014,** *50* (55), 7269-7272.

8. Vogler, A.; Kunkely, H. J. C. o. I. C., Inorganic Chromophores: Optical Charge Transfer in Coordination Compounds. *Comments Inrog. Chem.* **1997,** *19*, 283-306.

9. Lees, A. J., Luminescence properties of organometallic complexes. *Chem. Rev.* **1987,** *87* (4), 711-743.

10. Vogler, A.; Kunkely, H., Excited state properties of organometallic compounds of rhenium in high and low oxidation states. *Coord. Chem. Rev.* **2000,** *200-202*, 991-1008.

11. Wagenknecht, P. S.; Ford, P. C., Metal centered ligand field excited states: Their roles in the design and performance of transition metal based photochemical molecular devices. *Coord. Chem. Rev.* **2011,** *255* (5), 591-616.

12. Rochester, D. L.; Develay, S.; Záliš, S.; Williams, J. A. G., Localised to intraligand charge-transfer states in cyclometalated platinum complexes: an experimental and theoretical study into the influence of electron-rich pendants and modulation of excited states by ion binding. *Dalton Trans.* **2009,** (10), 1728-1741.

13. Han, X.; Wu, L. Z.; Si, G.; Pan, J.; Yang, Q. Z.; Zhang, L. P.; Tung, C. H., Switching between ligand-to-ligand charge-transfer, intraligand charge-transfer, and metal-to-ligand charge-transfer excited states in platinum(II) terpyridyl acetylide complexes induced by pH change and metal ions. *J. Chem.* **2007,** *13* (4), 1231-9.

14. Zhao, N.; Wu, Y.-H.; Wen, H.-M.; Zhang, X.; Chen, Z.-N., Conversion from ILCT to LLCT/MLCT Excited State by Heavy Metal Ion Binding in Iridium(III) Complexes with Functionalized 2,2′-Bipyridyl Ligands. *Organometallics* **2009,** *28* (19), 5603-5611.

15. Vogler, A.; Kunkely, H., Charge transfer excitation of organometallic compounds: Spectroscopy and photochemistry. *Coord. Chem. Rev.* **2004,** *248* (3), 273-278.

16. Luong, J. C.; Faltynek, R. A.; Wrighton, M. S., Ground and excited-state oxidation-reduction chemistry of (triphenyltin) and

(triphenylgermanium)tricarbonyl(1,10-phenanthroline)rhenium and related compounds. *J. Am. Chem. Soc.* **1980,** *102* (27), 7892-7900.

17. Slageren, J. v. Sigma-Bond-to-Ligand Charge Transfer Transitions and Excited States of d^6-Metal-Diimine Complexes. University of Amsterdam, 2000.

18. Djurovich, P. I.; Watts, R. J., Excited states of nitrogen, silicon-chelated transition metal complexes: characteristics of sigma-bond-to-ligand charge-transfer (SBLCT) excited states in fac-Ir[(6-isopropyl-8-quinolyl)diorganosilyl]$_3$. *Inorg. Chem.* **1993,** *32* (22), 4681-4682.

19. Yue, Y.; Grusenmeyer, T.; Ma, Z.; Zhang, P.; Schmehl, R. H.; Beratan, D. N.; Rubtsov, I. V., Full-electron ligand-to-ligand charge transfer in a compact Re(I) complex. *J. Phys. Chem. A* **2014,** *118* (45), 10407-15.

20. Vogler, A.; Kunkely, H., Ligand-to-ligand and intraligand charge transfer and their relation to charge transfer interactions in organic zwitterions. *Coord. Chem. Rev.* **2007,** *251* (3), 577-583.

21. Meng, Y.-S.; Sato, O.; Liu, T., Manipulating Metal-to-Metal Charge Transfer for Materials with Switchable Functionality. *Angew. Chem. Int. Ed.* **2018,** *57* (38), 12216-12226.

22. Dey, S.; Ricciardo, R. A.; Cuthbert, H. L.; Woodward, P. M., Metal-to-Metal Charge Transfer in AWO_4 (A = Mg, Mn, Co, Ni, Cu, or Zn) Compounds with the Wolframite Structure. *Inorg. Chem.* **2014,** *53* (9), 4394-4399.

23. Lever, A. B. P., *Inorganic Electronic Spectroscopy*. Elsevier: New York, United States, 1968.

24. McDonald, R. G.; Riley, M. J.; Hitchman, M. A., Angular overlap treatment of the variation of the intensities and energies of the d-d transitions of the

tetrachlorocuprate(2-) ion on distortion from a planar toward a tetrahedral geometry: interpretation of the electronic spectra of bis(*N*-benzylpiperazinium) tetrachlorocuprate(II) bis(hydrochloride) and *N*-(2-ammonioethyl)morpholinium tetrachlorocuprate(II). *Inorg. Chem.* **1988,** *27* (5), 894-900.

25. Abel, E. W.; Stone, F. G. A., The chemistry of transition-metal carbonyls: structural considerations. *Q. Rev. Chem. Soc.* **1969,** *23* (3), 325-371.

26. Varenne, A.; Salmain, M.; Brisson, C.; Jaouen, G., Transition metal carbonyl labeling of proteins. A novel approach to a solid-phase two-site immunoassay using Fourier transform infrared spectroscopy. *Bioconjugate Chem.* **1992,** *3* (6), 471-476.

27. Glowacka, P. C.; Maindron, N.; Stephenson, G. R.; Romieu, A.; Renard, P.-Y.; da Silva Emery, F., Synthesis and photophysical properties of iron-carbonyl complex–coumarin conjugates as potential bimodal IR–fluorescent probes. *Tetrahedron Lett.* **2016,** *57* (45), 4991-4996.

28. Varenne, A.; Vessières, A.; Salmain, M.; Brossier, P.; Jaouen, G., Production of specific antibodies and development of a non-isotopic immunoassay for carbamazepine by the carbonyl metallo-immunoassay (CMIA) method. *J. Immunol. Methods* **1995,** *186* (2), 195-204.

29. Salmain, M.; Vessières, A.; Brossier, P.; Butler, I. S.; Jaouen, G., Carbonylmetalloimmunoassay (CMIA) a new type of non-radioisotopic immunoassay: Principles and application to phenobarbital assay. *J. Immunol. Methods* **1992,** *148* (1), 65-75.

30. Salmain, M.; Vessieres, A.; Jaouen, G.; Butler, I. S., Fourier transform infrared spectroscopic method for the quantitative trace analysis of transition-metal carbonyl-labeled bioligands. *Anal. Chem.* **1991,** *63* (20), 2323-2329.

31. Vessières, A.; Kowalski, K.; Zakrzewski, J.; Stepien, A.; Grabowski, M.; Jaouen, G., Synthesis of CpFe(CO)(L) Complexes of Hydantoin Anions (Cp = η^5-C_5H_5, L = CO, PPh_3), and the Use of the 5,5-Diphenylhydantoin Anion Complexes as Tracers in the Nonisotopic Immunoassay CMIA of This Antiepileptic Drug. *Bioconjugate Chem.* **1999,** *10* (3), 379-385.

32. Salmain, M.; Vessières, A.; Varenne, A.; Brossier, P.; Jaouen, G., A new application of bioorganometallics: the first simultaneous triple assay by the carbonylmetalloimmunoassay (CMIA) method. *J. Organomet. Chem.* **1999,** *589* (1), 92-97.

33. Kong, K. V.; Chew, W.; Lim, L. H. K.; Fan, W. Y.; Leong, W. K., Bioimaging in the Mid-Infrared Using an Organometallic Carbonyl Tag. *Bioconjugate Chem.* **2007,** *18* (5), 1370-1374.

34. Niesel, J.; Pinto, A.; N'Dongo, H. W. P.; Merz, K.; Ott, I.; Gust, R.; Schatzschneider, U., Photoinduced CO release, cellular uptake and cytotoxicity of a tris(pyrazolyl)methane (tpm) manganese tricarbonyl complex. *Chem. Commun.* **2008,** (15), 1798-1800.

35. Meister, K.; Niesel, J.; Schatzschneider, U.; Metzler-Nolte, N.; Schmidt, D. A.; Havenith, M., Label-Free Imaging of Metal–Carbonyl Complexes in Live Cells by Raman Microspectroscopy. *Angew. Chem. Int. Ed.* **2010,** *49* (19), 3310-3312.

36. Policar, C.; Waern, J. B.; Plamont, M.-A.; Clède, S.; Mayet, C.; Prazeres, R.; Ortega, J.-M.; Vessières, A.; Dazzi, A., Subcellular IR Imaging of a Metal–Carbonyl Moiety Using Photothermally Induced Resonance. *Angew. Chem. Int. Ed.* **2011,** *50* (4), 860-864.

37. Gichumbi, J. M.; Friedrich, H. B., Half-sandwich complexes of platinum group metals (Ir, Rh, Ru and Os) and some recent biological and catalytic applications. *J. Organomet. Chem.* **2018,** *866*, 123-143.

38. Rudolf, B.; Salmain, M.; Wilczewska, A. Z.; Kubicka, A.; Misztalewska, I.; Fischer-Durand, N., Fabrication of multifunctional magnetic nanoparticles bearing metallocarbonyl probes and antibodies. *Colloids Surf. A Physicochem. Eng. Asp.* **2014,** *457*, 142-151.

39. Dewangan, S.; Barik, T.; Mishra, S.; Mawatwal, S.; Kumari, S.; Giri, S.; Das, S.; Dhiman, R.; Wölper, C.; Chatterjee, S., Half sandwich based rhodamine hydrazone single molecule probe: Light responsive, metal sensing and imaging properties. *Appl. Organometal. Chem.* **2018,** *32* (12), e4612.

40. Ganter, C., Chiral organometallic half-sandwich complexes with defined metal configuration. *Chem. Soc. Rev.* **2003,** *32* (3), 130-138.

41. Werner, H., Electron-Rich Half-Sandwich Complexes—Metal Bases *par excellence*. *Angew. Chem. Int. Ed.* **1983,** *22* (12), 927-949.

42. Hanif, M.; Moon, S.; Sullivan, M. P.; Movassaghi, S.; Kubanik, M.; Goldstone, D. C.; Söhnel, T.; Jamieson, S. M. F.; Hartinger, C. G., Anticancer activity of Ru- and Os(arene) compounds of a maleimide-functionalized bioactive pyridinecarbothioamide ligand. *J. Inorg. Biochem.* **2016,** *165*, 100-107.

43. Connell, T. U.; James, J. L.; White, A. R.; Donnelly, P. S., Protein Labelling with Versatile Phosphorescent Metal Complexes for Live Cell Luminescence Imaging. *Chem. Eur. J.* **2015,** *21* (40), 14146-14155.

44. Rudolf, B.; Zakrzewski, J., (η5-cyclopentadienyl)Fe(CO)$_2$-complex of maleimide anion: An organometallic carbonyl probe for biomolecules containing HS groups. *Tetrahedron Lett.* **1994,** *35* (51), 9611-9612.

45. Rudolf, B.; Zakrzewski, J.; Salmain, M. l.; Jaouen, G. r., A “second-generation” transition metallo-carbonyl reagent for protein labelling based on the (η^5-cyclopentadienyl)Fe(CO)$_2$(η^1-*N*-imidato) system. *Tetrahedron Lett.* **1998,** *39* (24), 4281-4282.

46. Rudolf, B.; Zakrzewski, J.; Salmain, M.; Jaouen, G. r., Metallo-carbonyl complexes based on the CpFe(CO)2(η1-N-imidato) system as protein labelling reagents: reactivity and selectivity studies using bovine serum albumin as a model protein. *New J. Chem.* **1998,** *22* (8), 813-818.

47. Salmain, M.; Jaouen, G.; Rudolf, B.; Zakrzewski, J., Inhibition and photo-deinhibition of glutathione (*S*)-transferase activity by an organometallic complex: (*S*)-[3-CpFe(CO)$_2$(η^1-*N*-succinimidato)]glutathione. *J. Organomet. Chem.* **1999,** *589* (1), 98-102.

48. Rudolf, B.; Palusiak, M.; Zakrzewski, J.; Salmain, M.; Jaouen, G., Sulfhydryl-Selective, Covalent Labeling of Biomolecules with Transition Metallocarbonyl Complexes. Synthesis of (η^5-C_5H_5)M(CO)$_3$(η^1-*N*-Maleimidato) (M = Mo, W), X-ray Structure, and Reactivity Studies. *Bioconjug. Chem.* **2005,** *16* (5), 1218-1224.

49. Kubicka, A.; Parfieniuk, E.; Fornal, E.; Palusiak, M.; Lizińska, D.; Gumieniczek, A.; Rudolf, B., Metallocarbonyl complexes: (η^5-C_5H_5)M(CO)$_n$(η^1-*N*-imidato) (M = Fe, Ru, Mo, W; n = 2, 3) as new photoactive CO-releasing molecules (CORMs). *J. Photochem. Photobiol. A: Chem.* **2018,** *351*, 115-123.

50. Kubicka, A.; Fornal, E.; Olejniczak, A. B.; Rybarczyk-Pirek, A. J.; Wojtulewski, S.; Rudolf, B., Oxa-Michael reaction of metallocarbonyl complexes bearing the maleimidato ligand. Reactivity studies with selected hydroxy compounds. *Polyhedron* **2016,** *107*, 38-47.

51. Rudolf, B.; Salmain, M.; Fornal, E.; Rybarczyk-Pirek, A., Metallocarbonyl complexes of bromo- and dibromomaleimide: synthesis and biochemical application. *Appl. Organometal. Chem.* **2012,** *26* (2), 80-85.

52. Jean, Y., *Molecular Orbitals of Transition Metal Complexes*. Oxford University Press: New York, United States, 2005.

53. Hoffmann, R.; Beier, B. F.; Muetterties, E. L.; Rossi, A. R., Seven-coordination. A molecular orbital exploration of structure, stereochemistry, and reaction dynamics. *Inorg. Chem.* **1977,** *16* (3), 511-522.

54. Lin, Z.; Hall, M. B., Geometric distortions in four-legged piano-stool cyclopentadienyl transition-metal complexes. *Organometallics* **1993,** *12* (1), 19-23.

55. Kosińska, A.; Wojtulewski, S.; Palusiak, M.; Tokarz, P.; Rudolf, B., A Useful Synthetic Route to *N*-Nonsubstituted Succinimides via Light-Induced Degradation of Metallocarbonyl Complexes. *Organometallics* **2021,** *40* (6), 663-673.

56. Mabire, A. B.; Robin, M. P.; Quan, W.-D.; Willcock, H.; Stavros, V. G.; O'Reilly, R. K., Aminomaleimide fluorophores: a simple functional group with bright, solvent dependent emission. *Chem. Commun.* **2015,** *51* (47), 9733-9736.

57. Rudolf, B.; Kubicka, A.; Salmain, M.; Palusiak, M.; Rybarczyk-Pirek, A. J.; Wojtulewski, S., Synthesis and characterization of new M(II) carbonyl complexes (M = Fe or Ru) including an η^1-*N*-maleimidato ligand. Reactivity studies with biological thiols. *J. Organomet. Chem.* **2016,** *801*, 101-110.

58. Stark, J. G., The oxidation states of molybdenum. *J. Chem. Educ.* **1969,** *46* (8), 505.

59. King, R. B., Organometallic Chemistry of the Transition Metals. XI. Some New Cyclopentadienyl Derivatives of Cobalt and Rhodium. *Inorg. Chem.* **1966,** *5* (1), 82-87.

60. Kruse, A. E.; Angelici, R. J., Reactions of the cyclopentadienylruthenium tricarbonyl cation with nucleophiles. *J. Organomet. Chem.* **1970,** *24* (1), 231-239.

61. Artero, V.; Fontecave, M., Hydrogen evolution catalyzed by {$CpFe(CO)_2$}-based complexes. *C. R. Chim* **2008,** *11* (8), 926-931.

62. Mattson, B. M.; Graham, W. A. G., Mechanism of halide abstraction from η^5-cyclopentadienyl(dicarbonyl)iodoiron by silver tetrafluoroborate. *Inorg. Chem.* **1981,** *20* (10), 3186-3189.

63. Dömötör, O.; Pape, V. F. S.; May, N. V.; Szakács, G.; Enyedy, É. A., Comparative solution equilibrium studies of antitumor ruthenium(η^6-*p*-cymene) and rhodium(η^5-C_5Me_5) complexes of 8-hydroxyquinolines. *Dalton Trans.* **2017,** *46* (13), 4382-4396.

64. Rudolf, B.; Palusiak, M.; Zakrzewski, J., Diels-Alder reaction with cyclopentadiene and electronic structures of (η^5-cyclopentadienyl)$M(CO)_x$(η^1-*N*-maleimidato) (M=Fe, Mo, W, x=2 or 3). *J. Organomet. Chem.* **2009,** *694* (9), 1354-1358.

65. Rudolf, B.; Salmain, M.; Martel, A.; Palusiak, M.; Zakrzewski, J., η^1-*N*-succinimidato complexes of iron, molybdenum and tungsten as reversible inhibitors of papain. *J. Inorg. Biochem.* **2009,** *103* (8), 1162-1168.

66. Kowalski, K.; Zakrzewski, J.; Rybarczyk-Pirek, A., [(η^5-C_5H_5)Fe$(CO)_2$](Fp)-complexes of the parabanic acid mono- and dianion: synthesis, X-ray structures and reactivity of the heterocyclic ligand. *Polyhedron* **2004,** *23* (8), 1441-1446.

67. Abdou, H. E.; Mohamed, A. A.; Fackler, J. P.; Ghimire, M. M.; Omary, M. A.; Schilter, D.; Rauchfuss, T. B.; Denny, J. A.; Darensbourg, M. Y.; Morshedi, M.; Simpson, P. V.; Babgi, B.; Green, K. A.; Moxey, G. J.; Jennaway, M. S.; Cifuentes, M. P.; Humphrey, M. G.; Eaves, S. G.; Low, P. J.; Nelson, K. J.; Miller, J. S.; Woods, T. J.; Dunbar, K. R.; Johnstone, T. C.; Starha, P.; Habtemariam, A.; Zalesskiy, S. S.; Ananikov, V. P.; Reay, A. J.; Fairlamb, I. J. S.; Geiger, W. E.; Zink, J. R.; Shaw, M. J.; Silvia, J. S.; Cummins, C. C.; Mindiola, D. J.; Damon, P. L.; Hayton, T. W.; Mindiola, D. J.; Reiners, M.; Ehrlich, N.; Walter, M. D.; Herve, A.; Sofield, C. D.; Andersen, R. A., Synthesis of selected transition metal and main group compounds with synhtetic applications. In *Inorganic Syntheses*, **2018**; pp 155-204.

68. Würth, C.; Grabolle, M.; Pauli, J.; Spieles, M.; Resch-Genger, U., Relative and absolute determination of fluorescence quantum yields of transparent samples. *Nat. Protoc.* **2013,** *8* (8), 1535-1550.

69. Xie, Y.; Husband, J. T.; Torrent-Sucarrat, M.; Yang, H.; Liu, W.; O'Reilly, R. K., Rational design of substituted maleimide dyes with tunable fluorescence and solvafluorochromism. *Chem. Commun.* **2018,** *54* (27), 3339-3342.

70. Eaton, D. F., Recommended methods for fluorescence decay analysis. *Pure Appl. Chem.* **1990,** *62* (8), 1631-1648.

71. Tsudaka, T.; Ohkubo, K.; Fukuzumi, S., Photocatalytic oxidation of iron(ii) complexes by dioxygen using 9-mesityl-10-methylacridinium ions. *Chem. Commun.* **2016,** *52* (36), 6178-6180.

72. Jiang, X.; Chen, L.; Wang, X.; Long, L.; Xiao, Z.; Liu, X., Photoinduced Carbon Monoxide Release from Half-Sandwich Iron(II) Carbonyl Complexes by Visible Irradiation: Kinetic Analysis and Mechanistic Investigation. *Chem. Eur. J.* **2015,** *21* (37), 13065-13072.

73. Zoski, C. G., *Handbook of Electrochemistry*. Elsevier: Amsterdam, The Netherland, 2006.

74. Allen J. Bard; Faulkner, L. R., *Electrochemical Methods: Fundamental and Applications*. 2nd ed.; John Wiley & Sons: Hoboken, NJ, 2001.

75. Elgrishi, N.; Rountree, K. J.; McCarthy, B. D.; Rountree, E. S.; Eisenhart, T. T.; Dempsey, J. L., A Practical Beginner's Guide to Cyclic Voltammetry. *J. Chem. Edu.* **2018,** *95* (2), 197-206.

76. Rong, B.; Zhong, W.; Gu, E.; Long, L.; Song, L.; Liu, X., Probing the electron transfer mechanism of the half-sandwich iron(II)-carbonyl complexes and their catalysis on proton reduction. *Electrochim. Acta* **2018,** *283*, 27-35.

77. Balland, V.; Banse, F.; Anxolabéhère-Mallart, E.; Ghiladi, M.; Mattioli, T. A.; Philouze, C.; Blondin, G.; Girerd, J.-J., Fe(II) and Fe(III) Mononuclear Complexes with a Pentadentate Ligand Built on the 1,3-Diaminopropane Unit. Structures and Spectroscopic and Electrochemical Properties. Reaction with H_2O_2. *Inorg. Chem.* **2003,** *42* (7), 2470-2477.

78. Čížková, M.; Cattiaux, L.; Mallet, J.-M.; Labbé, E.; Buriez, O., Electrochemical switching fluorescence emission in rhodamine derivatives. *Electrochim. Acta* **2018,** *260*, 589-597.

79. Alvarez, M. A.; García, M. E.; García-Vivó, D.; Rueda, M. T.; Ruiz, M. A.; Toyos, A.; Vega, M. F., Terminal vs. bridging coordination of CO and NO ligands after

decarbonylation of [$W_2Cp_2(\mu\text{-}PR_2)(CO)_3(NO)$] complexes (R = Ph, Cy). An experimental and computational study. *Dalton Trans.* **2017,** *46* (31), 10440-10451.

80. Relles, H. M., Organic chemistry in thionyl chloride. I. Dichloromaleimide chemistry. II. Thionyl chloride-pyridine method for the conversion of maleimides to dichloromaleimides. *J. Org. Chem.* **1972,** *37* (23), 3630-3637.

81. Robin, M. P. Bromo and thio maleimides for functionalisation and fluorescent labelling of polymers and polymer nanoparticles. University of Warwick, 2014.

82. Akita, M.; Terada, M.; Tanaka, M.; Morooka, Y., Some additional aspects of versatile starting compounds for cationic organoiron complexes: molecular structure of the aqua complex [$(\eta^5\text{-}C_5Me_4Et)Fe(CO)_2(OH_2)]BF_4$ and solution behavior of the THF complex [$(\eta^5\text{-}C_5R_5)Fe(CO)_2(THF)]BF_4$. *J. Organomet. Chem.* **1996,** *510* (1), 255-261.

83. Blackmore, T.; Cotton, J. D.; Bruce, M. I.; Stone, F. G. A., Chemistry of the metal carbonyls. Part LIII. Some dicarbonyl-(π-cyclopentadienyl)ruthenium complexes containing metal–metal bonds. *J. Chem. Soc. A* **1968,** (0), 2931-2936.

84. Abel, E. W.; Singh, A.; Wilkinson, G., Some π-cyclopentadienyl molybdenum and tungsten carbonyls. *J. Chem. Soc.* **1960,** (0), 1321-1324.

85. M'thiruaine, C. M.; Friedrich, H. B.; Changamu, E. O.; Bala, M. D., Synthesis and characterization of amine complexes of the cyclopentadienyliron dicarbonyl complex cation, $[Cp(CO)_2Fe]^+$. *Inorganica Chim. Acta* **2011,** *366* (1), 105-115.

CHAPTER 4: SYNTHESIS OF MALEIMIDE DERIVED LIGANDS FOR COMPLEXATION WITH LANTHANIDE METALS

4.1 Abstract

In recent years, a great deal of research has been focused on developing strategies to enhance the luminescence of the lanthanide(III) complexes. For this purpose, various organic chromophores have been employed as ligands to enhance the luminescence of the lanthanide(III) ions, through the overlap of appropriate energy levels of the ligand and the lanthanide metal ion. This chapter will focus on the design of stable maleimide-based ligands for the formation of complexes with trivalent europium and terbium ions. A series of carboxylate functionalized dichloromaleimide-based ligands were synthesized to develop red-fluorescent europium(III) complexes. The newly synthesized europium(III) maleimide complexes were analyzed by FTIR spectroscopy, thermal and elemental analysis. The stoichiometry ratio in these complexes was evaluated by the mole ratio method and their photophysical properties were explored in both solution and solid-state. Building on this, two aminochloromaleimide derivatives were developed, which provided two different coordinating positions on the maleimide ring *via* the carboxylate group. Notably, the optical properties of the Eu^{3+}/Tb^{3+} aminomaleimide complexes were enhanced by the charge transfer transitions, caused by the aminochloromaleimide ligands, thus overcame the limitation of weak metal-centered transitions.

4.2 Introduction

4.2.1 Enhanced photoluminescence of europium(III) and terbium(III) complexes by organic ligands

Lanthanide (Ln) complexes coordinated to organic chromophores have attracted great interest for use as bio-probes and sensors.[1, 2] This is due to their unique photophysical properties based on $f \rightarrow f$ transitions, including sharp emission bands and sensitized luminescence triggered by the excitation of a ligand.[3] For each lanthanide (Ln) ion, band assignments has been mapped on Dieke diagrams, with energy levels determined by helium photoelectron spectroscopy measurments.[4, 5] Fig. 4.1 illustrates the Dieke diagram of luminescence energy levels corresponding to the $f \rightarrow f$ transitions for trivalent europium and terbium ions. The bands corresponding to the $f \rightarrow f$ transitions determines the characteristics color of luminescence of the lanthanide ions.[6]

As they are parity-forbidden, the $f \rightarrow f$ transitions in the lanthanide trivalent ions display quite low molar absorption coefficients (~10^2 $M^{-1}cm^{-1}$). However, this drawback can be improved by enhancing the absorption, by using organic chromophores as an energy donor and lanthanide ions as acceptors, resulting in higher photoluminescence quantum efficiencies (Fig 4.1). This results in the superimposition between the emission band of the ligand and the absorption of the $f \rightarrow f$ transitions, leading to intramolecular energy transfer. This is known as the photo-antenna effect. For instance, in the case of europium(III) complexes, the ligand's excited state act as an energy donor, whereas the $^5D_0$ level of europium act as the acceptor. This gives a higher intensity luminiscence than the direct excitation of the lanthanide ions.[7]

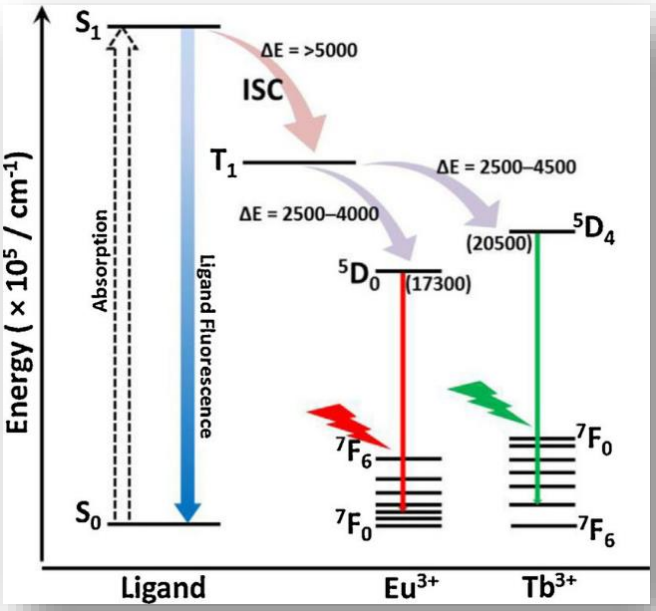

Fig. 4.1 Schematic representation of the energy absorption, excited electron migration and emission processes in lanthanide complexes, with Eu^{3+} and Tb^{3+}, as representatives, along with the ideal energy conditions. Adapted from the reference.[8] Copyright 2017 Elsevier.

Besides the photo-antenna effect, various organic chromophores (ligands) have also been rationally designed, to photosensitize the luminescence of lanthanide(III) ions. Such ligands result in the formation of lanthanide(III) complexes that may exhibit $\pi \rightarrow \pi^*$ transitions with large molar absorption coefficients (>10,000 $M^{-1}cm^{-1}$). The photosensitization of the luminescence from an organic ligand, can be achieved by controlling the triplet excited state (T_1),[9] influencing the charge transfer (CT) band and/or metal ions (i.e., light and transition metal) doping to the lanthanide metals.[10, 11] This chapter focuses on the energy transfer between the organic ligand (i.e. maleimide derivatives) and lanthanide metal ions, thus the metal ion doping strategy will not be discussed here.

In lanthanide(III) complexes, the organic ligand is first excited by photoirradiation at $\pi \rightarrow \pi^*$ transition band. The excited state relaxes from the S_1 state to the T_1 state, by the intersystem crossing (ISC) (Fig. 4.1). In a stable lanthanide(III) complex, the energy transfer occurs between the ligand's T_1 level (donor) and the lanthanides' $4f$-f' orbitals (acceptor). However, if the energy gap between the lanthanide(III) ion and the T_1 state is small, these complexes may undergo the energy back-transfer from the lanthanides to the ligand's excited triplet state. The energy transfer will occur efficiently, if the energy gap between the T_1 and emitting levels is less than 2500 cm^{-1}. Several studies of the energy gaps between T_1 state and emitting level of Eu^{3+} (~2500 cm^{-1}) and Tb^{3+} (~2400 cm^{-1}), in their complexes with carboxylate, β-diketonate and pyridyl ligands have been published.[12-15] Kitagawa *et. al*., reported lanthanide(III) complexes containing ligands with extended π-conjugations, such as phenanthrene and hexafluoroacetylacetonate complexes,[16, 17] or large metal clusters with salicylate derivatives,[18, 19] to induce the photosensitization of the europium(III) complexes .

The luminescence of the lanthanide complexes can also be photosensitized by influencing the charge transfer (CT) band, that controls the energy transfer process between the ligand and the lanthanide ions, and can be classified as intra-ligand CT, inter-ligand CT and ligand-to-metal CT (LMCT) (explained in Chapter 3). A series of ligands have been reported that provided effective push-pull systems, such as diketonate, and enhanced the luminescence of the lanthanide(III) complexes by intra-ligand CT.[20, 21] However, energy transfer *via* inter-ligand CT was first presented by Kuzmina and co-workers, who reported europium(III) and terbium(III) complexes containing hexafluoroacetylacetonate-based ligands, which possessed high energy transfer efficiency (81%) and quantum yields (58%).[22] It was also reported that inter-

CT transitions are more effective in the solid-state owing to the zig-zag arrangement in the molecular structure.[23] For instance, Hasegawa and co-workers reported europium(III) coordinated polymers containing thiophene-based bridging ligands packed in a zig-zag arrangement (Fig. 4.2a). These polymers displayed high energy transfer efficiency (~80%) and thermal stability (320ºC), compared to the linear europium(III) coordination polymers (Fig. 4.2b).[24] In short, the strong luminescent lanthanide(III) complex can be developed due the intraligand CT band, formed by incorporating donor groups into the ligands or due to formation of the inter-ligand CT band caused by steric strain in ligands, especially in the solid-state.

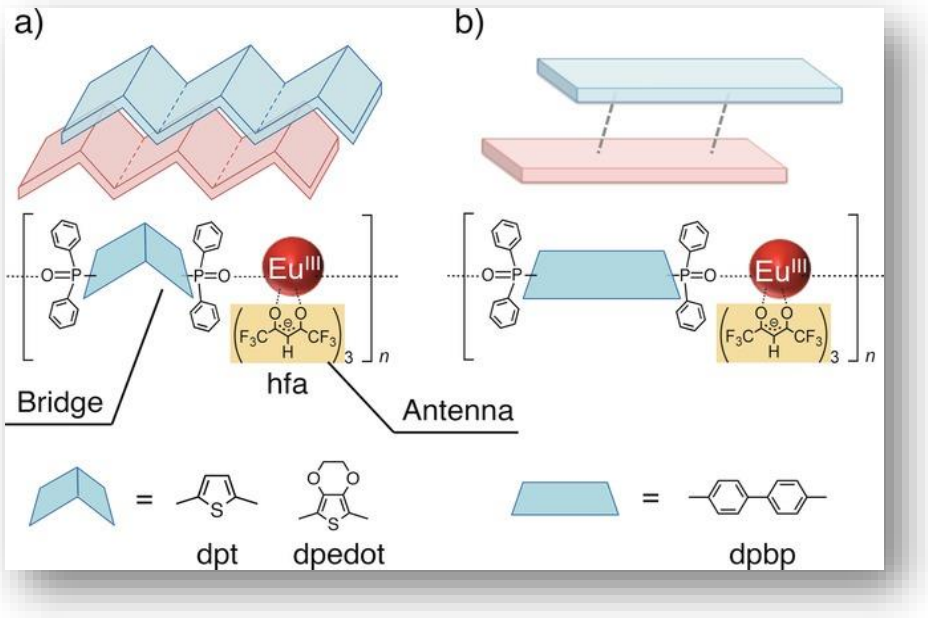

Fig. 4.2 Eu^{III} coordination zig-zag shaped polymers with thiophene-based bridges (a); and linear Eu^{III} coordination polymer (b). Adapted from the reference.[24] Copyright 2016 John Wiley and Sons.

As discussed in Chapter 1, the maleimide derivatives have been employed so-far as a conjugation tool when appended with other ligands, and not as chromophores (ligands) for complexation with the lanthanide metal ions. Hence, the work detailed in this chapter focuses on developing the maleimide-derived ligands capable of forming stable luminescent lanthanide(III) complexes. Given that, the fluorescent aminomaleimide derivatives are known to possess strong pull-push systems exhibiting strong $\pi \rightarrow \pi^*$ transitions,[25] they can act as potential chromophores. Building on this, the influence of complexation on the optical properties of the lanthanide ions and the maleimide can be explored, thus expanding the scope of using these complexes for potential applications, such as bioconjugation, imaging and sensing.

4.3 Results and Discussions

4.3.1 Design and synthesis of europium(III) dichloromaleimide complexes

The luminescence of trivalent lanthanide ions can be enhanced upon coordination with the chromophore ligands, as discussed in section 4.2. The ligands harvest light and provide ligand-to-metal energy transfer by preventing the non-radiative relaxation.[26, 27] In chapter 3, transition metal-based organometallic complexes containing the aminomaleimide ligands were studied. Following on from that study, in this chapter the development of maleimide derived ligands suitable for complexation with lanthanide metal ions was explored. The photophysical properties of the resultant complexes was also explored.

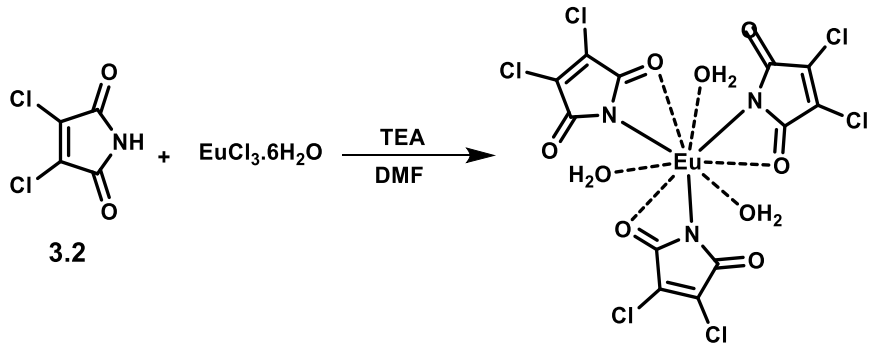

Scheme 4.1. Synthesis of a dichloromaleimide derived europium(III) complex.

Firstly, a previously developed dichloromaleimide ligand (**3.2**) was reacted with europium(III) chloride salt ($EuCl_3.6H_2O$) in the presence of a base and refluxed at 80℃, to prepare a Eu(III) maleimide complex (Scheme 4.1).[28] Triethylamine (TEA) was used

as a base to deprotonate the imide group, and the use of strong inorganic base, such as Na_2CO_3, was avoided to prevent the precipitation of europium. After the reflux, the solvent was removed under reduced pressure, and the solid obtained was washed with dichloromethane to remove any unreacted ligand. In order to make sure, that the complex **4.10** has not been washed off along with the unreacted ligand, the organic layer was dried and analyzed by NMR spectroscopy and thermal gravimetric analysis (TGA). The ^{1}H NMR spectrum of the organic layer was identical to the dichloromaleimide ligand **3.2**, with no additional peaks observed (experimental section 4.5.2). The TGA results also showed no presence of europium traces in the organic layer (Fig. 4.3), suggesting that the complex was not soluble in the organic layer and remained in the aqueous phase. However, the separation of the prepared europium(III) complexes, from any unreacted europium salt (precursor) left behind, was challenging, due to their similar solubilities. It is important to obtain the complex in high purity and free from any contamination which could interfere during the fluorescence analysis.[29] Consequently, an alternate synthetic strategy was proposed to achieve the targeted complexes.

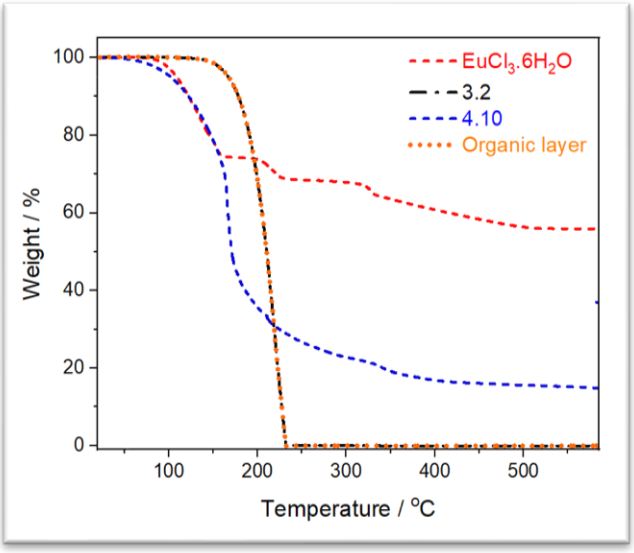

Fig. 4.3 Comparison of the TGA plot of the europium complex (**4.10**) with europium salt, dichloromaleimide ligand (**3.2**), and the solid obtained from the organic layer filtrate.

It is well-known that the lanthanide metal ions have a great affinity for carboxylate groups, and can form stable complexes with these ligands due to the chelate formation, thus establishing high coordination numbers.[6, 30] Therefore, to obtain the lanthanide-maleimide complexes, maleimide units were functionalized with a carboxylate moiety, in which a linker can coordinate with the europium metal ion instead of a direct attachment through the imide nitrogen. The *N*-acid functionalized dichloromaleimide derivatives (**4.1**–**4.5**) were synthesized, according to a previously reported procedure (experimental section 4.5.2).[31] 2,3-dichloromaleimide was refluxed in the presence of amino acids, such as glycine, alanine, etc., to synthesize the targeted maleimide-based ligands (Scheme 4.2). All compounds were purified by column chromatography and characterized by ^{1}H NMR, ^{13}C NMR and FTIR spectroscopy (Fig. 4.17–4.26).

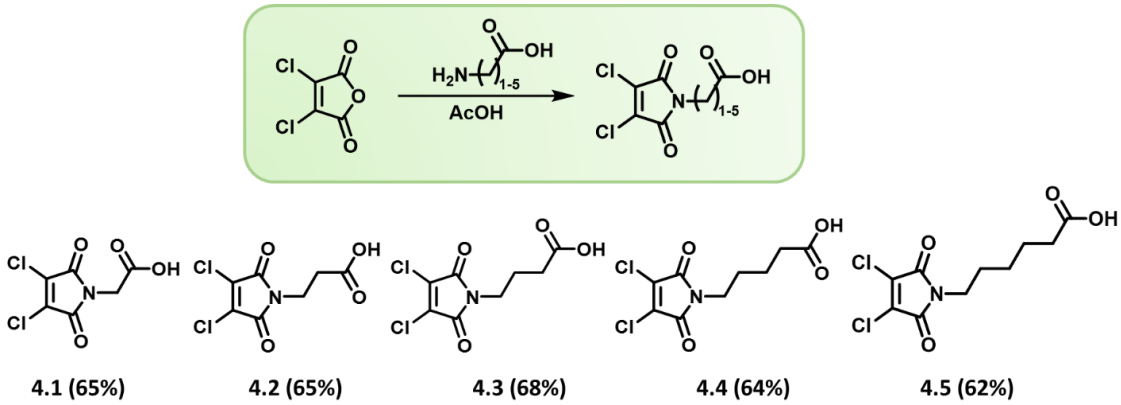

Scheme 4.2 Synthesis of acid functionalized dichloromaleimide ligands **4.1**–**4.5**.

Europium complexes containing maleimide-based ligands, **4.1**–**4.5,** were synthesized using stoichiometric amounts of europium(III) chloride hexahydrate and ligands (1:3 equiv.), in the presence of a base (Scheme 4.3). The complexes precipitated upon dropwise addition of a solution containing the ligand and triethylamine to a europium(III) chloride solution. The precipitated europium-maleimide complexes (**4.11**–**4.15**) were successfully isolated and washed with dichloromethane and water to remove any unreacted ligand and europium(III) chloride. Whilst dichloromaleimide ligands **4.1**–**4.5** are non-fluorescent under irradiation with UV-Vis light, complexes **4.11**–**4.15** exhibited bright red fluorescence. The europium(III) complexes (**4.11**–**4.15**) were analyzed by TGA, FTIR spectroscopy and elemental analysis (experimental section 4.5.3 and 4.5.4). These complexes were amorphous as synthesized, thus cannot be characterized by single crystal or powder X-Ray diffraction.

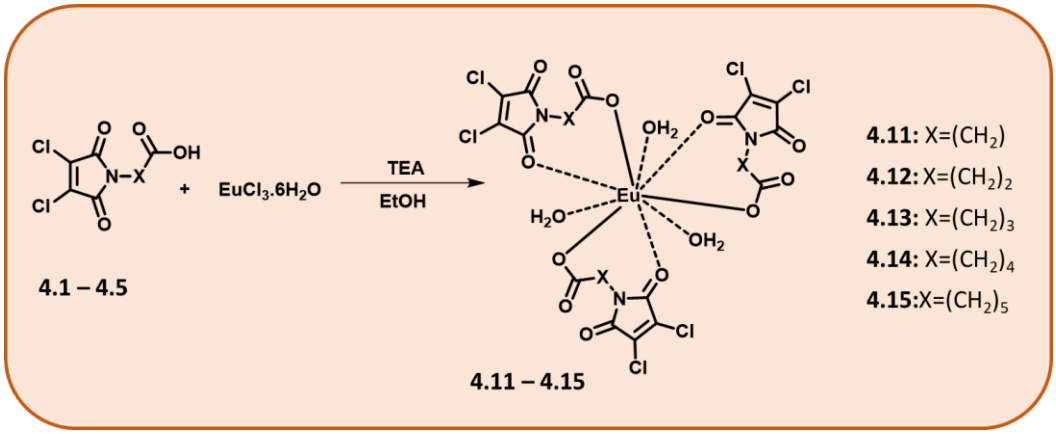

Scheme 4.3 Synthesis of europium(III) dichloromaleimide complexes **4.11**–**4.15**.

The stoichiometry of the Eu(III) complexes (**4.11**–**4.15**) was determined by the mole ratio method.[32, 33] The luminescence of the characteristic $^5D_0 \rightarrow {}^7F_2$ was measured as a function of the amount of Eu(III) added to the aqueous solution of the ligand. The break in the titration curve occurs when all of the ligand has been sequestered. Performing this with ligand **4.3**, shows that complex **4.13** has 1:3 stoichiometry (Fig 4.4). This was also in agreement with the results obtained from the elemental analysis (experimental section 4.5.3). Complexes **4.11**–**4.14** revealed a 1:3 stoichiometry (Table 4.1) while for complex **4.15**, it appeared to be 1:2.5. This might have occurred due to increased strain for the longer alkyl chain coordinated to the metal atom *via* carboxylate group.

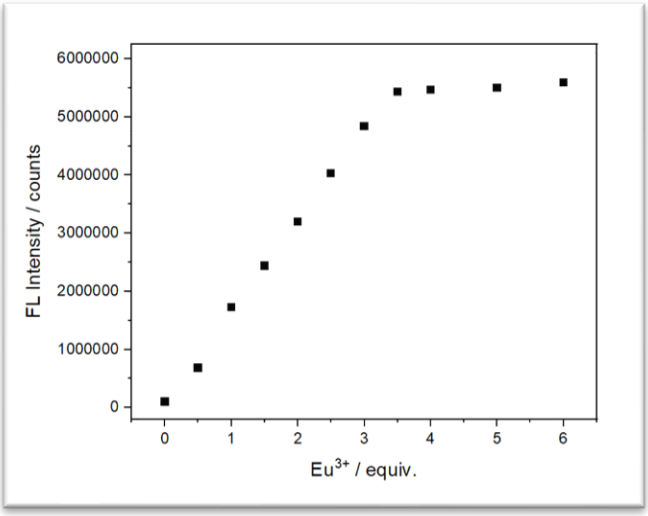

Fig. 4.4 Intensity of the $^5D_0 \rightarrow {}^7F_2$ transition peak as a function of Eu^{3+} added to a solution of ligand **4.3** (10 μM) in ethanol, in the presence of a base (λ_{ex} = 395 nm).

Table 4.1 Stoichiometric ratio for the synthesized europium(III) dichloromaleimide complexes, determined at ligand concentration of 10 μM.

Ligand	Complex	No. of CH_2 units	[Eu]/[ligand]
4.1	4.11	1	1:3
4.2	4.12	2	1:3
4.3	4.13	3	1:3
4.4	4.14	4	1:3
4.5	4.15	5	1:2.5

Table 4.2 Thermal data of the synthesized europium(III) dichloromaleimide complexes.

Complexes	Temperature range (℃)	Weight loss (%)	Assignments
4.11	20 – 140	5.68	H_2O
	140 – 500	52.79	Organic components
	500 –	41.53	Eu_2O_3 + C
4.12	20 – 140	5.26	H_2O
	140 – 500	69.61	Organic components
	500 –	25.13	Eu_2O_3 + C
4.13	20 – 140	4.05	H_2O
	140 – 500	68.09	Organic components
	500 –	27.86	Eu_2O_3 + C
4.14	20 – 140	4.42	H_2O
	140 – 500	56.12	Organic components
	500 –	40.46	Eu_2O_3 + C
4.15	20 – 250	3.23	H_2O
	250 – 500	53.13	Organic components
	500 –	43.64	Eu_2O_3 + C

The thermal behavior of europium(III) chloride hexahydrate, the ligands (**4.1**–**4.5**), and the respective europium(III) complexes (**4.11**–**4.15**) was investigated (Fig. 4.33; see experimental section). The ligands decomposed between 150 to 300℃, with an estimated mass loss of ~97–100%. For the europium(III) chloride salt and the europium(III) maleimide complexes (**4.11**–**4.15**), thermal decomposition occurs in three stages. The first decomposition stage corresponds to the elimination of hydrated water molecules,[34] and a mass loss of 4–6% was observed within the temperature

range of 20 – 140℃ for complexes **4.11**–**4.14** (Table 4.2). This is also in agreement with the calculated mass loss, i.e., ~5–6% for these complexes. For complex **4.15**, the mass loss of 3.23% was observed within the temperature range of 20–250℃, which is fairly less than the calculated mass loss (~5%). This decomposition process continues over second and third stage within the temperature range of 140–300℃ and 300–500℃ respectively, (with an estimated loss of 53% for **4.11**, 69% for **4.12**, 68% for **4.13**, 56% for **4.14** and 53% for **4.15**) (Table 4.2), which could be assigned to the loss of organic moieties. Eu(III) complexes were expected to end with a metallic residue of Eu_2O_3 and carbon atom residues in the final stage of thermal decomposition.[35]

The FTIR spectra of the free ligands **4.1**–**4.5**, and their complexes **4.11**–**4.15**, were also recorded and the significant changes in frequencies are tabulated below (Table 4.3). The ligands displayed strong band around ~2900 cm^{-1}, which corresponds to the characteristic carboxylic O-H group. Free water molecules display a strong and broad O-H band around 3100–3700 cm^{-1}. In comparison, europium(III) complexes presented medium-weak band with peaks located in the range of 3420–3536 cm^{-1} corresponding to the O-H stretching vibrations, indicating the presence of coordinated water molecules.[36, 37] The bands at around ~1720 cm^{-1} and ~1300 cm^{-1} corresponding to ν(C=O) and ν(C-O) stretching vibrations, respectively, displaced slightly to the higher frequencies for the complexes compared to the free ligands (Table 4.3). Higher N-C=O stretching vibration frequency was associated with better sigma donating ability of the maleimide moiety, resulting into a stronger C=O bond. Thus, the peaks corresponding to the ν(C=O) stretch around ~1680–1700 cm^{-1} for the ligands, shifted by ~25 for the europium(III) complexes, suggesting coordination through a carboxyl group with the europium metal ion.

Table 4.3 Selected IR bands for the europium(III) complexes (**4.11**–**4.15**) and the respective ligands (**4.1**–**4.5**).

Complex (Ligand)	Characteristic frequencies		
	ν(O-H) stretch (cm^{-1})	ν(C=O) (cm^{-1})	ν(C-O) (cm^{-1})
4.11 (4.1)	3454 (2884)	1723 (1714)	1388 (1243)
4.12 (4.2)	3420 (2919)	1727 (1706)	1393 (1221)
4.13 (4.3)	3536 (2942)	1729 (1704)	1398 (1204)
4.14 (4.4)	3473 (2951)	1713 (1691)	1395 (1199)
4.15 (4.5)	3489 (2930)	1708 (1683)	1245 (1197)

4.3.2 Photophysical properties of europium(III) dichloromaleimide complexes

The photophysical properties of the ligands and the europium(III) complexes are summarized in Table 4.4. All the synthesized complexes are insoluble in common non-polar solvents, e.g., chloroform and 1,4-dioxane, but are highly soluble in polar aprotic solvents, e.g., dimethylformamide (DMF) and dimethyl sulfoxide (DMSO). Hence, UV-Vis spectra of europium(III) dichloromaleimide complexes **4.11**–**4.15**, were measured in dimethylformamide (50 µM). Unbound dichloromaleimide ligands show the absorption maximum around 240 nm, corresponding to the $\pi \rightarrow \pi^*$ transitions,[38] which is difficult to observe in dimethylformamide, as the solvent itself starts to absorb below 268 nm. The complexes **4.11**–**4.15** gave two absorption bands around 273 nm and ~390 nm. (Table 4.4) The peak observed at 273 nm is identical for the europium(III) dichloromaleimide complexes, **4.11**–**4.15**. The other absorption peak slightly red

shifted, from 389 nm for **4.11** to 398 nm for **4.15**, and possibly associated with the metal-to-ligand charge transfer excitation.[39] It has been reported that the complexes with more electron donating ligands coordinated to lanthanide metal ions displayed more red-shifted absorption maxima.[40] Based on this, europium(III) complexes that displayed a more red-shifted absorption maxima are expected to have more electron donating capacity than the rest. These results were also in agreement with the observations from the FTIR analysis.

Fluorescence emission and excitation spectra were analyzed for the dichloromaleimide ligands **4.1**–**4.5,** and their europium(III) complexes **4.11**–**4.15,** to further understand the energy transfer processes of the excited states. The ligands did not display any fluorescence emission peak (Fig. 4.6). The complexes **4.11**–**4.15** showed two absorption bands around 270 nm and ~395 nm, along with the excitation maxima observed at 395 nm (Table 4.4). Subsequently, these complexes (**4.11**–**4.15**) were excited at 395 nm and the solution-state emission spectra were recorded in the range of 400–800 nm. Fig. 4.5 illustrates various phenomena involved leading to the fluorescence emission when the europium(III) complexes were excited around 395 nm.

Table 4.4 Photophysical properties of complexes **4.11**–**4.15** measured at 10 μM in dimethylformamide (λ_{max} = maximum absorption wavelength; ε_{max} = molar absorption coefficient; λ_{ex} = excitation wavelength ; λ_{em} = maximum emission wavelength; slit width ex 2.5 nm, em 2.5 nm; 25ºC).

Complex	λ_{max} (nm)	ε_{max} (M^{-1} cm^{-1})	λ_{ex} (nm)	λ_{em} (nm)
4.11	273, 398	9798, 3834	395	515,592,615,698
4.12	273, 396	9811, 3952	395	518,592,616,695
4.13	273, 394	1098, 4125	395	519,592,617,695
4.14	273, 393	1204, 4273	395	520,592,618,696
4.15	273, 389	1317, 4294	395	521,592,619,697

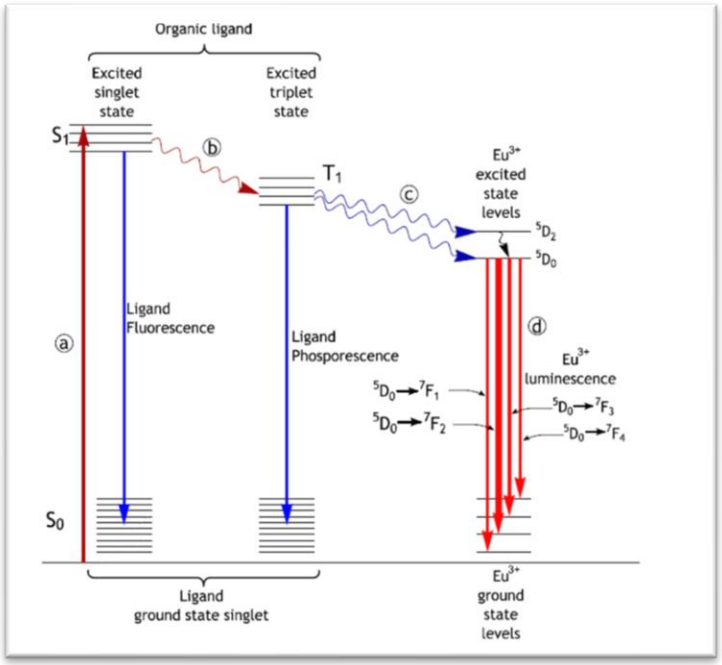

Fig. 4.5 Illustration of different processes involved leading to the fluorescence emission of the europium(III) complexes: (a) excitation; (b) intersystem crossing (ISC); (c) ligand-to-metal charge transfer (LMCT); (d) relaxation. Adapted from the reference.[41] Copyright 2009 Springer Nature.

Energy transfer occurs from the ligand's excited energy level to the $^5D_0$ of the europium ion. Multiple emissions occurred resulting from de-excitations of the $^5D_0 \rightarrow {}^7F_{1\text{-}4}$ (Fig. 4.5). The fluorescence emission spectra for the complexes **4.11**–**4.15,** were identical and presented in Fig. 4.6 and 4.35 (experimental section 4.5.5). The most intense transitions corresponds to $^5D_0 \rightarrow {}^7F_2$, and were observed at 617 nm for **4.13** (Table 4.4 and Fig 4.6). The other two peaks observed at 592 nm and 695 nm are attributed to the $^5D_0 \rightarrow {}^7F_1$ and $^5D_0 \rightarrow {}^7F_4$ transitions, respectively. The $^5D_0 \rightarrow {}^7F_2$ is an electric dipole allowed transition and its intensity is sensitive to the bonding environment of the Eu^{3+} ions, while the peak position usually remains unchanged. In contrary, $^5D_0 \rightarrow {}^7F_1$ is a magnetic dipole allowed transition, and therefore hardly differs due the bonding environment of the Eu^{3+} ions.[41] Notably, a broad band centered at 591 nm for the complex **4.13** was also observed, which corresponds to the combination of transitions from ligand to the europium ion i.e. $L \rightarrow Eu^{3+}$.[42] Moreover, the CIE chromaticity coordinates of the europium complexes **4.11**–**4.15,** in dimethylformamide, was interpreted in Fig. 4.6 to compare the emissions of the synthesized europium(III) dichloromaleimide complexes with the precursor europium(III) chloride hexahydrate.

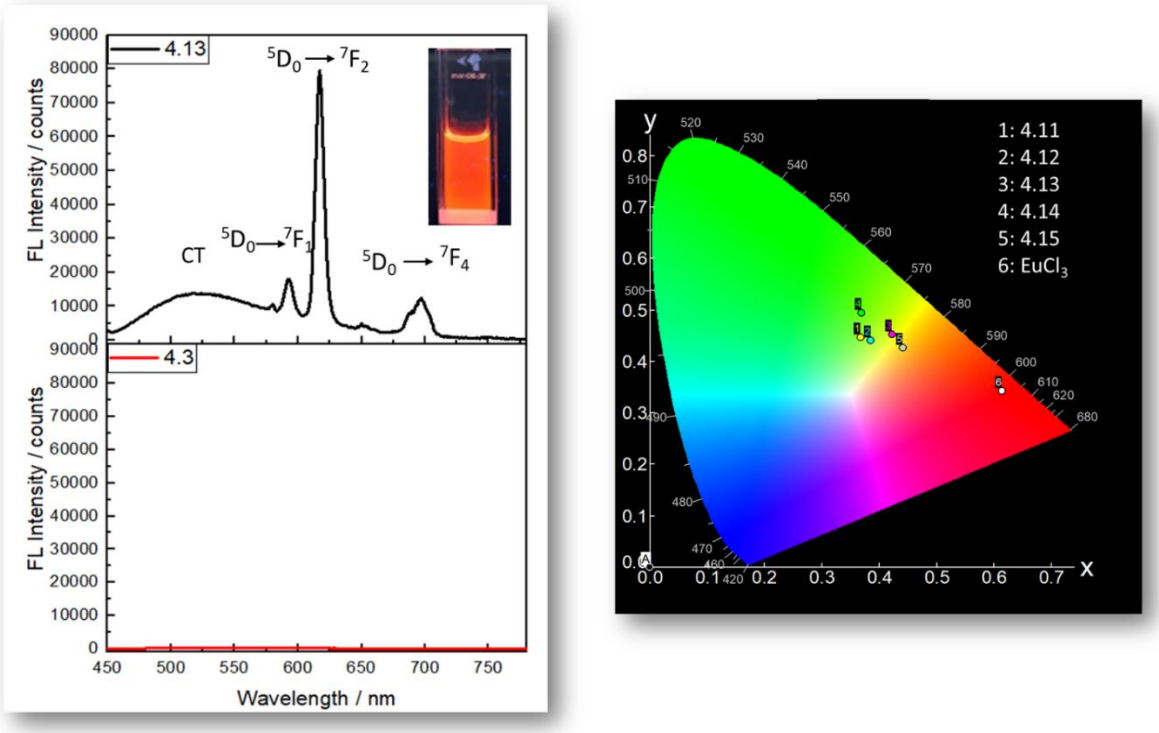

Fig. 4.6 Fluorescence emission spectra of the ligand (**4.3**; bottom) and its europium complex (**4.13**; top), the inset shows the image of complex 4.13 in dimethylformamide taken under UV-light (left); and CIE plot of the fluorescent emission wavelengths of europium complexes **4.11**–**4.15,** and the europium chloride salt in dimethylformamide (right).

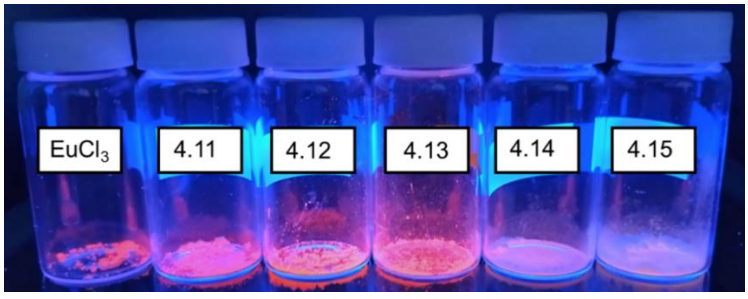

Fig. 4.7 Photographs illustrating fluorescence of europium(III) dichloromaleimide complexes **4.11**–**4.15** in the solid-state under UV light.

In order to obtain more insight into the photoluminescence of the synthesized europium(III) complexes, the solid-state spectroscopic analysis was performed. All the ligands **4.1**–**4.5** were non-fluorescent in the solid-state. However, for the complexes **4.11**–**4.15**, the absolute quantum yield was calculated using integration sphere.[29, 43] The absolute ϕ_f of the europium(III) complexes in the solid-state was 23% for **4.11**, 26% for **4.12**, 36% for **4.13**, 16% for **4.14** and 15% for **4.15**. Based on these results, the complex **4.13** appears to be the best potential candidate amongst all the synthesized europium(III) dichloromaleimide complexes, for further derivatization and fluorescence studies.

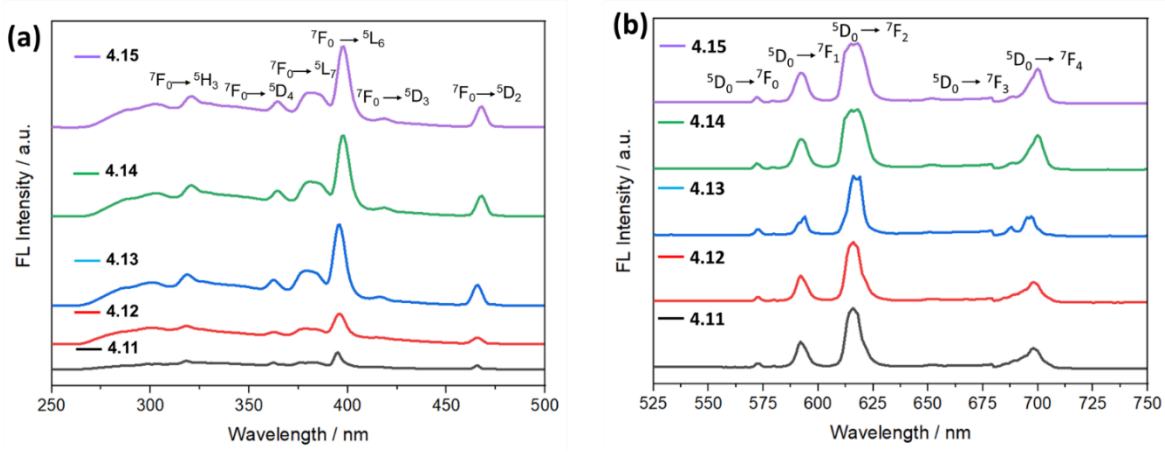

Fig. 4.8 Normalized excitation (**a**) and emission (**b**) spectra of the europium(III) dichloromaleimide complexes (**4.11**–**4.15**) in solid-state.

Fig. 4.8 represents the normalized excitation and emission scans for the europium dichloromaleimide complexes **4.11**–**4.15** in solid-state, and the photographs of the these complexes under UV light at 385 nm shown in Fig. 4.7. The emission spectra of the complexes **4.11**–**4.15** exhibited five emission peaks at 572 nm, 592 nm, 617 nm,

678 nm, and ~700 nm, which are attributable to the emission transitions, $^5D_0 \rightarrow {}^7F_0$, $^5D_0 \rightarrow {}^7F_1$, $^5D_0 \rightarrow {}^7F_2$, $^5D_0 \rightarrow {}^7F_3$, and $^5D_0 \rightarrow {}^7F_4$, respectively.[44] The $^5D_0 \rightarrow {}^7F_2$ transition is the dominant red emission for all the complexes (Fig. 4.8b). Three out of five of these transitions are also observed at similar wavelength in solution-state emission spectra (Table 4.4). These peaks are slightly red-shifted in comparison to the emission wavelength of the europium(III) chloride salt .i.e. 537 nm, 593 nm, 616 nm, 652, and 699 nm. Additionally, in the excitation spectra six peaks at 320 nm, 365 nm, 382 nm, 397 nm, 419 nm and 468 nm for complexes **4.11**–**4.15**, corresponding to the transitions $^7F_0 \rightarrow {}^5H_3$, $^7F_0 \rightarrow {}^5D_2$, $^7F_0 \rightarrow {}^5L_7$, $^7F_0 \rightarrow {}^5L_6$, $^7F_0 \rightarrow {}^5D_3$, and $^7F_0 \rightarrow {}^5D_2$, were identified (Fig. 4.8a). Among them, $^7F_0 \rightarrow {}^5L_6$ and $^7F_0 \rightarrow {}^5D_2$ are the most prominent excitations, which are located in the near-UV (~397 nm) and blue (468 nm) regions. Hence, these europium(III) complexes emit bright red fluorescence when excited by the light of wavelengths in the near-UV and blue regions.

4.3.3 Design and synthesis of europium(III) and terbium(III) aminochloromaleimide complexes

To further explore the optical properties of lanthanide-maleimide complexes, the synthesis of the fluorescent aminochloromaleimide ligands, and their corresponding europium(III) and terbium(III) complexes was explored. It has been reported that dichloromaleimides can undergo addition–elimination reaction with amines and can generate fluorophores in a single synthetic step.[25] Two new aminochloromaleimide derivatives were chosen, with the carboxyl functionality handle at different positions of the maleimide moiety. This was achieved by utilizing the previously synthesized acid-

functionalized dichloromaleimide ligand **4.3** (Section 4.3.1). This was reacted with *n*-butylamine *via* the addition-elimination reaction to obtain the aminochloromaleimide derivative **4.6** (Scheme 4.4). Similarly, the other aminochloromaleimide derivative **4.8**, was synthesized in two steps *via* the intermediate **4.7** (Scheme 4.4). Compounds **4.6** and **4.8** are regioisomers, with the acid group situated at either amine or imide position of the maleimide scaffold. Both the compounds **4.6** and **4.8** were characterized by ^{1}H, ^{13}C NMR spectroscopy and high resolution mass spectrometry (experimental section 4.5.2).

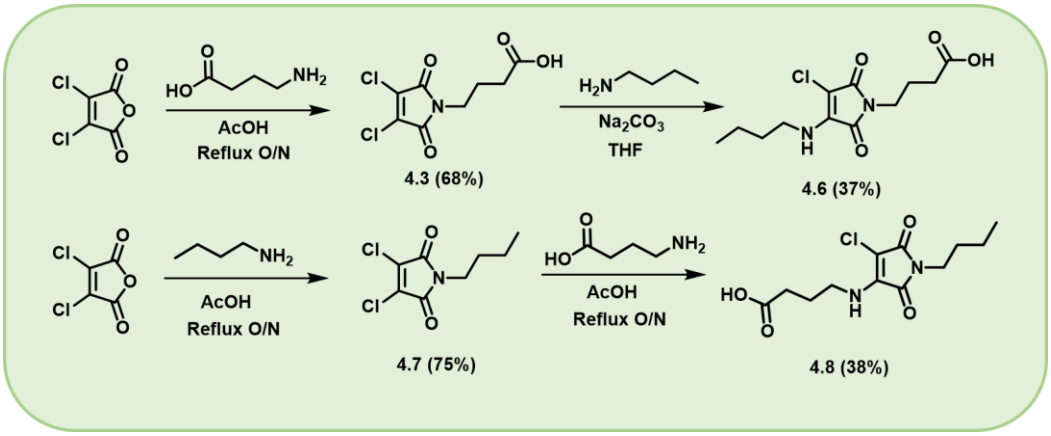

Scheme 4.4 Synthesis of acid functionalized aminochloromaleimide derivatives **4.6** and **4.8**.

Subsequently, aminochloromaleimide ligand **4.6** was reacted with europium(III) chloride hexahydrate and terbium(III) chloride hexahydrate (Section 4.3.1), to achieve **4.16** and **4.18** complexes, respectively (Scheme 4.5). Terbium(III) complexes have also been targeted in addition to the europium(III), to investigate the influence of using two different lanthanide metal ions on the fluorescence behavior of maleimides. Likewise, the aminochloromaleimide **4.8** was allowed to react with europium(III) and

terbium(III) salts in 3:1 equiv. to obtain **4.17** and **4.19**, respectively (Scheme 4.5). The synthesized lanthanide complexes were analyzed by TGA, FTIR spectroscopy and elemental analysis (experimental section 4.5.3).

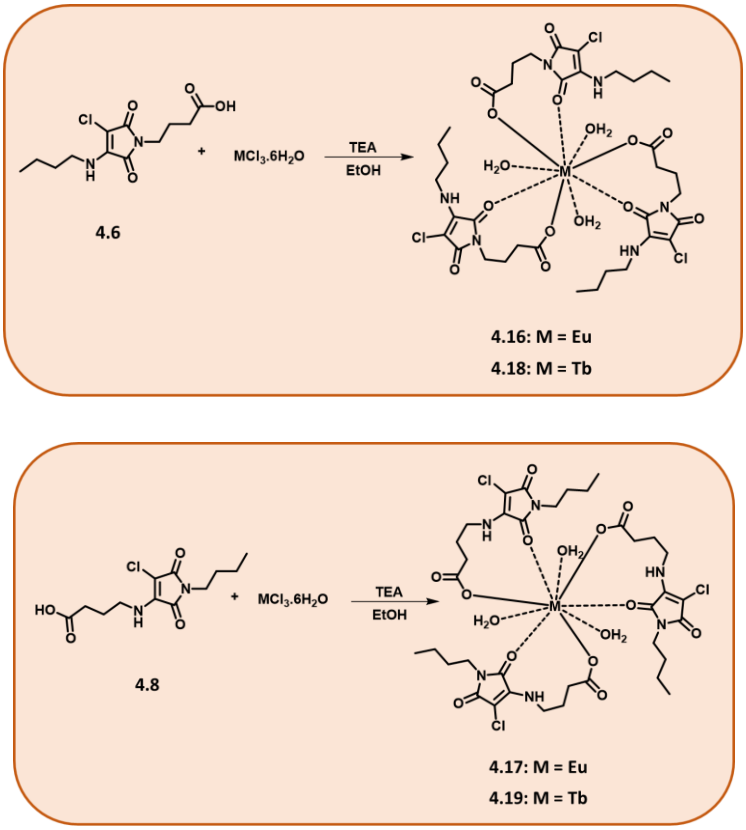

Scheme 4.5 Synthesis of europium(III) and terbium(III) aminochloromaleimide complexes **4.16**–**4.19**.

Similarly to the europium dichloromaleimide complexes, the stoichiometry for these newly synthesized lanthanide aminochloromaleimide complexes **4.16**–**4.19** was determined by the mole ratio method.[33] The Eu^{3+} and Tb^{3+} complexes were determined to possess 1:3 [M]/[L] ratio, when the change in luminescence intensity of $^5D_0 \rightarrow {}^7F_2$ and

and $^5D_4 \rightarrow {}^7F_6$ transition peaks, respectively, was monitored upon the addition of solution of lanthanide metal in ethanol to the ligand and showed in Fig. 4.9.

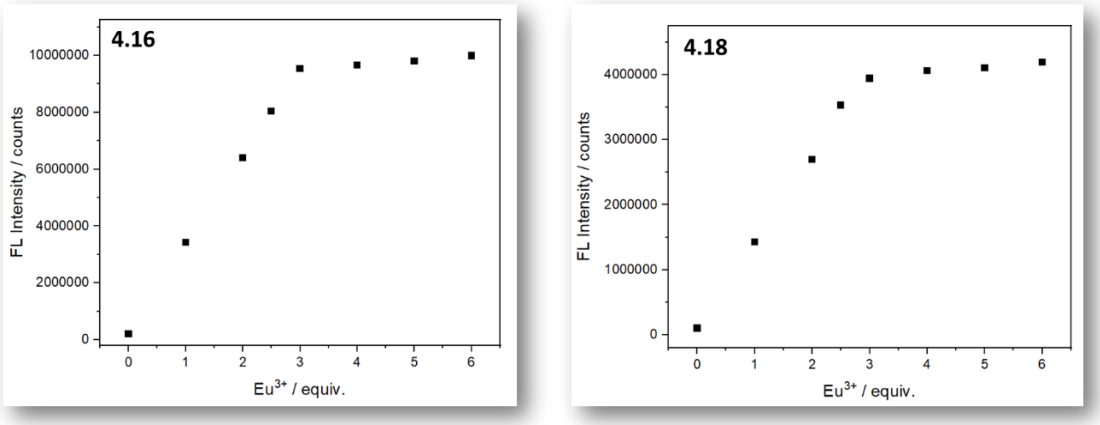

Fig. 4.9 Intensity of the $^5D_0 \rightarrow {}^7F_2$ and $^5D_4 \rightarrow {}^7F_6$ transitions peak as a function of Eu^{3+}(**4.16**; left) and Tb^{3+}(**4.18**; right) respectively, added to a ligand **4.6** solution in ethanol (10 μM), in the presence of a base (λ_{ex} = 395 nm).

The TGA profiles of the synthesized aminomaleimide ligands **4.6**–**4.8**, europium(III) aminomaleimide **4.16**–**4.17**, and terbium(III) aminomaleimide **4.18**–**4.19** complexes, were analyzed (Fig. 4.34; experimental section 4.5.4). The aminochloromaleimide ligands decomposed in the range of 150 to 500℃ with estimated mass loss of 86.25% and 84.32%, and left with the carbon residue after 500℃. In comparison, the europium(III) and the terbium(III) aminochloromaleimide complexes (**4.16**–**4.19**), showed thermal decomposition occurring in three stages. The first decomposition stage was observed to be 20–120℃ has been assigned to the loss of hydrated water molecules[34] and was observed within the temperature range of 20–120℃ for all the complexes (Table 4.5). The second and third stage of thermal decomposition was associated with the loss of organic components and happened within the temperature

range of 120–500℃. The final degradation stage suggested the formation of Eu_2O_3 (Tb_2O_3) for complexes **4.16** and **4.17** (**4.18** and **4.19**).[28]

Table 4.5 Thermal data of the aminochloromaleimide ligands **4.6** and **4.8**, and their europium(III) aminochloromaleimide **4.16** and **4.17**, and terbium(III) aminochloromaleimide **4.18** and **4.19** complexes.

Complexes	Temperature range (℃)	Weight loss (%)	Assignments
4.6	150 – 500	86.25	Organic components
	500 –	13.75	C
4.8	150 – 500	84.32	Organic components
	500 –	15.68	C
4.16	20 – 120	5.92	$3H_2O$
	110 – 500	53.17	Organic components
	500 –	40.91	Eu_2O_3 + C
4.17	150 – 120	4.81	$3H_2O$
	120 – 500	46.45	Organic components
	500 –	48.74	Eu_2O_3 + C
4.18	20 – 120	3.80	$3H_2O$
	120 – 500	50.67	Organic components
	500 –	45.53	Tb_2O_3 + C
4.19	20 – 120	6.99	$3H_2O$
	120 – 500	51.06	Organic components
	500 –	41.95	Tb_2O_3 + C

Furthermore, the FTIR spectra of the europium(III) and terbium(III) aminochloromaleimide complexes (**4.16**–**4.19**) were analyzed, and compared to the respective ligands **4.6** and **4.8**. The characteristic frequencies of interest for the ligands and their lanthanide(III) complexes are given in Table 4.6. The characteristic broad band observed at 3030 cm^{-1} for **4.6** and at 3013 cm^{-1} for **4.8**, corresponds to the O-H group in the free ligands. Also, the peaks at ~3319 cm^{-1} and 3339 cm^{-1} were assigned to N-H group for **4.6** and **4.8**, respectively. On complexation with the lanthanide(III) metal ions (i.e. Eu and Tb), the N-H stretching frequency shifted to a lower value, for instance ν(N-H) shifted from 3319 cm^{-1} (for ligand **4.6**) to 3313 cm^{-1} and 3309 cm^{-1} for complexes **4.16** and **4.18**, respectively. Notably, the N-H and O-H bands overlapped for all the complexes, as the ν(O-H) for the coordinated water molecules (~3300 cm^{-1}) observed within the same region of ν(N-H). While for free ligands, ν(O-H) and ν(N-H) were observed around ~3030 cm^{-1} and 3300 cm^{-1}, and well-separated by a distance of ~300 cm^{-1} (Table 4.6).[36] The vibration attributable to C=O, observed at 1702 cm^{-1} for **4.16** & **4.18** and 1712 cm^{-1} for **4.17** & **4.19**, compared to 1659 cm^{-1} and 1650 cm^{-1} for ligands **4.7** and **4.8**, indicates the coordination *via* carboxylic group oxygen to the lanthanide metal ions.

Table 4.6 Selected IR bands for the aminochloromaleimide ligands (**4.6** and **4.8**) and their europium(III) aminochloromaleimide (**4.16** and **4.17**) and terbium(III) aminochloromaleimide (**4.18** and **4.19**) complexes.

Complex (Ligand)	Characteristic frequencies			
	ν(O-H) stretch (cm^{-1})	ν(N-H) (cm^{-1})	ν(C=O) (cm^{-1})	ν(C-O) (cm^{-1})
4.6	3030	3319	1659	1225
4.8	3013	3339	1650	1269
4.16	3313		1702	1401
4.17	3322		1712	1401
4.18	3309		1702	1401
4.19	3322		1712	1401

4.3.4 Photophysical properties of europium(III) and terbium(III) aminochloromaleimide complexes

The photophysical properties of the synthesized aminomaleimide (ACM) ligands (**4.6** and **4.8**) and their lanthanide(III) complexes (Ln = Eu, Tb) (**4.16**–**4.19**) were measured in DMF and the corresponding data are summarized in Table 4.7.

Table 4.7 Photophysical properties of aminochloromaleimide ligands (**4.6** and **4.8**) and their complexes (**4.16**–**4.19**) in solution-state (10 μM in dimethylformamide) and solid-state (ϕ_f = relative quantum yield in DMF using quinine sulfate as reference, and absolute quantum yield in solid-state using integrating sphere; λ_{max} = maximum absorption wavelength; ε_{max} = molar absorption coefficient; B = Brightness; λ_{ex} = excitation wavelength ; λ_{em} = maximum emission wavelength; slit width ex 1.0 nm, em 1.0 nm; 25°C).

Ligand / Complex	State	ϕ_f / %	λ_{max} (ε_{max}) / nm ($M^{-1}cm^{-1}$)	B / $M^{-1}cm^{-1}$	λ_{ex} / nm	λ_{em} / nm
4.6	DMF	15	382 (4117)	61755	386	512
	Solid-state	26	-	-	384	516
4.8	DMF	15	381 (3185)	47775	382	528
	Solid-state	24	-	-	380	530
4.16	DMF	14	382 (10789)	151046	353, 408	507
	Solid-state	44	-	-	395	498
4.17	DMF	13	381 (8490)	110370	350, 413	507
	Solid-state	41	-	-	395	564
4.18	DMF	14	382 (10290)	144060	341, 383	506
	Solid-state	42	-	-	370	450
4.19	DMF	11	382 (7589)	83479	352, 420	507
	Solid-state	40	-	-	370	520

Earlier, the employed ligands (dichloromaleimide) were non-fluorescent and therefore, the observed transitions for the lanthanide-maleimide complexes were predominantly metal-centered ($f \rightarrow f$) (section 4.3.2). In comparison, the current aminochloromaleimide-based ligands, **4.6** and **4.8**, are bright green fluorophores, due to which the complexes, **4.16**–**4.19**, displayed green emissions as well (Fig. 4.10).

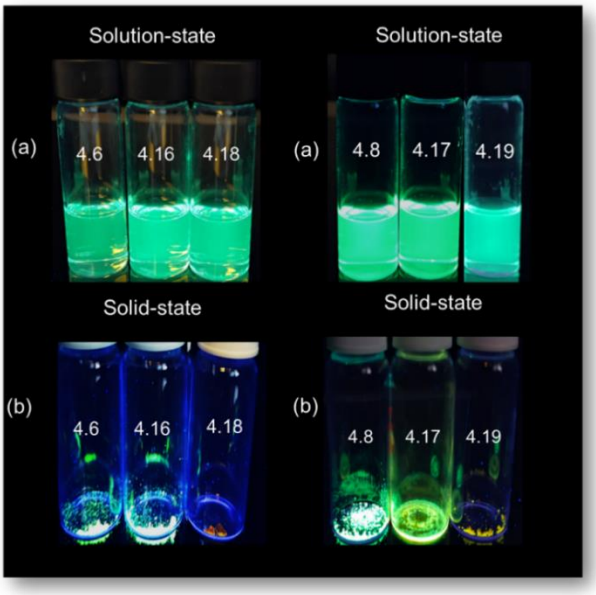

Fig. 4.10 Photographs illustrating fluorescence of the aminochloromaleimide ligands (**4.6** and **4.8**) and their lanthanide(III) complexes (**4.16**–**4.19**) in solution-state and solid-state under UV light.

In the UV-Vis absorption spectra, a band occurs at 382 nm (Table 4.7) which is attributable to the characteristic $n \rightarrow \pi^*$ transition of the ligand. Furthermore, for complexes having the same chromophore system, for instance **4.16** and **4.18**, the fluorescence spectra are very similar, displaying one broad band in the emission spectra with a maximum centered around 507 nm (Fig. 4.10). Interestingly, no metal centered transitions ($f \rightarrow f$) were observed in the emission and excitation scan of the synthesized complexes (Fig. 4.11 and 4.12). Instead, an intense band from the ligand was observed around ~507 nm. It has been reported, by our group previously, that the aminomaleimide-based fluorophores are strongly emissive dyes.[45] Moreover, the charge transfer occurring during the photoluminescence of the lanthanide(III) complexes involves intraligand CT, which eventually leads to ligand-to-metal (LMCT) states.[40] Building on this, it was hypothesized that the expected LMCT transitions may

have been outcompeted by the fast ILCT contributed by the organic ligand, as illustrated in Fig. 4.13.

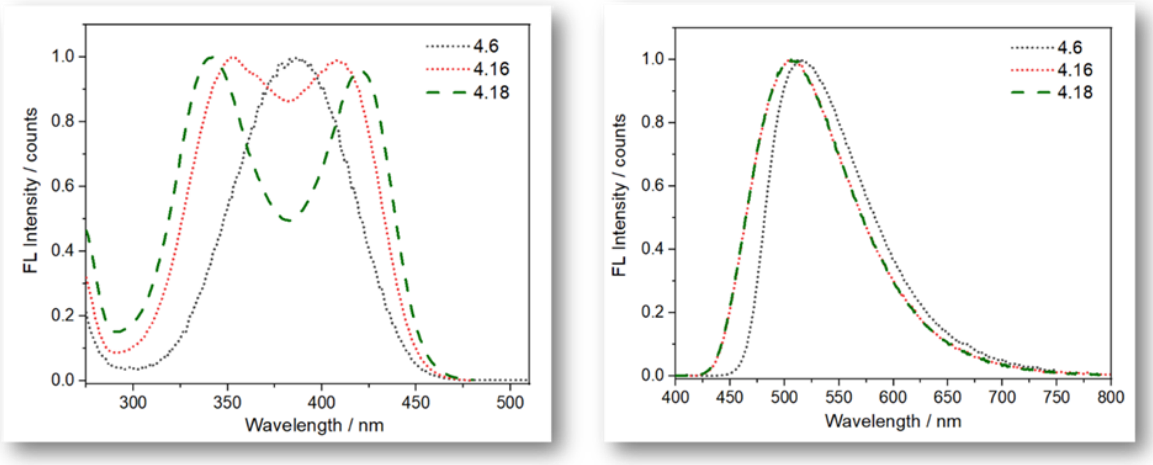

Fig. 4.11 Normalized excitation (left) and emission (right) spectra of aminochloromaleimide ligand (**4.6**), and its europium(III) (**4.16**) and terbium(III) (**4.18**) complexes in dimethylformamide (50 µM).

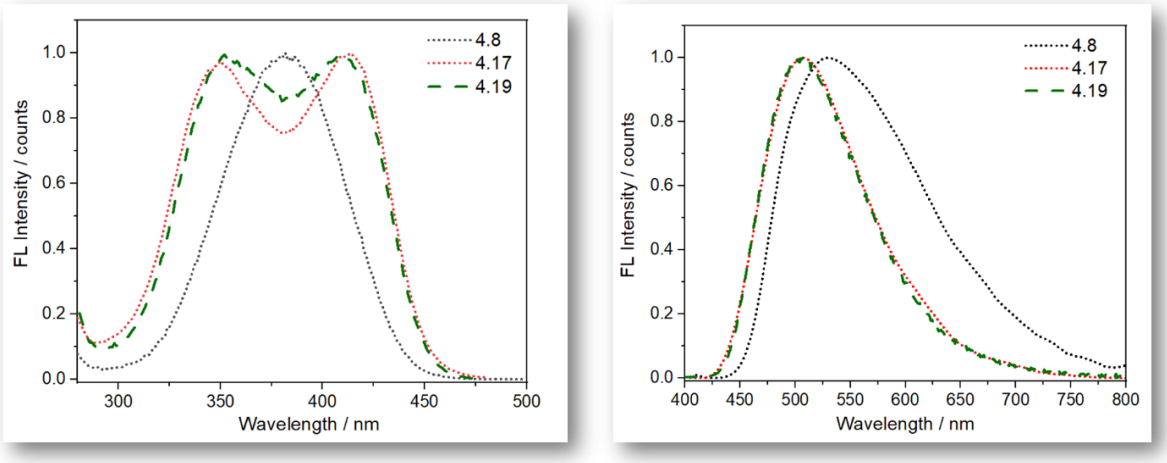

Fig. 4.12 Normalized excitation (left) and emission (right) spectra of aminochloromaleimide ligand (**4.8**), and its europium(III) (**4.17**) and terbium(III) (**4.19**) complexes in dimethylformamide (50 μM).

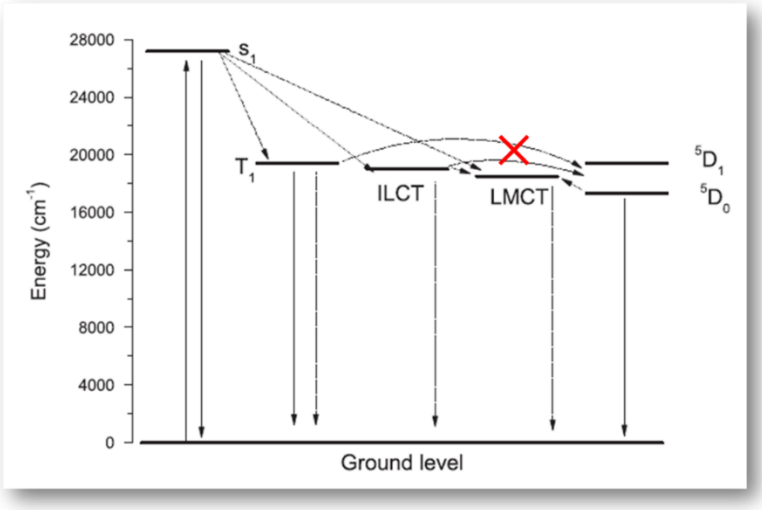

Fig. 4.13 Jablonski diagram for the Eu^{3+}(L) complex, illustrating various electronic states. Adapting from the reference.[40] Copyright 2014 Elsevier.

Compared to the dichloromaleimides, the aminochloromaleimide ligands give higher absorptions and better emission efficiencies, when coordinated to trivalent lanthanide ions. This is due to the back energy transfer from metal to ligand, thus suppressing the $f \rightarrow f$ transitions.[4] This was demonstrated by comparing the molar absorption coefficient (ε_{max}) of the europium(III) dichloromaleimide complexes (**4.11–4.15**) with that of the europium(III) aminochloromaleimide complexes (**4.16** and **4.18**). In dimethylformamide, **4.11–4.15** exhibited ε_{max} in the range of 3834 – 4294 $M^{-1}cm^{-1}$ (Table 4.4), which was lower than ε_{max} observed for **4.16** and **4.18**, which were 10789 $M^{-1}cm^{-1}$ and 7589 $M^{-1}cm^{-1}$, respectively (Table 4.7). Furthermore, in solid-state the ϕ_f evaluated for **4.16** (44%) and **4.18** (42%) was also higher than for **4.11–4.15** (16–30%) (Table 4.7). Based on these results, it was hypothesized that for lanthanide(III) aminochloromaleimide complexes, the parity forbidden $f \rightarrow f$ transitions are overruled by the ILCT transitions, and thus they exhibited higher emissions.

The reference quantum yield of the aminochloromaleimide ligands (**4.6** and **4.8**) and their complexes (**4.16**–**4.19**) in dimethylformamide was calculated using quinine sulfate (0.105 M $HClO_4$ as the standard reference (ϕ_{st} = 59%).[29] In solution state (i.e., dimethylformamide), the europium(III) and terbium(III) complexes possessed ϕ_f comparable to the ligands. Although, europium(III) complexes are observed to be the brightest with molar absorption co-efficient 10789 $M^{-1}cm^{-1}$ (for **4.16**) and 8490 $M^{-1}cm^{-1}$ (for **4.17**), compared to 10290 $M^{-1}cm^{-1}$ (for **4.18**) and 7589 $M^{-1}cm^{-1}$ (for **4.19**), calculated for the terbium(III) complexes. Additionally, the carboxyl functionality (coordinated to lanthanide(III) metal ion) present at imide position of the maleimide ring (ligand: **4.6**), formed brighter complexes (**4.16** and **4.18**) with higher ϕ_f (ε_{max}). For instance, ϕ_f = 14%, ε_{max} = 10290 $M^{-1}cm^{-1}$ and B = 144060 $M^{-1}cm^{-1}$ for **4.18**, compared

to ϕ_f = 11%, ε_{max} = 7589 $M^{-1}cm^{-1}$ and B = 83479 $M^{-1}cm^{-1}$ for **4.19** (Table 4.7). This is also in agreement with the other work where the effect of fluoroalkyl groups has more pronounced effect when attached *via* the imide nitrogen of the maleimide moiety.

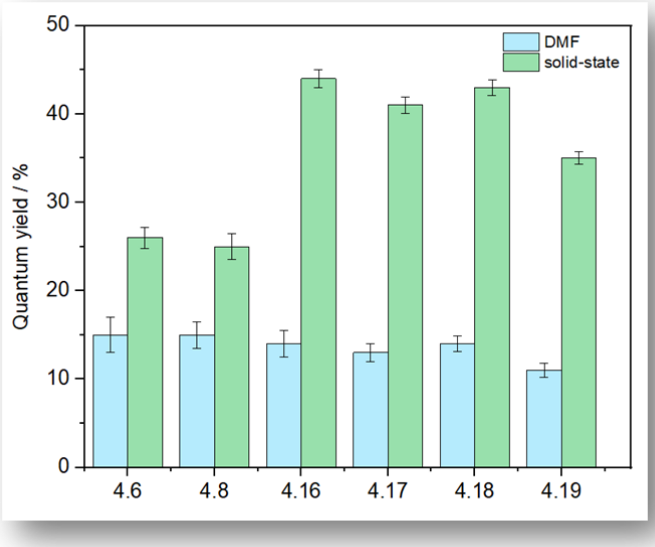

Fig. 4.14 Fluorescence quantum yield of the aminochloromaleimide ligands (**4.6** and **4.8**) and their complexes (**4.16**–**4.19**) in dimethylformamide and in solid-state, measured by using reference and absolute methods, respectively.

For solid-state, the quantum yields of the aminochloromaleimide ligands **4.6** and **4.8**, and their complexes **4.16**–**4.19**, were measured by the absolute method using the integrating sphere.[29] The observed trend reflected the results observed for the solution-state ϕ_f, with the exception that ligands displayed ϕ_f lower than the complexes (Fig. 4.14). Moreover, in solid-state the emission maxima is red-shifted for **4.17** (564 nm) and **4.19** (535 nm), compared to **4.16** (498 nm) and **4.18** (450 nm), respectively, which in turn was blue-shifted compared to the ligands, **4.6** (516 nm) and **4.8** (530 nm), respectively (Fig. 4.15). Based on these results, the europium(III) and terbium(III)

aminochloromaleimide complexes may serve as potential candidates for sensing applications.

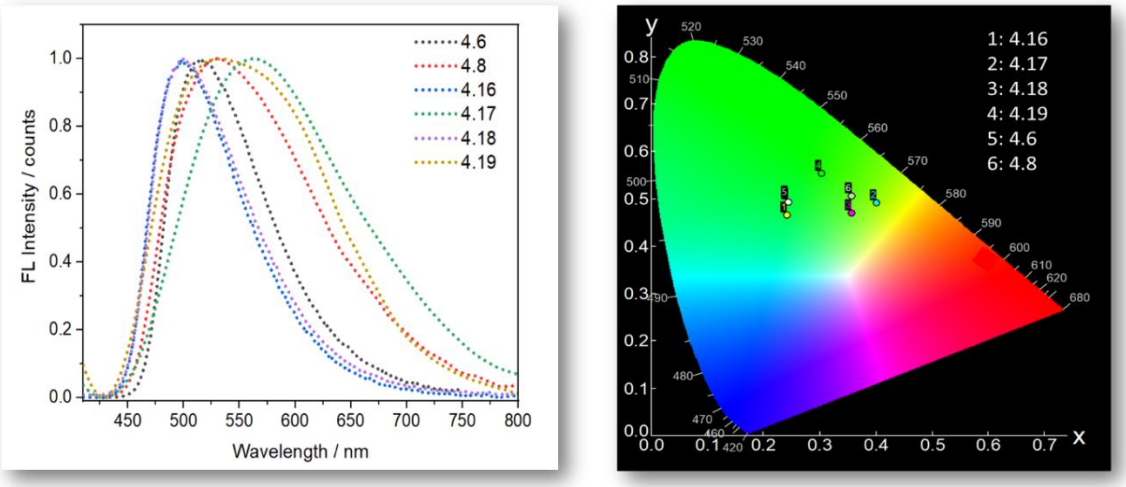

Fig. 4.15 Normalized emission spectra (left) and CIE plots (right) of the aminochloromaleimide ligands (**4.6** and **4.8**) and their europium(III) (**4.16** and **4.17**) and terbium(III) (**4.18** and **4.19**) complexes in solid-state.

4.4 Summary

In summary, a series of dichloromaleimide ligands containing carboxylate groups and their corresponding europium(III) complexes were synthesized. The ligands were characterized by ^{1}H NMR, ^{13}C NMR, FTIR spectroscopy and HR-MS, while the complexes were analyzed by elemental analysis, thermal gravimetric analysis, FTIR, UV-Vis and fluorescence spectroscopy. The complexes were found to contain 1:3 metal-to-ligand stoichiometry. The dichloromaleimide ligands were non-fluorescent before complexation, but exhibited red fluorescence upon complexation with europium(III), with absorption coefficients $>10^{3}$ $M^{-1}cm^{-1}$. The emission spectra of the europium(III) dichloromaleimide complexes displayed the most intense peak around ~617 nm corresponding to the $^{5}D_{0}\rightarrow{}^{7}F_{2}$ transitions, in solution as well as in solid-state. In solid-state, the europium(III) dichloromaleimide complexes possessed quantum yields in the range of 15–36%. Subsequently, two carboxylate functionalized aminochloromaleimide ligands were synthesized by derivatizing the most intense dichloromaleimide candidate. The photophysical properties of the corresponding europium(III) and terbium(III) complexes were analyzed as well. Interestingly, the metal-centered $f-f$ transitions for the Eu(III) and Tb(III) were dominated by the intense $\pi \rightarrow \pi^{*}$ transitions. Owing to these $\pi \rightarrow \pi^{*}$ transitions, contributed by the intra-ligand charge transfer, europium(III)/terbium(III) aminomaleimide complexes possessed good quantum yields and displayed the emission maxima at 507 nm in dimethylformamide (ϕ_f = ~14%) and 450 – 560 nm in solid-state (ϕ_f= ~14%). Based on this chapter, strongly luminescent europium(III)/terbium(III) maleimide complexes could serve as a promising candidate for various labelling and sensing applications by tuning their structural and photophysical properties.

4.5 Experimental

4.5.1 Materials and instrumentation

All chemicals and solvents were obtained from either: Sigma Aldrich, Alfa Aesar, or Fisher Chemicals, and used as received.

1D and 2D NMR spectra were recorded on a Bruker Advance 300 or a Bruker Advance III HD 400 at 300 and 400 MHz respectively. Shifts are quoted in δ in parts per million (ppm) and quoted relative to the internal standard tetramethylsilane (TMS).

High Resolution Mass Spectra (HR-MS) were conducted by Dr Christopher Williams (University of Birmingham) on a Bruker UHR-Q-ToF MaXis spectrometer with electrospray ionization. Elemental analysis was performed on CE instrument EA1110 elemental analyzer based on a dynamic flash combustion and G.C. separation system.

FTIR spectroscopy was carried out on neat samples using Agilent Technologies Cary 630 FTIR spectrometer. The spectra were corrected for background absorbance and 16 Scans were taken from 600 to 4000 cm^{-1} at a resolution of 4 cm^{-1}.

Thermogravimetric analysis (TGA) was performed on a TG550 in the temperature range of 20 to 600°C with a heating rate of 10℃ min^{-1}. The experiments were conducted under inert atmosphere and using aluminum pan. The weight loss percentage was calculated by the difference between the sample weights at 20℃ and at 600℃.

UV-Vis spectroscopy was carried out at room temperature on Evolution 350 UV-Vis spectrophotometer, equipped with Xenon Flash lamp light source, and silicon photodiode detectors. Quartz cells (170 - 2000 nm) from Hellma with two polished

sides were used for examining the absorption spectral data by using Thermo INSIGHT software.

Fluorescence emission and excitation spectra were obtained with Agilent Cary Eclipse Fluorescence spectrophotometer or Edinburgh Instruments FS5 Spectrofluorometer in quartz 3.5 mL cuvettes (Starna Cell, Type: 3/Q/10) for liquid samples (10–50 µM, 25 °C). The data was analyzed in Fluoracle (Edinburgh Instruments) and Origin 2019 (Origin Labs). A solution of quinine sulfate dihydrate in 0.105 M perchloric acid was used as standard (ϕ_{st} = 59%), for the evaluation of solution-state quantum yield analysis, according to previously reported literature procedure.[29] The absolute quantum yield in solid state is evaluated as an average of six replicate measurements, using the SC-30 integrating sphere module.

4.5.2 Synthesis of the ligands

2-(3,4-dichloro-2,5-dioxo-2,5-dihydro-1*H*-pyrrol-1-yl)acetic acid (4.1)

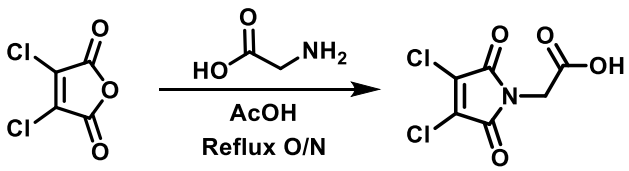

4.1 (65%)

Reaction was carried out according to published protocol.[31] 1.0 g of 3,4-dichloromaleic anhydride (6.0 mmol, 1.0 equiv.) and 495 mg (7.0 mmol, 1.1 equiv.) of glycine were dissolved in 25 mL of acetic acid. The reaction mixture was refluxed overnight at 110°C. After cooling to the room temperature, the solvent was removed under reduced

pressure and purified *via* column chromatography using hexane/ethyl acetate to obtain **4.1** as a colorless white crystalline solid.

R_f = 0.48 (hexane: ethyl acetate = 2:1); Yield = 875 mg, 65%.

^{1}H NMR (400 MHz, DMSO-d_6, 25℃, TMS) δ [ppm] = 13.41 (1H, s, H1), 4.28 (2H, s, H3).

^{13}C NMR (101 MHz, DMSO-d_6, 25℃, TMS) δ [ppm] = 168.8 (C2), 163.0 (C=O), 133.3 (C=C), 40.3 (C3).

FTIR (cm^{-1}): ν = 2884 (O-H) stretch, 1714 (C=O), 1614 (C=C), 1410 (O-H) bend, 1243 (C-O).

HR-MS (MaXis) $[M+H]^+$ - *m/z* found 224.9918; *m/z* calculated 224.9909.

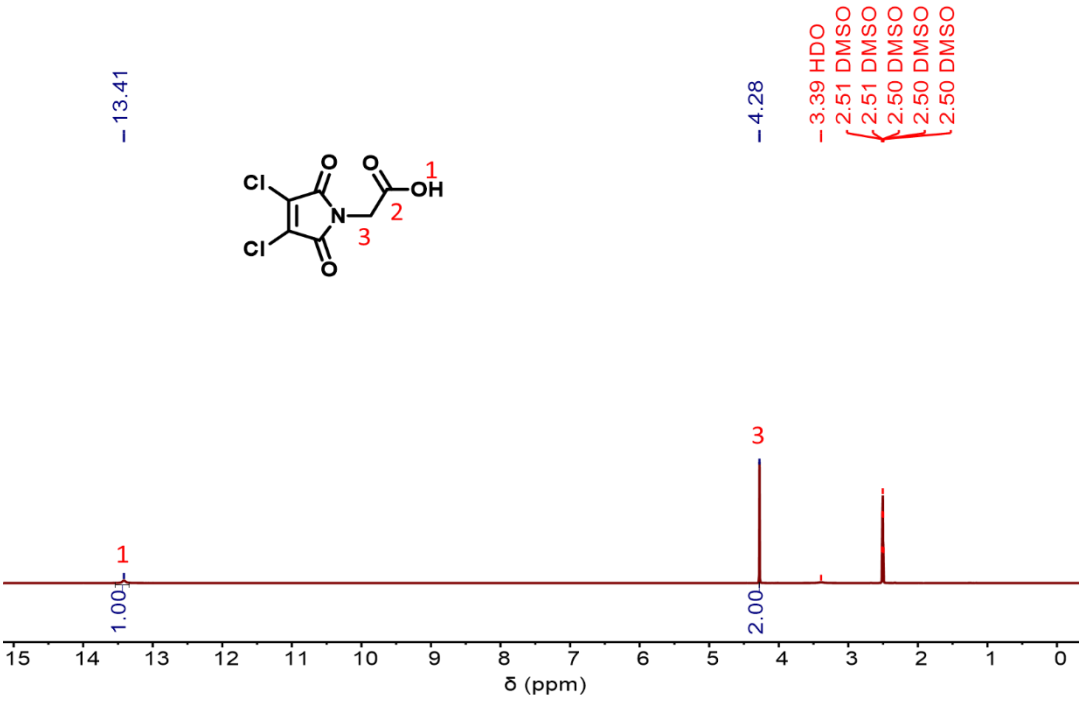

Fig. 4.16 ^{1}H NMR spectrum of **4.1** (400 MHz, DMSO-d_6).

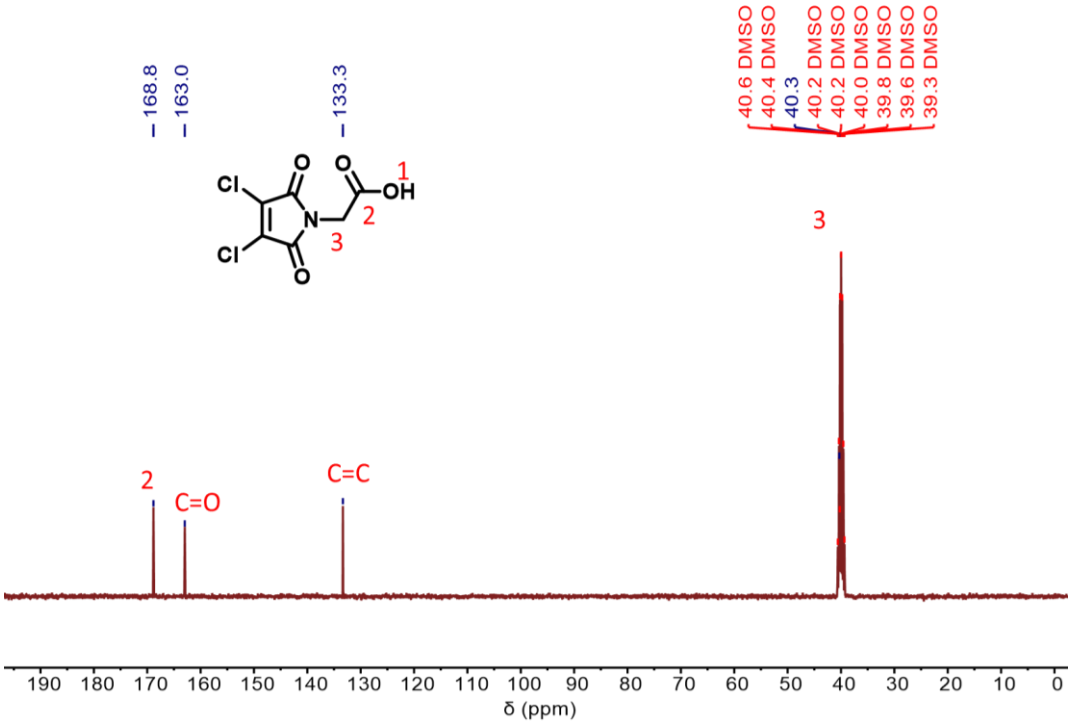

Fig. 4.17 ^{13}C NMR spectrum of **4.1** (101 MHz, DMSO-d_6).

3-(3,4-dichloro-2,5-dioxo-2,5-dihydro-1*H*-pyrrol-1-yl)propanoic acid (4.2)

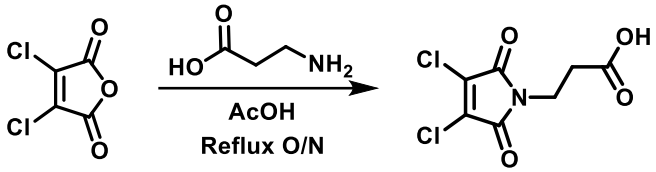

4.2 (65%)

Synthesis of the ligand was achieved by following the published protocol.[31] 1.0 g of 3,4-dichloromaleic anhydride (6.0 mmol, 1.0 equiv.) and 587 mg (7.0 mmol, 1.1 equiv.) of β-alanine were dissolved in 25 mL of acetic acid. The reaction mixture was refluxed overnight at 110℃. After cooling to the room temperature, the solvent was removed

under reduced pressure and purified *via* column chromatography using hexane/ethyl acetate to obtain **4.2** as colorless crystalline solid.

R_f = 0.50 (hexane: ethyl acetate = 2:1); Yield = 928 mg, 65%.

^{1}H NMR (400 MHz, DMSO-d_6, 25℃, TMS) δ [ppm] = 12.43 (1H, s, H1), 3.71–3.67 (2H, t, H4), 2.57–2.54 (2H, t, H3).

^{13}C NMR (101 MHz, DMSO-d_6, 25℃, TMS) δ [ppm] = 172.3 (C2), 163.2 (C=O), 132.9 (C=C), 35.1 (C4), 32.5 (C3).

FTIR (cm^{-1}): ν = 2919 (O-H), 1706 (C=O), 1606 (C=C), 1375 (O-H) bend, 1221 (C-O).

HR-MS (MaXis) $[M+H]^+$ - *m/z* found 239.0181; *m/z* calculated 239.0281.

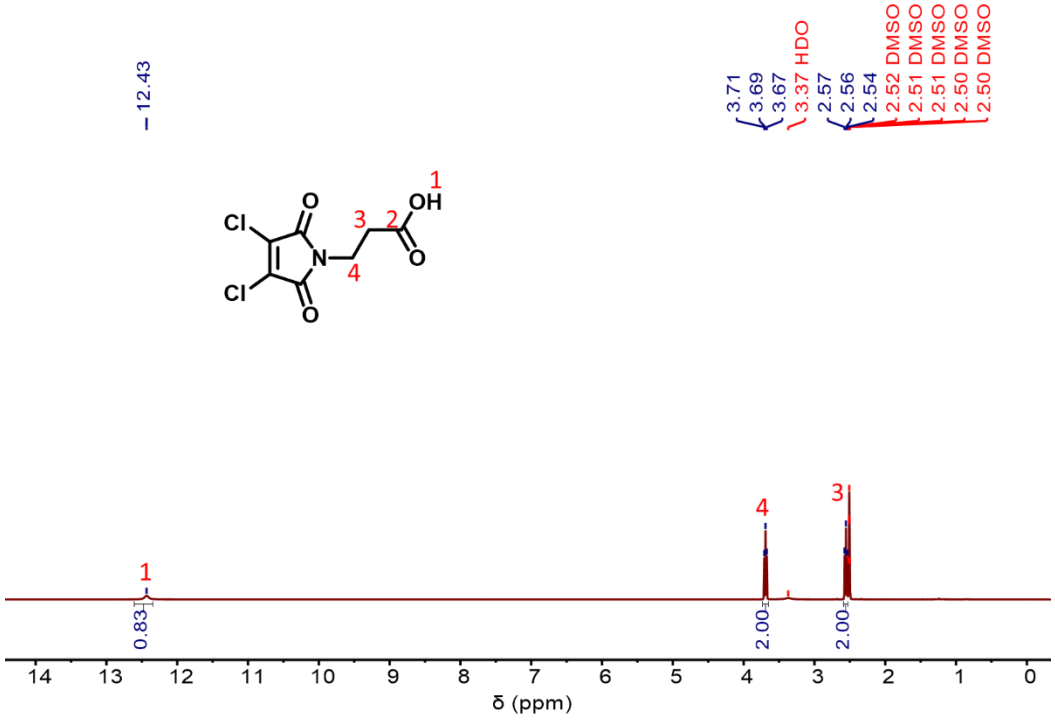

Fig. 4.18 ^{1}H NMR spectrum of **4.2** (400 MHz, DMSO-d_6).

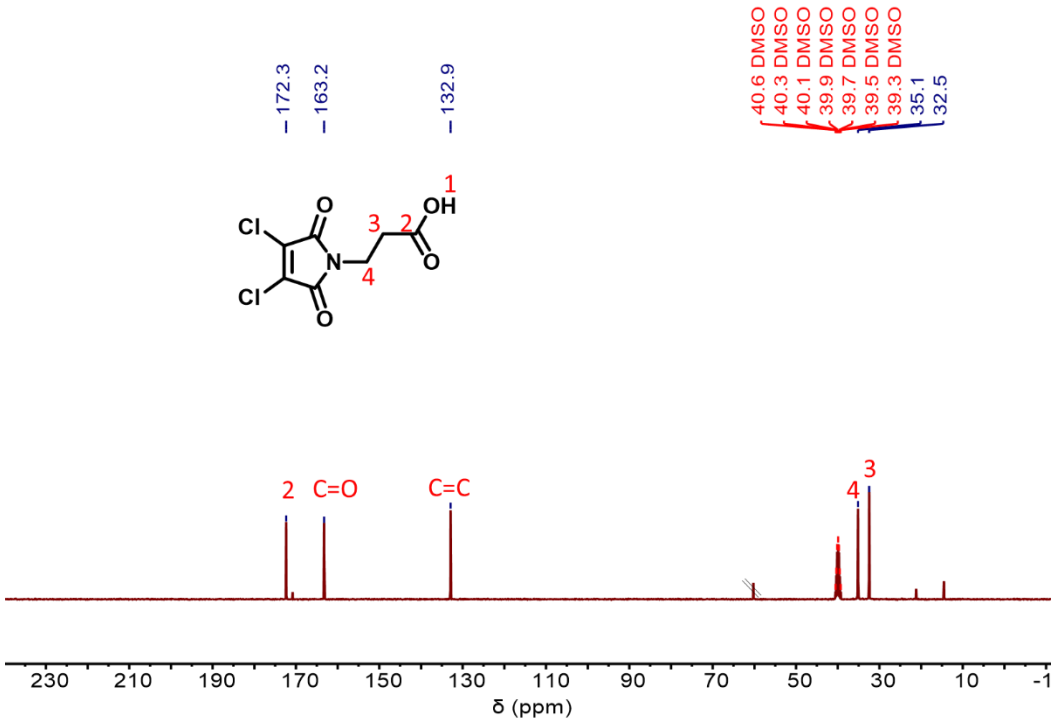

Fig. 4.19 ^{13}C NMR spectrum of **4.2** (101 MHz, DMSO-d_6).

4-(3,4-dichloro-2,5-dioxo-2,5-dihydro-1*H*-pyrrol-1-yl)butanoic acid (4.3)

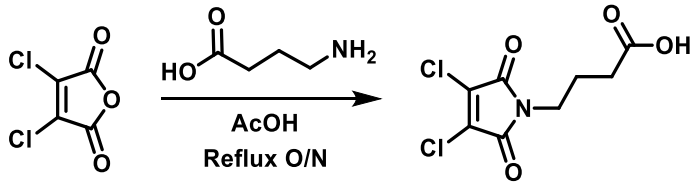

4.3 (68%)

Synthesis of the ligand was achieved by following the published protocol.[31] 1.0 g of 3,4-dichloromaleic anhydride (6.0 mmol, 1.0 equiv.) and 680 mg (7.0 mmol, 1.1 equiv.) of 4-aminobutanoic acid were dissolved in 20 mL of acetic acid. The reaction mixture was refluxed overnight at 110℃. After cooling to the room temperature, the solvent

was removed under reduced pressure and purified *via* column chromatography using hexane/ethyl acetate to obtain **4.3** as colorless crystalline solid.

R_f = 0.54 (hexane: ethyl acetate = 2:1); Yield = 1.0 g, 68%.

^{1}H NMR (400 MHz, DMSO-d_6, 25℃, TMS) δ [ppm] = 12.11 (1H, s, H1), 3.53–3.50 (2H, t, H5), 2.2–2.26 (2H, t, H3), 1.79–1.72 (2H, t, H4).

^{13}C NMR (101 MHz, DMSO-d_6, 25℃, TMS) δ [ppm] = 174.4 (C2), 163.7 (C=O), 132.8 (C=C), 38.6 (C5), 31.1 (C3), 23.6 (C4).

FTIR (cm^{-1}): ν = 2942 (O-H), 2938 (C-H), 1704 (C=O), 1612 (C=C), 1393 (O-H) bend, 1393 (C-O).

HR-MS (MaXis) $[M+H]^+$ - *m/z* found 253.0508; *m/z* calculated 253.0581.

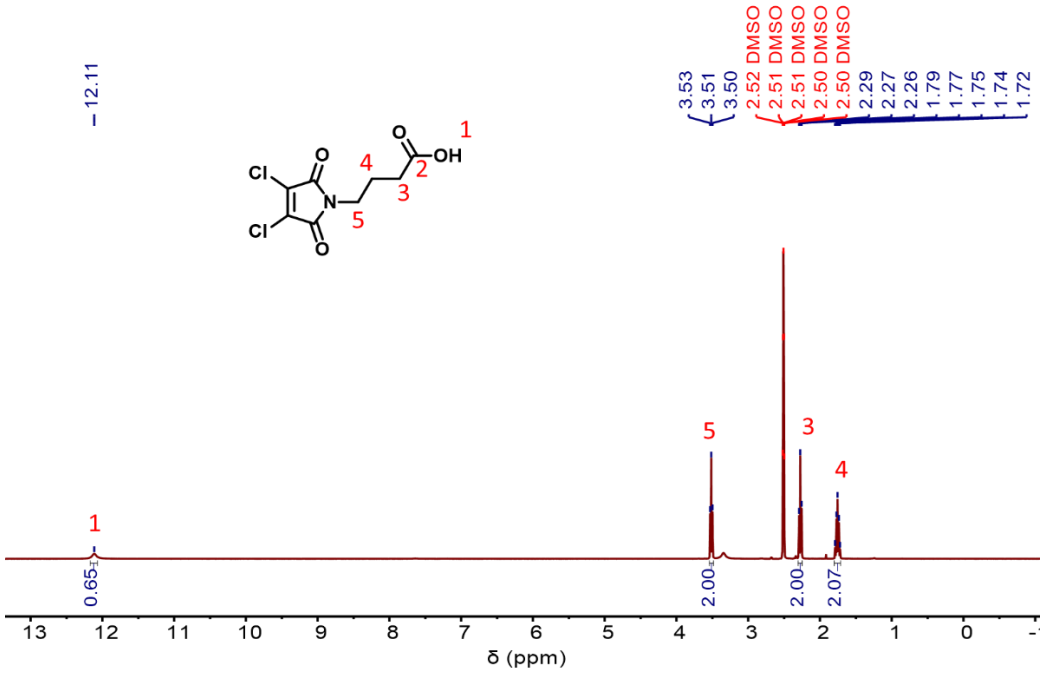

Fig. 4.20 ^{1}H NMR spectrum of **4.3** (400 MHz, DMSO-d_6).

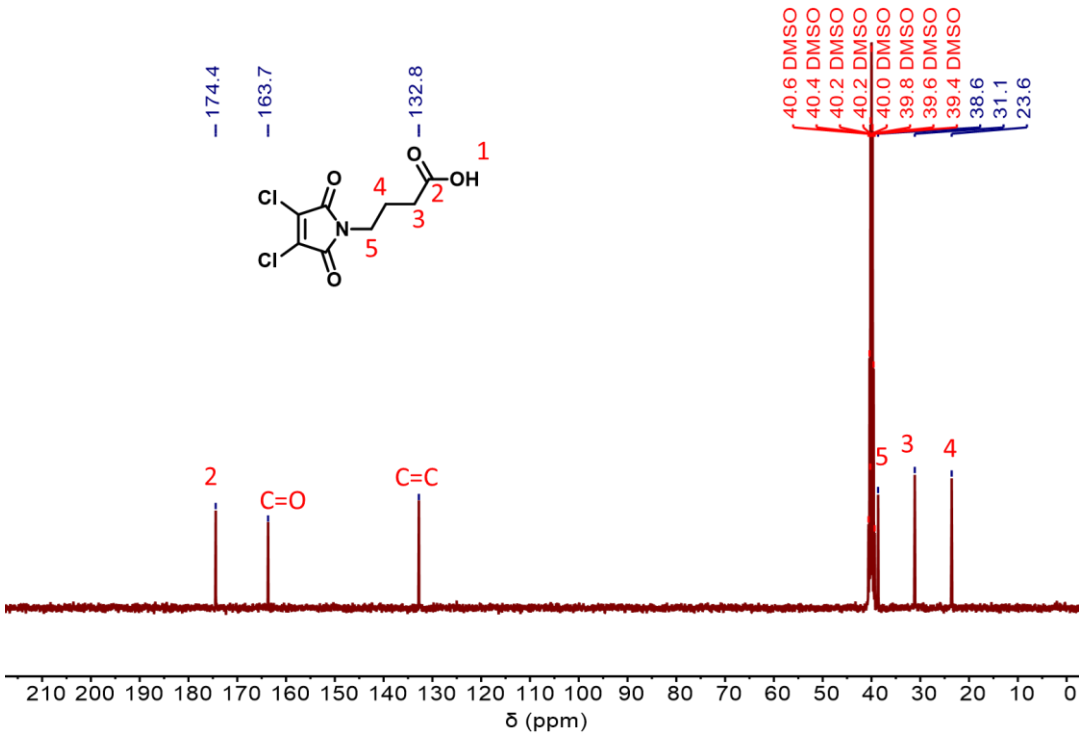

Fig. 4.21 ^{13}C NMR spectrum of **4.3** (101 MHz, DMSO-d_6).

5-(3,4-dichloro-2,5-dioxo-2,5-dihydro-1*H*-pyrrol-1-yl)pentanoic acid (4.4)

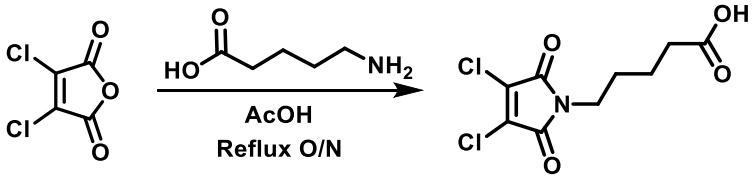

4.4 (64%)

Synthesis of the ligand was achieved by following the published protocol.[31] 1.0 g of 3,4-dichloromaleic anhydride (6.0 mmol, 1.0 equiv.) and 772 mg (7.0 mmol, 1.1 equiv.) of 5-aminopentanoic acid were dissolved in 20 mL of acetic acid. The reaction mixture was refluxed overnight at 110℃. After cooling to the room temperature, the solvent

was removed under reduced pressure and purified *via* column chromatography using hexane/ethyl acetate to obtain **4.4** as colorless solid.

R_f = 0.58 (hexane: ethyl acetate = 2:1); Yield = 1.0 g, 64%.

^{1}H NMR (400 MHz, $CDCl_3$, 25℃, TMS) δ [ppm] = 3.64–3.61 (2H, t, H6), 2.41–2.38 (2H, t, H3), 1.71–1.64 (4H, m, H4,H5).

^{13}C NMR (101 MHz, $CDCl_3$, 25℃, TMS) δ [ppm] = 178.8 (C2), 162.9 (C=O), 133.1 (C=C), 38.7 (C6), 33.0 (C3), 27.5 (C5), 21.4 (C4).

FTIR (cm^{-1}): ν = 2951 (O-H), 2933 (C-H), 1691 (C=O), 1623 (C=C), 1371 (O-H) bend, 1199 (C-O).

HR-MS (MaXis) $[M+H]^+$ - *m/z* found 267.0784; *m/z* calculated 267.0780.

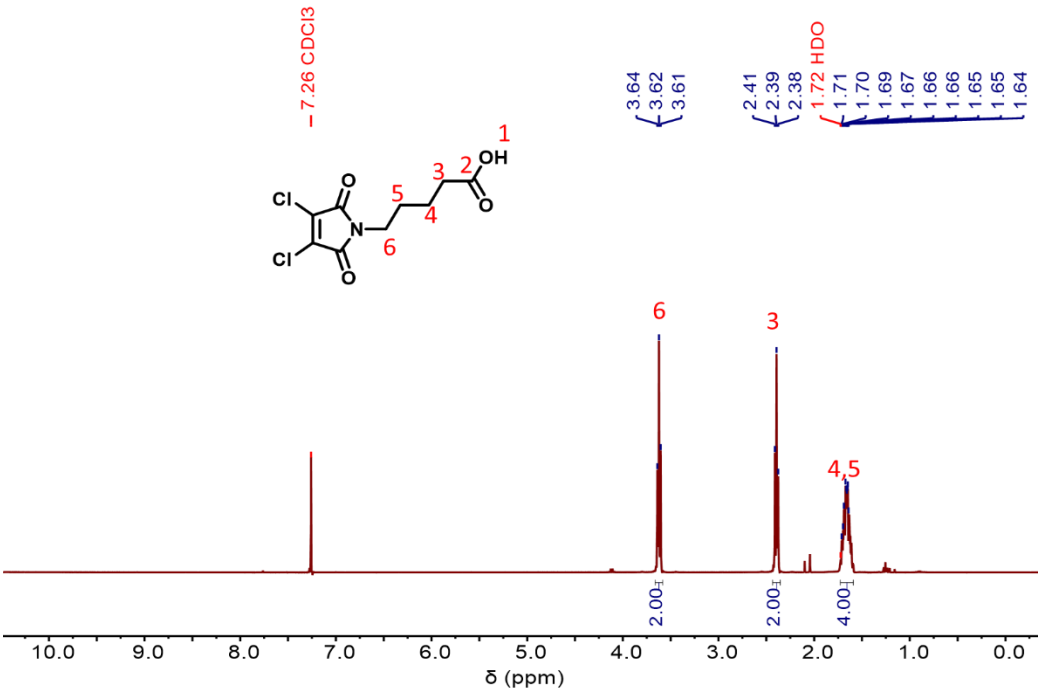

Fig. 4.22 ^{1}H NMR spectrum of **4.4** (400 MHz, $CDCl_3$).

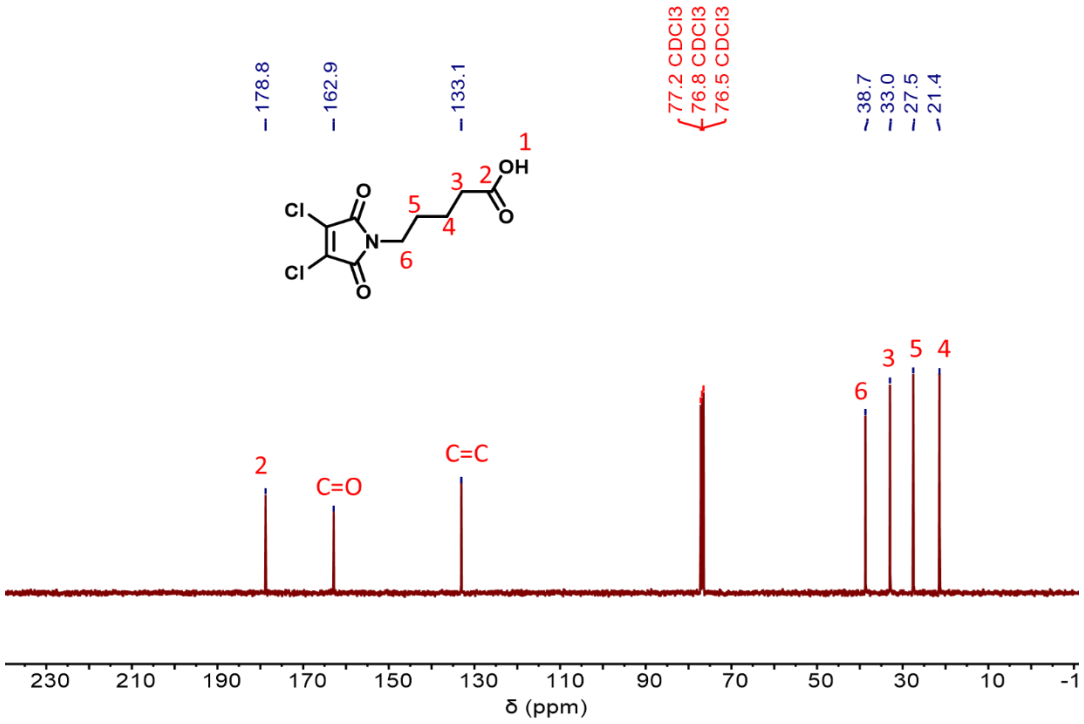

Fig. 4.23 ^{13}C NMR spectrum of **4.4** (101 MHz, $CDCl_3$).

6-(3,4-dichloro-2,5-dioxo-2,5-dihydro-1*H*-pyrrol-1-yl)hexanoic acid (4.5)

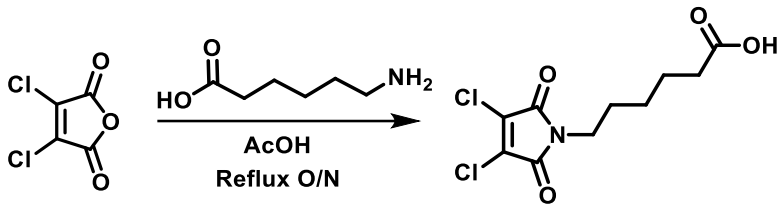

4.5 (62%)

The synthesis was carried out by following the already reported protocol.[31] 1.0 g of 3,4-dichloromaleic anhydride (6.0 mmol, 1.0 equiv.) and 865 mg (7.0 mmol, 1.1 equiv.) of 6-aminohexanoic acid were dissolved in 20 mL of acetic acid. The reaction mixture was refluxed overnight at 110℃. After cooling to the room temperature, the solvent

was removed under reduced pressure and purified *via* column chromatography using hexane/ethyl acetate to obtain **4.5** as colorless solid.

R_f = 0.61 (hexane: ethyl acetate = 2:1); Yield = 1.1 g, 62%.

^{1}H NMR (400 MHz, $CDCl_3$, 25℃, TMS) δ [ppm] = 3.62–3.58 (2H, t, H7), 2.37–2.34 (2H, t, H3), 1.68–1.62 (4H, m, H4,H6), 1.39–1.31 (2H, m, H5).

^{13}C NMR (101 MHz, $CDCl_3$, 25℃, TMS) δ [ppm] = 179.3 (C2), 163.2 (C=O), 133.4 (C=C), 39.3 (C7), 33.7 (C3), 28.2 (C6), 26.1 (C5), 24.1 (C4).

FTIR (cm^{-1}): ν = 2930 (O-H), 2927 (C-H), 1683 (C=O), 1621 (C=C), 1399 (O-H) bend, 1197 (C-O).

HR-MS (MaXis) $[M+H]^+$ - *m/z* found 281.1090; *m/z* calculated 281.1081.

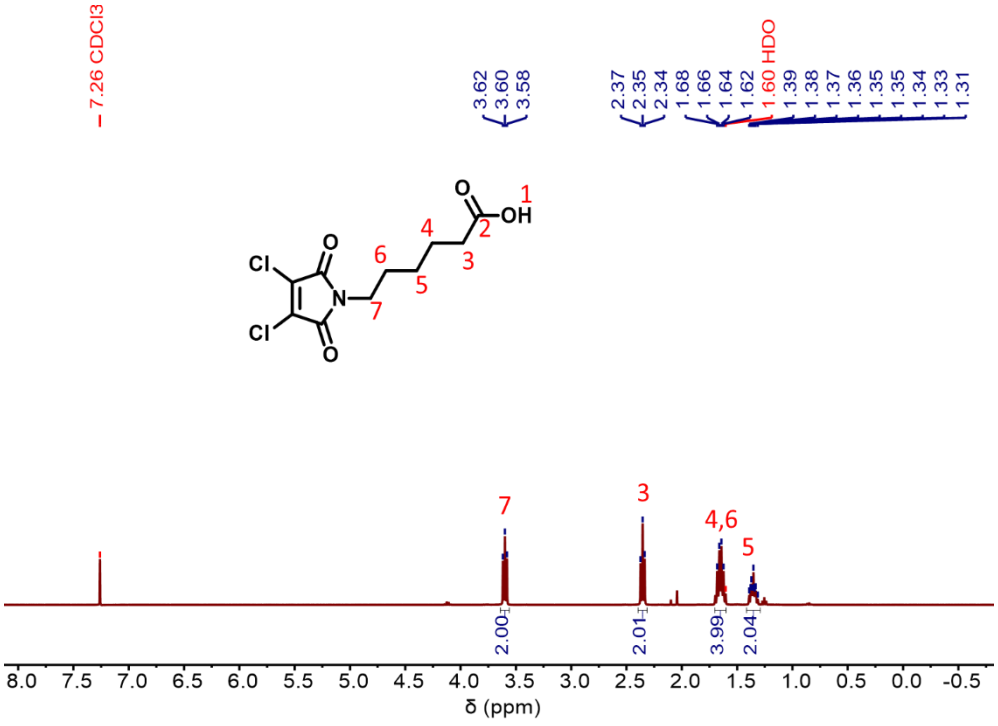

Fig. 4.24 ^{1}H NMR spectrum of **4.5** (400 MHz, $CDCl_3$).

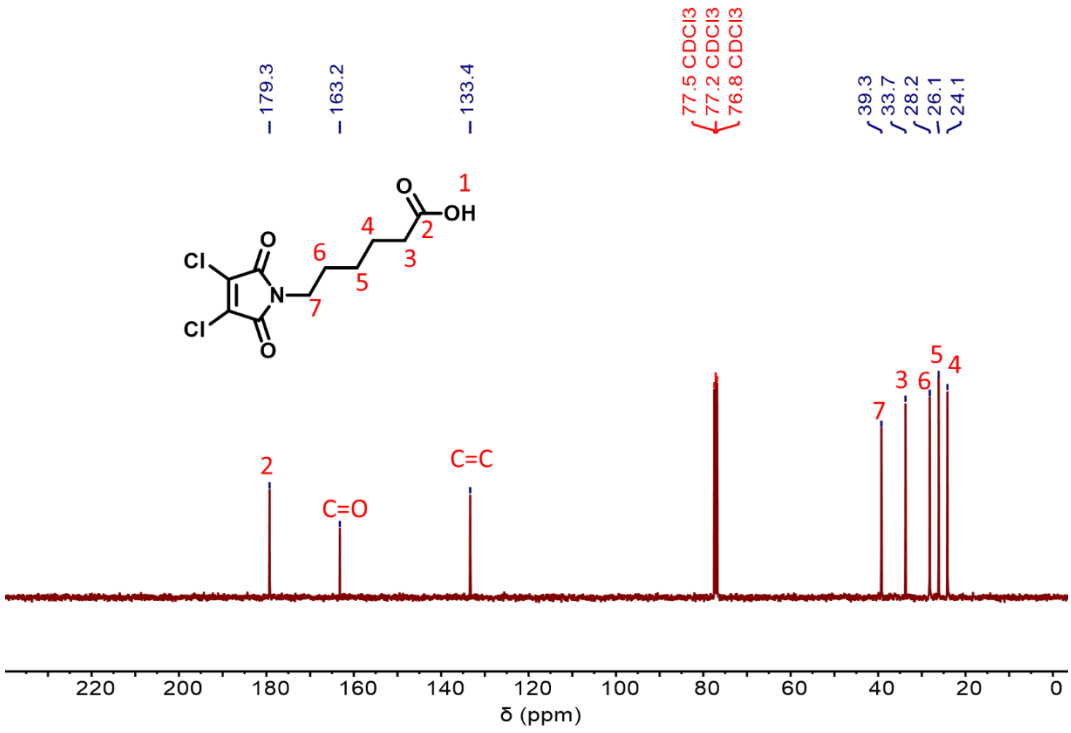

Fig. 4.25 ^{1}H NMR spectrum of **4.5** (400 MHz, $CDCl_3$).

4-(3-(butylamino)-4-chloro-2,5-dioxo-2,5-dihydro-1*H*-pyrrol-1-yl)butanoic acid (4.6)

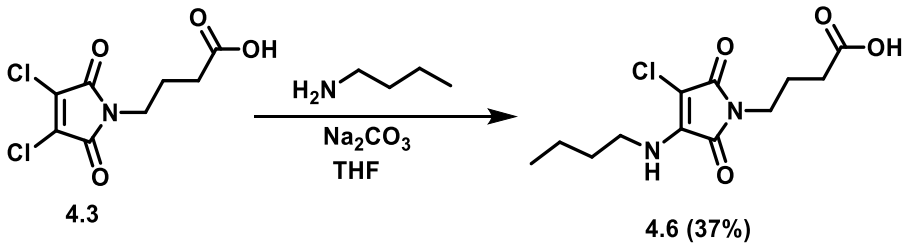

4.3 **4.6 (37%)**

Amine substitution of dichloromaleimide **4.3** was achieved following the already reported protocol.[45] 600 mg (2.4 mmol, 1.0 equiv.) of **4.3** was dissolved in 15 mL THF and mixed with 630 mg (6.0 mmol, 2.5 equiv.) of sodium carbonate, followed by the dropwise addition of 142 µL (2.68 mmol, 1.1 equiv.) *n*-butylamine at room temperature. The reaction progress was monitored by TLC and was completed within 30 min to 1 h.

The solvent was evaporated under reduced pressure and the residue was dissolved in 30 mL of CH_2Cl_2, washed with 3×30 mL of water, and dried over anhydrous magnesium sulfate. Purification *via* column chromatography on silica gel using hexane/ethyl acetate gave **4.6** as a yellow fluorescent solid.

R_f = 0.40 (hexane: ethyl acetate = 1:1); Yield = 260 mg, 37%.

^{1}H NMR (400 MHz, DMSO-d_6, 25℃, TMS) δ [ppm] = 12.14 (1H, s, H1), 7.97 (1H, s, H6), 3.53–3.44 (4H, t, H5,H7), 2.28–2.24 (2H, t, H3), 1.79–1.72 (2H, m, H4), 1.64–1.56 (2H, m, H8), 1.42–1.35 (2H, m, H9), 0.97–0.93 (3H, t, H10).

^{13}C NMR (101 MHz, DMSO-d_6, 25℃, TMS) δ [ppm] = 174.3 (C2), 167.9, 165.4 (C=O), 142.0 (C=C), 42.4 (C7), 37.5 (C5), 33.1 (C3), 31.3 (C8), 23.9 (C4), 19.6 (C9), 14.1 (C10).

FTIR (cm^{-1}): ν = 3319 (N-H), 3030 (O-H), 2924 (C-H), 1659 (C=O), 1519 (C=C), 1437 (O-H) bend, 1225 (C-O).

HR-MS (MaXis) $[M+H]^+$ - *m/z* found 289.7390; *m/z* calculated 289.7383.

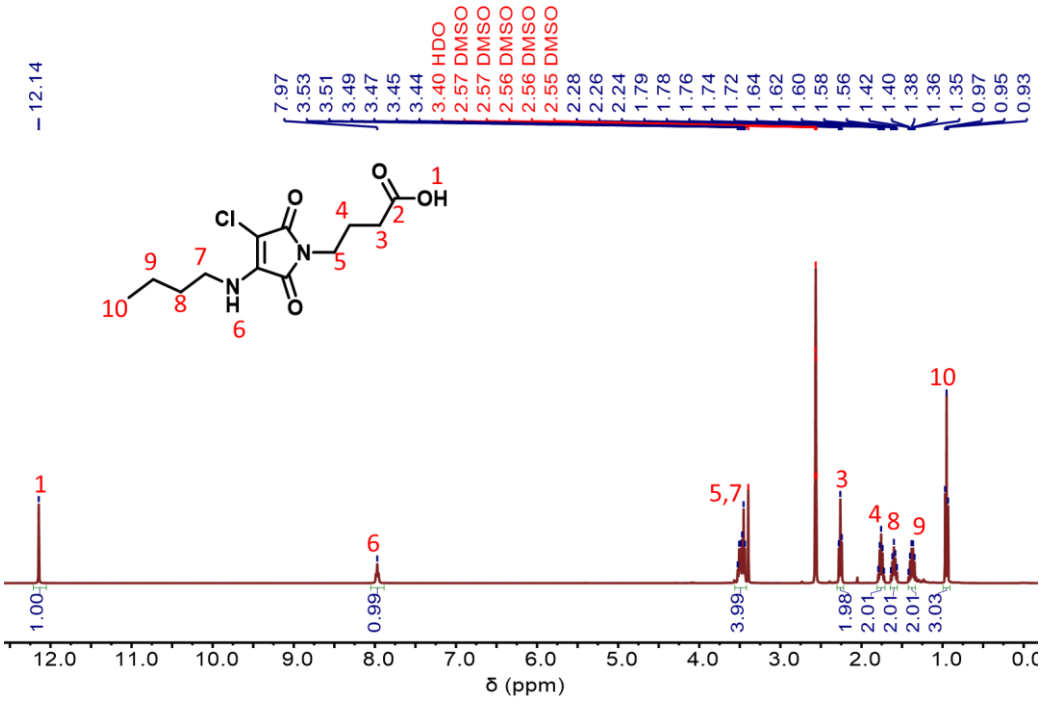

Fig. 4.26 ^{1}H NMR spectrum of **4.6** (400 MHz, DMSO-d$_6$).

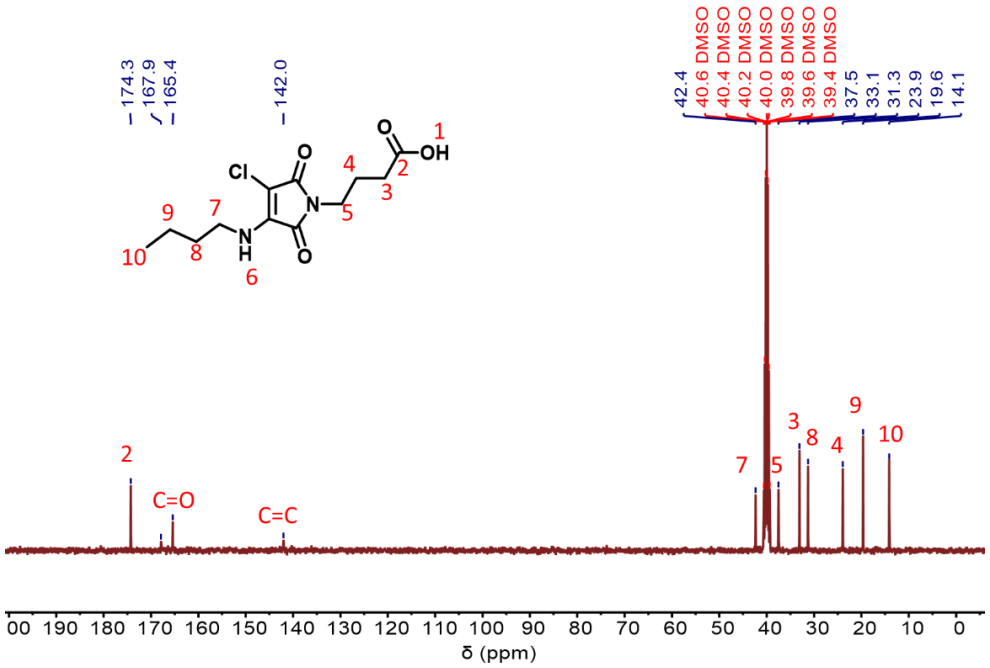

Fig. 4.27 ^{13}C NMR spectrum of **4.6** (101 MHz, DMSO-d_6).

1-butyl-3,4-dichloro-1*H*-pyrrole-2,5-dione (4.7)

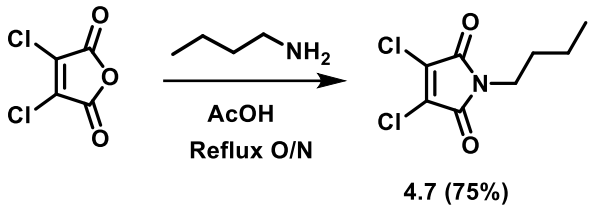

4.7 (75%)

Synthesis was carried out by following the already established protocol.[31] 1.0 g of 3,4-dichloromaleic anhydride (6.00 mmol, 1.0 equiv.) was dissolved in 20 mL of acetic acid, followed by the dropwise addition of 357 µL (7.00 mmol, 1.1 equiv.) of *n*-butylamine. The reaction mixture was refluxed overnight at 110℃. After cooling to the room temperature, the solvent was removed under reduced pressure and purified *via* column chromatography using hexane/ethyl acetate to obtain **4.7** as colorless powder.

R_f = 0.60 (hexane: ethyl acetate = 6:1); Yield = 998 mg, 75%.

^{1}H NMR (400 MHz, $CDCl_3$, 25℃, TMS) δ [ppm] = 3.61–3.58 (2H, s, H4), 1.63–1.55 (2H, m, H3), 1.36–1.27 (2H, m, H2), 0.95–0.91 (3H, t, H1).

^{13}C NMR (101 MHz, $CDCl_3$, 25℃, TMS) δ [ppm] = 162.9 (C=O), 133.0 (C=C), 39.0 (C4), 30.2 (C3), 19.7 (C2), 13.3 (C1).

ESI-MS (MaXis) $[M+H]^+$ - *m/z* found 223.09; *m/z* calculated 223.07.

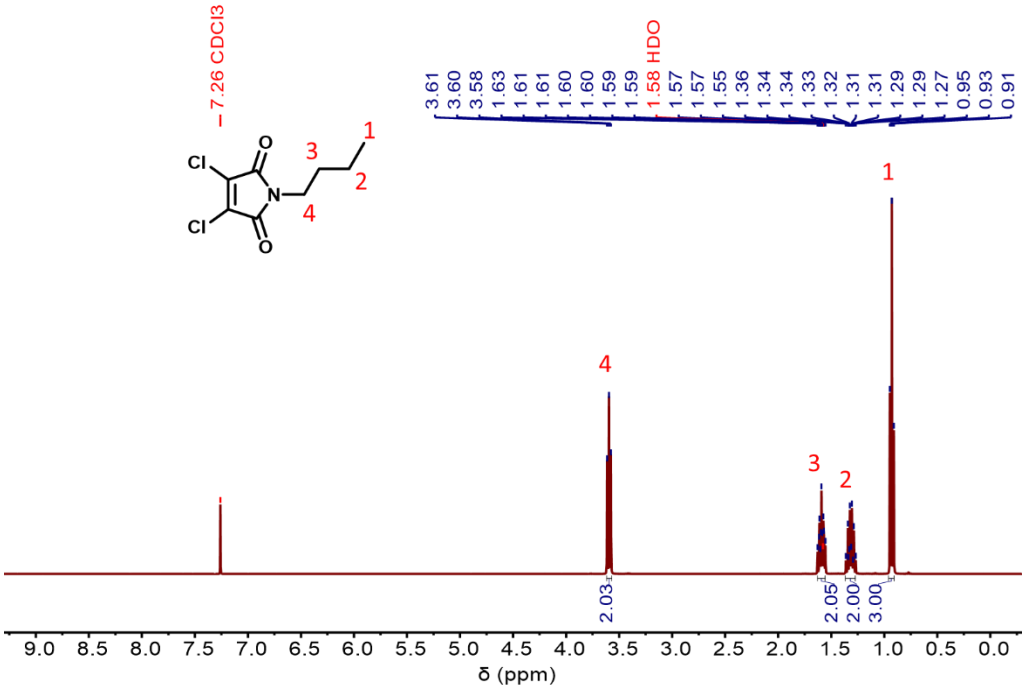

Fig. 4.28 ^{1}H NMR spectrum of **4.7** (400 MHz, $CDCl_3$).

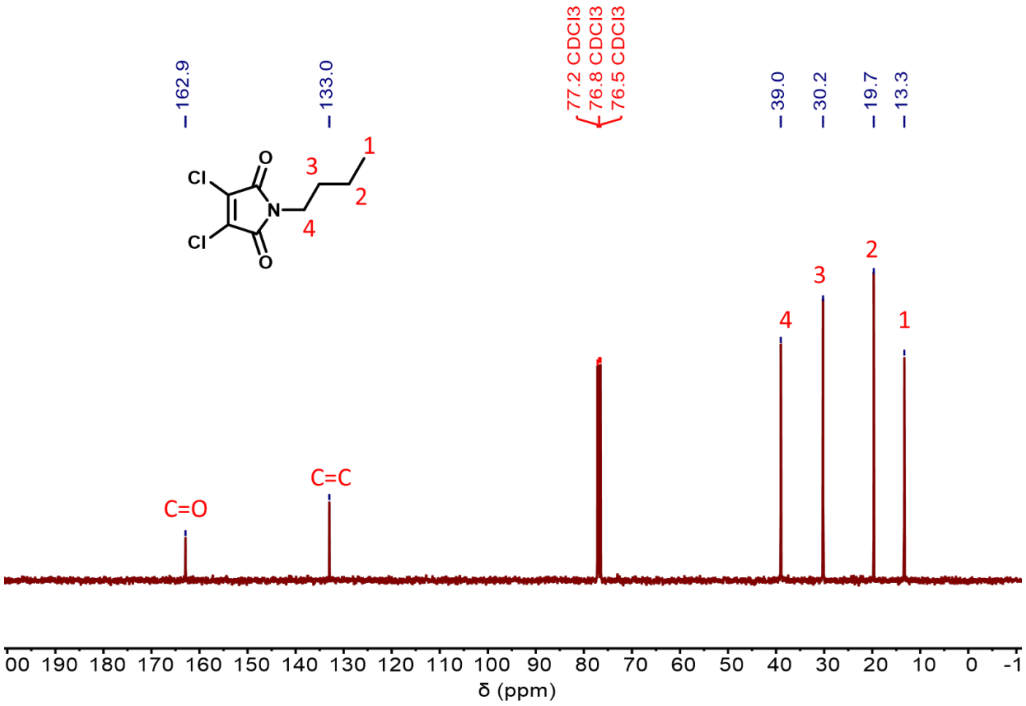

Fig. 4.29 ^{13}C NMR spectrum of **4.7** (101 MHz, $CDCl_3$).

4-((1-butyl-4-chloro-2,5-dioxo-2,5-dihydro-1*H*-pyrrol-3-yl)amino)butanoic acid (4.8)

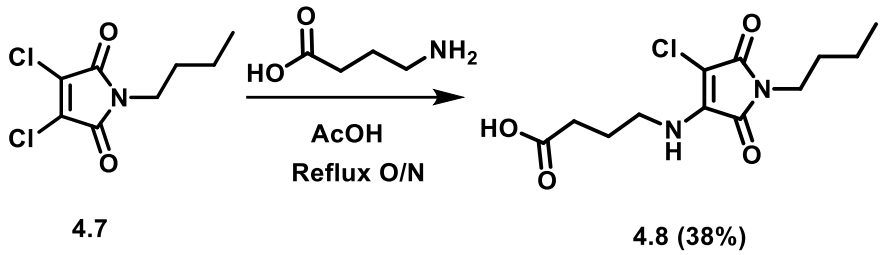

4.7 **4.8 (38%)**

Amine substitution of dichloromaleimide **4.7** was achieved following the already reported protocol.[45] 600 mg (2.7 mmol, 1.0 equiv.) of **4.7** was dissolved in 20 mL THF and mixed with 716 mg (7.0 mmol, 2.5 equiv.) of sodium carbonate, and 306 mg (2.97 mmol, 1.1 equiv.) of γ-aminobutyric acid at room temperature. The reaction progress was monitored by TLC and was complete within 30 min to 1 h. The solvent was evaporated under reduced pressure and the residue was dissolved in 30 mL of CH_2Cl_2, washed with 3×30 mL of water, and dried over anhydrous magnesium sulfate. Purification *via* column chromatography on silica gel using hexane/ethyl acetate gave **4.8** as a yellow fluorescent solid.

R_f = 0.42 (hexane: ethyl acetate = 1:1); Yield = 300 mg, 38%.

^{1}H NMR (400 MHz, DMSO-d_6, 25℃, TMS) δ [ppm] = 12.12 (1H, s, H10), 7.90 (1H, s, H5), 3.50–3.44 (2H, m, H4), 3.38–3.33 (2H, t, H6), 2.29–2.24 (2H, t, H8), 1.82–1.73 (2H, m, H7), 1.50–1.40 (2H, m, H3), 1.29–1.15 (2H, m, H2), 0.88–0.83 (3H, t, H1).

^{13}C NMR (101 MHz, DMSO-d_6, 25℃, TMS) δ [ppm] = 174.5 (C9), 167.9, 165.3 (C=O), 142.0 (C=C), 42.0 (C6), 37.7 (C4), 31.0 (C8), 30.6 (C3), 26.2 (C7), 19.8 (C2), 13.9 (C1).

FTIR (cm^{-1}): ν = 3339 (N-H), 3013 (O-H), 2915 (C-H), 1650 (C=O), 1526 (C=C), 1401 (O-H) bend, 1269 (C-O).

HR-MS (MaXis) $[M+H]^+$ - *m/z* found 289.7390; *m/z* calculated 289.7383.

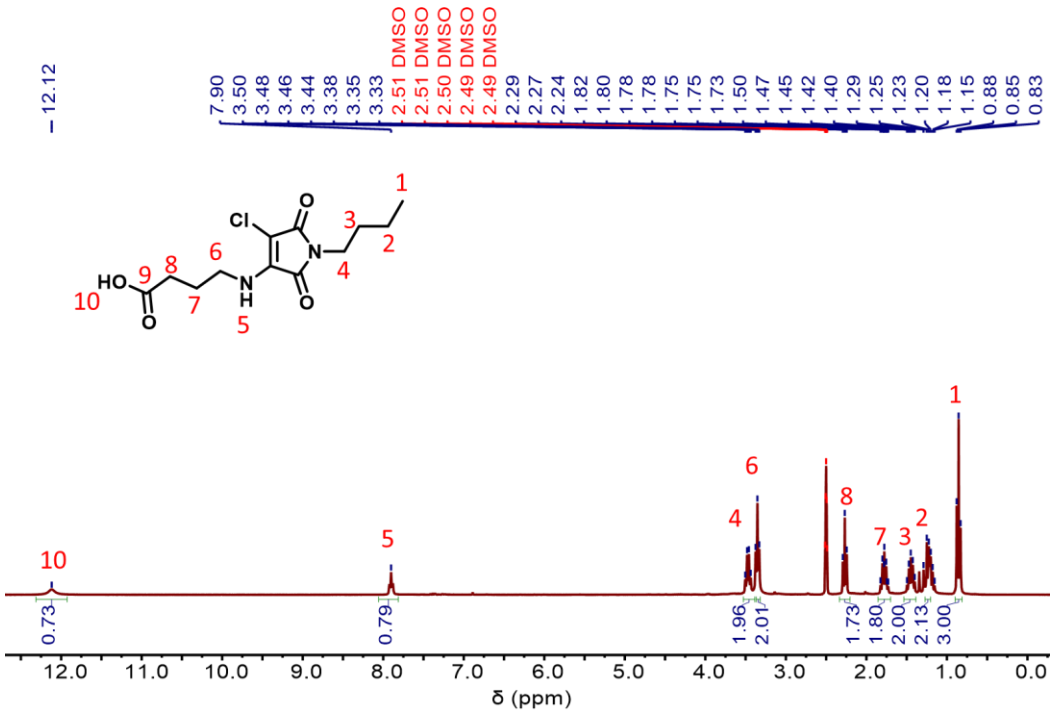

Fig. 4.30 ^{1}H NMR spectrum of **4.8** (400 MHz, DMSO-d_6).

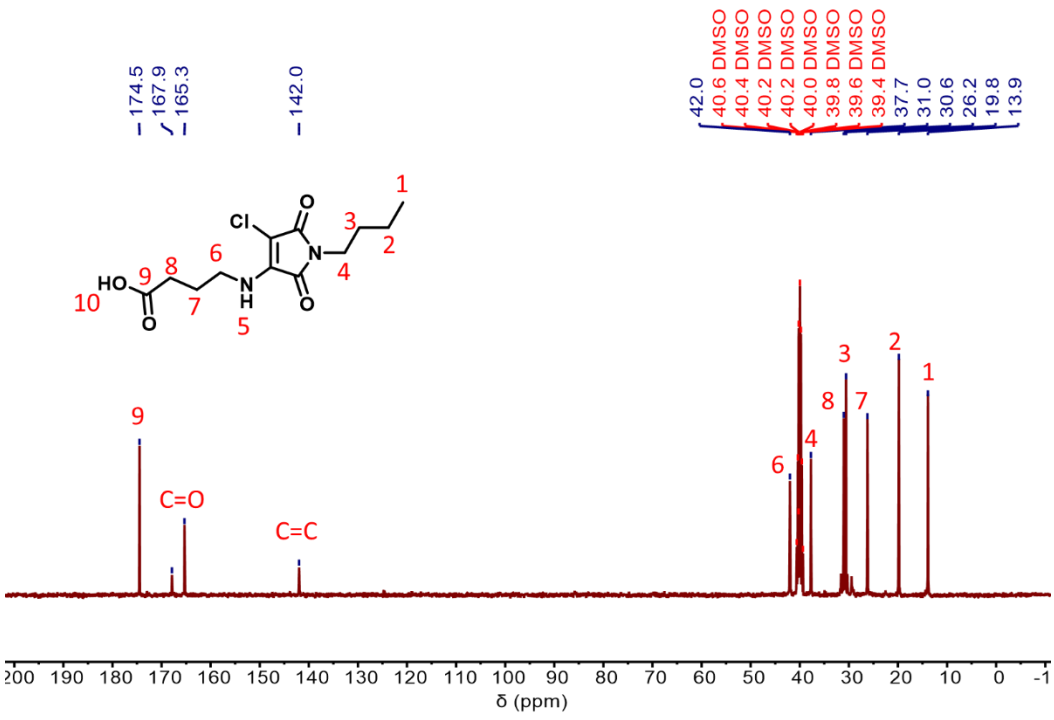

Fig. 4.31 ^{13}C NMR spectrum of **4.8** (101 MHz, DMSO-d_6).

4.5.3 Synthesis of lanthanide complexes

$Eu(C_6H_2Cl_2NO_4)_3.3H_2O$ (4.11)

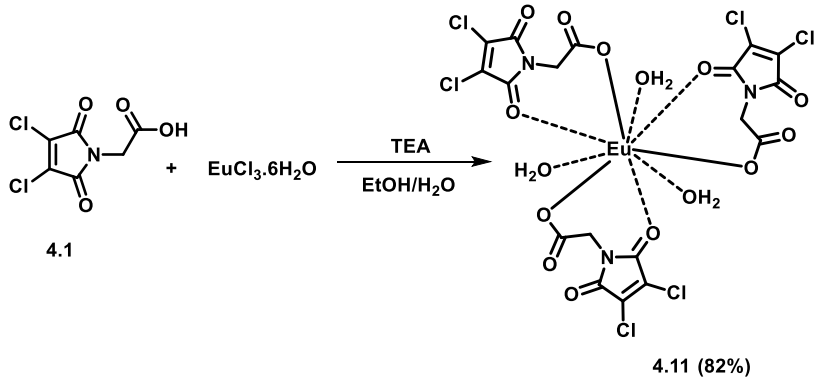

672 mg (3.0 mmol, 3.0 equiv.) of acid functionalized dichloromaleimide ligand (**4.1**) was dissolved in 5 mL of ethanol and 366 mg (1.0 mmol, 1.0 equiv.) of $EuCl_3.6H_2O$ was separately dissolved in 3 mL of ethanol. The europium(III) chloride solution was added to the ligand solution, followed by the dropwise addition of 73 µL of triethylamine (1.0 mmol, 1.0 equiv.) and the reaction mixture was stirred for 2 h at room temperature. The resulting precipitate of the complex was filtered, washed with ethanol and dichloromethane several times until the filtrate was clear. The resulting powder was dried under vacuum to yield the complex **4.11** as white powder.

Yield = 718 mg, 82%.

FTIR (cm^{-1}): ν = 3454 (H_2O-coordinated), 1723, 1632 (C=O), 1588 (C=C), 1420 (O-H) bend, 1388 (C-O).

Elemental analysis (%) for $C_{18}H_{12}EuCl_6N_3O_{15}$ – found: C 24.94, H 1.93, N 4.91. calculated: C 24.79, H 1.38, N 4.89.

$Eu(C_7H_4Cl_2NO_4)_3.3H_2O$ (4.12)

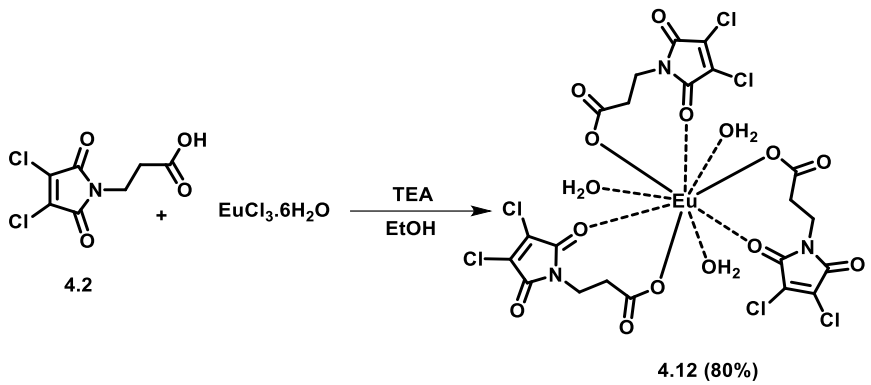

714 mg (3.0 mmol, 3.0 equiv.) of acid functionalized dichloromaleimide ligand (**4.2**) was dissolved in 5 mL of ethanol and 366 mg (1.0 mmol, 1.0 equiv.) of $EuCl_3.6H_2O$ was separately dissolved in 3 mL of ethanol. The europium(III) chloride solution was added to the ligand solution, followed by the dropwise addition of 73 µL of triethylamine (1.0 mmol, 1.0 equiv.) and the reaction mixture was stirred for 2 h at room temperature. The resulting precipitate of the complex was filtered, washed with ethanol and dichloromethane several times until the filtrate was clear. The resulting powder was dried under vacuum to yield the complex **4.12** as white powder.

Yield = 734 mg, 80%.

FTIR (cm^{-1}): ν = 3420 (H_2O-coordinated), 1727, 1630 (C=O), 1565 (C=C), 1446 (O-H) bend, 1393 (C-O).

Elemental analysis (%) for $C_{21}H_{18}EuCl_6N_3O_{15}$ – found: C 27.83, H 2.01, N 4.90. calculated: C 27.53, H 1.99, N 4.59.

$Eu(C_8H_6Cl_2NO_4)_3.3H_2O$ (4.13)

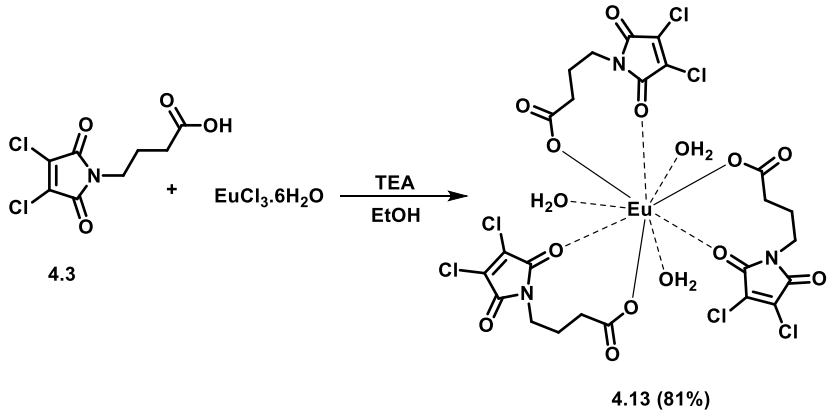

756 mg (3.0 mmol, 3.0 equiv.) of acid functionalized dichloromaleimide ligand (**4.3**) and 73 µL of triethylamine (1.0 mmol, 1.0 equiv.) were dissolved in 5 mL of ethanol. 366 mg (1.0 mmol, 1.0 equiv.) of $EuCl_3.6H_2O$ was separately dissolved in 3 mL of ethanol. The europium(III) chloride solution was dropwise added to the ligand solution under magnetic stirring for 2 h at room temperature. The resulting precipitate of the complex was filtered, washed with ethanol and dichloromethane several times until the filtrate was clear. The resulting powder was dried under vacuum to yield the complex **4.13** as white powder.

Yield = 778 mg, 81%.

FTIR (cm^{-1}): ν = 3536 (H_2O-coordinated), 2938 (C-H), 1729, 1626 (C=O), 1583 (C=C), 1544 (O-H) bend, 1398 (C-O).

Elemental analysis (%) for $C_{24}H_{24}EuCl_6N_3O_{15}$ – found: C 30.10, H 2.49, N 4.35. calculated: C 30.05, H 2.52, N 4.38.

HR-MS (MaXis) $[M+H]^+$ - *m/z* found 959.9952; *m/z* calculated 959.9930.

$Eu(C_9H_8Cl_2NO_4)_3.3H_2O$ (4.14)

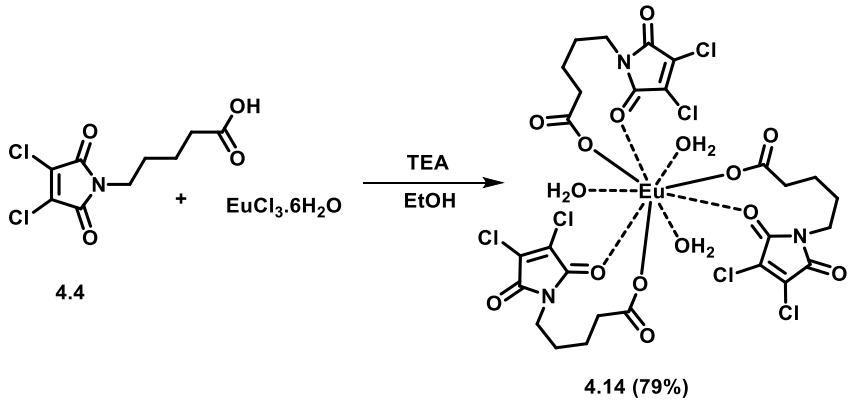

798 mg (3.0 mmol, 3.0 equiv.) of acid functionalized dichloromaleimide ligand (**4.4**) and 73 µL of triethylamine (1.0 mmol, 1.0 equiv.) were dissolved in 5 mL of ethanol. 366 mg (1.0 mmol, 1.0 equiv.) of $EuCl_3.6H_2O$ was separately dissolved in 3 mL of ethanol. The europium(III) chloride solution was dropwise added to the ligand solution under magnetic stirring for 2 h at room temperature. The resulting precipitate of the complex was filtered, washed with ethanol and dichloromethane several times until the filtrate was clear. The resulting powder was dried under vacuum to yield the complex **4.14** as white powder.

Yield = 791 mg, 79%.

FTIR (cm^{-1}): ν = 3473 (H_2O-coordinated), 2942 (C-H), 1713, 1623 (C=O), 1627 (C=C), 1535 (O-H) bend, 1395 (C-O).

Elemental analysis (%) for $C_{27}H_{30}EuCl_6N_3O_{15}$ – found: C 32.30, H 2.93, N 4.29. calculated: C 32.38, H 3.03, N 4.20.

$Eu(C_{10}H_{10}Cl_2NO_4)_3.3H_2O$ (4.15)

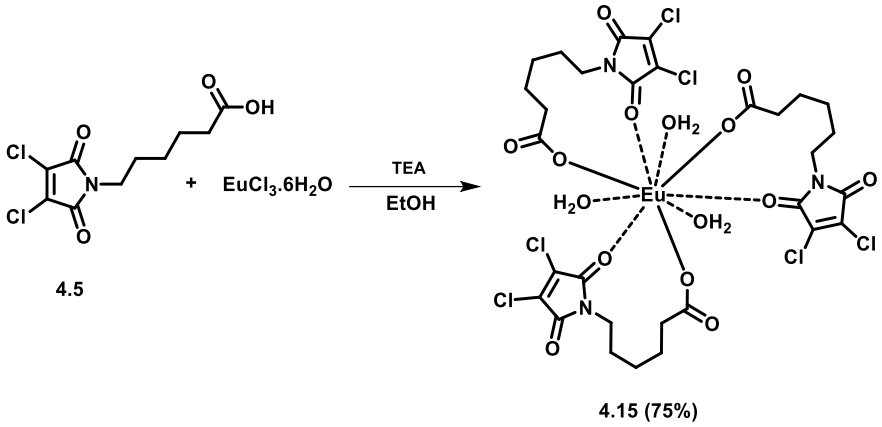

756 mg (3.0 mmol, 3.0 equiv.) of acid functionalized dichloromaleimide ligand (**4.5**) and 73 µL of triethylamine (1.0 mmol, 1.0 equiv.) were dissolved in 5 mL of ethanol. 366 mg (1.0 mmol, 1.0 equiv.) of $EuCl_3.6H_2O$ was separately dissolved in 3 mL of ethanol. The europium(III) chloride solution was dropwise added to the ligand solution under magnetic stirring for 2 h at room temperature. The resulting precipitate of the complex was filtered, washed with ethanol and dichloromethane several times until the filtrate was clear. The resulting powder was dried under vacuum to yield the complex **4.15** as white powder.

Yield = 783 mg, 75%.

FTIR (cm^{-1}): ν = 3489 (H_2O-coordinated), 2861 (C-H), 1708, 1670 (C=O), 1621 (C=C), 1403 (O-H) bend, 1245 (C-O).

Elemental analysis (%) for $C_{30}H_{36}EuCl_6N_3O_{15}$ – found: C 34.56, H 3.38, N 4.09. calculated: C 34.53, H 3.48, N 4.03.

$Eu(C_{12}H_{16}ClN_2O_4)_3.3H_2O$ (4.16)

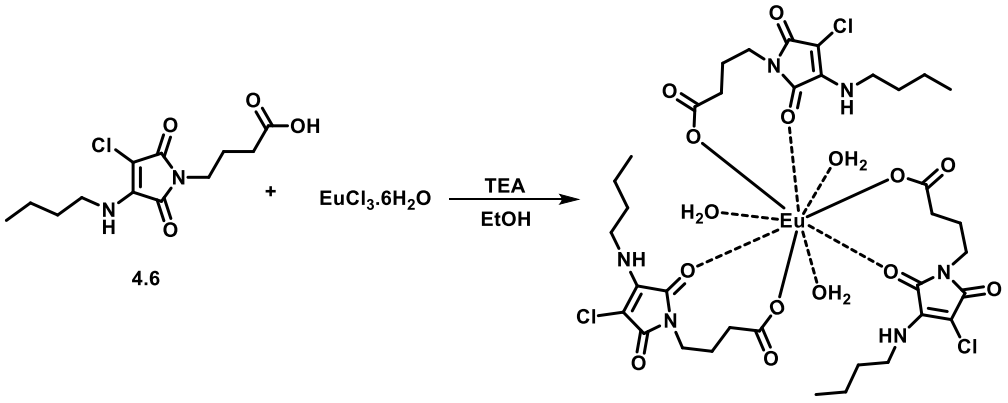

866 mg (3.0 mmol, 3.0 equiv.) of acid functionalized aminochloromaleimide ligand (**4.6**) and 73 µL of triethylamine (1.0 mmol, 1.0 equiv.) were dissolved in 5 mL of ethanol. 366 mg (1.0 mmol, 1.0 equiv.) of $EuCl_3.6H_2O$ was separately dissolved in 3 mL of ethanol. The europium(III) chloride solution was dropwise added to the ligand solution under magnetic stirring for 2 h at room temperature. The resulting precipitate of the complex was filtered, washed with ethanol and dichloromethane several times until filtrate was clear and non-fluorescent. The resulting powder was dried under vacuum to yield complex **4.16** as yellow solid.

Yield = 855 mg, 80%.

FTIR (cm^{-1}): ν = 3313 (N-H/H_2O-coordinated), 2915 (C-H), 1702 (C=O), 1640 (C=C), 1508 (O-H) bend, 1401 (C-O).

Elemental analysis (%) for $C_{36}H_{54}EuClN_6O_{15}$ – found: C 40.44, H 5.06, N 7.84.

calculated: C 40.47, H 5.09, N 7.86.

$Eu(C_{12}H_{16}ClN_2O_4)_3.3H_2O$ (4.17)

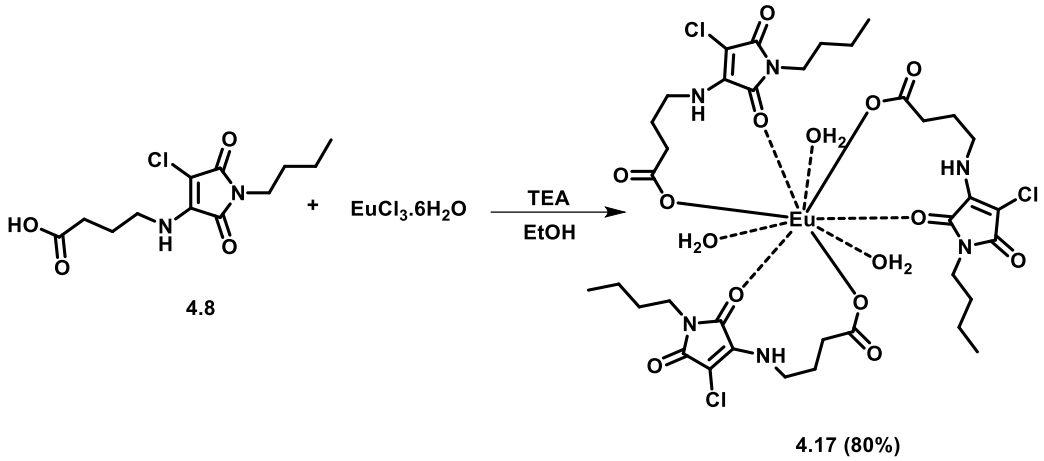

866 mg (3.0 mmol, 3.0 equiv.) of acid functionalized aminochloromaleimide ligand (**4.8**) and 73 µL of triethylamine (1.0 mmol, 1.0 equiv.) were dissolved in 5 mL of ethanol. 366 mg (1.0 mmol, 1.0 equiv.) of $EuCl_3.6H_2O$ was separately dissolved in 3 mL of ethanol. The europium(III) chloride solution was dropwise added to the ligand solution under magnetic stirring for 2 h at room temperature. The resulting precipitate of the complex was filtered, washed with ethanol and dichloromethane several times until filtrate was clear and non-fluorescent. The resulting powder was dried under vacuum to yield complex **4.17** as yellow solid.

Yield = 850 mg, 80%.

FTIR (cm^{-1}): ν = 3322 (N-H/H_2O-coordinated), 2932 (C-H), 1712 (C=O), 1659 (C=C), 1552 (O-H) bend, 1401 (C-O).

Elemental analysis (%) for $C_{36}H_{54}EuClN_6O_{15}$ – found: C 40.43, H 5.06, N 7,85. calculated: C 40.47, H 5.09, N 7.87.

$Tb(C_{12}H_{16}ClN_2O_4)_3.3H_2O$ (4.18)

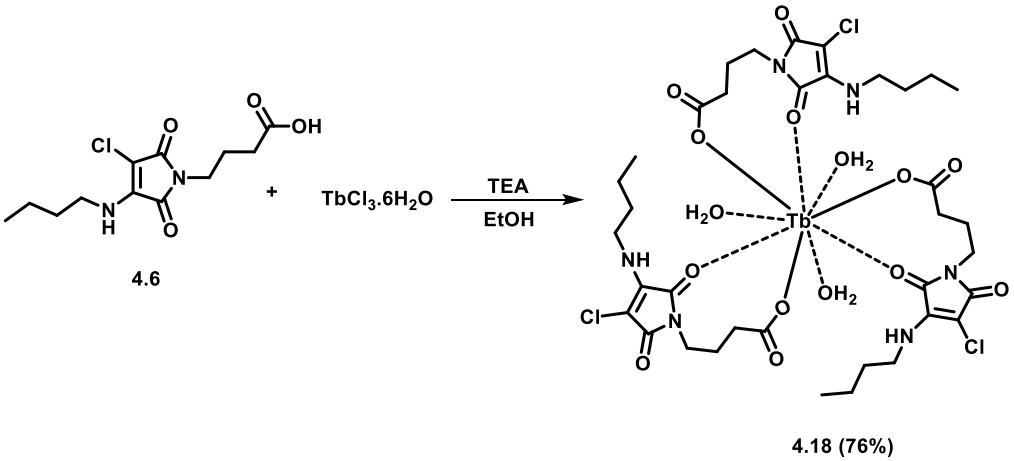

866 mg (3.0 mmol, 3.0 equiv.) of acid functionalized aminochloromaleimide ligand (**4.6**) and 73 µL of triethylamine (1.0 mmol, 1.0 equiv.) were dissolved in 5 mL of ethanol. 373 mg (1.0 mmol, 1.0 equiv.) of $TbCl_3.6H_2O$ was separately dissolved in 3 mL of ethanol. The terbium(III) chloride solution was dropwise added to the ligand solution under magnetic stirring for 2 h at room temperature. The resulting precipitate of the complex was filtered, washed with ethanol and dichloromethane several times until filtrate was clear and non-fluorescent. The resulting powder was dried under vacuum to yield complex **4.18** as yellow solid.

Yield = 817 mg, 76%.

FTIR (cm^{-1}): ν = 3309 (N-H/H_2O-coordinated), 2932 (C-H), 1702 (C=O), 1632 (C=C), 1512 (O-H) bend, 1401 (C-O).

Elemental analysis (%) for $C_{36}H_{54}TbClN_6O_{15}$ – found: C 40.24, H 5.04, N 7.84. calculated: C 40.21, H 5.06, N 7.82.

$Tb(C_{12}H_{16}ClN_2O_4)_3.3H_2O$ (4.19)

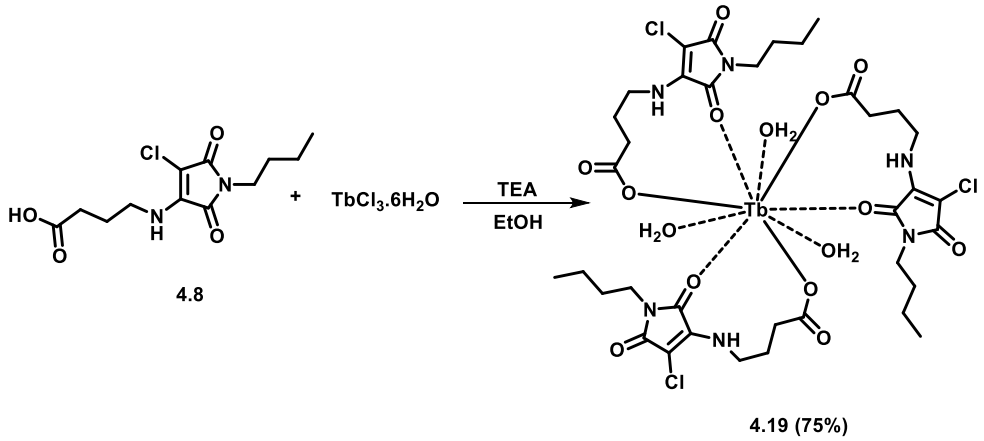

866 mg (3.0 mmol, 3.0 equiv.) of acid functionalized aminochloromaleimide ligand (**4.8**) and 73 µL of triethylamine (1.0 mmol, 1.0 equiv.) were dissolved in 5 mL of ethanol. 373 mg (1.0 mmol, 1.0 equiv.) of $TbCl_3.6H_2O$ was separately dissolved in 3 mL of ethanol. The terbium(III) chloride solution was dropwise added to the ligand solution under magnetic stirring for 2 h at room temperature. The resulting precipitate of the complex was filtered, washed with ethanol and dichloromethane several times until filtrate was clear and non-fluorescent. The resulting powder was dried under vacuum to yield complex **4.19** as yellow solid.

Yield = 806 mg, 75%.

FTIR (cm^{-1}): ν = 3322 (N-H/H_2O-coordinated), 2925 (C-H), 1712 (C=O), 1650 (C=C), 1498 (O-H) bend, 1401 (C-O).

Elemental analysis (%) for $C_{36}H_{54}TbClN_6O_{15}$ – found: C 40.23, H 5.05, N 7,85. calculated: C 40.21, H 5.06, N 7.82.

4.5.4 TGA plots of the synthesized complexes

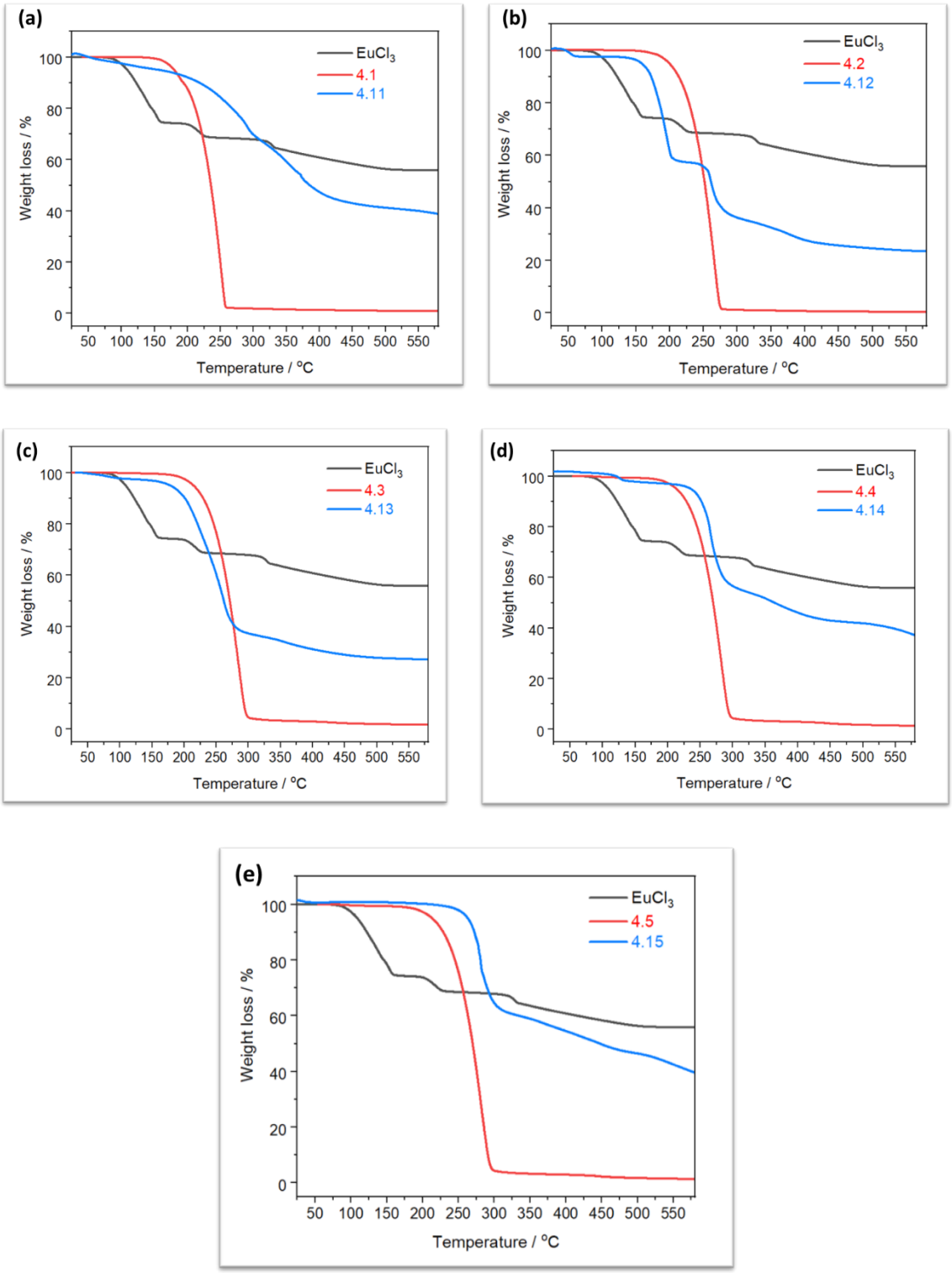

Fig. 4.32 TGA plots of the dichloromaleimide ligands **4.1**–**4.5** and their europium(III) complexes **4.11**–**4.15**.

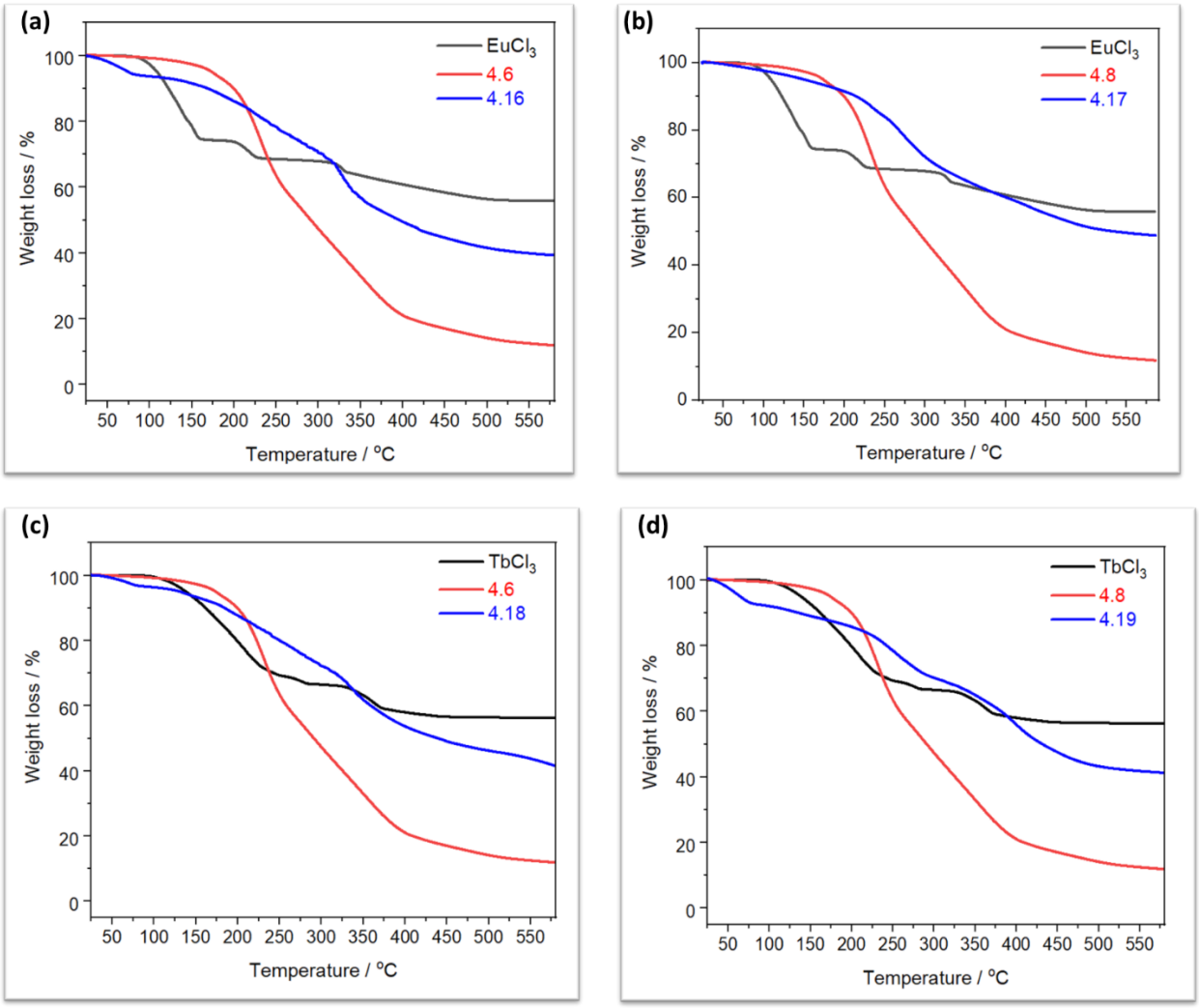

Fig. 4.33 TGA plots of the aminochloromaleimide ligands **4.6** and **4.8**, and their europium(III) complexes **4.16** and **4.17**, and terbium(III) complexes **4.18** and **4.19**.

4.5.5 Fluorescence emission spectra of the synthesized complexes

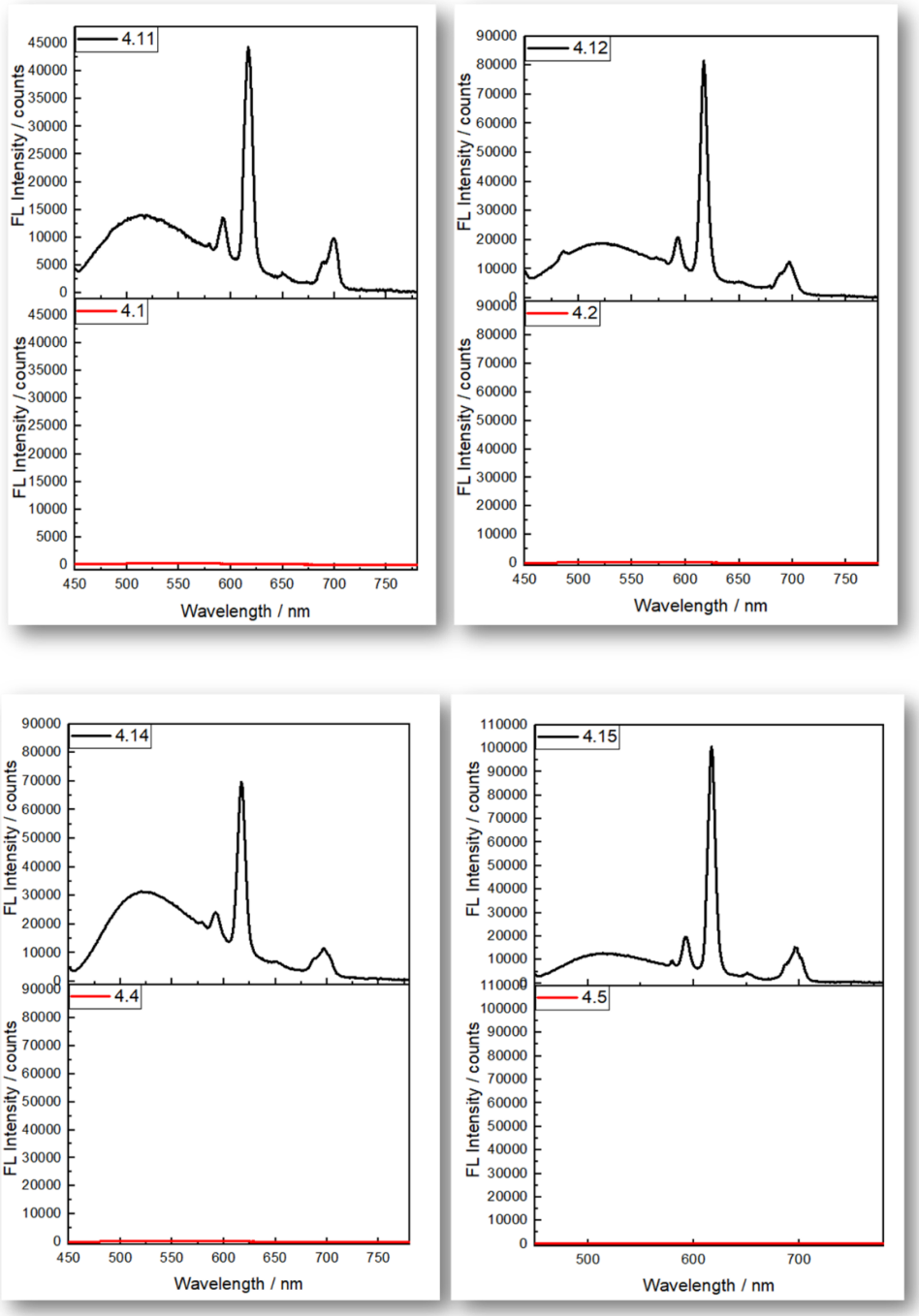

Fig. 4.34 Solution-state fluorescence emission spectra of the ligands **4.1**–**4.5** and their europium complexes **4.11**–**4.15**.

4.6 References

1. Bünzli, J.-C. G., Lanthanide Luminescence for Biomedical Analyses and Imaging. *Chem. Rev.* **2010,** *110* (5), 2729-2755.

2. Cable, M. L.; Levine, D. J.; Kirby, J. P.; Gray, H. B.; Ponce, A., *Luminescent lanthanide sensors*. Academic Press: **2011**; Vol. 63, p 1-45.

3. Li, M.; Wang, C.; Wang, D.; Li, J., Structure-Dependent Photoluminescence of Europium(III) Coordination Oligomeric Silsesquioxane: Synthesis and Mechanism. *ACS Omega* **2021,** *6* (1), 227-238.

4. Hasegawa, Y.; Wada, Y.; Yanagida, S., Strategies for the design of luminescent lanthanide(III) complexes and their photonic applications. *J. Photochem. Photobiol. C: Photochem. Rev.* **2004,** *5* (3), 183-202.

5. Dieke, G. H.; Crosswhite, H. M., The Spectra of the Doubly and Triply Ionized Rare Earths. *App. Opt.* **1963,** *2* (7), 675-686.

6. Roques, N.; Perruchas, S.; Maspoch, D.; Datcu, A.; Wurst, K.; Sutter, J.-P.; Rovira, C.; Veciana, J., Europium (III) complexes derived from carboxylic-substituted polychlorotriphenylmethyl radicals. *Inorganica Chim. Acta* **2007,** *360* (13), 3861-3869.

7. Hasegawa, M.; Ohmagari, H.; Tanaka, H.; Machida, K., Luminescence of lanthanide complexes: From fundamental to prospective approaches related to water- and molecular-stimuli. *J. Photochem. Photobiol. C: Photochem. Rev.* **2022,** *50*, 100484.

8. SeethaLekshmi, S.; Ramya, A. R.; Reddy, M. L. P.; Varughese, S., Lanthanide complex-derived white-light emitting solids: A survey on design strategies. *J. Photochem. Photobiol C: Photochem. Rev.* **2017,** *33*, 109-131.

9. Xiao, X.; Tian, W.; Imran, M.; Cao, H.; Zhao, J., Controlling the triplet states and their application in external stimuli-responsive triplet–triplet-annihilation photon upconversion: from the perspective of excited state photochemistry. *Chem. Soc. Rev.* **2021,** *50* (17), 9686-9714.

10. Pei, S.; Ge, X.; Sun, L., Metal Ions Doping for Boosting Luminescence of Lanthanide-Doped Nanocrystals. *Front. Chem.* **2020,** *8*, 610481-610481.

11. Hasegawa, Y.; Kitagawa, Y.; Nakanishi, T., Effective photosensitized, electrosensitized, and mechanosensitized luminescence of lanthanide complexes. *NPG Asia Mater.* **2018,** *10* (4), 52-70.

12. Susumu, S.; Masanobu, W., Relations between Intramolecular Energy Transfer Efficiencies and Triplet State Energies in Rare Earth β-diketone Chelates. *Bull. Chem. Soc. Jpn.* **1970,** *43* (7), 1955-1962.

13. Shavaleev, N. M.; Eliseeva, S. V.; Scopelliti, R.; Bünzli, J.-C. G., *N*-Aryl Chromophore Ligands for Bright Europium Luminescence. *Inorg. Chem.* **2010,** *49* (8), 3927-3936.

14. Latva, M.; Takalo, H.; Mukkala, V.-M.; Matachescu, C.; Rodríguez-Ubis, J. C.; Kankare, J., Correlation between the lowest triplet state energy level of the ligand and lanthanide(III) luminescence quantum yield. *J. Lumin.* **1997,** *75* (2), 149-169.

15. Samuel, A. P. S.; Xu, J.; Raymond, K. N., Predicting Efficient Antenna Ligands for Tb(III) Emission. *Inorg. Chem.* **2009,** *48* (2), 687-698.

16. Kitagawa, Y.; Ohno, R.; Nakanishi, T.; Fushimi, K.; Hasegawa, Y., Visible luminescent lanthanide ions and a large π-conjugated ligand system shake hands. *Phys. Chem. Chem. Phys.* **2016,** *18* (45), 31012-31016.

17. Kitagawa, Y.; Ohno, R.; Nakanishi, T.; Fushimi, K.; Hasegawa, Y., Solvent-dependent dual-luminescence properties of a europium complex with helical π-conjugated ligands. *Photochem. Photobiol. Sci.* **2017,** *16* (5), 683-689.

18. Zhang, B.; Xiao, T.; Liu, C.; Li, Q.; Zhu, Y.; Tang, M.; Du, C.; Song, M., Systematic Study of the Luminescent Europium-Based Nonanuclear Clusters with Modified 2-Hydroxybenzophenone Ligands. *Inorg. Chem.* **2013,** *52* (23), 13332-13340.

19. Omagari, S.; Nakanishi, T.; Seki, T.; Kitagawa, Y.; Takahata, Y.; Fushimi, K.; Ito, H.; Hasegawa, Y., Effective Photosensitized Energy Transfer of Nonanuclear Terbium Clusters Using Methyl Salicylate Derivatives. *J. Phys. Chem. A* **2015,** *119* (10), 1943-1947.

20. D'Aléo, A.; Picot, A.; Beeby, A.; Gareth Williams, J. A.; Le Guennic, B.; Andraud, C.; Maury, O., Efficient Sensitization of Europium, Ytterbium, and Neodymium Functionalized Tris-Dipicolinate Lanthanide Complexes through Tunable Charge-Transfer Excited States. *Inorg. Chem.* **2008,** *47* (22), 10258-10268.

21. Shavaleev, N. M.; Scopelliti, R.; Gumy, F.; Bünzli, J.-C. G., Visible-Light Excitation of Infrared Lanthanide Luminescence via Intra-Ligand Charge-Transfer State in 1,3-Diketonates Containing Push-Pull Chromophores. *Eur. J. Inorg. Chem.* **2008,** *2008* (9), 1523-1529.

22. Eliseeva, S. V.; Kotova, O. V.; Gumy, F.; Semenov, S. N.; Kessler, V. G.; Lepnev, L. S.; Bünzli, J.-C. G.; Kuzmina, N. P., Role of the Ancillary Ligand *N*,*N*-Dimethylaminoethanol in the Sensitization of EuIII and TbIII Luminescence in Dimeric β-Diketonates. *J. Phys. Chem. A* **2008,** *112* (16), 3614-3626.

23. Hasegawa, Y.; Tateno, S.; Yamamoto, M.; Nakanishi, T.; Kitagawa, Y.; Seki, T.; Ito, H.; Fushimi, K., Effective Photo- and Triboluminescent Europium(III)

Coordination Polymers with Rigid Triangular Spacer Ligands. *Chem. Eur. J.* **2017,** *23* (11), 2666-2672.

24. Hirai, Y.; Nakanishi, T.; Kitagawa, Y.; Fushimi, K.; Seki, T.; Ito, H.; Hasegawa, Y., Luminescent Europium(III) Coordination Zippers Linked with Thiophene-Based Bridges. *Angew. Chem. Int. Ed.* **2016,** *55* (39), 12059-12062.

25. Xie, Y.; Husband, J. T.; Torrent-Sucarrat, M.; Yang, H.; Liu, W.; O'Reilly, R. K., Rational design of substituted maleimide dyes with tunable fluorescence and solvafluorochromism. *Chem. Commun.* **2018,** *54* (27), 3339-3342.

26. Lehn, J.-M., Perspectives in Supramolecular Chemistry—From Molecular Recognition towards Molecular Information Processing and Self-Organization. *Angew. Chem. Int. Ed. Engl.* **1990,** *29* (11), 1304-1319.

27. Shavaleev, N. M.; Eliseeva, S. V.; Scopelliti, R.; Bünzli, J.-C. G., Influence of Symmetry on the Luminescence and Radiative Lifetime of Nine-Coordinate Europium Complexes. *Inorg. Chem.* **2015,** *54* (18), 9166-9173.

28. Stan, C. S.; Popa, M.; Marcotte, N., Photoluminescent Polymer Composites Based on New Tb(III) and Eu(III): Maleimide Complexes. *J. Inorg. Organomet. Polym.* **2014,** *24* (4), 676-683.

29. Würth, C.; Grabolle, M.; Pauli, J.; Spieles, M.; Resch-Genger, U., Relative and absolute determination of fluorescence quantum yields of transparent samples. *Nat. Protoc.* **2013,** *8* (8), 1535-1550.

30. Brunet, E.; Juanes, O.; Rodriguez-Ubis, C. J., Supramolecularly Organized Lanthanide Complexes for Efficient Metal Excitation and Luminescence as Sensors in Organic and Biological Applications. *Curr. Chem. Biol.* **2007,** *1* (1), 11-39.

31. Nirogi, R.; Dwarampudi, A.; Kambhampati, R.; Bhatta, V.; Kota, L.; Shinde, A.; Badange, R.; Jayarajan, P.; Bhyrapuneni, G.; Dubey, P. K., Rigidized 1-aryl sulfonyl tryptamines: synthesis and pharmacological evaluation as 5-HT6 receptor ligands. *Bioorg. Med. Chem. Lett.* **2011,** *21* (15), 4577-80.

32. Siaugue, J.-M.; Favre-Réguillon, A.; Dioury, F.; Plancque, G.; Foos, J.; Madic, C.; Moulin, C.; Guy, A., Effect of Mixed Pendant Groups on the Solution Properties of 12-Membered Azapyridinomacrocycles: Evaluation of the Protonation Constants and the Stability Constants of the Europium(III) Complexes. *Eur. J. Inorg. Chem.* **2003,** *2003* (15), 2834-2838.

33. Féau, C.; Klein, E.; Dosche, C.; Kerth, P.; Lebeau, L., Synthesis and characterization of coumarin-based europium complexes and luminescence measurements in aqueous media. *Org. Biomol. Chem.* **2009,** *7* (24), 5259-5270.

34. Brzyska, W.; Ożga, W., Thermal decomposition of yttrium and lanthanide complexes with mephenamic acid. *Thermochim. Acta* **1992,** *195*, 149-155.

35. Alghool, S.; Zoromba, M. S.; El-Halim, H. F. A., Lanthanide amino acid Schiff base complexes: synthesis, spectroscopic characterization, physical properties and in vitro antimicrobial studies. *J. Rare Earths* **2013,** *31* (7), 715-721.

36. Mohanan, K.; Thankamony, M.; Kumari, B. S., Synthesis, spectroscopic characterization, and thermal decomposition kinetics of some lanthanide(III) nitrate complexes of 2-(*N*-*o*-hydroxyacetophenone)amino-3-carboxyethyl-4,5,6,7-tetrahydrobenzo[b]thiophene. *J. Rare Earths* **2008,** *26* (4), 463-468.

37. Brubach, J.-B.; Mermet, A.; Filabozzi, A.; Gerschel, A.; Roy, P., Signatures of the hydrogen bonding in the infrared bands of water. *J. Chem. Phys.* **2005,** *122*, 184509.

38. Chiba, K.; Hashimoto, Y.; Yamaguchi, T., Dichloromaleimide (diCMI): A Small and Fluorogenic Reactive Group for Use in Affinity Labeling. *Chem. Pharm. Bull.* **2016,** *64* (11), 1647-1653.

39. Zhang, X.; Zhang, Y.; Yang, L.; Yang, R.; Jin, D., Synthesis and Characterization of Glycine Schiff Base Complexes of the Light Lanthanide Elements. *Synth. React. Inorg. Met. Org. Chem.* **2000,** *30* (1), 45-55.

40. Räsänen, M.; Takalo, H.; Rosenberg, J.; Mäkelä, J.; Haapakka, K.; Kankare, J., Study on photophysical properties of Eu(III) complexes with aromatic β-diketones – Role of charge transfer states in the energy migration. *J. Lumin.* **2014,** *146*, 211-217.

41. Grasso, A. N.; Teixeira Ldos, S.; Vieira, N. D., Jr.; Courrol, L. C., Optical properties of metacycline, oxytetracycline and chlortetracycline europium complexes in the presence of hydrogen peroxide. *J. Fluoresc.* **2009,** *19* (4), 715-21.

42. Liao, J.; Qiu, B.; Wen, H.-R.; Li, Y.; Hong, R.; You, H., Luminescence properties of monodispersed spherical $BaWO_4$:Eu^{3+} microphosphors for white light-emitting diodes. *J. Mater. Sci.* **2011,** *46* (5), 1184-1189.

43. de Mello, J. C.; Wittmann, H. F.; Friend, R. H., An improved experimental determination of external photoluminescence quantum efficiency. *Adv. Mater.* **1997,** *9* (3), 230-232.

44. Singh, L.; Singh, R., Synthesis and photophysical properties of new Ln(III) (Ln = Eu(III), Gd(III), or Tb(III)) complexes of 1-amidino-*O*-methylurea. *Chem. Pap.* **2014,** *68* (2), 223-232.

45. Mabire, A. B.; Robin, M. P.; Quan, W.-D.; Willcock, H.; Stavros, V. G.; O'Reilly, R. K., Aminomaleimide fluorophores: a simple functional group with bright, solvent dependent emission. *Chem. Commun.* **2015,** *51* (47), 9733-9736.

CONCLUSIONS AND FUTURE WORKS

In this thesis, various maleimide-based fluorescent probes have been presented for potential imaging applications. Maleimide-based fluorophores experience severe quenching in the polar protic solvents. With the aim of enhancing their emissions, a library of fluoroalkyl-substituted aminochloromaleimides and monoaminomaleimides were synthesized. The effect of derivatization with the fluoroalkyl groups on the optical properties of the maleimide has been discussed in Chapter 2. These small size, non-invasive fluorophores displayed enhanced emissions in protic solvents as well as in solid-state, providing an insight into the development of maleimide based dual-state emission probes. These dyes can potentially be utilized to synthesize responsive polymeric nanoparticles, for applications, such as disease diagnosis, surface studies, etc. The fluorinated maleimide unit can be incorporated into the polymeric backbone, through RAFT or ROMP polymerizations. These labeled amphiphilic polymers can then self-assemble into drug-loaded micelles, to obtain responsive polymeric nanostructures for bioimaging and therapeutic applications.

In Chapter 3, the scope was expanded from purely organic to organometallic luminophores. The synthesis of the fluorescent half-sandwich transition metal complexes has been achieved by coordinating with the maleimide ligands. The effect of the complexation, on the optical properties of the maleimide, was also addressed. The transition metal complexes have been widely employed for catalysis-based applications due to their excellent redox properties, however it is difficult to visualize their mechanism of actions (MoAs) due to the lack of fluorescence. The electrochemical studies for these half-sandwich complexes showed an on-to-off fluorescence switching as a result of electron transfer reactions. Such complexes could serve as potential candidates for the imaging of catalytic processes that occur in the

biological systems. These fluorescent half-sandwich maleimide complexes contain d^6-metal atoms that could catalytically generate reactive oxygen species, to restrict the migration of tumor cells in biochemical systems, and MoAs can be monitored by using fluorescence microscopy and flow cytometry. Further prospects of half-sandwich metal maleimide complexes involve their efficient conjugation with biomolecules, such as protein, peptides, DNA, etc., owing to the presence of reactive functionalities in the maleimide.

Finally, for the purpose of achieving stable lanthanide metal complexes, and the development of carboxylate groups containing maleimide ligands was presented. The maleimide derivatives employed as chromophores enhanced the luminescence of the lanthanides. The comparison of ligand- and metal-based electronic transitions provide some basic insight into the luminiscence mechanisms involved. However, to design future probes, useful for biomedical analyses and imaging, based on the current lanthanide-maleimide system, more research and understanding of the driving forces is required.